Acoustic Investigation of Perforated Liners in Gas Turbine Combustors

A dissertation presented in partial fulfilment of the requirements for the

Degree of Doctor of Philosophy (PhD)

In The University of Hull

By

Abdullah Shahjalal

January 2021

Faculty of Science and Engineering

University of Hull

Abstract

Modern combustion systems in industrial applications, from the gas turbine to aero or rocket engines, have become more critical during the last few years due to an exponential increase in commercial air traffic, resulting in an elevated level of atmospheric pollution in the form of exhaust smoke. To develop an efficient combustion system under variable load conditions, bias flow has been introduced progressively in the flame tube to decrease the temperature of the combustor liner in a consistent manner. Additionally, it is introduced as a passive damping device to increase the acoustic energy absorption from the system.

This thesis amalgamates gas turbine combustor liner acoustic and static pressure measurements, along with their predictions. The primary objective of this investigation is to identify the passive damper maximum acoustic energy absorption properties. It will also collect information for designers to develop a cylindrical combustor liner geometry, along with flow factor, thermodynamic property and acoustic factors. A series of experiments was conducted, and the outcome of the investigation was compared with prior research, simulated data, and predictions to validate how this examination can be fundamental in advancing modern combustion systems.

The results suggest that non-zero bias flow can greatly improve energy absorption and shift the peak frequency; the system operates as a Helmholtz resonator. Static pressure measurements suggest that as the mass flow rate changes, so too does pressure ratio, which creates a nonlinear absorption property of the combustor. The liner with the lowest porosity creates the pressure curve for double layer combustors. This could prove useful in assisting architects to utilize the combustor as a damper, metering liner or, indeed, a combination of both. A semi-empirical hybrid model is developed based on experimental data.

Acknowledgement

First and foremost I wish to express my sincere gratitude to Dr. Qin Qin. I cannot articulate in words how grateful I am for his assistance in this project and researching under his supervision has been a supportive and inspiring experience. Completing this thesis would have been difficult without his vigilant guidance and expertise. The compact theoretical learning and rigorous academic standards from him significantly helped my theoretical and experimental work.

For providing a supportive and friendly operational working environment, much gratitude goes to Professor Philip Rubini and my industrial supervisors at Siemens Lincoln. Working with the team has been a wonderful, enriching experience.

Finally, a huge thank you to my family. Completing this thesis would have been all the more arduous if not for the unwavering support of my wife Feroza Akter and my children. You boosted my attitude and confidence daily. A special thank you to my parents; I want you to know how grateful I am for everything you have done for me. I have succeeded because of you.

Contents

List of figures

List of tables

Nomenclature

$\mathring{A}$	Strength of small source of sound
A_O	The cross-sectional area of the aperture
$\bar{A}$	Amplitude
$\ddot{A}$	Interaction area
A_{ei}	Effective area of the inner liner
A_{eo}	Effective area of the outer liner
A_{ec}	Estimated effective area
A_{is}	Inner liner single orifice area
A_c	The cross-sectional area of the annular cavity
A_i	The cross-sectional area of the annular inner liner
A_u^+	Incident upstream complex amplitude of a plane wave
A_2	Area of the second aperture
A_t	The cross-sectional area of the tube or cavity
A_T	The total area of the duct
A_p	Perforated plate area
B	Bernoulli enthalpy
B'	Fluctuating stagnation enthalpy
B_u^-	Reflected upstream complex amplitude of a plane wave
$\hat{B}_1$	Fluctuating part of the stagnation enthalpy related to external liner
$\hat{B}_2$	Fluctuating part of the stagnation enthalpy related to cavity
c	Speed of sound
C_d	Discharge coefficient of the orifice
C_{di}	Inner liner discharge coefficient of the orifice
C_{do}	Outer liner discharge coefficient of the orifice
C_{de}	Estimated discharge coefficient of the orifice
C_d^+	The transmitted downstream complex amplitude of plane wave
c_f	Cavity factor
C_p	Specific heat capacity of an air
C_1	Circumferential area of the duct or inner liner
C_2	Circumference to the outer cylinder
C_c	Effective contraction coefficient
C_{pe}	Perforate constant
d	Cavity depth
d'	Effective cavity depth
d_o	Diameter of aperture
D	Duct diameter
D_a	Axial pitch distance
D_d^-	The reflected downstream complex amplitude of plane wave
D_v	Dissipation caused by the viscosity
E	Acoustic energy flux
E_c	The kinetic energy of air passing through the circular aperture
f	Frequency
$\dot{f}$	Darcy friction factor
f_r	Resonant frequency
f_1 , f_2	Arbitrary functions
f_u	Upper-frequency limit
f_l	Lower-frequency limit
$F(K_s r)$	Viscous effect
$F(K_{sp} r)$	Viscous and thermal effect
H_n	Helmholtz number
$H(x_1)$	Heaviside unit function
$H_{n.ref}$	Frequency response function
I_1	Modified Bessel function of the first kind
$I, \bar{I}$	Acoustic intensity and Average acoustic intensity
I_X	The inertial reactance of an orifice

i, j	Complex Number
J_0	Bessel function of zero order
J_1	Bessel function of first order
k	Wave Number or translation factor
$\ddot{K}$	Factor for circular cross-section
k_c	Wave number due to the cavity
k_1	Modified Bessel function of second kind
k_u^+	Upstream incident wave number
k_u^-	Upstream reflected wave number
k_d^+	Downstream transmitted wave number
k_d^-	Downstream reflected wave number
k_s	Viscous stokes wave number
k_T	Thermal conductivity of air
k_R	Rayleigh conductivity of acoustic
K_1	Conductance of single aperture
k_{RM}	Modified Howe's conductivity
k_{BF}	Acoustic conductivity due to the bias flow through the hole
k_{TH}	Acoustic conductivity due to the thickness of the hole
k_{sp}	Effective viscous stokes wave number
ℓ	increments of modulus of cavity pressure
L	length of the sample or tube
l	Length of the orifice
l_t	Thickness constant
l'	Extra Mass of the fluid
l'_a	End correction length Attalla and Sgard
l_b	End correction Bellucci
l_{r}	End correction due to radiation reactance
l_{in}	End correction due to orifice interaction
l_{bf}	End correction due to bias flow
l_{nl}	End correction due to nonlinear effect
l_e	Effective or end correction length plus thickness of the aperture
l_0	Equivalent length for no flow
l_c	Length of the cooling cavity
l_{imp}	Length of the impedance tube
m_c	Parameter specifying increments of phase of cavity pressure
m	Acoustic mass
$\dot{m}$	Mass flow rate
$\dot{m}_i$	Mass flow rate of inner liner single hole
$\dot{m}_o$	Mass flow rate of outer liner single hole
M	Mach number
M_b	Bias flow Mach number
M_i	Mean Mach bias flow through the inner liner
M_o	Mean Mach bias flow through outer liner
M_c	Cross-flow Mach number
n	Multiple numbers
p_s	Signal Power
p_n	Noise Power
P_m	Mean pressure in the cavity
P_p	Mean pressure in the plenum
P_{du}	Mean pressure in the duct
p	Acoustic pressure or pressure of the incoming sound wave
$\dot{p}$	Wave propagation positive acoustic pressure
$\bar{p}$	Wave propagation negative acoustic pressure
p_0	Reference sound pressure
$\bar{P}$	Average acoustic power
P_T	Total pressure
p_+	High mean pressure amplitude
p_-	Low mean pressure amplitude

p_u	Upstream pressure
p_d	Downstream pressure
ΔP	Pressure drop or pressure difference
p'	Fluctuating pressure
$p_{1,2}$	Pressure exerted by aperture 1 at aperture 2
p_c	Acoustic pressure in the cavity
p_{pc}	Starting acoustic pressure in the cavity
Pr	Prandtl number
P_1,P_2,P_3 P_4	Complex sound pressure signal followed by distance x_1, x_2, x_3 & x_4
P_A,P_B	The pressure at the liner and rear of the cavity
P_{be}	Pressure loss term external to the orifice
p_{max}	Maximum sound pressure measured in a tube
p_{min}	Minimum sound pressure measured in a tube
Q	Acoustic volume flow
Q_T	Total volume flow rate
r	The radius of the aperture or orifice
$\dot{r}$	The radial component of a cylindrical coordinate system
R	Acoustic resistance
R	Specific gas constant
R_m	Molar gas constant
R_b	Nonlinear resistance due to large amplitude of acoustic velocity
R_s	Specific acoustic resistance
R_{po}	Porous Reynolds number
R_l	Specific acoustic resistance for larger hole
R_i	Internal resistance due to viscous loss in the hole
R_e	External resistance due to external to the hole
$\dot{R}$	Reflection Coefficient
$\ddot{R}$	Dimensionless fluidic damping Coefficient
R_c	Acoustic resistance due to cross-flow
$\dot{R}_h$	Normal incident reflection coefficient hard-back
r_0	The radius of the aperture in a boundary
r_b	The radius of the tube
R_p	Poiseuille's coefficient
R_f	Resistance coefficient as a function of frequency
R_d	Downstream reflection coefficient
R_n	Nominal end correction resistance
R_{nlr}	Melling nonlinear resistance
R_{rad}	Radiation resistance
R_{osr}	Orifice surface resistance
R_{inh}	Ingard nominal Helmholtz type loss resistance term
R_{inp}	Ingard nominal Poiseuille type loss resistance term
R_{snh}	Sivian nominal Helmholtz type loss resistance term
R_{snp}	Sivian nominal Poiseuille type loss resistance term
s	Laplace variable
S	Attached mass area of the orifice
Sh	Shear number
S_i	Inner liner area
S_o	Outer liner area
S_p	The cross-sectional area of the duct
S_c	The cross-sectional area of the annular cavity along with the boundary condition
St	Strouhal number due to bias flow
St_{ac}	Acoustical Strouhal number
$\bar{S}$	Duct cross-section
S_p	The cross-sectional area of the duct
t	Time
$\dot{T}$	Transmission coefficient
TL_n	Normal incident transmission loss

ΔT	Temperature difference
u	Acoustic particle velocity
$\bar{u}$	Negative acoustic particle velocity
u_n	Nonlinear effect of acoustic velocity normal to the liner surface
U_T	Total acoustic particle velocity
u_h	Particle velocity through the single hole
u_{uc}	Orifice acoustic particle velocity in the cavity
$\dot{u}$	Perturbation velocity
U	Mean perturbation or bias flow velocity
u_c	Mean vortex shed velocity along the plane of the aperture due to bias flow
u_τ	Friction velocity of cross flow
u'	Fluctuating axial velocity
$\bar{u}_c$	Mean cross-flow velocity
$\hat{u}$	The complex amplitude of controlled flow velocity through the lined duct section
$\hat{u}_1$	The complex amplitude of the particle velocity in the cavity along the rigid wall
U_s	Tangential velocity amplitude
u_{rms}	Root mean square value of the acoustic particle velocity
v	Velocity related to the acoustic pressure
V_c	Combined hole velocity of the liner
V_w	The radial mean velocity of the inner liner
V_S	RMS signal voltage
V_N	RMS noise voltage
V_n	Average duct velocity
$\hat{v}_1$	In word fluctuating liner bias flow velocity
W_i	Incident sound power
W_t	Transmitted sound power
x	Axis or co-ordinate
X	Reactance
X_c	Combined mass reactance
x_i	Length of the inner liner
x_o	Length of the outer liner
X_c	Reactance due to cross-flow
y_i	Width of the inner liner
y_o	Width of the outer liner
p_T	Total acoustic pressure
v_T	Total acoustic velocity
Z	Acoustic impedance
Z_a	Normal surface impedance due to anechoic termination
Z_c	Characteristic Impedance
Z_e	Impedance due to end correction
Z_p	Non-dimensional specific acoustic Impedance of the perforated plate
Z_h	Non-dimensional specific acoustic Impedance of the single hole
z_l	Impedance due to thickness
$\Delta Z_i, \Delta Z_o$	The specific acoustic impedance of inner and outer liner orifice
Z_b	The impedance of the perforation due to bias flow
Z_t	Total Impedance
$\mathrm{z_s}$	Specific acoustic impedance
Z_e	Impedance due to the radiation reactance or external
Z_x	Specific acoustic reactance
Z_d	Normal surface impedance of the air layer
Z_{ca}	Impedance due to the cavity
Z_{per}	Impedance due to the perforation
Z_{ie}	Impedance due to interaction end correction
Z_{ab}	Total collected impedance
Z_{sr}	Helmholtz type surface resistance
Z_s	Impedance due to the surface resistance
Z_{cr}	Impedance per unit length Crandall solution
$Z_{1,2}$	Interaction specific impedance

Z_{be}	Bellucci impedance due to perforation
Z_{bes}	Bellucci perforated screen impedance with cavity
Z_{Jing}	Jing and sun normalised specific acoustic impedance
Z_{me}	Melling impedance term
Z_{betts}	Betts impedance term
Z_{th}	Thurston impedance term
	Greek Symbols
ρ	Density of air
β	Viscous penetration depth
γ	Real part of the resistance
δ	Imaginary part of the reactance
ω	Angular frequency
$\dot{\omega}$	Curl Vorticity
$\ddot{\omega}$	Mean perturbation vorticity
$\overline{\omega}$	Perturbation vorticity along azimuthal direction
σ	Porosity
σ_1	The porosity of the inner liner
σ_2	The porosity of the outer liner
ς	Pressure loss coefficient assumed time independent
ξ	Fluid displacement particle velocity
δp_c	An argument for change in modulus of starting pressure in the cavity
$\delta\varphi_{pc/p}$	Change in starting pressure in the cavity
$\mho_o, \mho_i$	Outer and inner liner orifice acoustic velocity
$\bar{\rho}$	Fluctuating density
ρ, ρ_c, ρ_o	The density of air corresponding to local duct, cavity, and outer liner
c, c_c, c_o	Speed of sound local corresponding to duct, cavity, and outer liner.
φ	Pressure gradient parallel to the x-axis
$\emptyset$	Equivalent diameter
ψ^+, ψ^-	Characteristics quantities forward and backwards travelling wave
ω	Angular frequency
ν	Kinematic viscosity
ν'	Effective kinematic viscosity
$\psi(\sigma)$	Polynomial approximation of Fok function
ζ	Interaction parameter or correction factor
$\dot{\gamma}$	The ratio of specific heat capacity
μ	Dynamic viscosity
μ'	Effective dynamic viscosity
λ	Wavelength
γ_c	Specific heat capacity in the cavity
Δ	Absorption coefficient
$\ddot{\Delta}$	Dissipation coefficient
η_1	Compliance of the inner liner
η_2	Compliance of the outer liner
η_t	Total compliance of the liner
δ_{12}	Interaction end correction
$\hat{v}_1$	Inward fluctuating bias flow velocity
$\hat{v}_2$	Inward fluctuating bias flow velocity through the outer liner
	Subscript and Superscript
$+$	Positive x-direction, in word flow
$-$	Negative x-direction, out word flow
e	External
i	Internal or in
o	Out
c	Cavity
a	Anechoic termination
b	Rigid or open-end termination

Acronyms

FRF	Frequency Response Function
FFT	Fast Fourier Transform
SNR	Signal to Noise Ratio
SPL	Sound Pressure Level
RMS	Root mean square
MPP	Micro-Perforated Panel
OHV	Orifice Hole Velocity
HAT	Hot Acoustic Test
TMM	Two Microphone Method
PBF	Perforate Bias Flow
TL	Transmission Loss
$UHARC$	University of Hull Acoustic Research Centre
FFT	Fast Fourier Transform
UHC	Unburnt Hydrocarbon
KTH	Royal Institute of Technology
NLR	National Aerospace Laboratory
DLR	German Aerospace Centre
$ASTM$	American Society for Testing and Materials

1 Introduction

In a gas turbine, the layout of the holes in a combustor's wall geometry is determined by combustion and cooling requirements. In new combustor designs, conversion of acoustic energy into mechanical energy, thus increasing the output turbine efficiency, plays a vital role in the current marketplace. Tighter emission controls and concerns to reduce combustion noise levels are also imperative in new designs. The function of a conventional combustion chamber can be explained as follows. The combustion liner introduces additional air in the combustion process, which cools down hot gas before it enters the turbine. It also cools down the combustion chamber wall and controls the total amount of air introduced into the combustion process (Soares, 2011).

In a modern combustor, flow distribution has changed drastically. Lean combustion systems demand more air in the combustion chamber and, as a result, reduction of the cooling of hot gases before they enter the turbine becomes necessary. Usually, the combustor operates at high pressure and high temperature, with a relatively low mean velocity within the combustion chamber (Lefebvre & Ballal, 2010). The overall pressure ratio is defined as the pressure at the inlet and the pressure delivered to the combustor (Saunders, 1996). Standing gas turbines characteristically operate at pressure ratios between 10 and 25. The turbine inlet temperature is known as the characteristic temperature, which is the temperature of the flow from the combustor towards the inside of the turbine. From an efficiency point of view, a high-temperature inlet flow is essential. The maximum temperature is limited to the material characteristics of the turbine blade and a functional cooling system. At present, a temperature of around 1900K can be accomplished (Gas-Turbine-Industries, 2011), whereas theoretical values are between 1300-1700K (Bräunling). However, the flame temperature inside the combustor can be as high as 2200-2600K (Bräunling). The lean-burn temperature is usually below 2000K (Lefebvre & Ballal, 2010). The cooling of air delivered by the compressor is normally between 500-800K (Saunders, 1996). For pre-mixed flames, the flow velocity is restricted by the flashback and blow-off limits. A flashback occurs at low flow velocities while the flame propagates upstream to the source, where flow velocity is slower than the flame speed. In order to stabilise the flame, the flow velocity exceeds the flame speed of a real combustor. The upper limit of the flow velocity is given by the blow-off

condition, where the flame cannot be stabilised and is convected downstream by the flow (Lieuwen, 2012). From the second restriction, the mean Mach number in the combustor is fairly low - commonly around 0.05 (Lieuwen & Yang, 2005). The velocity of the bias flow through the perforated wall is determined by the pressure drop across the wall from a static pressure measurement. At typical operating conditions there is a 3 % pressure drop (Rupp et al., 2012). Thermo-acoustic instabilities in a gas turbine combustor are typically observed at a frequency range of 100-1000 Hz (Krebs et al., 2005; Mongia et al., 2005). In this present investigation, calculations are carried out over a frequency range of 0-1000 Hz, as described in section 4.14, and overall energy balance plus signal analysis, in section 5.3, over a frequency range of 50-1000 Hz. The actual frequency range depends on the combustor geometry and the operating conditions. Thus, the frequency is not fixed, but potentially changes during operation. The performance factors of gas turbine combustors include a multitude of parameters that might be relevant for the acoustic performance of the liner; these parameters are commonly classified into four groups based on their physical derivation, as set out below.

- Geometric factors
  a) Orifice geometry
  b) Orifice orientation
  c) Cavity depth
- Thermodynamic factors
  a) Pressure
  b) Temperature
- Flow factors
  a) Bias flow
  b) Cross-flow
- Acoustic factors
  a) Frequency
  b) Amplitude

Some of these factors are fixed by the operating conditions and cannot be modified. Thus, an additional classification can be made into dependent and independent factors. The dependent factors cannot be manipulated as a design tool to increase acoustic performance; they are fixed by the operational requirements of the gas turbine combustor. Nonetheless, their impact on performance is of great importance. The independent parameters can be adjusted within certain limits to optimise the damping process (Lahiri, 2014).

1.1 Instabilities

In a gas turbine combustion system, due to unsteady heat release by the propagation of the flame, combustion instability occurs. The majority of the instabilities occurring in gas turbine combustors is due to the resonance interaction between the combustion and coupling mode. When the natural resonance time-period of the flow comes close to the characteristic time-period of the combustion process, combustion instability occurs. The response process

relates from the downstream flow to the upstream flow section, in which condition perturbations are initiated (Lieuwen, 2012). Consequently, acoustic wave propagation is typically responsible for the response path. This coupling process may involve convective modes such as entropy waves, stagnation enthalpy, temperature fluctuations, and vorticity convection etc. In such a fluctuation, the downstream end of the combustor flow is reflected in the form of upstream propagating pressure waves. Aside from acoustic instability, other forms of instability can disturb the system, such as unsteady heat release, unsteady strain rate, flame propagation, vortex interaction, flame coupling, and the interaction of perturbed flame within the boundaries (Goh & Morgans, 2013).

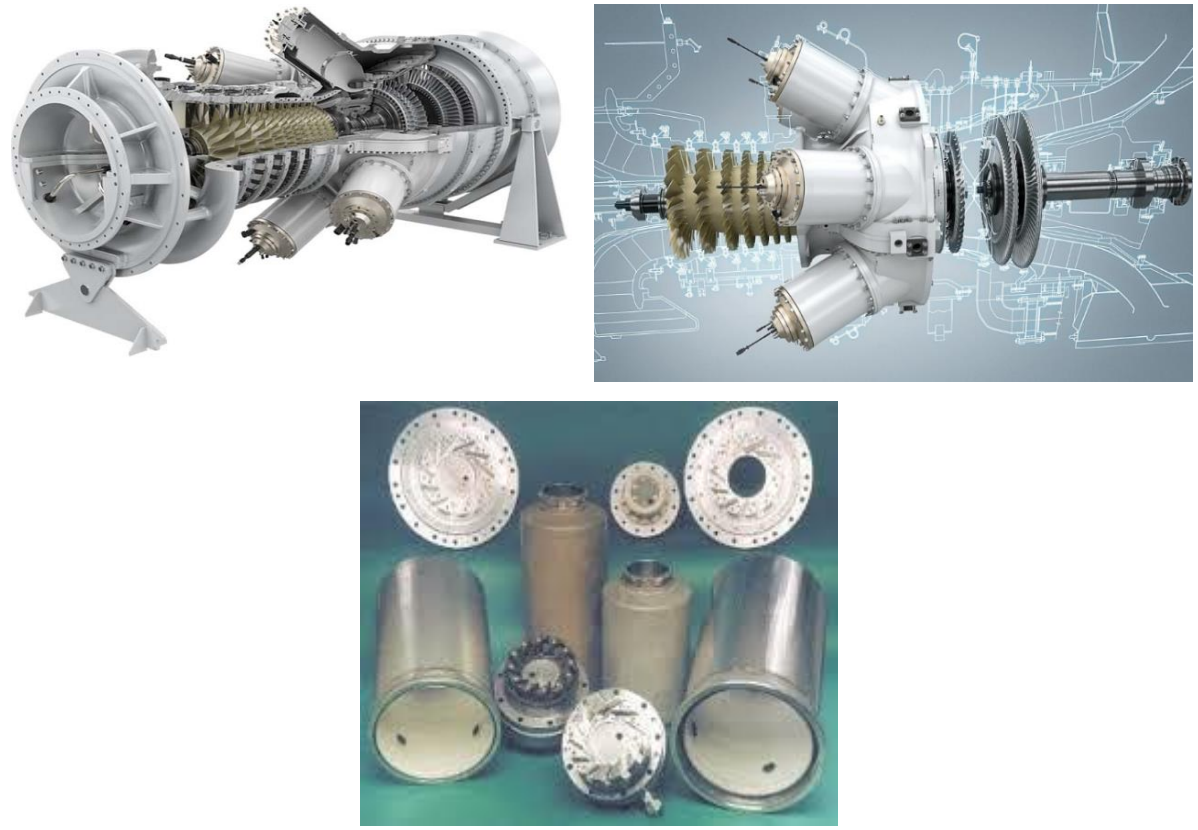

Figure 1.1 Siemens SGT-400 gas turbine & combustion hardware

(Siemens, 1996 – 2019; Welch & Igoe, 2013).

Siemens SGT-400 Gas Turbine is a twin shaft engine for mechanical drive power generation (Siemens, 1996 – 2019). Figure 1.1 shows the cross-sectional view of the SGT-400 Gas Turbine above and the Siemens small Gas Turbine combustion hardware below. These dampers are known as passive acoustic dampers and have been investigated by many researchers in order to optimise their performance (Ingard, 1953; Keller & Zauner, 1995; Rayleigh, 1945a). The

properties of absorption or dissipation depend on the geometry of the perforation and acoustic excitation (Cummings, 1984; Hersh et al., 2003; Ingard & Ising, 1967; Maa, 1998).

1.2 Motivation

Acoustic waves are a different type of pressure disturbance, which can propagate through a compressible fluid. When sound waves propagate through a compressible fluid such as air, the molecules move back and forth – or vacillate – in the direction of propagation, producing adjacent regions of compression and expansion. This introduces momentary changes to the ambient values of pressure and density (Seybert, 2000). The ambient pressure and density are assumed to be independent of the position of the point, i.e. the fluid is assumed to be homogeneous. The disturbance to the ambient pressure is known as acoustic pressure, which is a scalar. The process of compression and expansion also results in motion of the particles of the fluid about the point. The velocity of this motion is so-called particle velocity, which is a vector. The term particle of the fluid means a volume element large enough to contain millions of molecules so that the fluid may be viewed as a continuous medium, yet small enough that all acoustic variables may be considered nearly constant throughout the volume element (Kinsler et al., 1999). In order to articulate the mathematical description of acoustic waves, several assumptions are commonly employed: viscous forces are neglected, the fluid is inviscid; body forces such as gravity are neglected; fluid properties are homogeneous, isotropic, and perfectly elastic or obey the Ideal Gas Law; and the acoustic disturbances are small. In most cases of noise control, acoustic variables such as acoustic pressure and particle velocity are much less than the ambient value. The analysis of small disturbances to the ambient state of the fluid is referred to as linear acoustics (Seybert, 2000).

1.3 Framework

In a conventional combustor, chamber holes are used for cooling requirements. Early gas turbine engines used a single chamber called a can-type combustion chamber, or flame holder. The cooling chamber allows the neck and cavity to be cooled with compressed airflow. The oldest combustion chamber has larger holes towards the rear of the liner for dilution and cooling purposes, before the gas enters the turbine. The total amount of air introduced in the combustion chamber is usually classified as primary air introduced through the whirler, and secondary air presented through the larger holes (Foltz, 1993). A recent investigation (Lahiri, 2014) shows that introducing airflow through the liner not only cools the combustor chamber,

but also absorbs the acoustic pressure. Researchers and developers are investigating orifice shape, geometry and orientation and, additionally, introducing modified bias flow to control thermoacoustic instability and lower co_2 emissions from the exhaust system. Bias flow velocity is the velocity that is related to the absorption of sound. Efficient combustion has become more and more critical during the last few years because of the rapid growth in commercial air traffic and consequent increase in atmospheric pollution in the form of exhaust fumes (Gerendas et al., 2003). Advanced combustors are designed for low emissions and higher efficiency, which is achieved by rearranging the liner walls and introducing a large number of small holes into the system. Variable parameters are orifice angle, orifice orientation, porosity, axial pitch distance, wall thickness, the diameter of the orifice, and the introduction of a double-layer combustor liner. The temperature of hot air produced by a combustor is much too high to enter the turbine. To cool down the hot air uniformly, bias flow has been introduced progressively in the flame tube. Approximately a third of it is used to reduce the gas temperature in the zone of dilution, and rest is used for cooling the combustor walls. This is carried out by introducing bias flows that flow along the internal surface of the flame tube, isolating it from combustion gases (Haynes et al., 2006). Usually, a gas turbine operates at high temperature and pressure, with low mean flow velocity. The gas turbine has a lower pressure ratio compared to aero engines. The terms compression ratio and pressure ratio are used interchangeably. Gas turbine characteristics depend on performance ratings, based on the temperature of the flow from the combustor and inward bound to the turbine. For efficiency, the turbine inlet temperature is critical; meanwhile, the maximum temperature is limited by the material characteristics of the turbine blade and cooling system.

1.4 Thesis objective

The objective of this thesis is to measure the damping effect in a range of liners. This can be done by using the two-microphone method or the transfer-matrix method. The two-microphone method (TMM) is used for acoustic analysis as, when both calculations were tested, it was found that this method provides greater accuracy. Therefore, on successfully determining the liner-damping effect based on single and double-layer liners, it is necessary to outline the effect of bias flow in a cylindrical combustor liner. To execute that experimental analysis effectively, 13 different sets of combustor liner arrangement have been laid out,

including a dummy liner, as shown in Table 4.5. Dummy liner acoustic analysis provides a benchmark and indicates the accuracy of the acoustic measurement technique. A one-dimensional plane wave was considered for this experiment but acoustic energy flowed from the upstream section to the downstream section, thus the one-sided definition of absorption or dissipation is applied to the experiments and models. An experiment is carried out for the no flow and non-zero bias flow cases. The semi-empirical hybrid model is developed for the no flow acoustic analysis only. For each combustor liner configuration, acoustic analysis is carried out to measure transmission loss, absorption, or dissipation coefficient, resistance and reactance terms. Static pressure measurement is carried out to calculate the discharge coefficient of the orifice, Mach number, pressure ratio, and orifice hole velocity etc. Subsequently, comparison of the prediction with the experiment dummy liner signal analysis, and overall energy balance calculation, is analysed to develop two-factor authentication and model validation.

1.5 Thesis outline

This thesis is organised into five chapters and two appendices as follows:

Chapter 1 - the introduction, discusses instabilities, the research motivation, framework, and thesis objective. Furthermore, gas turbine operating boundary conditions, thermo-acoustic instabilities, pressure drops, and various physical parameters are also discussed.

Chapter 2 discusses the background theory and contains a literature review of the current state of the art technology, which includes past and recent developments of various analyses and models, including end correction, and orifice interaction effect.

Chapter 3 examines the preliminary impedance model. The numerical analysis is undertaken to represent the prediction of experiment for the no flow condition. It describes the impact of total impedance such as impedance due to perforation, impedance due to the end correction, impedance due to surface resistance, impedance due to the interaction end correction, and impedance due to the cavity. From the collected impedance, the magnitude of the reflection and absorption profile is developed.

Chapter 4 discusses static pressure measurement and acoustic analysis. Static pressure measurement explains how the discharge coefficient of the orifice is developed. It is essential for real combustor design to discuss the procedure of developing a discharge coefficient of the orifice. It is also essential to designate whether the liner acts as a damper or pressure

controller, or both. In addition, discharge coefficient versus mass flow rate, and discharge coefficient versus pressure ratio are exhibited. A one-dimensional plane wave is introduced into the cylindrical combustor liner to draw acoustic analysis. No flow and non-zero bias flow cases are presented in terms of transmission loss, absorption, and dissipation coefficient.

Chapter 5 evaluates the validation of numerical analysis and presents a comparison of the prediction with data and experiments carried out in UHARC. This semi-empirical hybrid model can predict liner resistance and reactance terms along with the absorption profile. For simplicity, to create a two-factor authentication a dummy liner acoustic analysis is compared with the prediction. Additional acoustic analysis is interpreted in terms of signal and integrated energy, which can be beneficial to designers.

Chapter 6 summarises the conclusions and achievements of this research contribution. In addition, the limitations of the model, drawbacks of the experiment and suggestions for future research are discussed.

Appendix-A describes a Hot Acoustic Temperature (HAT) test rig project proposal. The main purpose of designing the test rig is to examine the impedance effect in high temperature regions. No flow and non-zero bias flow experiments can be carried out up to 773K temperature region with a usable frequency range of 85-2000 Hz.

Appendix-B demonstrates the resonator performance factor of circular orifice and slots type shape. The purpose of this additional experiment is to examine the behaviour of circular and slots type orifice damping factors, magnitude, and phase in frequency response function (FRF).

2 Literature review

In this literature review section, the primary focus is to establish the current technological development, along with previous findings, to define more clearly acoustic impedance, acoustic analysis of transmission loss, and absorptive and dissipative energy loss from the gas turbine combustor in the presence of bias flow.

2.1 Acoustic impedance

There are common boundary conditions for the solution of the Helmholtz equation, which are categorised as either active or passive boundary conditions. Active boundary conditions are those in which there is either motion or sound pressure on the boundary (Seybert, 2000). An active boundary condition occurs when the sound pressure is acknowledged. The second type of active boundary condition occurs when the normal velocity is acknowledged. A passive boundary condition occurs when sound is reflected from a passive surface, i.e. absorbing the material in contact within the medium. When acoustic waves come into contact with the surface of the fluid, the amplitude and the phase of the reflected wave relative to the incident wave depend on the acoustic impedance Z of the surface or boundary. Acoustic impedance is the ratio of complex acoustic pressure p to acoustic volume flow Q (Rayleigh, 1870; 1945c) shown in equation (3.21), where acoustic particle velocity u passes through the aperture area A. The acoustic impedance at a particular frequency indicates how much sound pressure is generated by the vibration of molecules of a particular acoustic medium at a given frequency.

$$Z = \frac{p}{Q} = \frac{p}{Au} \tag{2.1}$$

The acoustic impedance determines the acoustic interaction between coupled regions of fluid because it indicates the degree of similarity between the acoustic properties of the regions. This determines the degree to which acoustic waves in one region are reflected and transmitted at the interface. It is also used to analyse the interaction between the fluid and solid systems with regards to sound absorption, reflection, and transmission. The acoustic impedance is a vector since it is the ratio of complex acoustic pressure as a scalar, and acoustic particle velocity as a vector (Dietrich, 2013). The direction of impedance is determined by the direction of particle velocity passing through the aperture area. The ratio of acoustic pressure

in a medium to the associated particle velocity is defined as the specific impedance z_s . It can be expressed in units of Rayl.

$$ZA = z_s = \frac{p(x,t)}{u(\mathrm{x,t})} \tag{2.2}$$

For progressive plane waves, specific impedance is a real quantity called the characteristics impedance since the pressure and particle velocity are in phase.

$$z_s = \frac{p(x,t)}{u(x,t)} = \frac{\rho c j\omega A e^{j(\omega t - kx)}}{j\omega A e^{j(\omega t - kx)}} = \rho c = Z_c \tag{2.3}$$

The product of the fluid density by the speed of sound c in fluid density ρ defines a characteristic property of the medium, and therefore it is often called the characteristic impedance Z_c. For standing plane waves and diverging waves, specific impedance is a complex quantity, where j is the complex number, ω is the angular frequency, k is the wavenumber, and t is the time.

2.1.1 Superposition of two waves propagating in opposite directions

The pressure and the velocity, for a wave propagating toward the positive x-direction

$$\dot{p}(x,t) = A_u^+ e^{j(\omega t - kx)} \tag{2.4}$$

$$u(x,t) = \frac{A_u^+}{Z_c} e^{j(\omega t - kx)} \tag{2.5}$$

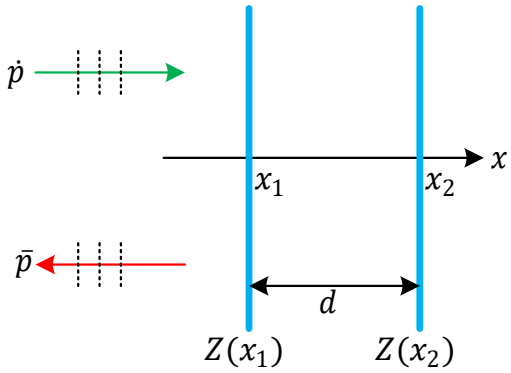

Figure 2.1 Plane waves propagate both in the x direction and in the opposite direction.

The pressure and the velocity, for a wave propagating toward the negative x-direction

$$\bar{p}(x,t) = B_u^- e^{j(\omega t + kx)} \tag{2.6}$$

$$\bar{u}(x,t) = -\frac{B_u^-}{Z_c} e^{j(\omega t + kx)} \tag{2.7}$$

Where A_u^+ is the incident and B_u^- is the reflected complex amplitude of a plane wave, $\dot{p}$ and $\bar{p}$ is the wave propagating positive and negative acoustic pressure, u and $\bar{u}$ is the wave

propagating positive and negative acoustic particle velocity (Allard & Attala). Figure 2.1 shows that two waves propagate in opposite directions parallel to the x- axis. If the acoustic field is a superposition of the two waves described by the above equations (2.4),(2.5),(2.6),(2.7) then the total pressure $P_T(x,t)$, and total velocity $U_T(x,t)$ are

$$P_T(x,t) = A_u^+ e^{j(\omega t - kx)} + B_u^- e^{j(\omega t + kx)} \tag{2.8}$$

$$U_T(x,t) = \frac{A_u^+ e^{j(\omega t - kx)} - B_u^- e^{j(\omega t + kx)}}{Z_c} \tag{2.9}$$

A superposition of several waves of the same ω and k propagating in a given direction is equivalent to one resulting wave propagating in the same direction (Mathews Jr, 1986). The ratio $P_T(x_2,t)/U_T(x_2,t)$ is called impedance at x_2. Also, we can evaluate the following expression

$$Z(x_1) = Z_c \frac{-jZ(x_2)\cot(kd) + Z_c}{Z(x_2) - jZ_c\cot(kd)} \tag{2.10}$$

where d is a depth between $x_2 - x_1$. The impedance at $Z(x_1)$ equation (2.10) is known as the transcendental equation (Allard & Attala). The details of the transmission line theory will be discussed in section 3.4.

2.1.2 Cavity impedance for double liner

An alternative cavity impedance model for a double liner equation is given below with a cavity-backed thin layer

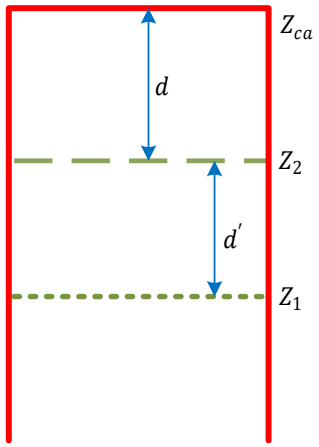

Figure 2.2 Double liner impedance model for cavity-backed thin layer.

Figure 2.2 shows an alternative cavity impedance model for double liner cavity-backed thin layer. Where d is the cavity depth, Z_1 represents the effective characteristic impedance of the 'layer' (ρc to a first approximation) of thickness d' is the effective cavity depth (distance

in between the perforated cylinders), Z_{ca} is the impedance due to the cavity, and Z_2=cot($-jkd$).

$$Z_{ca} = Z_1\left[\frac{\{Z_2 - iZ_c\tan(kd')\}}{\{Z_c - iZ_2\tan(kd')\}}\right] \quad (2.11)$$

Double liner cavity-backed thin layer impedance model equation given in (2.11).

2.1.3 The acoustic impedance of a single hole

From equation (2.3) the specific acoustic impedance of a single hole can be written as the pressure difference across the hole over the particle velocity through the hole $z_s = p_+ - p_-/u_h$

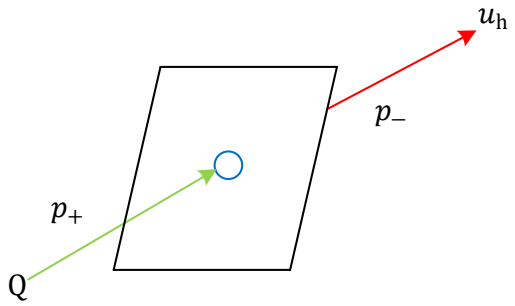

Figure 2.3 Schematic diagram of acoustic pressure difference of a single hole.

Figure 2.3 displays the acoustic impedance of a single hole, where u_h is the acoustic particle velocity through the single hole and $p_+ - p_-$ represents pressure amplitude difference across the hole. Unfolding the neck or hole dynamics the specific impedance of the hole can be written as

$$z_s = ZA = \frac{p_+ - p_-}{Q}\ A = \rho l' s \quad (2.12)$$

where l' is the extra mass of the fluid (BARON RAYLEIGH, 1871; Rayleigh, 1945a). By changing the Laplace variable s in equation (2.12) to $j\omega$ results in the specific acoustic impedance in the frequency domain (Deicon Dynamics & Control, 2009). This frequency-dependent, complex specific acoustic impedance is given in equation (2.13)

$$z_s = j\rho l'\omega \quad (2.13)$$

The specific acoustic impedance of a single hole Z_h is generally made dimensionless by dividing the characteristic impedance of its medium Z_c

$$Z_h = \frac{z_s}{Z_c} = \left(\frac{p_+ - p_-}{u_h}\right) * \frac{1}{\rho c} \quad (2.14)$$

where Z_h is the non-dimensional specific acoustic impedance of a single hole Tournadre et al. (Tournadre et al., 2016b).

2.1.4 Non-dimensional specific acoustic impedance

The non-dimensional specific acoustic impedance of the perforated plate is defined as

$$Z_p = \frac{p_+ - p_-}{uZ_c} \tag{2.15}$$

where Z_p is the perforated plate non-dimensional specific acoustic impedance. Acoustic particle velocity of the medium adjacent to the perforated plate, using the conservation of mass particle velocity through the hole, can be related to u as given below in equation (2.16) (Guess, 1975b).

$$u = \sigma u_h \tag{2.16}$$

where σ is the porosity of the perforated plate. Therefore, the impedance of the perforated plate in terms of porosity can be written as

$$Z_p = \frac{Z_h}{\sigma} \tag{2.17}$$

The impedance of the plate given in equation (2.17) is commonly used in the acoustic analysis of the liners. There exist several empirical and semi-empirical relationships for the specific acoustic impedance of perforated plates (Bauer, 1977).

2.2 Model analysis and evaluation of previous work

There exist several analytical, empirical and semi-empirical models to predict orifice impedance under various flow conditions. There have been investigations of the impedance of a circular orifice involving different geometric parameters with a no flow condition, i.e., acoustic flow only. Other studies have determined the full-scale cylindrical combustor liner absorption characteristics with various geometric parameters, such as orifice diameter, orifice thickness, orifice spacing, orifice orientation, and perforation ratio concerning frequency. Acoustic liners are ostensibly used to reduce noise in many industrial applications such as aircraft engines, gas turbines, and exhaust silencers. There is another aim of using perforated liners as a passive sound absorbing medium under various locations of the sound source. In order to build low emission combustion systems in modern gas turbines and aero engines, optimising the bias flow control became imperative for development. A definition of the acoustic properties of the Helmholtz resonator was first attempted by Rayleigh (Rayleigh, 1945b; Rayleigh, 1940). The concept of acoustic conductivity is similar to Ohm's law in

electricity. Electric conductivity is defined as the ratio of electric current to the potential difference, and the acoustic conductivity of an orifice is defined as the ratio of volume flow through the orifice to the pressure difference across the orifice. The Helmholtz resonator takes two principal forms; single resonators and distributed resonators. Two common characteristics of the Helmholtz resonator are the cavity and the opening area where the sound energy enters the cavity. For a distributed Helmholtz resonator, the cavity is generally shared by the resonator opening area, and each opening area is connected with the cavity volume, determined by the distance between the perforations. The acoustic properties of bias flow have been examined intensely in the past half-century in order to recognise the acoustic vortex interface mechanism, which generally occurs in the lined acoustic medium triggering sound absorption. Ingard and Ising (Ingard & Ising, 1967) found a linear relationship between pressure and velocity amplitudes for oscillatory flow with sufficiently low amplitudes and large amplitudes. The effect of acoustic properties in the presence of various flow conditions will be discussed below.

2.3 Rayleigh conductivity in acoustics

Rayleigh conductivity describes the transmission of acoustic waves through an orifice; when flow passes through a hole, it effectively behaves like a piston of air, whose length is larger than the depth of the hole due to inertial effect. The ratio between the rate of change of mass flow rate and the pressure difference is defined as acoustic conductivity (Morse & Ingard), usually expressed in the frequency domain. Lord Rayleigh (Rayleigh, 1870; 1945c) developed an analytical formulation of K_R in which two core assumptions were made. Inviscid and incompressible flows were taken into consideration. Flow through the aperture has a high Reynolds number, but a low Mach number. The Navier-Stoke equation for inviscid and incompressible flow, known as the Euler equation, is given below.

$$\frac{\partial u}{\partial t} + (u.\nabla)u + \frac{\nabla p}{\rho} = 0 \tag{2.18}$$

With no bias flow, the nonlinear term is negligible, and the Euler equation simplifies to

$$\frac{\partial u}{\partial t} + \frac{\nabla p}{\rho} = 0 \tag{2.19}$$

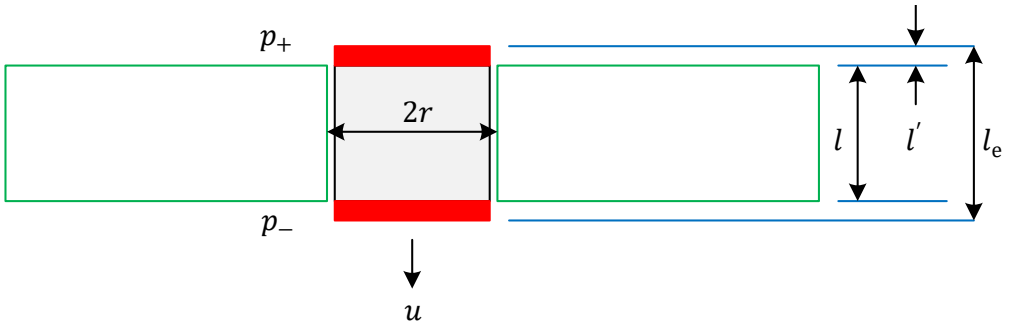

Figure 2.4 Rayleigh conductivity of an orifice.

From Figure 2.4 Rayleigh conductivity of an orifice is determined by considering the plane wave of propagation through the orifice with respect to time t, upstream pressure $p_u = Re\left(p_+ e^{j\omega t}\right)$ and downstream pressure $p_d = Re\left(p_- e^{j\omega t}\right)$. Therefore, the difference between up and downstream pressure becomes $Re\{(p_+ - p_-)e^{j\omega t}\}$ which produces a fluctuating volume of velocity $Q' = Re(Q)e^{j\omega t}$ through the orifice. When the flow refers to a property in a medium whose density is constant and the orifice is acoustically compact after extended manipulation, the relationship between mass flow rate and pressure, (Rayleigh, 1870; 1945c) conductivity K_R can be expressed as

$$K_R = \frac{\dot{m}}{\Delta P} = \frac{j\omega\rho Q}{(p_+ - p_-)} \tag{2.20}$$

where K_R is the Rayleigh conductivity of an orifice, $\dot{m}$ is the mass flow rate, ΔP is the pressure drop, p_+ is the high mean pressure amplitude, p_- is the low mean pressure amplitude previously described in section 0. For an ideal fluid, the Rayleigh conductivity is determined by the orifice geometry of a circular orifice in a wall of an infinitesimal thickness (Rayleigh, 1870; 1945c), which indicated that in the absence of bias flow,

$$K_R = 2r \tag{2.21}$$

where r is the radius of the aperture. For an orifice in a wall of finite thickness, the Rayleigh conductivity is expressed as the ratio of the area of the orifice and an effective length (Rayleigh, 1870; 1945c)

$$K_R = \frac{A}{l_e} \tag{2.22}$$

where l is the length of the orifice or thickness, l' is the extra mass of the fluid, l_e is the effective length of the orifice. Figure 2.4 shows that effective length of the orifice is larger than the physical length of the orifice. Due to mean jet velocity and incompressibility, a function of the fluid adds an extra mass of the fluid that takes part in the oscillation motion

of the orifice, commonly known as end correction for both ends (BARON RAYLEIGH, 1871; Rayleigh, 1945a)

$$l_e = l + 2l' \tag{2.23}$$

For end correction, Rayleigh (BARON RAYLEIGH, 1871; Rayleigh, 1945a) derives the upper and lower limit of the conductivity.

$$\frac{\pi r^2}{l + \frac{16}{3\pi} r} < K_R < \frac{\pi r^2}{l + \frac{\pi}{2} r} \tag{2.24}$$

For $l = 0$ the upper limit ties with equation (2.21) and the end correction can be considered from equation (2.24) in the limit of $0.785r < l' < 0.849r$. In an additional investigation, Rayleigh (BARON RAYLEIGH, 1871; Rayleigh, 1945a) proposes $l' \approx 0.82r$ as the suitable value for an orifice in an infinite wall.

$$l' = \frac{8}{3\pi} r \approx 0.85r \tag{2.25}$$

End correction term remains negligible for $l \gg r$; however, it could become increasingly important when $l \to 0$. Rayleigh conductivity is an unknown quantity; their relation appeared as the ratio between unsteady volume fluxes across the aperture to the unsteady pressure drop across the orifice. Therefore, conductivity appears as inversely proportional to the volume velocity impedance.

2.4 Crandall's model

Crandall has carried out a generalised form of the impedance of a single hole in a perforated panel as an infinite tube. The explanation of Crandall's (Crandall, 1926b) impedance model is specified below.

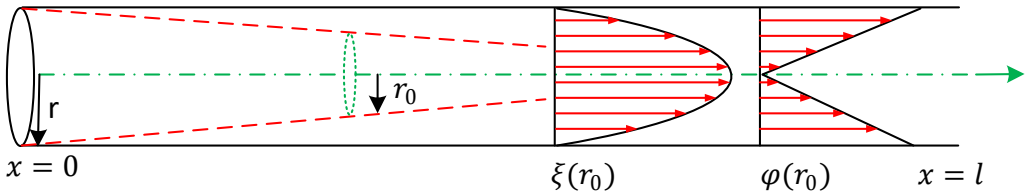

Figure 2.5 Shows the particle velocity and pressure gradient profiles due to viscous shear assumed in Crandall's impedance model.

The size of the hole is small compared to the wavelength. Flow-through the hole is considered as incompressible. The velocity profile is assumed to have only radial variations and to be constant through the length of the duct. Nonlinear terms replaced by time-averaged acoustic parameters and the velocity inside the tube is assumed to have a simple harmonic time

dependence. Figure 2.5 shows the Crandall impedance model for a viscous shear layer. The axis of the tube is represented as x and the circular section πr_0^2 of fluid is substituted for the circular membrane, the axial driving force now being φdx per unit area; $\varphi(r_0)$ is a negative pressure gradient parallel to the axis of the tube. The total driving force on an annular ring of fluid of volume $2\pi r dr dx$ is $\varphi dx 2\pi r dr$ which is opposed by a reactance $j\omega\rho 2\pi r dr dx$ due to inertia. The opposing resistive force due to friction on the inner surface of the ring is

$$-2\pi r dx \mu \left(\frac{\partial \xi}{\partial r}\right) \tag{2.26}$$

By using the negative velocity gradient from opposing resistive force due to friction, the effective fluid displacement particle velocity $\xi(r_0)$ decreases with increasing r. Therefore, the net force on the annulus due to the resistive part of the friction is:

$$\partial/\partial r(-2\pi r dx * \mu * \tfrac{\partial \xi}{\partial r}) \tag{2.27}$$

where $\varphi(r_0)$ represents a pressure gradient parallel to the x axis viscous force distribution, $\xi(r_0)$ is the effective fluid displacement particle velocity. From the above explanation, Crandall's impedance model equation of motion can be written as

$$\varphi = \left[j\omega\rho - \frac{\mu}{r}\frac{\partial}{\partial r}\left(r\frac{\partial}{\partial r}\right)\right]\xi \tag{2.28}$$

Since ξ is a function of r this can be written as

$$\frac{\varphi}{\mu} = -\left[\frac{\partial^2}{\partial r^2} + \frac{1}{r}\frac{\partial}{\partial r} + {k_s}^2\right]\xi \tag{2.29}$$

$$k_s = \sqrt{\left(\frac{-j\rho\omega}{\mu}\right)} \tag{2.30}$$

where k_s is the phase constant or viscous Stokes wave number philosophy specified by Stokes (Stokes, 1851) approximated by Helmholtz (Von Helmholtz, 1863), Kirchhoff (Kirchhoff, 1868a), Kinsler & Frey (Frey & Kinsler, 1950), Crandall (Crandall, 1926b), Melling (Melling, 1973b), Maa (1998), Allard (Allard, 1993) and many others. The solution being, for finite velocity, $r = 0$ then $\text{Å}J_0$, the solution of equation (2.29) can be written as

$$\xi = -\frac{\varphi}{\mu k_s^2} + \text{Å}J_0(k_s r) \tag{2.31}$$

where Å is the strength of a small source of the sound, J_0 represents the Bessel function of the zero order. To determine Å for boundary condition $r = r_0$ the velocity must vanish at the boundary, and the velocity is

$$\xi(r) = -\frac{\varphi}{\mu k_s^2}\left[1 - \frac{J_0(k_s r)}{J_0(k_s r_0)}\right] \tag{2.32}$$

Integrating $\xi(r)$ over the area of the cross-section gives mean velocity:

$$\xi = \frac{2}{r_0^2}\int_0^{r_0} \xi r dr = -\frac{\varphi}{\mu\kappa^2}\left[1 - \frac{2}{r_0^2 k_s^2 J_0(k_s r_0)}\int_0^{r_0} J_0(k_s r)\cdot k_s r \cdot k_s dr\right] \tag{2.33}$$

$$\xi = -\frac{\varphi}{\mu k_s^2}\left[1 - \frac{2J_1(k_s r_0)}{k_s r_0 J_0(k_s r_0)}\right] \tag{2.34}$$

The magnitude in brackets is equation (2.34), which represents the velocity profile function in the form $\xi = \varphi/R_f$. $R_f = \mu\beta(1+j)$, where resistance coefficient R_f as a function of frequency J_1 represents the Bessel function of the first order. The pressure difference across the tube end is

$$\Delta P = \int_o^l \varphi \, dx \tag{2.35}$$

where ΔP is the pressure difference across the tube, and l is the length of the tube. Using the following expression together with the mean velocity gives the specific acoustic impedance per unit cross-sectional area of the short tube by Crandall (Crandall, 1926b)

$$Z_{cr} = \frac{p(x,t)}{u(\mathrm{x,t})} = \frac{j\omega\rho l}{\left[1 - \frac{2J_1(k_s r_0)}{k_s r_0 J_0(k_s r_0)}\right]} = \frac{j\omega\rho l}{F(k_s r_0)} \tag{2.36}$$

where Z_{cr} is the specific acoustic impedance per unit cross-sectional area of the short tube (Crandall, 1926b), k_s is the viscous Stokes wave number earlier designated in equation (2.30) and relates to the viscous boundary layer thickness represented as

$$\beta = \sqrt{\frac{2\mu}{\omega\rho}} \tag{2.37}$$

where β is the viscous penetration depth, the argument $|k_s r_0| = \sqrt{2} r_0/\beta$ determines the acoustic behaviour of the orifice. Therefore, $|k_s r_0|$ is the ratio of orifice radius to the boundary layer thickness apart from the factor of $\sqrt{2}$; $|k_s r_0| = r_0\sqrt{-j\rho\omega/\mu} = \sqrt{-j r_0 \rho c H_n/\mu}$; $H_n = \omega r_0/c$ represents the Helmholtz number, which expresses the diffusion of momentum by viscosity during the period of oscillation. Based on the principles of viscous Stokes number, equation (2.36) has two limiting values $|k_s r_0| < 2 \; and \; |k_s r_0| > 10$

(Melling, 1973b). Equation (2.36) defines the function $F(k_s r_0)$ which appears in subsequent analyses.

I. If $|k_s r_0| < 2$ ($r_0^2 f < 0.1$) Bessel function of the first two terms only considered, $|k_s r_0|$ is not greater than unity

$$J_0(k_s r_0) = J_0(x) = 1 - \frac{x^2}{4} + \frac{x^4}{64} \tag{2.38}$$

$$J_1(k_s r_0) = J_1(x) = \frac{x}{2}\left(1 - \frac{x^2}{8} + \frac{x^4}{192}\right) \tag{2.39}$$

From equations (2.38) and (2.39) using only three terms of this expansion, it can be written as

$$1 - \frac{2J_1(x)}{xJ_0(x)} = \frac{1 - \frac{x^2}{4} + \frac{x^4}{64} - 1 - \frac{x^2}{8} - \frac{x^4}{192}}{1 - \frac{x^2}{4}} = -\frac{x^2}{8}\frac{1 - \frac{x^2}{12}}{1 - \frac{x^2}{4}} = -\frac{x^2}{8}\frac{1}{1 - \frac{x^2}{6}} \tag{2.40}$$

$$\xi = -\frac{\varphi r_0^2}{8\mu}\frac{1}{1 - \frac{r_0^2 k_s^2}{6}} = \frac{\varphi}{Z_{cr}} \tag{2.41}$$

By considering a tube of thickness l

$$Z_{cr} = \frac{8\mu l}{r_0^2} + \frac{4}{3}j\omega\rho l = R_p + jX \tag{2.42}$$

Equation (2.42) shows that pure resistance Z_{cr} coefficient as a function of frequency, expression of Poiseuille's Coefficient $R_p = 8\mu l/r_0^2$ for laminar flow of viscous fluids in a narrow tube. The reactance part of the impedance represents $X = 4\omega\rho l/3$, which has a total effective mass $4\rho l/3$ of which 1/3 is increase in effective mass density due to the diffusion effects in the narrow tube, as compared with the reactance $j\omega\rho$ in the unlimited medium. Though implicitly independent of the viscosity coefficient, this additional attached mass is a direct result of the velocity profile. If $|k_s r_0| = 1$ inertial reactance is only 1/6 of the resistance factor (Picolet, 1927).

II. If r_0 is 0.01 m and $\omega > 20$ in air $|k_s r_0| > 10$ ($r_0^2 f > 5$) for all acoustic frequencies, application of a simple formula, to evaluate the Bessel functions, whose arguments are complex variables of large absolute value gives

$$\frac{J_1(x\sqrt{-j})}{J_0(x\sqrt{-j})} = -j\colon (x\sqrt{-j}) = r_0\sqrt{\frac{-j\rho\omega}{\mu}} \tag{2.43}$$

$$Z_{cr} = \frac{l}{r_0}\sqrt{2\rho\mu\omega} + j\omega\rho l\left[1 + \frac{1}{r_0}\sqrt{\frac{1}{\beta}}\right] \qquad (2.44)$$

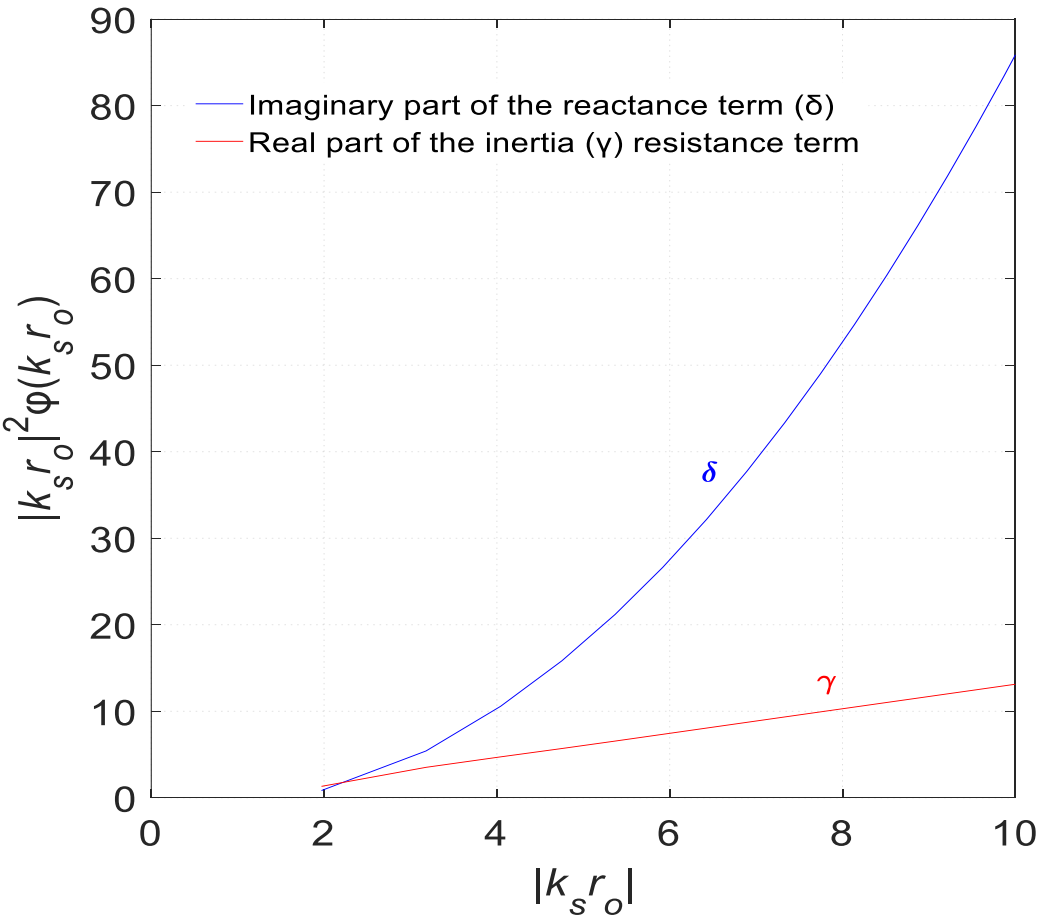

Figure 2.6 Variation of real and imaginary parts of specific acoustic impedance per unit cross-sectional area with ratio of orifice radius to the boundary layer thickness (according to equation (2.44)).

The variations of real and imaginary parts of specific acoustic impedance per unit cross-sectional area with ratio of orifice radius to the boundary layer thickness (according to equation (2.44)) are shown in Figure 2.6. From equation (2.44) the real part of the impedance is frequency dependent. Helmholtz (Von Helmholtz, 1863) has developed the expression for the resistance term. The inertia reactance $j\rho\omega$ is the normal inertia effect present in many cases. The principal interest in this solution of the resistance problem lies in the additional reactance $2J\mu\beta/r_0$ due to the combined viscosity and inertia effects in a tube of moderate width. Equations (2.42) and (2.44) represent the specific acoustic impedance of a hole, and β represents the viscous penetration depth and Crandall (Crandall, 1926b) introduces the expression for the impedance per unit length to viscous flow within an infinite tube.

2.5 Thurston's model

George B. Thurston (Thurston, 1952b) investigated incompressible periodic flow through a circular tube of a large length to diameter ratio. This measurement method was established based on an electrical series circuit, with the impedance of acoustic elements working at the resonant frequency of this circuit, and the pressure across and volume flow through the series circuit was measured (Thurston, 1952a). The ratio of the pressure to volume flow at that point contributes to the total resistance of the circuit. As a result, the resistance of the enclosed air volume must be deducted from the total measured resistance to provide the resistance of the tube. If the capability of the surrounding air volume is identified, then the inductance of the tube may be considered from the resonance frequency. The theory of the impedance of an enclosed air volume was presented by Daniels (Daniels, 1947). George B. Thurston (Thurston, 1952b) proposed that an extra length of end correction might be applied to the resistive and reactive component. This was subsequently verified by Thurston and Martin (Thurston & Martin Jr, 1953) for fluid flow through a circular orifice using water and silicon fluid. Values of $|k_s r_0| = r_0\sqrt{-j\rho\omega/\mu}$ as low as 1.55 were investigated. This indicated that total specific impedance due to the viscous influence of

$$Z_{th} = \frac{k}{\sigma}(l + 1.7r_0)[Re\{F(k_s r_0)\} + jIm\{F(k_s r_0)\}] \tag{2.45}$$

Stinson and Shaw (Stinson & Shaw, 1985) presented experimental evidence that equation (2.45) is valid for $2.3 < |k_s r_0| < 8.7$. Thus, according to that expression, the resistance of an orifice is almost constant at low frequencies and increases as $\omega^{0.5}$ at sufficiently high frequencies, as expected from the Bessel function expansion (although it is somewhat overestimated for $|k_s r_0| < 8.7$) . Parameters proportional to the real and imaginary components equation (2.45) are plotted in Figure 2.6.

2.6 Cross-flow impedance

When fluid flow (primary air) through the combustor liner is tangential it is known as cross-flow, or grazing flow. Cross-flow introduced into the combustor through the swirler and the effect depends on the acoustic impedance of resistance and reactance terms. The cross-flow model was developed by ignoring amplitudes (reactance) and by considering the resistance effect of the boundary layer thickness (Heidelberg et al., 1980; Rice, 1971). This empirical acoustic resistance for a single hole can be expressed as

$$R_c = \frac{0.3M_c}{\sigma} \tag{2.46}$$

where R_c represents a contribution to the resistance which is proportional to the cross-flow Mach number M_c and inversely proportional to the porosity (Bauer, 1977; Guess, 1975b; Heidelberg et al., 1980; Rice, 1971). The reactance model developed by Rice (Rice, 1971) is specified below

$$X_c = \frac{\omega l}{\sigma c} - cot\frac{\omega d}{c} \tag{2.47}$$

where X_c represents reactance due to cross-flow, l is the thickness of the aperture or perforated plate, d is the cavity depth referred to the backing wall. There are several cross-flow models available (Grace et al., 1998; Howe, 1979; Jing et al., 2001; Lee & Ih, 2003). During the cross-flow effect, two types of velocity are generally considered; friction velocity and mean flow velocity. The significance of friction velocity compared to the mean flow velocity was investigated by (Goldman & Panton, 1976; Heidelberg et al., 1980). Further investigation by (Peat et al., 2003) suggested that the influence of friction velocity is negligible when the boundary layer is turbulent.

2.7 Melling's model

Melling's (Melling, 1973b) comprehensive investigation of the impedance of a perforated plate considers both the linear and nonlinear effects of resistance and reactance terms. The two-microphone method of impedance measurement and model was used to deliver an applied method of predicting the acoustic behaviour of the resistive part of the impedance of perforated materials. Melling (Melling, 1973b) considered both the linear and non-linear increase of resistance and mass reactance. The established expression for single orifices concluding with the Rayleigh (Rayleigh, 1940) correction factor for the effective increase in hole length per end was adequate when estimating the attached mass, which demonstrates that the model for resistance and mass reactance is the nil frequency estimation of the Crandall (Crandall, 1926b) model, which can be referred to as the Poiseuille model. Melling's (Melling, 1973b) Z_{me} impedance model developed an expression for orifice impedance from the exact theory of flow in a short tube, including effects of viscosity based on the Crandall (Crandall, 1926b) model.

Melling (Melling, 1973b) considered the contributions of Sivian (Sivian, 1935) and Ingard (Ingard, 1953) for determining the end correction for resistance and mass reactance. Original

nomenclature of Sivian (Sivian, 1935) and Melling (Melling, 1973b) convention was [1]switched in Melling's (Melling, 1973b) model. The difference can be seen in equation (2.143) and (2.48). Melling (Melling, 1973b) also mentioned the effect of radiation resistance, but assumed that it could be negligible. In addition, Melling (Melling, 1973b) introduced a correction factor for the effects of interaction among the orifices. Melling[2] applied the Fok (Fok, 1941) interaction factor, which predicts interaction better than Ingard's (Ingard, 1953) approach. Therefore, Melling's (Melling, 1973b) impedance model, including end correction on resistance and mass reactance of an array of orifices, can be written as

$$Z_{me} = \frac{jk}{\sigma}\left[\frac{l}{F(K_s r_0)} + \frac{1.7 r_0}{F(K_{sp} r_0)\psi(\sigma)}\right] \tag{2.48}$$

Melling (Melling, 1973b) provided detailed discussion of the nonlinear contribution to the resistance and reactance terms. The resistance or reactance term depends on acoustic velocity in the orifice, which refers to the sound pressure level (SPL). At high amplitudes, the acoustic behaviour of the orifice becomes nonlinear (Melling, 1973b; Munjal & Doige, 1990). Therefore, the impedance of a circular orifice depends on the amplitude of the oscillation. This impedance formulation approach has been followed by several researchers (Bolt et al., 1949; Ingard, 1953; Ingard & Ising, 1967; Ingård & Labate, 1950; Parrott & Zorumski, 1971; Salikuddin & Ahuja, 1983). Therefore, Melling's (Melling, 1973b) assumption for the nonlinear specific acoustic resistance contribution can be written as

$$R_{nl} = \frac{1}{\rho c}\left[R_\mu + \frac{1.2}{c_d^2}\left(\frac{1-\sigma^2}{\sigma}\right)\frac{\rho}{2}u_{rms}\right] \tag{2.49}$$

where u_{rms} is the root mean square value of the acoustic particle velocity, R_μ is the linear regime resistance, R_{nl} is Melling's nonlinear specific acoustic resistance term, when terms resulting from the non-ideal flow case are disregarded $(1-\sigma^2/\sigma^2 c_d^2)$, the nonlinear acoustic

[1] Orifice resistance at low velocities Sivian Sivian, L. J. (1935) Acoustic impedance of small orifices. *The Journal of the Acoustical Society of America*, 7(2), 94-101. uses the difference between two viscosities, the original prime convention of Sivian's investigation was switched in Melling's Melling, T. H. (1973b) The acoustic impendance of perforates at medium and high sound pressure levels. *Journal of Sound and Vibration*, 29(1), 1-65. model. This switch of prime convention will be unchanged in this discussion.

[2] There is a mismatch of handling of the Fok function in Melling's equation (2.48). Melling has described up to ascending power series in his paper, the Fok function is the reciprocal of ascending power series. [Melling, T. H. (1973b) The acoustic impendance of perforates at medium and high sound pressure levels. *Journal of Sound and Vibration*, 29(1), 1-65.], Explanation of the Fok function is given in equations (2.158) & (2.159) in Figure 2.14. Therefore, division of $\psi(\sigma)$ with the end correction term is correct.

resistance depends on velocity in a way identical to that derived by (Sirignano, 1966); namely $4\rho/3\pi$, which is one half the value obtained by (Zinn, 1970). The critical part of this impedance process depends on acoustic particle velocity u, which can not be measured directly. It can be developed from acoustic pressure captured by microphone (Elnady, 2004) $|u| = |\mathrm{P}|\left(\rho c\sqrt{R^2 + X^2}\right)$. For a plane wave, the relationship between the acoustic particle velocity and pressure can be used to determine the magnitude of acoustic particle velocity (Betts et al., 2000)

$$u_{rms} = \frac{1}{2c\sigma c_d}\frac{P_0 10^{\frac{SPL}{20}}}{\rho c} \tag{2.50}$$

where P_0 is the reference sound pressure. In the low-frequency range, the contribution to the resistance term has been assumed to be negligible by Melling (Melling, 1973b). By eliminating interaction effects, the radiation resistance of a vibrating slug of air in the orifice of a perforated plate is the same as that of a vibrating piston in an infinite baffle. The radiation resistance for an array of orifices in a perforated plate can be written as Morse (Morse, 1968) and Ingard (Ingard, 1953).

$$R_{rad} = \frac{1}{\sigma}\left(1 - \frac{2J_1 kr_0}{kr_0}\right) \tag{2.51}$$

For small values of kr_0 equation (2.51) can be modified to equation (2.52) for a better prediction of radiation resistance as a function of kr_0

$$R_{rad} = \frac{(kr_0)^2}{2\sigma} \tag{2.52}$$

2.7.1 Effect of resistance and mass reactance

In this section, the primary concern is with experimental technique and measurement evaluation of the acoustic characteristics of the sample specified. The geometrical characteristics (Melling, 1973b) sample were valid for material, which may be employed in typical in-engine applications. Hole diameter to plate thickness ratio ranged from $1{:}\,1$ to $1{:}\,5$. This range of hole diameter gave a sensible variation in both Reynolds and Strouhal number for the same plate porosity. The range of plate thickness to hole diameter was adequate to illustrate the behaviour of end effect or attached mass of the orifice with the sound pressure level. The variety of hole diameter to plate thickness ratio was also satisfactorily responsible for the applicability of discharge coefficients to non-ideal orifices. Since interaction effects would depend on orifice axial pitch distance, and therefore on porosity, a maximum

acceptable porosity was considered to be 22 %. Three standard porosities were initially chosen: 22 %, 15 % and 7.5 %. This consideration was chosen from the contributions of Sivian (Sivian, 1935) and Ingard (Ingard, 1953) to the determination of the end corrections for resistance and mass reactance.

2.7.2 Nonlinear resistance contribution

The prediction of the non-linear impedance of perforation investigated by Melling (Melling, 1973b) was given in equation (2.49). The primary objective is to analyse the relationship between reactance and resistance terms. It stated that the discharge coefficient of the orifice is the most important parameter, which depends on the orifice Reynolds number and orifice geometry, and, further, this parameter, as expected from the work on steady flows, is sensitive to orifice thickness to hole diameter. It was also observed that in the case of perforates, backing cavity is sensitive to the porosity. In a real application it is not essential to determine the discharge coefficient, but rather the acoustic non-linear resistance can be derived directly from the steady flow resistance (or static pressure measurement can be designated as a pressure drop) velocity characteristics simply by its multiplication by an appropriate constant.

$$R_{nlr} = \frac{1}{\rho c}(R_s + 1.2\Delta \mathrm{P} u_{rms}) \tag{2.53}$$

where R_{nlr} is the nonlinear resistance, R_s is the nominal specific acoustic resistance, $\Delta \mathrm{P}$ is the pressure drop across an orifice or can be designated as steady flow resistance velocity curve and u_{rms} is the root mean square particle velocity. Remarkably, the discharge coefficient is sensitive to geometric parameters of the orifice shape. This physical appearance of the non-linear term can be determined by the discharge coefficient, and then presumably a limited amount of modification to the non-linear resistance behaviour can be plotted. The discharge coefficient of the orifice with different shapes indicates lower or upper resistance or velocity characteristics. The nonlinear parameter 1.2 has a good correlation with Umnova et el.'s (Umnova et al., 2003) theory and experiment. Forchheimer's nonlinearity (Forchheimer, 1901) with an equivalent fluid model has been investigated against data for three types of hard-backed rigid-porous layers. Umnova et el.'s (Umnova et al., 2003) model gives valid predictions of both impedance and reflection coefficient behaviour at high sound amplitudes (up to 500 Pa) over a wide range of frequencies. This simple empirical relationship in equation (2.53) between the acoustic non-linear behaviour and steady flow behaviour

should extend up to the condition where the orifice becomes choked - a condition that is unlikely to occur in practice. Over this range, the error in the slope of the resistance or velocity curve should be no more than 10 %. Consequently, for both the incident and reflected waves the ratio of pressure to velocity must be equal to the characteristic impedance of air. Consistently, equation (2.50) presents that the total velocity at the surface of the absorber is equal to twice the incident pressure divided by the series sum of the specific impedance of the liner, plus the characteristic impedance of the air.

2.8 Bias flow impedance model

Fluid flow (secondary air) through the orifices of a combustor liner wall is known as bias flow. Bias flow is introduced into the combustor for wall cooling, increasing the liner damping effect, and dilution. Bias flow impedance models can be classified into two categories, linear and nonlinear (Hersh & Rogers, 1976). According to Hersh and Roger (Hersh & Rogers, 1976) if the perforated plate thickness is too thin, if duct flows through the perforations are very small, and end corrections have been overlooked, then the significant component of the model shows viscous losses. This viscous loss does not occur inside the perforation but at the surface of the perforation. In Hersh and Roger's model (Hersh & Rogers, 1976), the linear and nonlinear regimes are determined by $u/2\sigma\omega r_0$. If the ratio is $u/2\sigma\omega r_0 < 1$ then the regime is linear, but if it is $u/2\sigma\omega r_0 > 1$ it is nonlinear. Dean (Dean & Tester, 1975) has developed a bias flow model based on the same assumption as the Hersh and Roger (Hersh & Rogers, 1976) model, where the nonlinear model expressing the acoustic particle velocity is replaced by bias flow velocity, with the assumption that the bias flow velocity is much higher than the acoustic particle velocity $u/2\sigma\omega r_0$. Therefore, it is concluded that Dean's (Dean & Tester, 1975) model pays no attention to the effect on the sound pressure level (SPL) caused by changes in the acoustic particle velocity. There are several expressions for specific acoustic resistance and reactance for bias flow effect described in several papers (Baldwin et al., 1969; Bauer, 1977; Dean & Tester, 1975; Ingard & Ising, 1967; Sullivan & Crocker, 1978; Zinn, 1970). A mathematical model is described by Bauer (Bauer, 1977), given below:

$$R_s = R_i + R_l + R_b M_b + R_C M_\infty \tag{2.54}$$

where R_s is the specific acoustic resistance, R_b is the nonlinear effect due to the large amplitude of acoustic velocity normal to the liner surface u_n moreover, corresponding to bias flow Mach number $M_b = u_n/\mathrm{c}$, $R_C M_\infty$ is the cross-flow effect. R_i is the internal resistance

due to viscous loss in the hole, or resistance of the surface with small holes, where the flow is entirely viscous and the porous Reynolds number R_{po} is much less than 1, R_l is the resistance of the surface with a larger hole where the flow is not entirely viscous and the porous Reynolds number $R_{po} = \rho\omega r^2/\mu$ is much higher than 1. For a perforated plate, R_i is equal to zero as the porous Reynolds number is much higher than 1 and R_l can be written as

$$R_i = \frac{\sqrt{8\mu\rho\omega}}{\rho c\sigma}\left(1 + \frac{l}{2r_0}\right) \tag{2.55}$$

For a sheet with circular orifices, Zinn (Zinn, 1970) obtained the expression given in equation (2.56), and the factor of 1.15 comes from $4/3\pi c_d^2$ where c_d=0.61

$$R_b = \frac{1.15M_b}{\sigma^2} \tag{2.56}$$

The second cases combine the effect of Melling's (Melling, 1973b) nonlinear specific acoustic resistance term plus bias flow velocity in one single resistance term. Later Premo (Premo, 1999) derived a flow model by using a time-domain approach with combined velocity effect of $\sqrt{(1.15u_{rms})^2 + (2U)^2}$. Also Betts's (Betts et al., 2000; Betts, 2000) perforate bias flow (PBF) model applies a bias flow correction to existing impedance models, where acoustic particle velocity is replaced by $1.2u_{rms} + 2U$. By adding the term $2U$ into equation (2.49), the specific acoustic resistance term of the combined approach can be written as

$$R_s = \frac{8}{3\pi}\left[\frac{1}{2c}\frac{1-\sigma^2}{\sigma^2 c_d^2}\right]u_{rms} + 2U \tag{2.57}$$

2.9 Bauer's model

Bauer's (Bauer, 1977) impedance model relates the two microphone measurements to liner impedance. The developed model for air cavity liners is extended to apply to porous, point reacting liners, which includes the effect of bias and cross flow.

$$Z_s = \frac{\sqrt{8\mu\rho\omega}}{\rho c\sigma}\left(1 + \frac{l}{d}\right) + \frac{0.3\mathrm{M_g}}{\sigma} + \frac{1.15\mathrm{M_b}}{\sigma} + i\frac{k(l + 0.25d)}{\sigma} \tag{2.58}$$

Bauer (Bauer, 1977) is applied when the flow is not entirely viscous; the specific acoustic resistance of Ingard's (Ingard, 1953) term is described in equation (2.55). The effect of cross-flow expression considered by Rice (Rice, 1971) is described in equation (2.46). The effect of

bias flow[3] expression was considered by Zinn (Zinn, 1970), described in equation (2.56). An expression for the reactance term was derived by Dean (Dean, 1975) and Rice's (Rice, 1976) experimental data. The factor of 0.25 in the reactance term provides an excellent result when the cross-flow is present. Bauer (Bauer, 1977) carried out an experiment on a porous surface sheet backed by a cavity filled with air or porous material and developed a mathematical model by using the two-microphone method. A liner consisting of a single layer of either air-filled or porous cavities covered by a thin porous sheet was found to possess good agreement with the model. However, multilayer liners did not act like porous cavity liners. The source of this problem is that the impedance of a single layer liner fluctuates rapidly with frequency; therefore, a recommended preparation is a multilayer liner configured to have a near-optimum impedance over a bandwidth significantly broader than is possible for a single layer liner. Comprehensive discussion is based on Bauer's (Bauer, 1977) normalized specific impedance, described in equation (2.58), which includes bias and cross-flow terms. The present model is based on no flow acoustic analysis. Hence, the bias flow and cross-flow terms will not be considered for recurrent model comparisons.

$$Z_s = \frac{\sqrt{8\mu\rho\omega}}{\rho c\sigma}\left(1+\frac{l}{d}\right)+i\,\frac{k(l+0.25d)}{\sigma} \qquad (2.59)$$

Subsequently, equation (2.59) is considered for comparison. This mathematical model displays a remarkable agreement with Bauer's (Bauer, 1977) carried out experiment when using a porous liner instead of the air-filled liner. For a multilayer liner, the experiment appears to disagree with the model. The source of this disagreement is unknown and requires further investigation to alleviate the problem. It may be self-generated noise due to the influence of bias and cross-flow, or it may require additional term impedance due to the cavity for single and double layer liners.

2.10 Howe's model

In the presence of mean flow through the hole and for acoustic perturbations of small amplitude, acoustic-vortex interaction is the principal absorption mechanism. Howe (Howe,

[3] In Bauer Bauer, A. B. (1977) Impedance theory and measurements on porous acoustic liners. *Journal of Aircraft*, 14(8), 720-728. impedance model equation (2.58) the bias flow term is divided by σ instead of σ^2 as the square root of the porosity refers to an unreasonable explanation shown in equation (2.56). Therefore, only division by σ is considered.

1979) built two models to evaluate the amount of energy transferred from acoustic to vortical energy. In his first model, Howe (Howe, 1979) used a single circular orifice where the thickness of the perforation is assumed to be zero and flow through the hole has a high Reynolds number. Moreover, the hole spacing-to-radius ratio is considered substantial (porosity is small) so that apertures do not interact with one another. Subsequently, he modified his model to account for the thickness of the perforation, although the assumptions of a large Reynolds number and low porosity were left in place. By the use of vector properties, Howe (Howe, 1984; 1995; 1997; Howe & Howe, 1998) converted the Euler equation into a form which contains vorticity.

$$\frac{\partial u}{\partial t} + \nabla\left(\frac{1}{2}u^2 + \frac{p}{\rho}\right) = u \times \dot{\omega} \tag{2.60}$$

From Bernoulli enthalpy $B = \frac{u^2}{2} + \frac{p}{\rho}$ by applying the divergence on the equation and using the interchangeability property between partial derivative and divergence, equation (2.60) can be written as

$$\frac{\partial}{\partial t}(\nabla u) + \nabla^2 B = \nabla(u \times \dot{\omega}) \tag{2.61}$$

where B is the stagnation enthalpy, u being the velocity, and $\dot{\omega}$ is the curl of u vorticity. Introducing incompressibility of the fluid into the explanation, the divergence of the momentum equation for an incompressible, inviscid flow may be set in the form.

$$\nabla^2 B = \nabla(u \times \dot{\omega}) \tag{2.62}$$

To simplify equation (2.61) the perturbation theory was introduced into the hypothesis by viewing the variables as the sum of their fluctuating and mean values, i.e. $\dot{\omega} \times u = \ddot{\omega} \times \dot{u} + \overline{\omega} \times U + \ddot{\omega} \times U$. Equation (2.63) shows that the effect of shed vorticity is contained in the second term of the right-hand side and fits the linearized approximation, and this is equivalent to the radial component of $\dot{u}$ in $\ddot{\omega} \times \dot{u}$. In incompressible flow with the vector potential, the approximation may be justified because the details of the vorticity-induced flow in the aperture are insensitive to the precise radial locations of the cores of the elementary vortex rings of the axisymmetric shear layer (Lamb, 1932).

$$\nabla^2 B = \nabla(U \times \overline{\omega}) \tag{2.63}$$

where, $\ddot{\omega} = \ddot{\omega}(x_1)$ is the mean perturbation vorticity, $\overline{\omega} = \overline{\omega} e_\phi$ represents perturbation vorticity along the azimuthal direction e_ϕ, $\dot{u}$ is the perturbation velocity, which has been neglected, $U = U(x_1)$ represents mean perturbation velocity and u_c represents mean vortex

shed velocity along the plane of the aperture due to bias flow. On the linear theory the shed vorticity $\overline{\omega}$ constitutes a succession of vortex rings of radius r whose cores are infinitesimal. At the positive x_1 axis the mean velocity is $U \approx 0.5u_c$, which is taken to be constant. Vortices, which are created by the aperture, are removed by the bias flow with a convected downstream shed velocity (u_c) along a straight vortex tube. The presence of turbulent fluctuations caused by the natural instability of the jet would also lead to linearized contributions to the right-hand side of equation (2.62). Such terms may be ignored, as included in the specification of the properties of the mean flow, since they produce fluctuations in the aperture flow, which does not correlate with the applied pressure (Howe, 1979). From this conclusion, it is expected that the vortex rings generated by $\overline{\omega}$ perturbation vorticity oscillation are travelling through the $U(x_1)$ mean perturbation velocity in the axial direction of x_1 . On the assumption of mean perturbation vorticity fluctuation and by its incident pressure oscillation of the fluctuating vorticity, it can be written as:

$$\overline{\omega} = \bar{A}kH(x_1)\delta(\dot{r} - R_v)\exp[-j\omega(t - x_1/U)] \qquad (2.64)$$

where $\bar{A}$ is the amplitude of the shed vorticity, $H(x_1)$ is Heaviside unit function, R_v is the vortex ring of the radius with its centre at the origin o, and $\dot{r}$ is the radial component of the cylindrical coordinate system. Heaviside unit function represents that vorticity is only shed downstream of the orifice ($x_1 \geq 0$). The magnitude of the amplitude depends on the Strouhal number, which is determined by the condition that fluctuating velocity and pressure are finite by the rim of the aperture. The delta δ function lies with the assumption that vorticity is shed within the infinitesimal thin cylindrical shear layer of radius $2r$. By substituting equation (2.64) into equation (2.63) and suppressing the time factor $e^{-j\omega t}$, Howe's inhomogeneous, axi-symmetric Laplace equation becomes

$$\frac{1}{r}\frac{\partial}{\partial r}\left(r\frac{\partial B}{\partial r}\right) + \frac{\partial^2 B}{\partial x_1^2} = -\left(\frac{\bar{A}UR_v}{r}\right)H(x_1)\delta'(\dot{r} - r)e^{jkx_1} \qquad (2.65)$$

where $\delta'(x_1)$ is the derivative of the δ function and $B \equiv -\frac{\partial \phi}{\partial t}$ outside of the shed vorticity. The explanation must satisfy the condition $\frac{\partial B}{\partial x_1} = 0$ on the rigid plate. By approximating the harmonic pressure difference across the orifice, this leads to the periodic shading of the vorticity. After a long manipulation, Howe expresses the relationship between mass flow rate and pressure in the presence of bias flow, which is also called Howe Rayleigh Conductivity.

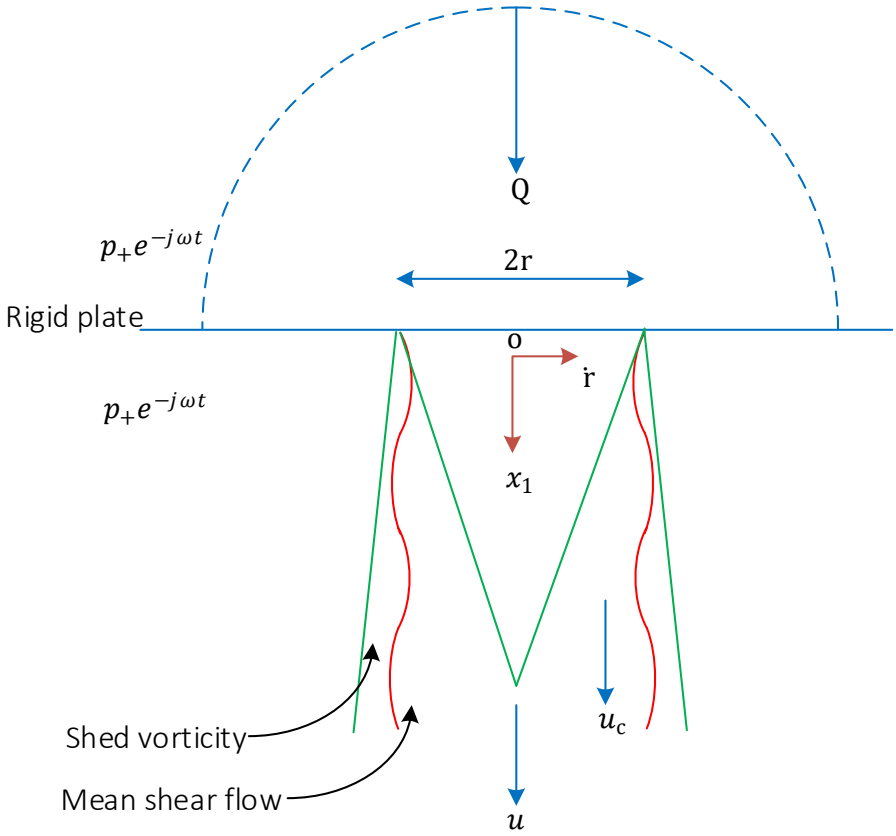

Figure 2.7 Howe's unsteady axisymmetric vorticity shed from the rim of the aperture.

Figure 2.7 represents the schematic diagram of the aperture flow. Unsteady, axisymmetric vorticity shed from the rim of the aperture is assumed to convect at constant velocity U parallel to the x_1 axis within the shear layer of the mean flow, where the real and imaginary components γ, δ are determined by

$$K_R = 2r(\gamma - j\delta) = 1 - \frac{\left[\frac{\pi}{2} I_1(St)e^{-St} - jK_1(St)\sinh(St)\right]}{St\left[\frac{\pi}{2} I_1(St)e^{-St} + jK_1(St)\cosh(St)\right]} \qquad (2.66)$$

$St(kr), \left(k = \frac{\omega}{u} > 0\right)$, remains positive for all values of the Strouhal number, which is based on vorticity convection velocity, and the magnitude of amplitude of the shed vorticity depends on the Strouhal number. Accordingly, the details of the fluctuating flow will be independent of the Reynolds number but must be expected to depend on the Strouhal number (Howe, 1979). I_1 and K_1 are modified Bessel functions of the first and second kinds, γ represents the real part of the orifice impedance as the inertia resistance term, and δ represents the imaginary part of the orifice impedance as the reactance term.

$$\gamma = \frac{I_1(St)^2\left(1 + \frac{1}{St}\right) + \left(\frac{4}{\pi^2}\right)\exp(2St)cosh(St)K_1(St)^2\left[cosh(St) - \frac{sinh(St)}{St}\right]}{I_1(St)^2 + \left(\frac{4}{\pi^2}\right)\exp(2St)cosh^2(St)K_1(St)^2} \qquad (2.67)$$

$$\delta = \frac{\frac{2}{\pi(St)} I_1(St)K_1(St)exp(2St)}{I_1(St)^2 + \left(\frac{4}{\pi^2}\right)\exp(2St)cosh(St)K_1(St)^2} \quad (2.68)$$

In Howe's models, the vorticity is assumed to be determined in an axisymmetric vortex sheet separating two regions of potential flow, the jet and the rest of the domain. The vortex sheet being pulsated by acoustic perturbation results in periodic shedding of vortex rings. These shed vortex rings are assumed to have the diameter of the aperture and to be convected at the mean velocity in the hole. It should be mentioned that several researchers (Bellucci et al., 2004a; Dowling & Stow, 2003; Eldredge & Dowling, 2003; Hughes & Dowling, 1990b; Lahiri et al., 2011; Scarpato et al., 2012; Wendoloski, 1998) experimentally verified Howe's model.

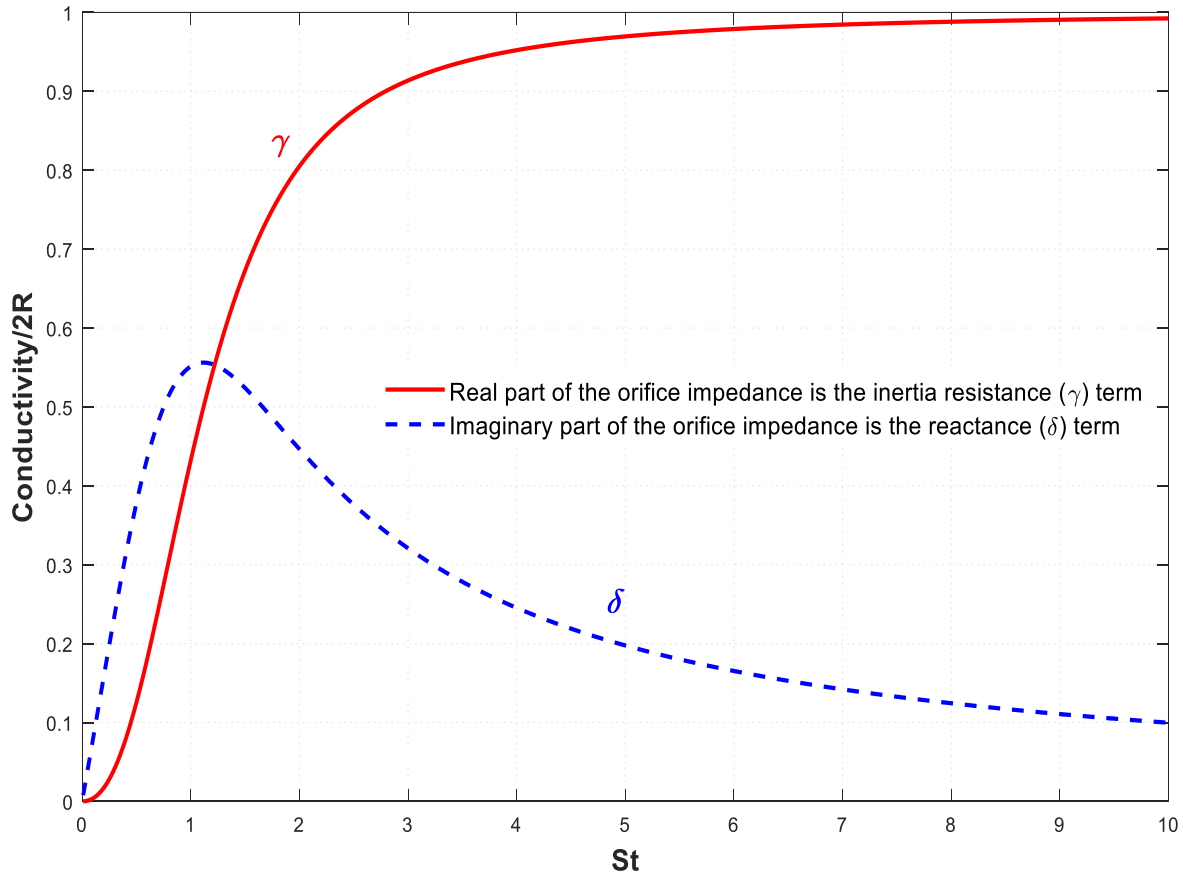

Figure 2.8 Howe's parameters in theory: Real & Imaginary parts.

The reliance of the aperture conductivity real part γ of the inertia and imaginary part δ of the reactance term on the Strouhal number is shown in Figure 2.8. In this formation, when a high Reynold's number flow passes through the hole viscosity is neglected, except at the rim of the orifice, where it becomes limited to the separation of the flow. Under these circumstances, the acoustic pressure difference across the orifice leads to periodic shedding of vorticity, and subsequently acoustic energy is converted into mechanical energy.

2.11 Maa's model

Maa (1998) has developed an impedance model for micro-perforated panel absorbers (MPP) within both linear and non-linear terms, based on Crandall (Crandall, 1926b). According to Maa's model, the acoustic impedance of an MPP absorber is determined by the perforate constant, which is proportional to the ratio of the perforation radius to the viscous boundary layer thickness inside the hole. Maa (Maa, 1998) suggested that the MPP absorber be designed according to the required absorbing characteristics in terms of the perforation constant, the radius of the aperture, and resonance frequency. Maa's (Maa, 1998) model is based on wave propagation in narrow tubes, in which the oscillatory viscous boundary layer spans the aperture diameter. The normalized specific acoustic resistance R and reactance X of a perforated liner can be expressed as

$$R = \frac{8\mu l}{\sigma \rho c r_0^2}\left[\left(1+\frac{{k_s}^2}{32}\right)^{0.5} + \frac{\sqrt{2}}{16}k_s\frac{r_0}{l}\right] \tag{2.69}$$

$$X = \frac{\omega l}{\sigma c}\left[1+\left(1+\frac{{k_s}^2}{2}\right)^{-0.5} + \frac{0.85 r_0}{l}\right] \tag{2.70}$$

$$\Delta = \frac{4R}{(1+R)^2 + \left[X - cot\left(\frac{2\omega r_0}{c}\right)\right]^2} \tag{2.71}$$

for finite velocity, when $r = r_0$, r_0 represents the orifice radius of a short tube, l is the aperture thickness or tube thickness, σ is the porosity, and Δ is the absorption coefficient. This model highlights that MPP absorbers, which are relative to acoustic resistance R, need the application of reactance X to determine the absorption coefficient Δ.

2.12 Modified Howe model

Acoustic properties of impedance due to the wall thickness have been introduced by Jing and Sun (Jing & Sun, 1999) into Howe's model. Into this circumstance, the normalised acoustic impedance of an orifice is introduced. Impedance due to hole thickness, impedance due to bias flow, and total impedance are considered.

$$Z_t = Z_b + z_l \tag{2.72}$$

where Z_b represents impedance due to bias flow, z_l represents impedance due to the thickness and Z_t represents total impedance. As the thickness of the property adds to the impedance, the conductivity needs to be added reciprocally. The mathematical expression of Howe's modified conductivity is

$$\frac{1}{K_{RM}} = \frac{1}{K_{BF}} + \frac{1}{K_{TH}} \tag{2.73}$$

where K_{RM} is Howe's modified conductivity, K_{BF} is the acoustic conductivity due to the bias flow through the hole, and K_{TH} is the acoustic conductivity due to the thickness of the hole. Using the Rayleigh (Rayleigh, 1870; 1945c) conductivity K_R is inversely proportional to the impedance of the hole. Substituting the values of K_{BF} acoustic conductivity due to the bias flow through the hole into equation (2.66), and K_{TH} acoustic conductivity due to the thickness of the hole into equation (2.22) in equation (2.73) results in the modified assumptions listed above, and the vortex sheet strength can be assessed by using the Runge Kutta method. The expression of modified Howe's Rayleigh conductivity K_{RM} of a hole with an aperture radius r, plate thickness l, and mean jet velocity of U of an aperture in a circular orifice of finite wall thickness with bias flow is written as

$$K_{RM} = 2r\left[\frac{1}{(\gamma - j\delta)} + \frac{2l}{r\pi}\right]^{-1} \tag{2.74}$$

2.13 Jing & Sun's liner investigation

Jing and Sun (Jing & Sun, 2000) have investigated the acoustic properties of a perforated liner in the low-frequency range sound absorption of a perforated liner in the presence of bias flow. Their experimental result shows that the absorption coefficient and effective bandwidth of a perforated liner increase. Orifice plate thickness plays a vital role to manipulate the acoustic properties of a liner with bias flow. In addition, blowing and suction of air exerts different effects on mean shear flow over the surface of a perforated liner (Jing & Sun, 1999). The acoustic behaviour of an aperture is described by Rayleigh's (Rayleigh, 1870; 1945c) conductivity K_R equation (2.20), undertaken to solve the complex system of the Howe model (Howe, 1979).

$$K_R = \frac{j\omega\rho Q}{p_+ - p_-} = 2r(\gamma - i\delta) \tag{2.75}$$

where γ and δ are functions of the Strouhal number (St) Pulsating perturbation Q is the amplitude of the volume flow rate fluctuations through the aperture and p_+ and p_- are the amplitudes of pressure fluctuations measured below and above the aperture (Howe, 1998). Considering bias flow, and subsequent to splitting real and imaginary parts, the normalised specific acoustic impedance z_s (end correction term) of the aperture can be written as the form of Rayleigh (Rayleigh, 1870; 1945c) conductivity:

$$z_s = \frac{\pi k A \delta}{2(\gamma^2 + \delta^2)} - j\frac{\pi k A \gamma}{2(\gamma^2 + \delta^2)} \quad (2.76)$$

By considering the rigid plate of finite thickness the sum of the acoustic impedance of the aperture must contain the effect of finite plate thickness. Without normalised mean flow, the specific acoustic impedance is reliant on the thickness of a single aperture with radius $r > 0.01/\sqrt{f}$ Beranek (Beranek, 1954)

$$z_l = \frac{\sqrt{2v\omega l}}{cr} - j\frac{\omega l}{c} \quad (2.77)$$

Aperture thickness increases the mass inertia of the system (v -kinematic viscosity). Therefore, for a circular orifice of finite thickness with respect to bias flow, the total normalised specific acoustic impedance Z_{Jing} (Jing & Sun, 1999) is described below.

$$Z_{Jing} = z_s + z_l \quad (2.78)$$

In the presence of bias flow, the effect of finite plate thickness is considered, and total acoustic impedance is equal to the sum of the thickness term and end correction term. If the thickness of the plate is too small or large compared to the aperture radius r, end correction of the resistance term is more important than the thickness of the viscous term from the bias flow at low frequency.

$$Z_{Jing} = \frac{\pi k A \delta}{2(\gamma^2 + \delta^2)} - j\frac{\pi k A \gamma}{2(\gamma^2 + \delta^2)} + kl \quad (2.79)$$

2.14 Betts' model

The PBF impedance model proposed by Betts et al. (Betts et al., 2000; Betts, 2000) was developed based on Melling's (Melling, 1973b) impedance model and the nonlinear effect described in equations (2.48) and (2.49). The resistance term in his model is composed of Poiseuille-type resistance and Helmholtz-type resistance and an expanded term to take into account the non-linear and inertial effect. His modification of the non-linear term, including bias flow, is explained in equation (2.57).

$$Z_{betts} = \frac{4\mu l}{c\sigma C_d {r_0}^2} + \frac{\sqrt{2\omega\mu}l}{c\sigma C_d r_0} + \frac{1-\sigma^2}{(\sigma C_d)^2}|1.2u_{rms} + 2U| + i\left(\frac{kl}{\sigma C_d} + \frac{\sqrt{2\omega\mu}l}{c\sigma C_d r_0} + \frac{16r_0}{3\pi\psi}\right) \quad (2.80)$$

The PBF model runs into the problem that Bessel functions in the linear component of the impedance obscure its physical relationship to geometrical parameters. The low and high-frequency approximations to the PBF model do not account for intermediate frequencies. Therefore, a single model that does not contain the Bessel functions, and works for all

frequencies is desirable. One such correction is similar to one undertaken by Kraft and Kwan (Kraft et al., 1999). Equation (2.80) is referred to as the perforate bias flow intermediate frequency model.

2.15 Eldridge and Dowling's model

Absorption coefficient can be calculated by using stagnation enthalpy or total enthalpy. Eldredge & Dowling (Eldredge & Dowling, 2003) have calculated the difference between the incident and reflected enthalpy relative to the incident enthalpy. Variation in density is due to changes in both pressure and entropy. In addition, they computed the absorption by such a liner hard-walled duct section flow along with upstream and downstream sections, and tackled the complications of an outer liner co-axial within the inner chamber liner shown in Figure 2.9. The result is an annular cavity, and axial acoustic waves in the cavity interact with those in the chamber duct to modify the driving acoustic pressure across the orifice. Once again they constructed a one-dimensional lined duct model with effective compliance for the liner based on the results of Howe (Howe, 1979) for a single aperture with a steady flow circular duct of uniform cross-section.

One-dimensional plane waves were introduced into the duct to propagate along it and create a harmonic pressure fluctuation in the upstream section. Eldredge & Dowling (Eldredge & Dowling, 2003) have described the acoustic energy in terms of stagnation enthalpy.

$$B' = \frac{p'}{\bar{\rho}} + \bar{u}_c u' \tag{2.81}$$

where B' is the fluctuating stagnation enthalpy, p' is the fluctuating pressure, u' is the fluctuating axial velocity, $\bar{u}_c$ is the mean cross-flow velocity, $\bar{\rho}$ is the fluctuating density, Upstream stagnation enthalpy has the form $x < 0$

$$B'(x,t) = \hat{B}(x)e^{-j\omega t} = A_u^+ e^{j(\omega t - k_u^+ x)} + B_u^- e^{j(\omega t + k_u^- x)} \tag{2.82}$$

Downstream stagnation enthalpy has the form $x > L$

$$B'(x,t) = \hat{B}(x)e^{-j\omega t} = C_d^+ e^{j(\omega t - k_d^+ x)} + D_d^- e^{j(\omega t + k_d^- x)} \tag{2.83}$$

where $\hat{B} = A_u^+ + B_u^- = C_d^+ + D_d^-$ is the stagnation enthalpy represents forward and backward amplitudes of the upstream and downstream sections and k_u^+,k_u^- plus k_d^-, k_d^+ are the forward and backward travelling wave numbers. By using velocity fluctuation, stagnation enthalpy, velocity perturbation, and balance of mass and momentum with respect to a control volume they derived a continuous flow distribution equation. Then the one-

dimensional Euler equation is simplified by introducing the mean flow harmonic forms of the quantities and matching the terms with a linear dependence on fluctuation components derived by the acoustic form of the perturbation equation.

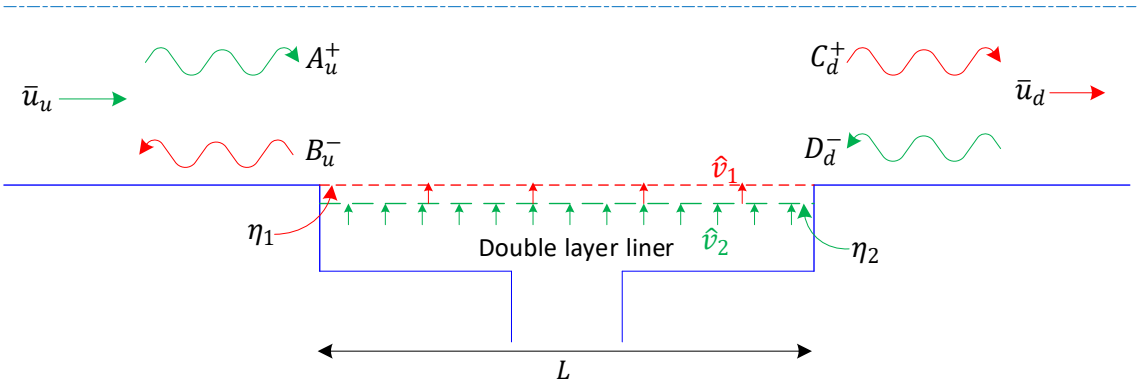

Figure 2.9 Combined liner acoustic waves and flow quantities in a lined duct.

$$jkL\hat{B} + 2\bar{u}_c \frac{d\hat{B}}{dx} + (1 - \bar{u}_c^2)\frac{d\hat{u}}{dx} = \frac{C_1 L}{S_p}\hat{v}_1 \tag{2.84}$$

$$jkL\hat{u} + \frac{d\hat{B}}{dx} = 0 \tag{2.85}$$

where L is the length of the lined section, C_1 is the circumferential area of the duct, S_p is the cross-sectional area of the duct, $\hat{v}_1$ is the fluctuating liner bias flow velocity, $\hat{u}$ is the complex amplitude of controlled flow velocity through the lined duct section. Also, the model displays steady flow velocity in the upstream section $\bar{u}_u$ and steady flow velocity in the downstream section $\bar{u}_d$. Equations (2.84) and (2.85) are given below in terms of characteristic quantities with a boundary condition for a more comfortable solution. Combined liner acoustic waves and flow quantities in a lined duct parameter are shown in Figure 2.9.

$$\psi^+ \equiv \frac{1}{2}(1 + \bar{u}_c)\left[\hat{B} + (1 - \bar{u}_c)\hat{u}\right] \tag{2.86}$$

$$\psi^- \equiv \frac{1}{2}(1 - \bar{u}_c)\left[\hat{B} - (1 + \bar{u}_c)\hat{u}\right] \tag{2.87}$$

A one-dimensional plane wave obeys the relation of fluctuating axial flow velocity $u' = \pm\frac{B'}{(1\pm M)}$. Moreover, for the characteristic quantities Eldredge & Dowling (Eldredge & Dowling, 2003) applied a boundary condition to forward travelling waves $(\psi^+, \psi^-) = (\hat{B}, 0)$ and backward travelling waves $(\psi^+, \psi^-) = (0, \hat{B})$. When those quantities are inserted into equations (2.84) and (2.85) they arrived at

$$\frac{d\psi^+}{dx} = -\frac{jkL}{1+\bar{u}_c}\psi^+ + \frac{1}{2}\frac{C_1 L}{S_p}\hat{v}_1 \tag{2.88}$$

$$\frac{d\psi^-}{dx} = \frac{jkL}{1-\bar{u}_c}\psi^- - \frac{1}{2}\frac{C_1 L}{S_p}\hat{v}_1 \tag{2.89}$$

The boundary conditions of $x = 0$ and $x = 1$ are substituted into stagnation enthalpy and velocity perturbations through the characteristic quantities of ψ^+ and ψ^-. Eldredge & Dowling (Eldredge & Dowling, 2003) developed a first-order equation and enforced two boundary conditions for the system. Forward upstream amplitude is assumed to be known as B_u^+ from microphone pressure data. Other amplitudes can be measured similarly. In the downstream section, reflection depends only on mean flow conditions and geometry arrangement. Within the two boundary conditions characteristic quantities are expressed as

$$\psi^+(0) = B_u^+ \tag{2.90}$$

$$\psi^-(1)e^{-jk_d^- L} - \psi^+(1)R_d e^{jk_d^+ L} = 0 \tag{2.91}$$

Equations (2.88) and (2.89) are not closed, and the fluctuating liner flow $\hat{v}_1$ must be considered. Considering the compliance of the liner η_1, creates a local relationship between in word fluctuating liner flow velocity $\hat{v}_1$ and the difference in stagnation enthalpy fluctuations across the liner. Using a linearised momentum equation in conjunction with stagnation enthalpy perturbation normal to the direction of propagation and relation between stagnation enthalpy and characteristic quantities $\hat{B}$=$\psi^+ + \psi^-$ are expressed as

$$\hat{v}_1(x) = \frac{\eta_1}{jkL}\left[\hat{B}_1(x) - \psi^+(x) - \psi^-(x)\right] \tag{2.92}$$

where $\hat{B}_1$ is the fluctuating part of the stagnation enthalpy related to the external liner and η_1 is the compliance of the inner liner, R_d is the downstream reflection coefficient. Eldredge & Dowling (Eldredge & Dowling, 2003) considered three configurations: an open exterior, an annular cavity enclosed by a rigid wall, and an annular cavity enclosed by a second liner. The first configuration is not as significant as the latter two.

2.15.1 Open exterior

In this configuration, the liner is exposed to the ambient environment. Since it exposed to ambient pressure, the pressure fluctuation outside the liner is zero.

$$\hat{v}_1(x) = \frac{\eta_1}{jkL}\hat{B}(x) = -\frac{\eta_1}{jkL}[\psi^+ + \psi^-] \tag{2.93}$$

Thus, in this configuration inward fluctuating liner flow velocity is expressed in equations (2.88), (2.89) and (2.93) is closed. This relation to be appropriate, the exterior of the liner need only be exposed to a region in which pressure fluctuations are negligibly small.

2.15.2 Annular cavity enclosed by a rigid wall

In this configuration, a rigid cylinder has been used to form a cavity; the cavity should be shallow enough to create a one-dimensional plane wave in the duct.

$$\frac{d\hat{B}_1}{dx} = -jkL\hat{u}_1 \tag{2.94}$$

$$\frac{d\hat{u}_1}{dx} = -jkL\hat{B}_1 - \frac{C_1 L}{S_c}\hat{v}_1 \tag{2.95}$$

where $\hat{u}_1$ is the complex amplitude of the particle velocity in the cavity along the rigid wall and S_c is the cross-sectional area of the annular cavity along with the formation of a boundary.

$$\hat{u}_1(0) = 0, \hat{u}_1(1) = 0. \tag{2.96}$$

In this configuration, bias flow is not present because the cavity is completely closed. Equations (2.88),(2.89),(2.93) and (2.94),(2.95) now form a closed system of four differential equation of four unknowns ψ^+, ψ^-, $\hat{B}_1$ and $\hat{u}_1$, which can be solved by using a shooting method in Mat-lab.

2.15.3 Annular cavity enclosed by a second liner

In this configuration, the setting is almost identical to the previous one, but a second liner is present with a slightly larger hole, along with a line where bias flow is introduced. Therefore, the equations are

$$\frac{d\hat{B}_1}{dx} = -jkL\hat{u}_1 \tag{2.97}$$

$$\frac{d\hat{u}_1}{dx} = -jkL\hat{B}_1 - \frac{C_1 L}{S_c}\hat{v}_1 + \frac{C_2 L}{S_{c2}}\hat{v}_2 \tag{2.98}$$

$$\hat{v}_2(x) = \frac{\eta_2}{jkL}\hat{B}(x) = -\frac{\eta_1}{jkL}\left[\hat{B}_2(x) - \hat{B}_1(x)\right] \tag{2.99}$$

Equation (2.98) illustrates that a second liner is present inside the cavity. Where η_2 is the compliance of the second liner, C_2 is the circumference to the outer cylinder, $\hat{v}_1$ is the inward fluctuating bias flow velocity, and $\hat{v}_2$ is the inward fluctuating bias flow velocity through the outer liner. In terms of stagnation enthalpy the difference across the liner by the boundary conditions for this configuration is identical to the previous one. Equations (2.88),(2.89),(2.93)

and (2.96) to (2.99) represent a closed system. Fluctuating stagnation enthalpy external to the second liner is very small compared to the nearby insertion; therefore $\hat{B}_2 = 0$ is assumed. Considering the conservation of mass, bias flow through the first and second liners is related.

$$M_i = \frac{C_2}{C_1}\frac{\sigma_2}{\sigma_1}M_o \tag{2.100}$$

where M_i is the mean Mach number of the hole of the inner liner, M_o is the mean Mach number of the hole of the outer liner, σ_1 is the porosity of the inner liner, and σ_2 is the porosity of the outer liner. Since the system is considered one-dimensional, propagating mode for the duct should be one dimensional, and for a circular duct it is limited to its maximum frequency,

$$kL < 1.841\left(\frac{1}{2}\frac{C_1 L}{S_p}\right) \tag{2.101}$$

where S_p is the cross-sectional area of the duct. For liner compliance, Eldredge & Dowling (Eldredge & Dowling, 2003) developed acoustic behaviour of a single aperture for an expression of the compliance of a homogenous screen. Hughes and Dowling (Hughes & Dowling, 1990c) also adapted Rayleigh's (Rayleigh, 1945c) conductivity of a single aperture for a perforated screen in the presence of bias flow. To make the system simpler, Eldredge and Dowling (Eldredge & Dowling, 2003) composed a perforated screen of a square grid aperture with a linearised momentum equation, which expresses the relationship with the conductivity of a single component aperture in an infinitely thin wall, derived by Howe (Howe, 1979). Howe's model states that vorticity is created on the rim of the aperture due to the viscous effect; other features, such as wall thickness and boundary layer dissipation are ignored. Therefore, the damping effect expression for the total compliance as the inertia effect of the liner thickness approximated to stagnation enthalpy difference across the liner is:

$$\frac{1}{\eta_t} = \frac{\pi r^2}{\sigma^2}\frac{1}{K_R} + \frac{1}{\sigma L} \tag{2.102}$$

where η_t is the total compliance of the liner. Considering acoustic energy inside the liner, Eldredge and Dowling (Eldredge & Dowling, 2003) developed an equation based on the forward and backward travelling energy change, defined as the net energy absorbed by the liner, scaled by the energy incident upon the lined section.

$$\Delta = 1 - \frac{|C_u^+|^2 + |B_u^-|^2}{|A_u^+|^2 + |D_d^-|^2} \tag{2.103}$$

2.16 Bellucci's model

Bellucci et al's. (Bellucci et al., 2004b; Bellucci et al.) impedance model was developed based on Crandall's (Crandall, 1926b) impedance model. They considered a large shear number $Sh = |k_s r_0| > 10$ for their perforated screen. The shear number Sh represents the ratio between the hole radius r_0 and the acoustic boundary layer.

$$z_s = \frac{ikl}{\sigma}\left[\left(1 + \frac{\sqrt{2}}{Sh}\right) - i\left(\frac{\sqrt{2}}{Sh}\right)\right] \tag{2.104}$$

Several terms are added to their end effect with a shear number $Sh = r_0/\sqrt{\omega/\nu}$. Bellucci et al's. (Bellucci et al., 2004b; Bellucci et al.) end effect $l_b = l_r l_{in} l_{bf} l_{nl}$ term is clarified below. They introduced correction factors due to the radiation reactance l_{r} Norris & Sheng (Norris & Sheng, 1989), orifice interaction l_{in} Ingard (Ingard, 1953), bias flow l_{bf} Zing, Rienstra (Jing & Sun, 2000; Rienstra, 1983) and nonlinear effect l_{nl} Peters (Peters et al., 1993).

$$l_r = 2 \cdot 0.8216\, r_0 \left[1 + \frac{(0.77 H_n)^2}{1 + 0.77 H_n}\right]^{-1} \tag{2.105}$$

$$l_{in} = 1 - \sqrt{\frac{\sigma}{2}} \tag{2.106}$$

$$l_{bf} = \frac{0.3\left(\frac{6.0}{St^2}\right) + 1}{\frac{6.0}{St^2} + 1} \tag{2.107}$$

$$l_{nl} = 1 - \frac{0.3}{St_{ac}^{0.6}} \tag{2.108}$$

l_{r} is the end correction length for the two orifice ends, H_n represents the Helmholtz number previously discussed in Crandall's (Crandall, 1926b) model, l_{in} is the correction factor for interaction among the neighbouring orifices, l_{bf} is the correction factor due to high bias flow velocities, and l_{nl} is the nonlinear effects acceptable in their experiment. Bias flow Strouhal number represents $St = \omega r_0/U$, previously discussed in section 2.4. Similarly, St_{ac} represents the acoustic Strouhal number $St = \omega r_0/|u|$ considered in this model. The effect of high bias flow velocity and nonlinear effect due to high amplitudes on acoustic pressure loss term P_{be} can be written as

$$P_{be} = \rho \varsigma G\left(\frac{U}{|u|}\right)|u|u \tag{2.109}$$

where P_{be} is Bellucci et al's. (Bellucci et al., 2004b; Bellucci et al.) pressure loss term caused by the flow external to the orifice, $G\left(\frac{U}{|u|}\right) = G(x)$ is given by (Batchelor, 1967) as

$$G(x) = \begin{cases} \dfrac{2x}{\pi\left[\arcsin(x) + 0.66\sqrt{1-x^2}\,(2+x^2)\right]} & if\ x \le 1 \\ x & if\ x > 1 \end{cases} \tag{2.110}$$

The term ς is the pressure loss coefficient, assumed to be time-independent evaluated from external flow to the orifice depending on the ratio of bias flow velocity U to acoustic particle velocity u.

$$1/c_d^2 \qquad if\ U = 0, St_{ac} \le (St_{ac})_{qs} \tag{2.111}$$

$$0.5(3\pi/4)St_{ac}^{1/3} \qquad if\ U = 0, St_{ac} > (St_{ac})_{qs} \tag{2.112}$$

$$\pi\delta St/2(\gamma^2 + \delta^2) \qquad if\ U \ge u \tag{2.113}$$

$$\varsigma_{Uo=0}(1-G) + \varsigma_{Uo\ge u}(G - 4/3\pi)/(1 - 4/3\pi) \qquad if\ 0 < U < u \tag{2.114}$$

In equation (2.113) γ represents the real part and δ represents the imaginary part of Howe's Rayleigh's (Rayleigh, 1870; 1945c) conductivity of the orifice previously described in equation (2.66). In equation (2.114), the term $\varsigma_{Uo=0}$ is given by equation (2.111) or (2.112) and $\varsigma_{Uo\ge u}$ by equation (2.114). Bellucci et al's. (Bellucci et al., 2004b; Bellucci et al.) model assumed the quasi-steady assumption to be valid for the case without bias flow and with the acoustic Strouhal St_{ac} number lower than a limit value. The limit for the quasi-steady assumption for the acoustic Strouhal number is given by $(St_{ac})_{qs} = 0.61/c_d^6$ and transformed into a vortex-sheet model. By combining equations (2.104) and (2.109) and the values of l_{b} Bellucci et al's. (Bellucci et al., 2004b; Bellucci et al.) model for impedance Z_{be} due to perforation can be written as

$$Z_{be} = \rho \varsigma G\left(\frac{U}{|u|}\right)|u|u + \frac{jk}{\sigma}\left[l\left(1 + \frac{\sqrt{2}}{Sh}\right) - i\left(\frac{\sqrt{2}}{Sh}\right) + l_b\right] \tag{2.115}$$

Bellucci et al. (Bellucci et al., 2004b; Bellucci et al.) determined the acoustic particle velocity u by applying the Newton-Raphson method root finding algorithm. Their suggested acoustic particle velocity u is approximated to Betts' (Betts et al., 2000) magnitude of the Mach number in a perforate without bias flow term in the cavity.

$$u = \frac{1}{2c\sigma C_d}\left[\frac{P_{ref}10^{\frac{SPL}{20}}\sqrt{2}}{\rho c}\right] \tag{2.116}$$

The validation of this model is performed for low-Mach and low-Helmholtz numbers by varying screen geometry, acoustic pressure amplitude, and bias flow velocity. This discussion was based on the impedance model Z_{be} due to perforation. In this context, screen impedance in front of the perforated screen is acquired in the presence of the backing cavity.

Bellucci et al's. (Bellucci et al., 2004b; Bellucci et al.) hosted transmission line theory in their model can be referred to as impedance due to the cavity $-j\rho ccot(kd)$. In addition, the nonlinear effect due to high amplitudes on acoustic resistance caused by the flow external to the orifice is calculated under a quasi-steady assumption. This pressure loss term reduces to the linear expression when $U > |u|$, meaning bias flow velocity, is larger than the axial acoustic velocity. However, for larger values of $|u|$, for example, if the acoustic particle velocity $U < |u|$ is larger than the mean bias flow velocity, nonlinear behaviour arises.

$$Z_{bes} = j\omega\rho\left[\left(\frac{1}{\sigma}\right)\{lF(k_s r_0) + 1.7r_0\} - \frac{1}{k}cotkd\right] + \frac{P_{be}}{\sigma u} \tag{2.117}$$

where Z_{bes} is the Bellucci perforated screen impedance with cavity effect. Equation (2.117) allows for the use of unperforated back screen and assuming plane wave propagation into the cavity. Bellucci model will be compared with the data later in chapter 5.

2.17 Luong's model

Luong et al. (2005) approached Rayleigh's (Rayleigh, 1870; 1945c) conductivity and Howe's model of equation (2.75). Concentrating on Rayleigh's (Rayleigh, 1870; 1945c) conductivity shear number, and Cummings' (Cummings, 1984; Cummings, 1986) Bernoulli-type empirical equation to derive a simplified formula for Rayleigh's (Rayleigh, 1870; 1945c) conductivity of a circular aperture mean or bias flow velocity U;

$$l_e\frac{du}{dt} + \frac{1}{2{C_c}^2}(u+U)|u+U| = \frac{\Delta P + pcos(\omega t)}{\rho} \tag{2.118}$$

where $\Delta P + pcos(\omega t)$ represents the acoustic pressure difference across the orifice or driving pressure, where u and U are the acoustic particle velocity and mean bias flow velocity in the orifice respectively. The term resistive force $1/2{C_c}^2(u+U)|u+U|$ is defined as the pressure drop across the orifice and $C_c \approx 0.75$. Cummings uses an effective contraction

coefficient for an infinitesimally thin wall. Therefore, the Rayleigh (Rayleigh, 1870; 1945c) conductivity of a given form of the linearized equation (2.66) is simplified as

$$K_R = 2r(\gamma - j\delta) = 2r\left(\frac{\omega r/U}{\omega r/U \ + 2i/\pi {C_c}^2}\right) \tag{2.119}$$

This expression holds for both linear and nonlinear regimes; the bias flow conductivity for a thin wall is well approximated by the simple equation (2.119). The attenuation of sound by vorticity production at surfaces and edges is greatly enhanced when a mean flow is present to sweep away vorticity energised by the sound. The primary effect of nonlinearity is a small reduction in the mean bias flow velocity.

2.18 Atalla's model

Atalla and Sgard (2007) conceived a perforated screen as a corresponding fluid following the Johnson-Allard approach (Champoux & Allard, 1991; Johnson et al., 1987). The density of the medium is modified by the dynamic tortuosity of the perforated region, and an acoustic impedance model for a perforated panel backed with an air cavity is derived from being the case of perforated panels as a Helmholtz resonator. The system is known as a distributed Helmholtz resonator with cavity volume, cavity neck as aperture thickness, and cavity depth.

$$Z_s = \left(\frac{2l}{r_0} + 4\frac{l'_a}{r_0}\right)\frac{R_{osr}}{\sigma} + \frac{j\omega\rho}{\sigma}(2l'_a + l) - j\rho\,\mathrm{ccot}(kd) \tag{2.120}$$

where $R_{osr} = 0.5\sqrt{\mu\omega\rho}$ is the orifice surface resistance (Ingard, 1953), d is the cavity depth and end correction length given by Atalla and Sgard (2007) $l'_a = 0.85r_0\left(1 - 1.14\sqrt{\sigma}\right)$ from Rayleigh (BARON RAYLEIGH, 1871; Rayleigh, 1945a) end correction, previously discussed in equation (2.25). Whereas Maa's model (Maa, 1998) is only applicable to micro-perforated panel absorbers, Atalla and Sgard's (Atalla & Sgard, 2007) model applies to both small and large diameters of perforated panel absorber. This model is capable of handling perforated plates or screens backed by cavities filled with acoustic materials, including sub-millimetre perforation configurations. Also, the mass of the perforated screen or perforated plate can be accounted for by extending the model to include the inertia of the solid phase.

2.19 Chris Lawn's acoustic absorption in ducts with perforated liner

The acoustic wave in the main duct was treated as one-dimensional with the traverse acoustic flow through the perforation of uniform acoustic pressure in the cavity. When a second liner

or double liner is present, acoustic flow in the cavity may be two dimensional in reality. Chris Lawn (Lawn, 2015) introduced the theory with classical analysis of Crandall (Crandall, 1926b)

$$\frac{\omega}{c}F(kr_0) \equiv -\frac{\omega}{c}j\frac{J_0(\kappa r_0)}{J_2(\kappa r_0)} \tag{2.121}$$

where $\kappa = \sqrt{-j\omega\rho/\mu}$ is the viscous Stokes wave number previously discussed in section 2.4. J_0 and J_2 represent zero and second-order Bessel function, r_0 represents the radius of the aperture or orifice, and $F(kr_0)$ represents the function solution of Crandall's (Crandall, 1926b) viscous effect [4].

2.19.1 Orifice impedance due to no flow

Lawn (Lawn, 2015) has approximated the formula for liner orifice impedance for no flow through the orifice in the absence of cross and bias flow formulation given by Melling (Melling, 1973b), [5] earlier discussed in equation (2.48). Also considered was Howe's theory (Howe, 1979) modified by Jing and Sun (Jing & Sun, 1999), which depends on the Strouhal number (St) instead of frequency. From Rayleigh's (Rayleigh, 1870; 1945c) conductivity K_R, discussed previously in equation (2.20), and Howe's (Howe, 1979), the results are presented in terms of Rayleigh's (Rayleigh, 1870; 1945c) conductivity, discussed in equation (2.66). From equation (2.66) the specific impedance involves a change of sign in Rayleigh's (Rayleigh, 1870; 1945c) conductivity. Chris Lawn (Lawn, 2015) implemented the following equation as surface resistance.

$$z_s = j\frac{\omega}{c}\frac{\pi r_0}{2}\frac{1}{(\gamma + j\delta)} \tag{2.122}$$

For orifice impedance with bias flow, if the flow is not reversing Lawn (Lawn, 2015; 2016) applied Lee et al's (Lee et al., 2007) impedance of orifice with a finite thickness of orifice plate based on Strouhal number St.

$$Re(z_s) = M_b\left\{1.10 + 0.90sin(1 - St)\frac{\pi}{2}\right\} \tag{2.123}$$

[4] The notation for classical analysis of Crandall initially started with a Bessel function of zero order to first order. C. J. Lawn has implemented a Bessel function of zero order to second order.

[5] Orifice impedance due to no flow condition, C. J. Lawn uses the prime convention of coefficient of air viscosities based on Sivian's (Sivian, L. J. (1935) Acoustic impedance of small orifices. *The Journal of the Acoustical Society of America*, 7(2), 94-101.), but considered Melling's (Melling, T. H. (1973b) The acoustic impendance of perforates at medium and high sound pressure levels. *Journal of Sound and Vibration*, 29(1), 1-65.) model.

Lee et al's (Lee et al., 2007) computed result shows a similar result to their experiment. Decreasing resistance from close to the Howe limit at low St number $St > 2$ of only 0.1-.02 M_b with $l = r_0$. M_b represents the bias flow Mach number. $St < 2$ is a satisfactory description, and when applied to $l = 1.5\, r_0$, 1.10 becomes 1.00 for a better fit computationally. The reactance measured and computed by Lee et al. (Lee et al., 2007) is affected by porosity, but for porosities of less than 2 % and for $l = r_0$ described by

$$Im(z_s) = M_b\ (0.1 + 0.75St^2) \tag{2.124}$$

fitting a curve to Lee et al's (Lee et al., 2007) results. At low Strouhal numbers, it is comparable to Howe's (Howe, 1979) solution.

2.19.2 Impedance due to cross-flow

Chris Lawn (Lawn, 2015) has applied correlation of Dickey et al.'s (Dickey et al., 2001) cross-flow of inner liner estimated values of specific acoustic impedance across the orifice of inner liner based on mean starting velocities into and out of the cavity. When there is a flow along the surface containing the orifice, the vortex shedding arising from the acoustic jets is modified and the impedance, even in the absence of a mean bias flow, is radically altered.

$$l_0 = r_0\ \left(1.40 + 0.072\frac{r_0\omega}{u_\tau}\right) \tag{2.125}$$

where l_0 is the equivalent length for no flow, u_τ is the friction velocity of cross-flow. Dickey et al. (Dickey et al., 2001) measured the effect of a range of cross flows, and described their results in terms of friction velocity. They omitted an examination of no cross-flow evidence, but there remains some data evidence to express the resistance and reactance given below.

$$Re(z_s) = 9.57\frac{u_\tau}{c} - \frac{\omega r_0}{c} \equiv 9.57\sqrt{\dot{f}\,/6}\,M_c - 0.64kr_0 \tag{2.126}$$

$$I_m(z_s) = \frac{\omega l_0}{c}\left\{0.58 + 0.42exp\left(-23.6\frac{u_\tau}{2\omega r_0}\right) - 0.03\right\} \tag{2.127}$$

where M_c is the cross-flow Mach number, and $\dot{f}$ represents Darcy friction factor for the duct. However, for $u_\tau/r_0\omega < 0.06$ represents $l_0 = 2.6r_0$ closes Dickey et al's. (Dickey et al., 2001) relation. If the resistance term is $u_\tau/r_0\omega < 0.1$ reverse to Melling's (Melling, 1973b) correlation at this limit $l_0 = 2.1r_0$.

2.19.3 Impedance due to bias and cross flow

The interaction of bias and cross-flow was examined by Sun et al. (Sun et al., 2002) for a range of frequencies up to 850 Hz with the orifice radius from 0.75 - 1.75 mm. The bias flow Mach

number was up to 0.17 and the Strouhal numbers up to 3 followed by cross flow Mach number M_c 0, 0.087 and 0.174. Chris Lawn applied their correlation in this model.

$$Re(z_s) = M_b \left[2.10 - 0.332 \frac{M_c}{M_b} + \left(\frac{M_c}{M_b} \right)^2 \right] \tag{2.128}$$

This resistance term is consistent with Howe's theory with low Strouhal numbers, and there is some limitation not covered by this correlation. The measured reactance shows a linear reduction with increasing bias flow Mach number M_b to negative values. It appears to work for $\frac{M_c}{M_b} > 0.2$ even though M_c is as small as 0.087.

2.19.4 Liner starting section

The properties of air are calculated at every nodal point to allow for variations in pressure and temperature along the lined duct. The increase of acoustic pressure, velocity, acoustic cavity, and axial acoustic velocity are solved by the 4th order Runge-Kutta method. The mean Mach bias flow condition is specified as M_i for average flow through the inner liner and M_o for the outer liner. Therefore, mean pressure in the cavity is defined as

$$P_m = P_{du} \left[1 + \frac{\gamma_c - 1}{2} \frac{M_i^2}{C_d^2} \right]^{\frac{\gamma_c}{\gamma_c - 1}} \tag{2.129}$$

where P_m refers to the mean pressure in the cavity, γ_c represents the ratio of specific heat capacity in the cavity, M_i is the Mach bias flow through the inner liner, M_o is the Mach bias flow through the outer liner, and C_d is the discharge coefficient of the orifice. Mean pressure will be generated at the end of the cavity to estimate the actual cavity pressure. Mean pressure in the plenum is

$$P_p = P_m \left[1 + \frac{\gamma_c - 1}{2} \frac{M_o^2}{C_d^2} \right]^{\frac{\gamma_c}{\gamma_c - 1}} \tag{2.130}$$

Acoustic pressure at the starting end of the cavity is calculated from modulus and phase. If uniform pressure is selected, an estimate of that pressure is made by the mean value at the start and end of the cavity. To determine the specific acoustic impedance of the orifice, the outcomes of various experimental investigations are applied in sections 2.19.1 to 2.19.4. where P_p represents mean pressure in the plenum.

$$p_c = (p_{pc} + \ell |\delta p_c|) e^{jm_c \delta \varphi \frac{\rho c}{p}} \tag{2.131}$$

where p_c is the acoustic pressure in the cavity, m_c is a parameter specifying increments of a phase of cavity pressure, ℓ denotes increments of modulus of cavity pressure, p_{pc} is the starting acoustic pressure in the cavity, δp_c is change in modulus of starting pressure in the cavity, and $\delta\varphi_{\frac{pc}{p}}$ is change in starting pressure in the cavity wavelength because the axial velocity must vanish against the end wall of the cavity.

2.19.5 Acoustic flow through the orifice

Acoustic flow through the orifice is calculated from the impedance definition, such as inner and outer liner acoustic velocity

$$\mathcal{v}_o = \frac{(0 - p_c)}{\Delta Z_s} \frac{2}{(\rho_o c_o + \rho_c c_c)} \tag{2.132}$$

$$\mathcal{v}_i = \frac{(p_c - p)}{\Delta Z_s} \frac{2}{(\rho c + \rho_c c_c)} \tag{2.133}$$

where $\mathcal{v}_o$ and $\mathcal{v}_i$ are the outer and inner liner orifice acoustic velocity, ΔZ_s is specific acoustic impedance across the orifice, p is acoustic pressure in the main duct, ρ, ρ_c, ρ_o is the density of air corresponding to the speed of sound c, c_c, c_o at the temperature of a gas in the local duct, cavity and outer liner.

2.19.6 Acoustic pressure in the main duct and cavity

Acoustic pressure is calculated from the acoustic momentum equation from the main duct and cavity

$$\frac{\partial p}{\partial x} = -j\omega\rho u - \rho Q \frac{\partial u}{\partial x} - \frac{p}{c^2} Q \frac{\partial Q}{\partial x} \tag{2.134}$$

$$\frac{\partial p_c}{\partial x} = -j\omega\rho_c u_{uc} \tag{2.135}$$

where $u_{uc}$is the orifice acoustic velocity in the cavity, u is the acoustic velocity in the main duct, p/c^2 represents fluctuation in acoustic density, and p represents acoustic pressure in the main duct.

2.19.7 Axial acoustic velocity in the main duct and cavity

The acoustic pressure is assumed negligible in the large volume of the outer plenum. Axial acoustic velocity in the main duct and the cavity is the sum of mass conservation and fluctuating mass through the liner. The acoustic velocities are given by

$$\rho \frac{\partial u}{\partial x} = -j\omega \frac{p}{c^2} - \frac{Q}{c^2} \frac{\partial p}{\partial x} - \frac{p}{c^2} \frac{\partial Q}{\partial x} + \frac{S_i}{A_i L} \left(\frac{p_c}{c_c^2} V_w + \mathcal{v}_i \frac{\rho_c + \rho}{2} \right) \tag{2.136}$$

$$\rho_c \frac{\partial u_{uc}}{\partial x} = -j\omega \frac{p_c}{c^2} - \frac{S_i}{A_c L}\left(\frac{p_c}{c_c^2} V_w + \vartheta_w \frac{\rho_c + \rho}{2}\right) + \frac{S_o}{A_c L}\left(\vartheta_o \frac{\rho_c + \rho_o}{2}\right) \quad (2.137)$$

Starting acoustic pressure was specified from (2.131) velocity gradient through equation (2.137). For each iteration axial acoustic velocity at the end of the cavity was compared with the zero-target value, such as m_c and ℓ.

2.19.8 Incident acoustic energy absorption

To aid the convergence of the iterations to a solution fitting the acoustic velocity vanishing condition, a trial function is applied that has approximately the correct variation but does not fit the boundary conditions

$$u_{uc} = u_{uc}^* \sin(k_c x) \quad (2.138)$$

Equation (2.48) was introduced into these equations. Solutions were obtained for u_{uc}^* & k_c

$$\rho_c \frac{\partial u_{uc}}{\partial x} = \mathcal{C} p_c + \mathcal{D} p \quad (2.139)$$

and $\mathcal{C}$ & $\mathcal{D}$ are functions determined from equations (2.136) and (2.137)

$$\mathcal{C} = \frac{j\omega}{c^2} + \frac{S_i}{A_c L}\left(\frac{p_c}{c_c^2} + \frac{\rho_c + \rho}{\rho_c c_c + \rho}\frac{1}{\Delta Z_i}\right) + \frac{S_o}{A_c L}\left(\frac{\rho_c + \rho_o}{\rho_c c_c + \rho_o c_o}\frac{1}{\Delta Z_o}\right) \quad (2.140)$$

$$\mathcal{D} = \frac{S_i}{A_c L}\left(\frac{\rho_c + \rho}{\rho_c c_c + \rho}\frac{1}{\Delta Z_i}\right) \quad (2.141)$$

where ΔZ_i and ΔZ_o are the specific acoustic impedance of the inner and outer liner orifice, S_i and S_o are the inner and outer liner area, A_c and A_i the cross-sectional area of the annular cavity and inner liner, L the length of the liner, and V_w the radial mean velocity of the inner liner. At the end of the liner section, the flux of acoustic energy in the main duct was recorded to determine the absorption Δ of acoustic energy

$$\Delta = 1 - \frac{E_o}{E_i} \quad (2.142)$$

where $E_o = A_d Re\{conj(u)\}$ and $E_i = A_u Re\{conj(u)\}$. A_d and A_u are the cross-sectional area of the main duct alongside the liner and upstream or at the beginning of the liner, E_o and E_i represent acoustic energy out of and into the system. If the initial parameters are negative, then the physical solution is in the opposite direction.

2.20 End correction

End correction of a short tube or perforated plate depends on the aperture radius and thickness. The effective length needs to be able to account for both real and imaginary parts of the impedance (BARON RAYLEIGH, 1871; Rayleigh, 1945a; Rayleigh, 1945b; Rayleigh,

1940). The real part or resistance in the end correction impedance corresponds to viscous frictional losses on the surface of the perforated plate during air flow through the holes. The imaginary part or reactance in the end correction impedance represents the radiation impedance at the hole openings. This extra length l' of the fluid contributes to the process by the reactive part of the radiation impedance of a circular mass piston of air in an infinite baffle. Approximate values of mass end correction are obtained by considering both ends of the aperture $2l' = 1.7r_0$ (Lawrence et al., 2000). Sivian (Sivian, 1935) derived an expression for the end correction resistance and mass reactance terms. Ingard (Ingard, 1953) introduces friction loss on the wall surrounding the orifice proportional to $2r_0$.

2.20.1 Sivian's end correction: Resistance

In 1935 Sivian (Sivian, 1935) investigated circular orifices of diameter from 0.00034 m to 0.01 m with respect to different particle velocities, and with corresponding Reynolds numbers varying from approximately 0.7 to 3000. Sivian (Sivian, 1935) considered that total orifice aperture impedance is to be equal to internal impedance and external impedance, $Z_t = Z_i + Z_e$. The subscript 'e' refers to the external impedance and 'i' refers to the internal impedance of the orifice. Similarly, for the resistance Sivian (Sivian, 1935) has explained that in $R_t = R_i + R_e$, total resistance is equal to internal resistance and external resistance. R_i refers to viscous loss in the hole and R_e refers to viscous loss external to the hole.

$$R_t = R_i + R_e = \frac{j\omega\rho}{\pi r_0^2}\left[\frac{l}{\left\{1 - \frac{2J_1(k_{sp}r_0)}{k_{sp}r_0 J_0(k_{sp}r_0)}\right\}} + \frac{l_e}{\left\{1 - \frac{2J_1(k_s r_0)}{k_s r_0 J_0(k_s r_0)}\right\}}\right] Re \qquad (2.143)$$

where l is the length of the short tube relates to a viscous loss in the hole's internal part, k_s is the viscous Stokes wave number external to the hole in the highly conducting wall, and k_{sp} is the viscous Stokes wave number in the non-thermal conducting wall of the hole. Sivian (Sivian, 1935) considered that viscous resistance end correction is similar to mass end correction. Sivian (Sivian, 1935) used the derivation of Rayleigh's (Rayleigh, 1870; 1945c) end correction described in equation (2.25) for inductance $l_e = 16r_0/3\pi$ based on the assumption of the piston-like motion of a perfect fluid at both ends, which is approximately $0.85r_0$. Regarding the overall expression for acoustic resistance of an orifice proposed by Sivian (Sivian, 1935), he found that acoustic resistance of such a conduit given by the computed values agreed with the experimentally observed resistance within 17 % or better.

Considering the orifice wall as a good insulator, the effect of heat conductivity of the air may be ignored if the channel of the orifice is small compared to the isothermal wavelength. The insulation and conduction behaviour of the specific internal impedance of the orifice given by Crandall (Crandall, 1926b) is shown in equation (2.36). If the orifice area is small relative to the thermal wavelength and walls are maintained at a constant temperature, equation (2.36) holds approximately, but k_{sp} is replaced by k_s

$$\mu' = \mu\left[1 + \frac{\dot{\gamma} - 1}{\sqrt{Pr}}\right]^2 \tag{2.144}$$

where $Pr = \mu c_p / K_T$ is the Prandtl number, c_p is the specific heat of air at constant pressure, K_T is the thermal conductivity of air, and $\dot{\gamma}$ is the ratio of specific heat in the air. The effective Stokes wave number k_{sp} considers viscosity and thermal conductivity losses in a non-conducting wall $k_{sp} = \sqrt{-j\omega\rho/\mu'}$

2.20.2 Ingard's end correction: Resistance

In 1953 Ingard (Ingard, 1953) investigated end correction resistance term both theoretically and experimentally. If a porous material is placed inside the resonator, the acoustic dissipation is mainly due to viscosity and thermal conductivity on the surface of the resonator. Ingard's (Ingard, 1953) work relies on viscous loss of the Helmholtz type. Ingard (Ingard, 1953) considered both linear and non-linear effects of the system and additional loss due to frictional loss over the parallel plate face surfaces surrounding the hole. The effect of linear loss due to the viscosity calculation can be solved from the integral equation (2.145) given by Cremer (Cremer, 1948)

$$D_v = \frac{1}{2}\int_S R_{osr}\,|U_s|^2 ds \tag{2.145}$$

where D_v is the dissipation caused by viscosity, $R_{osr} = 0.5\sqrt{\mu\omega\rho}$ is the orifice surface resistance, U_s is the tangential velocity amplitude at the surface S. Ingard's (Ingard, 1953) experiment insisted upon using uniform velocity in the aperture, and used incompressible non-viscous flow distribution with a velocity going to infinity at the sharp edges. It indicates that the actual value for viscous end correction is larger than the value found. The viscous end correction obtained experimentally was found to be close to $2r_0$ rather than the value r_0 obtained from theory, based on uniform velocity distribution. Thus, this leads to a total end

correction length of r_0, as compared with a value of Rayleigh's (Rayleigh, 1870; 1945c) $1.7r_0$ approximated by Sivian's (Sivian, 1935) assumptions.

$$R_n = \left[\frac{j\omega\rho(l+2r_0)}{\left\{1-\frac{2J_1(k_s r_0)}{\kappa r_0 J_0(k_s r_0)}\right\}}\right] Real \qquad (2.146)$$

The difference between their nominal end correction resistance R_n shows that Ingard (Ingard, 1953) maintained the same coefficient of viscosity, whereas Sivian (Sivian, 1935) used two different types of viscosity. For the limiting cases of Poiseuille-type and Helmholtz-type losses, and the specific case of $l = 2r_0$, the two formula can be compared as follows;

	Ingard	Sivian
Helmholtz-type losses ($r_0^2 f > 0.05$)	$R_{inh} = \sqrt{\mu}(l+2r_0)$	$R_{snh} = \sqrt{\mu}\left(l + 1.7r_0\sqrt{(\mu'/\mu)}\right)$
Poiseuille-type losses ($r_0^2 f < 0.1$)	$R_{inp} = \mu(l+2r_0)$	$R_{snp} = \mu\left(l + 1.7r_0\sqrt{(\mu'/\mu)}\right)$

Table 2.1 Shows the difference between Ingard's and Sivian's end correction resistance

Comparison between Sivian's (Sivian, 1935) and Ingard's (Ingard, 1953) Helmholtz-type losses shows that Sivian's (Sivian, 1935) prediction is only 80 % of the nominal value predicted by using Ingard's (Ingard, 1953) empirical factor.

2.20.3 End correction: Reactance

The reactance of an orifice generally has two contributions, mass reactance due to inertia, and viscosity. In equation (2.42) the resistive part of the end correction was discussed. It has been established that the inertial component of a mass reactance is $\pi {r_0}^2 \rho(l+2l')$ (Rayleigh, 1870; 1945c); $\pi {r_0}^2$ is the core mass hole area, l is the length of the orifice, and l' is the end correction, involving both sides of the orifice or aperture. It is difficult to determine the end correction of an open tube end when there is an infinite flange.

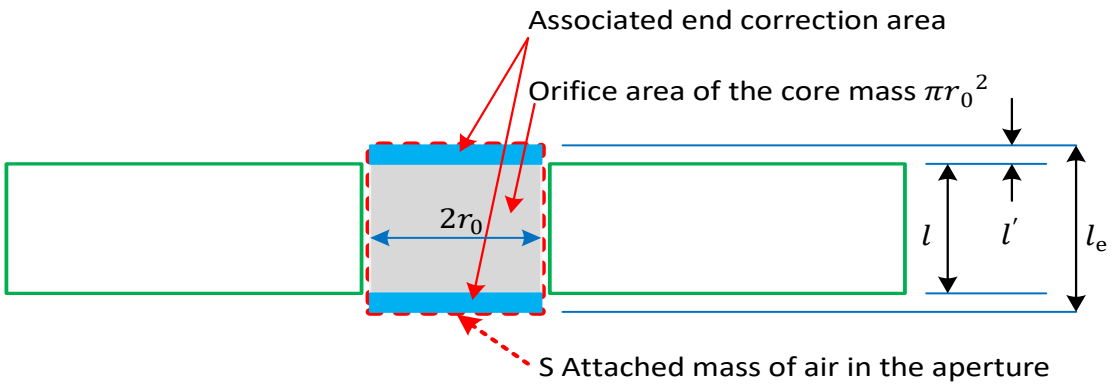

Figure 2.10 Shows the attached mass of air, associated end correction area and core mass.

$\lambda \gg 2\sqrt{{r_0}^2}$ can be expressed for a vibrating piston in a mass baffle, provided that the end correction of a resultant mass is greater than $\pi r_0/4$, and less than Rayleigh (Rayleigh, 1940) ($8r_0/3\pi$). Therefore, the inertial reactance I_X of an orifice can be written as

$$I_X = \pi r_0 \rho\{l + 2(8r_0/3\pi)\} \tag{2.147}$$

Similarly, specific acoustic reactance Z_X can be written as

$$Z_X = \rho(l + 16\, r_0/3\pi) \tag{2.148}$$

From the above equation the end correction factor $16\, r_0/3\pi$ is independent of an internal mass attached to the orifice determined by equations (2.42) and (2.44). Therefore, the total orifice mass reactance for the limiting case may now be written as follows; for Poiseuille-type losses ($r_0^2 f < 0.1$) the specific acoustic impedance of a single hole can be written as

$$Z_{cr} = 1.3j\omega\rho l + 1.7j\omega\rho r_0 \tag{2.149}$$

For Helmholtz-type losses ($r_0^2 f > 0.05$)

$$Z_{cr} = j\omega\rho\left\{l\left(1 + r_0^{-1}\sqrt{\beta^{-1}}\right) + 1.7j\omega\rho r_0\right\} \tag{2.150}$$

Both equations were previously evaluated in section 2.4. Sivian's (Sivian, 1935) and Ingard's (Ingard, 1953) theoretical and experimental values led to the one-sided Rayleigh (Rayleigh, 1870; 1945c) correction $0.85r_0$ for the limiting case of a single aperture in an infinite wall. Bies and Wilson (Bies & Wilson Jr, 1957) suggested that Rayleigh's (Rayleigh, 1870; 1945c) end correction supports good correlation with the experimental results. Several models for end correction resistance and reactance can be summarised below.

End correction	Resistance	Reactance
Elandy et el.	$0.2d + 200d^2 + 16000d^3$	$0.5d$
Bauer	$16r_0/3\pi$	$0.25d$
Ingard	$0.5d$	$16r_0/3\pi$
Rayleigh	$16r_0/3\pi$	$16r_0/3\pi$
Sivian	$16r_0/3\pi$	$16r_0/3\pi$

Table 2.2 Models for end correction impedance.

Table 2.2 compares several models for end correction impedance.

2.21 Orifice interaction

In the middle of the 20th century, the interaction effect between holes was theoretically and experimentally investigated by Ingard (Ingard, 1953) and Fok (Fok, 1941). Later, Nesterov (Nesterov, 1941) validated Fok's work experimentally by showing that an increase in porosity

refers to a reduction in end correction thickness. Recent investigation of Rostand Tayong (Tayong, 2013) shows that the holes interaction and heterogeneity distribution effects on the acoustic properties of air-cavity backed perforated plates are sensitive to the interaction effects between the apertures and their distribution for low sound excitation regime.

2.21.1 Ingard's interaction effect

Ingard (Ingard, 1953) investigated the interaction effect by considering two apertures in a wall – firstly, far apart from one another, and then very close together. In the first case, the combined acoustic reactance of the two independent apertures in parallel is $X/2 = 0.48\rho\omega/\sqrt{A}$, and in the second case, when the two apertures combined into one, a combined mass reactance equal to $X_c/2 = \sqrt{2}X/2$ was observed. These two reactance analyses suggest that based on Ingard's (Ingard, 1953) interaction between two circular apertures, the combined mass reactance of a hole is $\sqrt{2}$ times larger than when the holes are far apart.

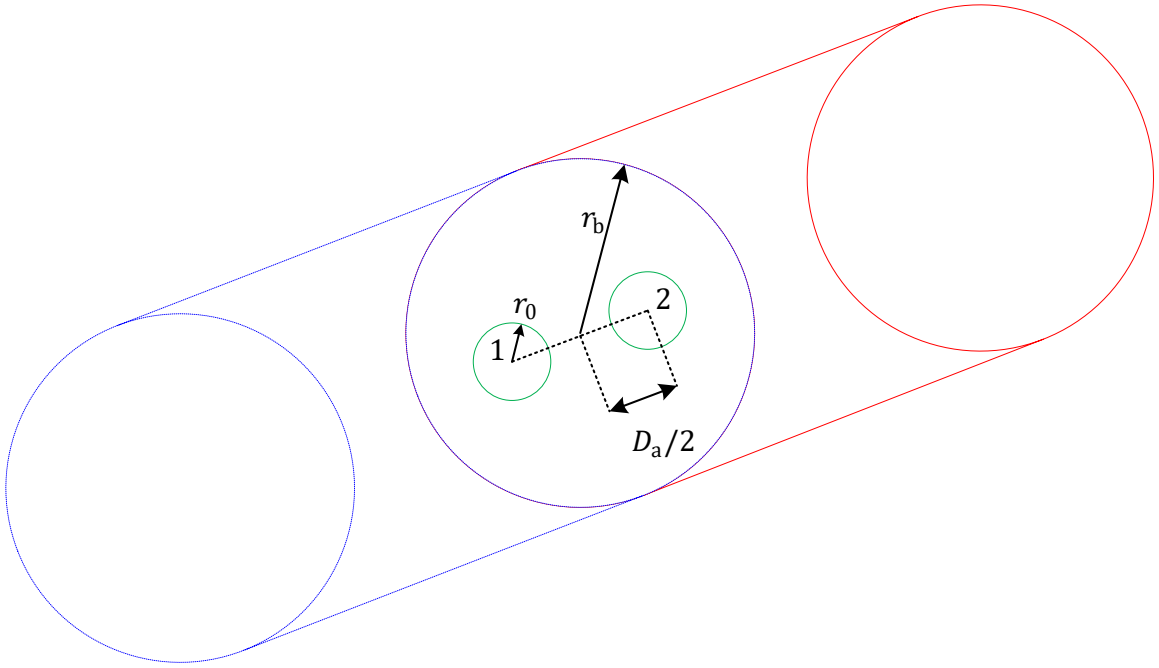

Figure 2.11 Interaction impedance between two eccentric circular apertures in a tube.

The interaction effect of a hole is a function of axial pitch distance between the holes. The pressure $p_{1,2}$ caused by particle velocity U through the aperture was investigated by Ingard (Ingard, 1953) shown in Figure 2.11.

$$Z_{1,2} = \frac{1}{UA_2}\int_{A_2} p_{1,2}dA_2 \qquad (2.151)$$

where $p_{1,2}$ is the pressure exerted by aperture 1 at aperture 2, and U is the particle velocity in the second aperture. Both apertures are symmetrical and circular with a radius of r_0 and

pointed at a distance $D_a/2$ from the axis of the tube radius r_b. To evaluate the resultant pressure analysis of the concentric aperture combination of integral theorem and Bessel function applied by Ingard (Ingard, 1953), equation (2.151) quantifies the end correction due to the interaction effect of the impedance. For this kind of geometry, it can become complicated when attempting to solve it analytically. Ingard expressed that interaction impedance can be written as

$$Z_{1,2} = -j\omega\pi r_0^2 \rho \delta_{12} \tag{2.152}$$

where δ_{12} is the interaction end correction corresponding to the $Z_{1,2}$ interaction impedance. The interaction end correction is a function of aperture axial pitch distance D_a for the particular value of $\zeta = r_0/r_\mathrm{b} = 0.15$. The largest value of the total combined end correction equals $0.42\sqrt{A}$ when the two apertures touch one another. The minimum value of the same quantity is $0.20\sqrt{A}$ corresponding to $\zeta \simeq 0.6$. The maximum combined total acoustic reactance of the two apertures is thus $0.84\rho\omega/2\sqrt{A}$ and the minimum value is $0.40\rho\omega/2\sqrt{A}$. Therefore, Ingard's (Ingard, 1953) interaction effect of two adjacent apertures can be written in terms of porosity, σ, as

$$\psi(\sigma) = 1 - \sqrt{\sigma/2} \tag{2.153}$$

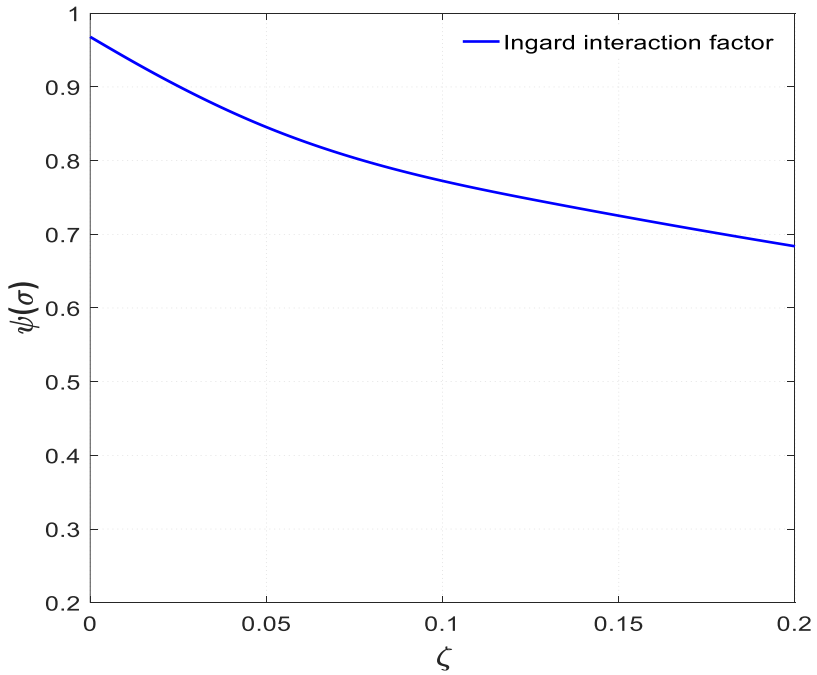

Figure 2.12 Ingard's interaction factor $\psi(\sigma)$ plotted over the interaction parameter ζ.

where $\psi(\sigma)$ reduces the end correction by increasing porosity, ζ is the interaction parameter or correction factor. The interaction end correction δ_{12} has been computed as a function of

the correction factor shown in Figure 2.12. It is clear that in order to obtain maximum acoustic reactance of a given open area in a partition, one should concentrate the open area into one single hole in the centre of the tube (Ingard, 1953).

2.21.2 Fok's Interaction effect

Investigation of the orifice interaction effect was carried out by Rzhevkin and Fok (Fok, 1941; Rzhevkin, 1963). The solution for the case of an infinitely thin plate expressed this correction factor, or interaction parameter, as a function of the ratio of hole diameter r_0 to tube diameter r_b. The interaction effect outside the aperture is linked to the propagation inside the aperture (Ingard, 1953). Propagation inside a circular aperture is the acoustic conductance (Rayleigh, 1940) given for low frequencies $E_c = \frac{\rho Q^2}{2K_R}$, where E_c represents kinetic energy of air passing through the circular aperture, and K_R is the conductance of the aperture wall (associated zone area). This demonstrates that aperture wall conductance K_R is inversely proportional to the oscillating mass $m_o = \rho A^2/K_R = \rho A^2/2r_0\Psi$, where A is the aperture area and Ψ represents a polynomial approximation of the Fok function, and m_o is the oscillating mass. The problems of the attached mass of a circular aperture in a partition across a tube can be solved without assuming piston motion is the same way that Rayleigh (Rayleigh, 1870; 1945c) approached a circular aperture in an infinite partition. Fok (Fok, 1941) solved the mathematical expression for the attached mass of a circular aperture in a wall put across a tube.

$$K_R = \frac{2r_0}{M(\zeta)} \tag{2.154}$$

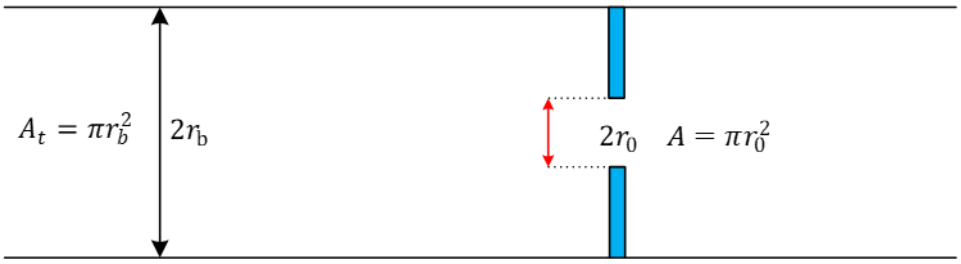

Figure 2.13 Aperture in a partition across a tube diameter $2r_\mathrm{b}$ and aperture diameter $2r_0$.

Figure 2.13 shows that passage of sound through a circular orifice cut in the centre of the partition wall. As previously discussed in the literature review section, Rayleigh's (Rayleigh, 1870; 1945c) conductivity of acoustic equations (2.23) and (2.25) end correction thickness

effect needs to consider them during an acoustic interaction investigation Fok, Nesterov, Rzhevkin, Ingard (Fok, 1941; Ingard, 1953; Nesterov, 1941; Rzhevkin, 1963).

$$l' = \frac{16r_0}{3\pi\psi(\zeta)} \tag{2.155}$$

The end correction term as given by Rayleigh (Rayleigh, 1870; 1945c). $16r_0/3\pi$ applies to a single orifice in an infinite plate (Kinsler et al., 1982). The term $\psi(\zeta)$ is defined as a polynomial of the Fok Function. The mathematical expression can be written as

$$M(\zeta) = (1 + x_1\,\zeta + x_2\,\zeta^2 + x_3\,\zeta^3 + x_4\,\zeta^5 + \cdots\cdots\cdots\cdots) \tag{2.156}$$

where $M(\zeta)$ is an ascending power series in $\zeta = \frac{r_0}{r_{\mathrm{b}}}$ with a constant term equal to unity, which is $M(0) = 1$. Subsequently, when $r_{\mathrm{b}} \gg r_0$ equation (2.154) transforms into Rayleigh's (Rayleigh, 1870; 1945c) equation (2.21) which is a particular instance of the Fok function. When $\zeta = 1$ represents there is no partition in the tube, Fok (Fok, 1941) has shown that the function $M(\zeta)$ tends to approach zero, while the conductivity according to equation (2.154) becomes infinite. For practical purposes, it is convenient to introduce $\psi(\zeta)$ instead of $M(\zeta)$, which is reciprocal quantity. $\psi(\zeta) = \frac{K_R}{2r_0} = \frac{1}{M(\zeta)}$is the reciprocal of the Fok Function and ζ its correction factor. The agreement expresses that the conductivity increases in the tube compared to the conductivity of the same orifice in a screen of infinite extrusion (Rzhevkin, 1963). Therefore, equation (2.156) can be written as

$$\psi(\zeta) = (1 + x_1\,\zeta + x_2\,\zeta^2 + x_3\,\zeta^3 + x_4\,\zeta^5 + \cdots\cdots\cdots\cdots)^{-1} \tag{2.157}$$

$$\psi(\zeta) = \left(\sum_{n=0}^{12}[x_n\zeta^n]\right)^{-1} \tag{2.158}$$

The coefficients of x_n have the values given in the table below

x_0= 1	x_1=-1.4092	x_2=0	x_3=0.33818	x_4=0	x_5=0.06793	x_6=0.02287
x_7=0.03015	x_8=-0.01641	x_9=0.01729	x_{10}=-0.01248	x_{11}=0.01205	x_{12}=-0.00985	

Table 2.3 Coefficients of Fok function

The ratio of the aperture area to the tube area refers to porosity $\sigma = r_0^2/r_b^2$. Therefore, the Fok function argument can be written in terms of porosity, where $\zeta = \sqrt{\sigma}$

$$\psi(\sigma) = \left(\sum_{n=0}^{12}\left[x_n\sqrt{\sigma}^n\right]\right)^{-1} \tag{2.159}$$

Nesterov (Nesterov, 1941) validated Fok's (Fok, 1941) work experimentally, showing that equations (2.158) and (2.159) are valid for both single and multiple apertures.

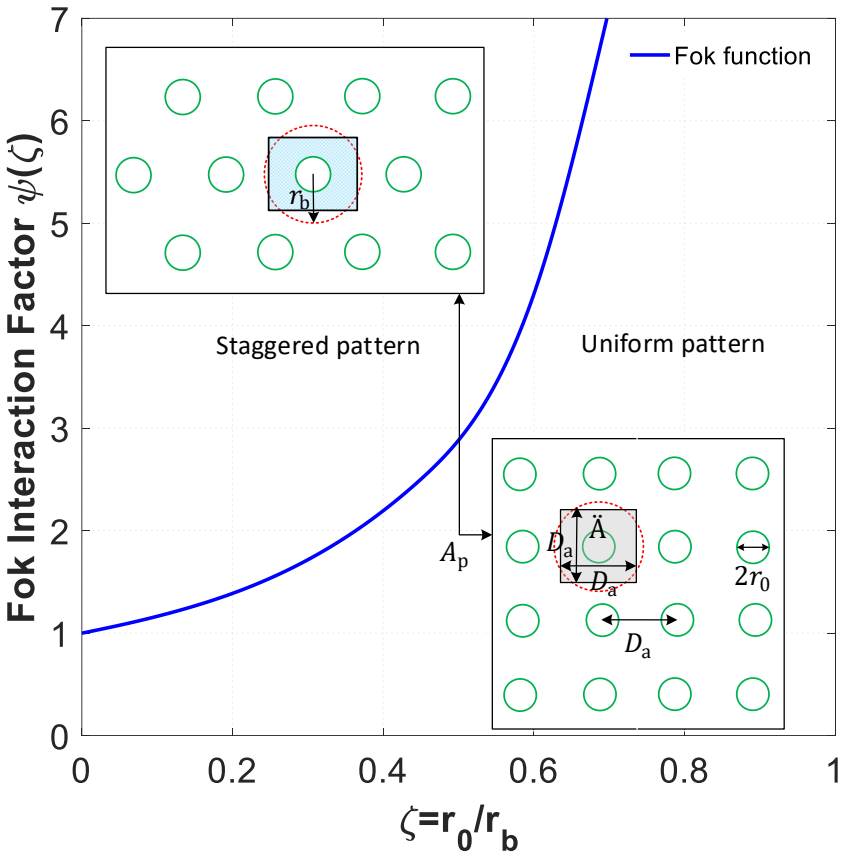

Figure 2.14 Depicts the Fok function interaction factor.

The function $\psi(\zeta)$ is always greater than the unity. If $\zeta \to 1$ it suggests infinity, which indicates that attached mass tends to be zero. If $\zeta \to 0$ then it tends to unity. If the ratio $\zeta = r_0/r_b < 0.2$ there is no interaction effect $K_R \approx 2r_0$. If the ratio $\zeta = r_0/r_b < 0.8$ the attached mass m_0 disappears as the aperture on the lines of current becomes small because K_R becomes a very large quantity. Figure 2.14 shows two different types of perforation hole geometry: uniform and staggered pattern. In addition, it shows that single aperture interaction area $\ddot{A} = D_a^2$ belongs to a single aperture. In order to determine the interaction effect of multiple apertures n, which is exposed on the area of a perforated plate A_p of a partition in a tube, where each aperture $2r_0$ is confined within an axial pitch distance D_a, then the equivalent diameter of $r_b = 2\sqrt{\ddot{A}/\pi}$ can be calculated from the interaction area. Based on Fok's (Fok, 1941) conclusion, it can be assumed that the conductance of each aperture is approximately independent of the distance between them, which is equal to Rayleigh (Rayleigh, 1940) $K_1 = d_o$. Therefore, total conductance can be written as $K_t = nK_1 \approx n2r_0$ and total attached mass $m_t = nm_1 = n\,\rho A^2/K_1$. Acoustic units of attached mass of a single aperture are $m_1 = \rho A^2/K_1$ and the attached mass of n holes is $m_n = \rho A^2/K_t =$

$\rho A^2/nK_1 = m_1/n$. Electrically this is analogous to the fact that the inductance of n identical parallel circuits is n times less than the inductance of one circuit. If the apertures are very close to each other, the attached mass of each aperture inclines to zero, which can be observed from the Fok Function equations (2.158) and (2.159) and the curve in Figure 2.14.

2.22 Conclusion

In this chapter, the concepts behind the theory of the Rayleigh conductivity model, impedance models, end correction, and interaction end correction are discussed. Methodologies in the frequency domain in the presence of bias flow, cross flow, thickness effect, viscosity effect, and thermal conductivity effect are explained in an isentropic condition. The mathematical strategies, concerning an overall structure for the exploration of the interactions between acoustic, vorticity and entropy perturbations, are described in sections 2.4 and 2.15. The diverse combination mechanisms between the bias flow and cross-flow impedance effects are explained separately with a semi-empirical model.

The propagation of coupled acoustic mass, end correction effect of aperture resistance and reactance is checked through a set of chosen references from theory. Several models with no flow and non-zero bias flow effects have been assessed for the case of a single hole and overall perforation. Acoustic impedance models, end correction, and interaction end correction models have been verified from the literature and presented in this thesis, which is an excellent contribution to science. This can be designated as a reiteration, or complementation, of previous work for future accomplishment. Later, in Chapter 3, this coding system will be implemented to develop the semi-empirical hybrid model.

3 Preliminary semi-empirical hybrid model

In this chapter, the impedance model is developed for no flow acoustic analysis of the perforated liner. The impedance model will be subject to experimental analysis. There have been a few significant approaches to the acoustic impedance modelling of a perforated liner, which are reviewed in this chapter. In one approach, thin perforated plates were considered for the orifices to be modelled as cylindrical ducts (Hersh & Rogers, 1976), and Sivian (Sivian, 1935) applied this approach where the end effects and boundary layers are significant. Crandall's (Crandall, 1926b) velocity profile magnitude considered losses in the hole. To determine the surface impedance (resistance), Ingard (Ingard, 1953) examined dissipation caused by the viscosity (Cremer, 1948) within the device, modified by using the thickness term of oscillatory flow over an infinite plane surface model. The third approach is to model the perforate orifices end correction by using Rayleigh's (Rayleigh, 1870; 1945c) term, which are surrounded by cylindrical ducts. By considering the cavity size as much smaller than the acoustic wavelength, Panton and Miller's (Goldman & Panton, 1976) transcendental equation has been modified to determine impedance due to the cavity. To complete the impedance model interaction end correction term, Melling's (Melling, 1973b) modification of Sivian's (Sivian, 1935) approach was appropriated, and adiabatic effective kinematic viscosity was considered in a non-conducting wall, along with the Fok (Fok, 1941) function. All these approaches are used to develop acoustic impedance models for perforates.

3.1 Impedance due to the perforation

A straight cylinder with several circular orifices requires less input in comparison with a non-uniform cross-section. The propagation of sound in a circular tube was first investigated by Kirchhoff (Kirchhoff, 1868b) and Rayleigh (Rayleigh, 1870; 1945c). Their theories both account for viscous and thermal conductivity. A one-dimensional plane wave $\lambda \gg r$ and flow is considered as incompressible and the orifice is acoustically compact. Rayleigh's (Rayleigh, 1870; 1945c) conductivity can be expressed as

$$K_R = \frac{\dot{m}}{\Delta P} = \frac{j\omega\rho Q}{(p_+ - p_-)} \tag{3.1}$$

This is discussed in section 2.3 in equation (2.20), where K_R represents Rayleigh's (Rayleigh, 1870; 1945c) conductivity of an orifice, $\dot{m}$ is the mass flow rate, ω is the angular frequency, ρ is the density, ΔP is the pressure drop, p_+ is the high mean pressure amplitude, p_- is the low

mean pressure amplitude, and r is the radius of the aperture. Acoustic impedance is analogous to the Rayleigh conductivity. The non-dimensional specific acoustic impedance Z_p of a perforated plate can be defined as the ratio of fluctuating plane wave pressure difference across the perforated plate to the characteristic impedance, as expressed in chapter 2, section 2.1.4 in equation (2.17)

$$Z_p = \frac{Z_h}{\sigma} \tag{3.2}$$

where Z_p is the perforated plate's non-dimensional specific acoustic impedance, σ is the porosity of the plate, $Z_h = p_+ - p_-/\rho c u_h$ is the non-dimensional specific acoustic impedance of a single hole, and u_h is the acoustic particle velocity through the single hole. The division of porosity σ over the non-dimensional specific acoustic impedance of a single hole refers to the conversion of single hole impedance into the impedance of the entire perforation (Guess, 1975b). A plane wave normal velocity before or after the perforated plate has been approximated by (Allard, 1993; Bauer, 1977; Bellucci et al., 2004b; Betts, 2000; Crandall, 1954; Melling, 1973b; Thurston, 1952b) and many other researchers. Orifice resistance at low velocities investigated by Sivian (Sivian, 1935), previously discussed in section 2.20.1, shows that radiation resistance is negligibly small in comparison with the resistance, due to viscosity and heat conductivity. When the size of the hole is very small compared to the wavelength, flow through the hole is considered as incompressible. Sivian (Sivian, 1935) has applied the difference between the two viscosities, conducting wall and the non-conducting wall, including viscous and thermal effects in a tube. In the absence of mean flow, Crandall (Crandall, 1926b) has carried out a generalised form of orifice impedance, where viscosity waves are diffused in the x direction, normal to the oscillating plane. The velocity profile is assumed to have only radial variations and to be constant through the thickness of the duct. Nonlinear terms are replaced by time-averaged acoustic parameters, and velocity inside the tube is assumed to have a simple harmonic time dependence. The internal impedance of an orifice is considered, without an end correction term. A discussion of Crandall's (Crandall, 1926b) solution for an expression of impedance per unit length to viscous flow within an infinite tube can be found in Chapter 2, section 2.4 in equation (2.36). The quantity in the square brackets in equation (3.3) is a velocity profile function given by Crandall (Crandall, 1926b) and approximated by (Allard, 1993; Bellucci et al., 2004b; Boden & Zhou, 2012; Melling, 1973b; Sivian, 1935; Thurston, 1952b) and many others. For this

instance, impedance due to the perforation case, if the orifice walls are maintained at a constant temperature and isothermal conditions approached in a conducting wall, the viscous Stokes wave number is considered along with characteristic impedance over porosity, given below.

$$Z_{per} = \frac{C_{pe}\rho c[F(k_s r)]}{\sigma} \tag{3.3}$$

Where Z_{per} is the impedance due to the perforation, C_{pe} is the perforate impedance constant and the value of C_{pe} is 0.0024, k_s is the viscous Stokes wave number (phase constant), briefly discussed in equation (2.30), and $|k_s r|$ is the ratio of orifice radius to the boundary layer thickness, which determines the acoustic behaviour of the orifice. The function $F(k_s r)$ represents the viscous effects given by Stokes (Stokes, 1851) and approximated by Helmholtz (Von Helmholtz, 1863) Kirchhoff (Kirchhoff, 1868a) and Kinsler & Frey (Frey & Kinsler, 1950), Crandall (Crandall, 1926b), and many others. It can be expanded as

$$F(K_s r) = 1 - \frac{4}{K_s r}\frac{J_1(k_s r)}{J_0(k_s r)} \tag{3.4}$$

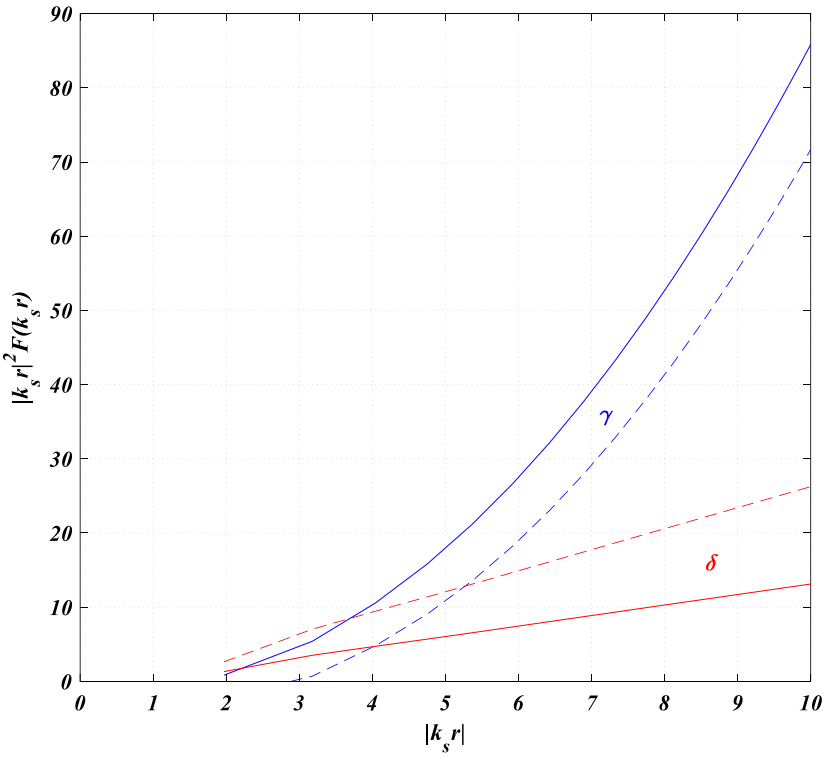

Figure 3.1 Crandall model γ represents the real and δ represents the imaginary part.

where J_0 represents the Bessel function of zero-order and J_1 represents the Bessel function of the first order. The acoustic velocity profile magnitude considered on both sides of the

orifice is provided in equation (3.4). The difference between one-side (dashed line) and both sides (Solid line is the same as Figure 2.6) of the real and imaginary parts of the velocity profile magnitude is shown in a generalised form of Crandall's (Crandall, 1926b) model, in Figure 3.1.

3.2 Impedance due to surface resistance

In this present calculation of the resonant frequency $f_r = (c/2\pi)\sqrt{\frac{\rho}{md}}$, the method allowed the absorption coefficient and surface impedance to be determined for all frequencies, where $m = \rho l_e {D_a}^2/\pi r^2$ is the acoustic mass, d is the cavity depth, l_e is the thickness of the aperture plus end corrections length and D_a is the axial pitch distance shown in Figure 3.5. The losses within the device must be modelled for prediction. In general, losses are determined by the surface resistance Z_{sr}. For a Helmholtz device with no additional absorbent liner, the absorber can be implemented by using Guess (Guess, 1975a)

$$Z_{sr} = \frac{\rho}{\sigma}\sqrt{8\nu\omega}\left(1 + \frac{l}{2r}\right) \tag{3.5}$$

where ν is the kinematic viscosity, and l is the thickness of the aperture. Equation (3.5) assumes that the hole radius is not sub-millimetre in size, to ensure it is larger than the boundary layer thickness. An alternative for this resistive term $\sqrt{2\omega\rho\mu}/2$ was implemented by Ingard (Ingard, 1953). As a result, proposed dissipation caused by the viscosity considered as impedance due to the surface resistance Z_s with the effect of the aperture thickness can be written as

$$Z_s = \frac{(l_t + 0.1l/2r)\sqrt{2\omega\rho\mu}}{2\sigma} \tag{3.6}$$

where l_t is the thickness constant that is based on empiricism and is the value of 0.025. One side of the perforated plate surface is considered in equation (3.6). It can be considered twice if surface resistance considers both sides of the plate. To apply the thickness effect in this present model, impedance due to surface resistance, in equation (3.5) orifice length to diameter ratio of the aperture is taken into account. The empirical value of thickness constant is 0.025, plus 10-30 % of the orifice length to diameter of the aperture, and is mapped with the current experimental analysis. Under this mapping, this empirical model provides an increase or decrease absorption profile by changing the orifice length. The model analysis suggests that by changing its length to a diameter ratio combustor liner thickness effect can

be deployed. The effect of length to diameter ratio applied on to configurations 1 and 7 are provided below.

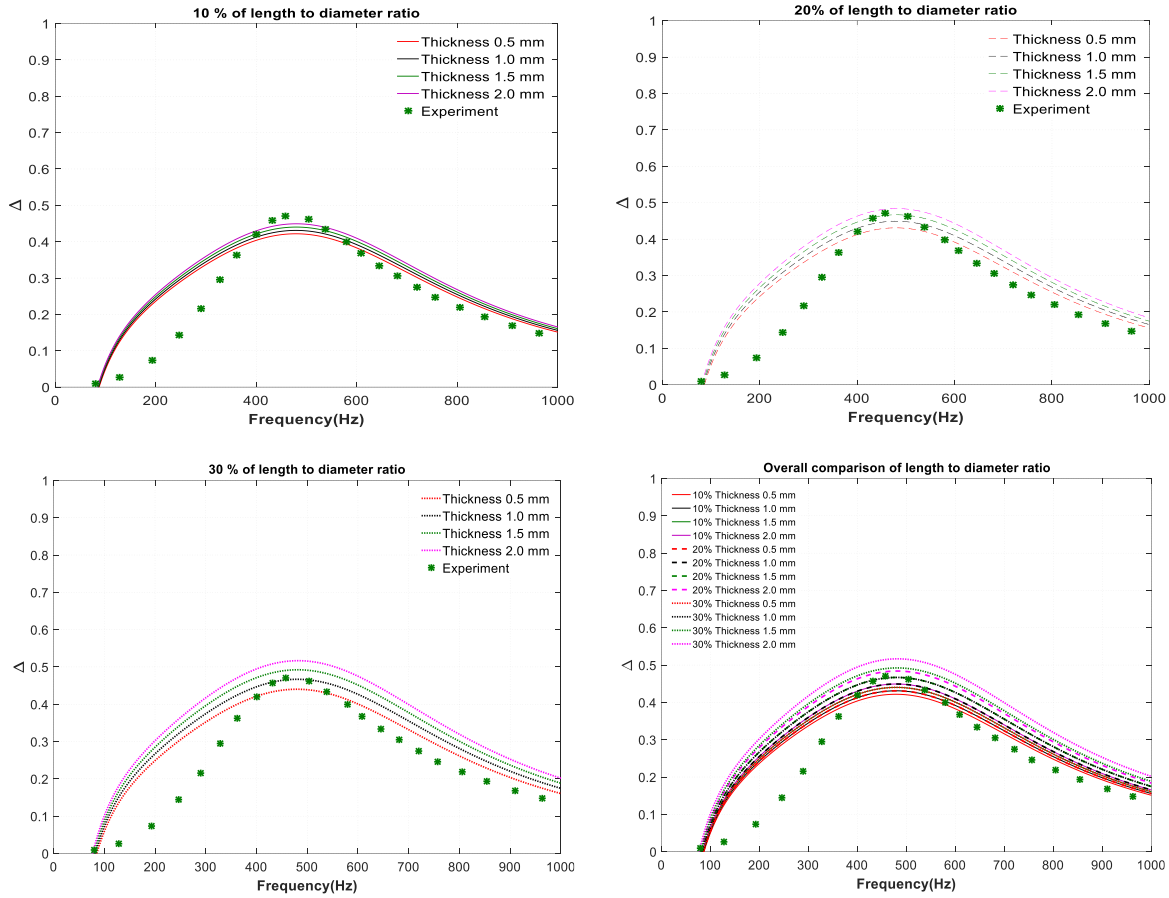

Figure 3.2 Thickness effect on configuration 1.

Configuration 1's thickness (0.5 mm, 1 mm, 1.5 mm and 2 mm) effect is analysed based on 10-30 % of length to diameter ratio with thickness constant, and the results are shown in Figure 3.2. The green asterisk marker shows that the absorption profile of Lahiri et al.'s (Lahiri, 2014; Lahiri & Bake, 2017; Lahiri et al., 2011) experimental result, and the liner has 1 mm thickness. It can be observed from the hybrid model analysis that as the thickness increases, so does the absorption profile. Furthermore, it also shows that 10 % of length to diameter ratio with 1 mm thickness is overlapped with 20 % of length to diameter ratio with 0.5 mm thickness. There are four overlapping cases identified, which demonstrates that by increasing length to diameter ratio orifice length can be decreased.

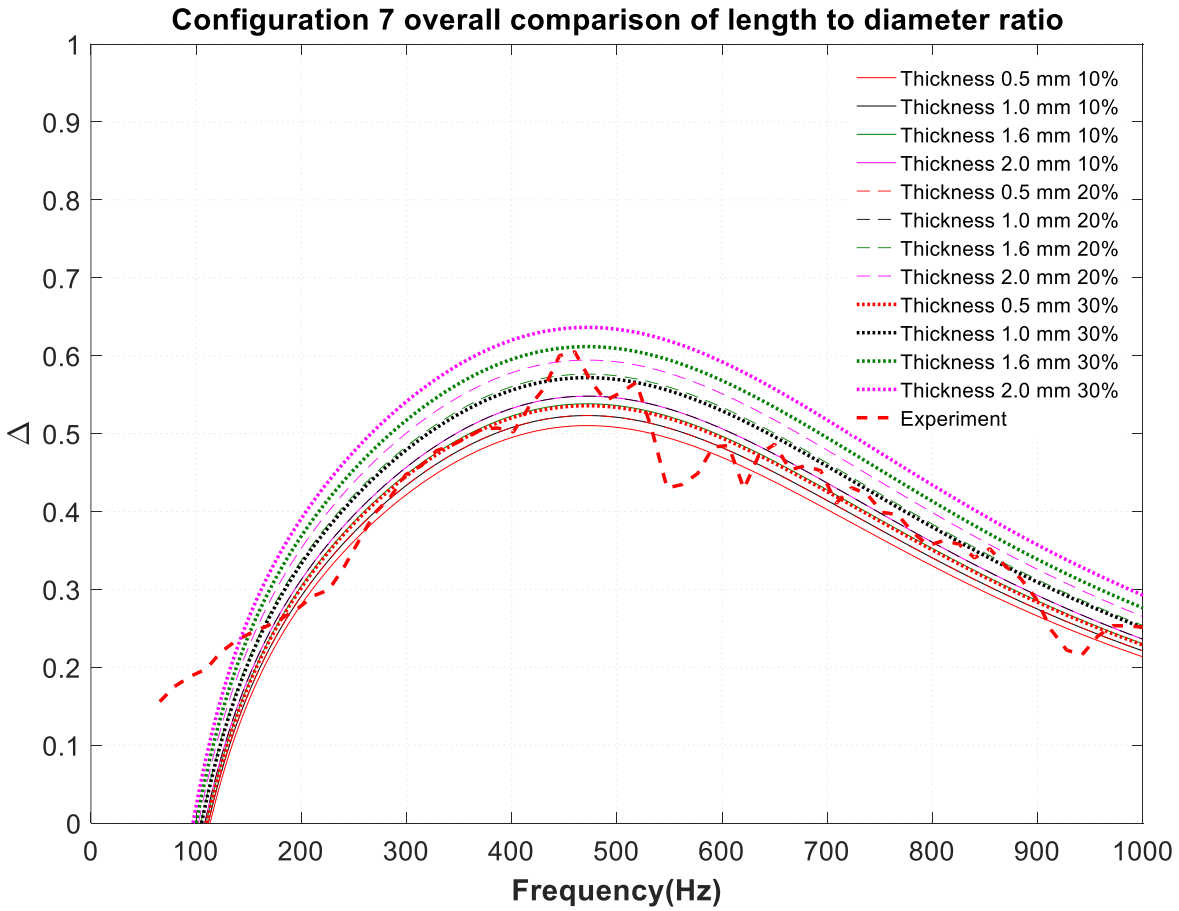

Figure 3.3 Thickness effect on configuration 7.

Rather than four, only one instance of the figure will be considered for this description: configuration 7's overall length to diameter ratio, including the thickness constant effect shown in Figure 3.3. Four different types of thickness (0.5 mm, 1 mm, 1.6 mm and 2 mm) effect is analysed in this configuration. The red dashed line shows an absorption profile for configuration 7, which has a thickness of 1.6 mm. The data from this investigation suggests that an increase in liner thickness provides an increase in the absorption profile. It also demonstrates at least four cases of overlapping. Both investigations showed that 10 % of the length to diameter ratio containing 1 mm thickness creates the same profile as 20 % of the length to diameter ratio containing 0.5 mm thickness. To optimise the thickness constant plus 10 % of orifice length to diameter ratio, equation (3.6) is implemented into the model analysis.

3.3 Impedance due to end correction

An inertial mass end correction term Z_e, the radiation reactance of a circular aperture piston in an infinite plane resulting from Rayleigh (Rayleigh, 1870; 1945c) and approximated by

Morse (Morse, 1948) $(16/3\pi)\, r \simeq 1.7r$, previously described in equation (2.25), is repeated below to provide an explanation of model implementation.

$$Z_e = j\omega\rho \frac{16r}{3\pi} \tag{3.7}$$

The absorption effect of the perforated liner depends on its location. For ideal absorption, it ought to be engaged where the acoustic particle velocity is the highest. A perforated liner's absorption property works primarily by viscous losses as sound penetrates the small orifice. To take full advantage of this effect, the air movement must be at its highest, and this occurs where particle velocity is largest. For a Helmholtz resonator, this means that the absorber should be as close to the openings as possible, or even in the openings.

3.4 Impedance due to the cavity

The effect of placing an air gap between the perforated liner and the air absorber is to reduce the resistance, and in most cases this will result in a decrease in absorption (Davern, 1977). Consequently, the design equation can be altered depending on the cavity depth d. The impedance of the perforated liner forms the Helmholtz device from acoustic resistance and mass. Panton and Miller (Panton & Miller, 1975) showed that the likelihood of long wavelengths compared to the resonator length (all dimensions) is small and can be dismissed. The resonance frequency for a cylindrical Helmholtz resonator can be found by solving a transcendental equation $cotkL$, approximated by Tournadre et al., Bauer, Andrew B., Schultz et al., Elandy et al. (Bauer, 1977; Elnady et al., 2004; Schultz et al., 2009; Tournadre et al., 2016a) and many others.

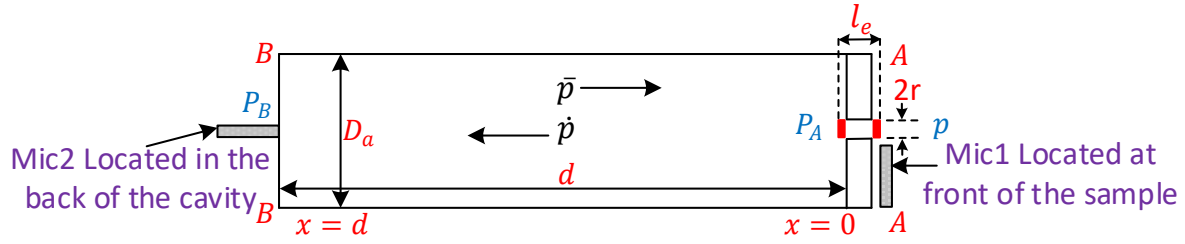

Figure 3.4 Classical resonant cavity as a Helmholtz resonator.

By considering the case of a cavity with a distributed surface impedance $A - A$ of a Helmholtz resonator, the resonant frequency is independent of the shape of cavity depth d. This result arises from an assumption that all dimensions are small compared to the wavelength, and wave motion is in the x direction only, as shown in Figure 3.4. The resonator has a cylindrical tube. One end has an orifice at $x = 0$ and $x = d$.

The orifice area is A_O and effective length is l_e including end correction on both sides of the orifice, as previously described in chapter 2, section 2.3. The walls of the cavity are assumed to be sufficiently large enough so that the surface impedance is locally reacting, meaning that no transmission is allowed in directions perpendicular to x. Any wave entering the cavity is assumed to be totally reflected at the back wall. Therefore, an incident pressure wave $\dot{p} = A_u^+ e^{j[\omega t - kx]}$ and reflected pressure wave $\bar{p} = B_u^- e^{j[\omega t + kx]}$ resulted in the following expression for the acoustic volume velocities of these two waves: $Q_+ = \frac{\dot{p}}{\frac{\rho c}{A_\mathrm{t}}}$ and $Q_- = \frac{\bar{p}}{\frac{\rho c}{A_t}}$.

Thus, an expression for the acoustic impedance at any point in the cavity is

$$Z = \frac{\dot{p} + \bar{p}}{Q_+ + Q_-} = \frac{\rho c}{A_\mathrm{t}} \cdot \frac{A_u^+ e^{-jkx} + B_u^- e^{jkx}}{A_u^+ e^{-jkx} - B_u^- e^{jkx}} \tag{3.8}$$

This equation (3.8) is evaluated at $x = o$ and $x = d$, then A_u^+ and B_u^- are eliminated in favour of Z_0 and Z_d .The reflection coefficient is frequency-dependent. In a cylindrical tube, a standing wave is recognised as a result of the incoming and outgoing wave. If the resulting complex amplitude of the pressure field in the tube is the same, the wall at $x = d$ becomes infinite, and the pressure of the standing wave in the cavity (Dean, 1974) is

$$p = 2A_u^+ e^{j\omega t} \cos(kd) \tag{3.9}$$

From a linearised (Euler's) momentum equation,

$$\rho \frac{\partial u}{\partial t} = -\frac{\partial p}{\partial x} \tag{3.10}$$

The normal acoustic particle velocity in the tube or cavity, u can be obtained, giving

$$u = -j \frac{2A_u^+}{\rho c} e^{j\omega t} sin(kd) \tag{3.11}$$

Equations (3.9) and (3.11) designate a standing sound wave. The interchanging sound pressure at all points d varies with the identical phase and as a function of time; the particle velocity fluctuates in phase coincidence also as a function of time. Pressure and particle velocity, therefore, are shifted in phase with respect to time by 90^0 from each other. The maximal values of pressure and velocity are distributed spatially, as a $cosine$ and a sin function respectively. At the end of the tube $x = d$, the particle velocity is always zero; however, the sound pressure is maximal. Amplitudes of pressure and velocity are a function of co-ordinate d. The velocity nodes occur at distances $d = \frac{n\lambda}{2} (n = 0,1,2, \dots)$ in front of the rigid end, and the antinodes at the points $d = \frac{n\lambda}{2} + \frac{\lambda}{4}$. The maximal values of the sound

pressure are displaced by ¼ wavelength with respect to the velocity. The cavity filled with air is considered as acoustically compact, so that the particle velocity normal to the liner at $A-A$ is identical to that inside the cavity, and towards the end of the cavity is given by $B-B$ Meyer Erwin (Meyer, 2012).

$$u_A = j\frac{2P_A}{\rho c}e^{j\omega t}sin(kd) = j\frac{P_B}{\rho c}e^{j\omega t}sin(kd) \tag{3.12}$$

where P_A and P_B is the pressure at the liner and rear of the cavity, ρc is the characteristic impedance of the medium. Now the cavity itself can be considered to have an impedance. If the cross-sectional area of the tube is represented by A_{t} then the specific acoustic impedance of the tube can be written as

$$Z_d = \frac{p}{u} = \frac{2A_u^+ e^{i\omega t}\cos(kd)}{-j\frac{2A_u^+}{\rho c}e^{i\omega t}\sin(kd)} = -j\rho c cot(kd) \tag{3.13}$$

Equation (3.13) represents the normal surface impedance of the air layer Z_d between the perforated plate and rigid wall, which has a cavity depth d implemented in the numerical analysis. Comparisons have been made with the results obtained by (Lahiri, 2014; Lahiri & Bake, 2017; Lahiri et al., 2011) and experiments carried out at the UHARC, where the perforated liners have been tested in a duct with different cavity depths or diameters. The overall comparison shows that the results are inconsistent due to the differences in test rig boundary conditions. An extended form of this simplified theory is to consider acoustically thick liners, or to consider situations where acoustic particle velocity is converted into turbulent particle velocity (Melling, 1973a). Such demonstration indicates that modification is required to add a cavity factor into the equation. Additional exploration indicates that the inconsistencies of the geometric outline of the test rig can be hypothetically solved by implementing a cavity factor, which is a function of cavity depth. Therefore, a cavity factor c_f has been introduced into this numerical model for endorsement in equation (3.14). Establishment of the cavity factor is clarified in equations (3.16).

$$Z_d = -j\rho c cot\left(kdc_f\right) \tag{3.14}$$

Equation (3.14) is applied to the numerical model for computation to develop the liner absorption or dissipation profile.

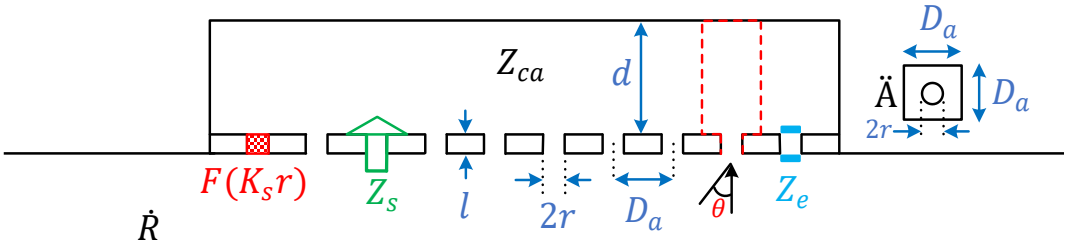

Figure 3.5 Single liner configuration used for computation showing the notation used for the perforations.

Single liner geometry for the computation and notation of perforation is shown in Figure 3.5. Equation (3.13) with the added cavity factor is specified in equation (3.14), which matches with the few single liner configurations demonstrated in sections 5.3 to 5.20, but disagrees with double layer combustor liner experimental analysis. The additional model analysis reveals that the modification of acoustic particle velocity in the tube is required for a double layer liner, which is perpendicular to the propagation of incident sound source. This simple relationship between cavity pressure and particle velocity implies that pressure can be measured anywhere in the cavity, but the rear wall is convenient from a practical point of view. Thus, only the sound pressure at the front surface and at the rear cavity wall, together with their relative phases, are needed to evaluate the total impedance. More complex liner configurations would, of course, require a set of re-derived equations, but in many cases, it may not be possible to derive explicit relationships between pressures in such configurations (Dean, 1974). The complexity of the double liner geometry, the extended form of computation and notation of perforation, is given below.

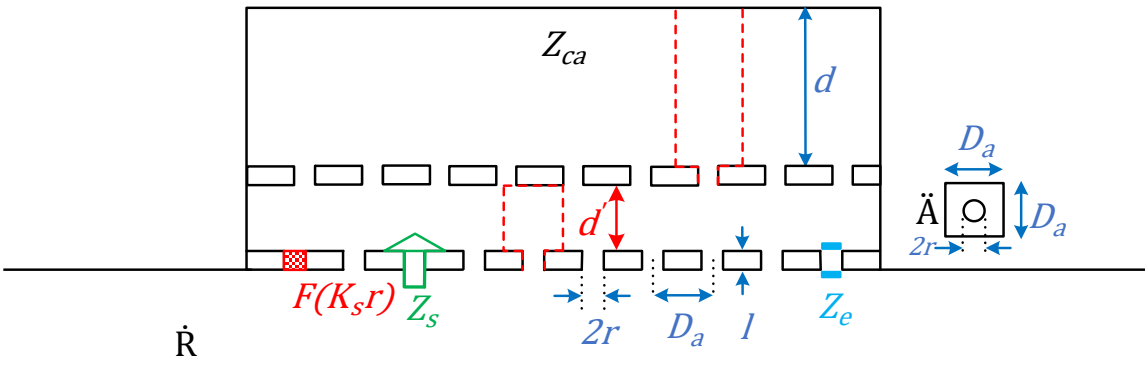

Figure 3.6 Double liner configuration used for computation showing the notation used for the perforations.

Geometry for the double liner computation and notation of the perforation is shown in Figure 3.6, which has an additional parameter effective cavity depth d' implemented in alternative cavity impedance model earlier discussed in section 2.1.2 in equation (2.11). This indicates that cavity depth for a double layer liner is slightly shorter, and contains a distributed Helmholtz resonator. Due to the variation of cavity depth and resonance effect, modification of acoustic particle velocity in the cavity is required, according to equations (3.11) or (3.14). In this modification of an attenuation-free case, the acoustical input impedance of a tube with acoustically hard termination in equation (3.14) represents only (purely imaginary) reactive impedance and is a cotangent function of the tube length d. For positive values of the imaginary part, the column of the medium in the tube behaves like an inert mass. For a negative value, it behaves like a flexible spring (Meyer, 2012).

The cotangent function in equation (3.13) or (3.14) is replaced by the cosine function of its argument. Justification of this modification is the improved fit with experimental data for absorption and dissipation profiles. The background foundation of the cosine function is not established in this research and can be designated for future research. Thus, a modified equation is applied for a double layer liner's normal acoustic particle velocity and pressure at the surface, then the cavity itself is considered to have an impedance, giving

$$Z_{ca} = -j\rho c \cos\left(kdc_f\right) \tag{3.15}$$

where Z_{ca} represents liner impedance due to the cavity, k is the wavenumber, d is the cavity depth and c_f is the cavity factor. Suggested modification of the cos function fits better than that of the cot function with experimental analysis and backing volume impedance, due to the irregular or large shape of the device with an air-filled cavity. The proposed modification of the impedance term triggered by the cavity can be designated as equation (3.15) with the added cavity factor. Equation (3.15) with the added cavity factor appears to fit with both a single and double liner. The difference between the cot & cos functions will be discussed later in chapter 5, section 5.3. Also, the predictions of an alternative cavity impedance model for double liner physically more justifiable earlier discussed in section 2.1.2 is considered in Chapter 2 will be discussed later in Chapter 5, section 5.7, 5.8, 5.15 and 5.16. This present numerical model introduces the cavity factor due to the variation of cavity depth set in Table 4.5. The values of cavity factor c_f play a vital role in predicting liner impedance due to the variation of cavity depth. The cavity factor numerically optimises the model, and the

determination of the cavity factor is governed by a power log equation. For the single and double liners, the establishment of the cavity factor is given below.

$$c_f = a(d^{-m}) + c \tag{3.16}$$

			Single liner				
d	0.049	0.463	0.465	0.47	a	m	c
c_f	2.1	0.16	0.16	0.16	0.009151	1.782	0.1243
			Double liner				
d	0.023	0.038	0.463	0.465	0.009257	1.996	0.2771
c_f	17.5	6.6	0.32	0.32			

Table 3.1 Values of cavity factor, script coefficients and cavity depth

The script coefficients (a, m & c) of the power log equation and geometric dimensions of cavity depth are given in Table 3.1. The values of cavity depth and script coefficients are plugin to the power log equation (3.16) provides the cavity factor, which is a function of cavity depth, as shown in Figure 3.7 for single and double layer liners. Cavity factor is developed from the dimensions of the configurations tested by Lahiri et al. (Lahiri, 2014; Lahiri & Bake, 2017; Lahiri et al., 2011) and the dimensions of the configurations experiment carried out at the UHARC.

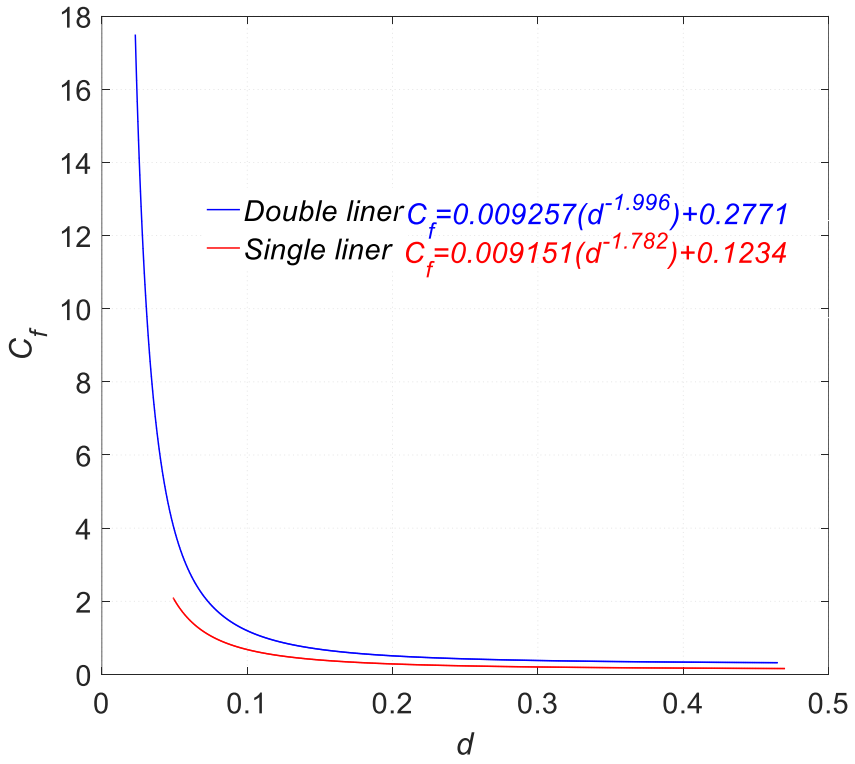

Figure 3.7 Cavity factor is a function of cavity depth.

Figure 3.7 shows the establishment of cavity factor based on two different test rig boundary conditions. Further investigation may be required for more clarification on how the variation of cavity depth influences the liner absorption or dissipation profile.

3.5 Impedance due to interaction end correction

The final term of this numerical model represents interaction end correction in conjunction with Melling's (Melling, 1973b) approach of adiabatic effective dynamic viscosity μ' and Fok (Fok, 1941) function. For this instance, μ' represents the non-conducting wall maintained at constant entropy. Therefore, the process applied here is considered as an adiabatic condition. Sivian (Sivian, 1935) applied the difference between the two viscosities, described previously in section 2.20.1 in equation (2.144).

$$\mu' = \mu\left[1 + \frac{\dot{\gamma} - 1}{\sqrt{Pr}}\right]^2 \tag{3.17}$$

where $Pr = \mu c_p / K_T$ is the Prandtl number, c_p is the specific heat of air at constant pressure, K_T is the thermal conductivity of air, and $\dot{\gamma}$ is the ratio of specific heat in the air. The Stokes wave number k_{sp} considers adiabatic effective kinematic viscosity and thermal conductivity losses in a non-conducting wall $k_{sp} = \sqrt{-j\omega\rho/\mu'}$, according to Melling's (Melling, 1973b) modification of Sivian's (Sivian, 1935) work. The function $F(k_{sp}r)$ introduces the viscous effects given by Stokes (Stokes, 1851) and Crandall's (Crandall, 1926b) velocity profile magnitude can be written as

$$F(k_{sp}r) = 1 - \frac{4}{k_{sp}r}\frac{J_1(k_{sp}r)}{J_0(k_{sp}r)} \tag{3.18}$$

An orifice interaction effect was analysed by (Ingard, 1953) and (Fok, 1941) between two adjacent orifices in a circular aperture in a wall put across a tube. The Fok function is slightly stronger than Ingard's interaction. Therefore, Fok's function interaction will be introduced in the present numerical model. Fok's (Fok, 1941) interaction factor in terms of porosity, is shown in equation (2.158) and described earlier in section 2.21.2.

$$\psi(\sigma) = \left(\sum_{n=0}^{12}[x_n\sigma^n]\right)^{-1} \tag{3.19}$$

The correction factor $\psi(\sigma)$ is a polynomial approximation of the Fok function. The Fok function $\psi(\sigma)$ is always greater than unity. If $\sigma \to 1$ it tends to infinity, i.e. the attached mass tends to zero, but if $\sigma \to 0$, it tends to unity. The Fok (Fok, 1941) function orifice interaction factor earlier shown in .

$$Z_{ie} = \frac{1.7j\omega\rho r}{\psi(\sigma)F(k_{sp}r)} \tag{3.20}$$

where Z_{ie} represents the interaction end correction impedance. For interaction end correction, equation (3.7) has been taken into account once again to determine the effect of constant phase and interaction factor, similar to Melling's (Melling, 1973b) approach. The function $\psi(\sigma)$ is the Fok (Fok, 1941) interaction factor. The division by the interaction factor $\psi(\sigma)$ and $F(k_{sp}r)$ phase constant converts the impedance of a single orifice into the impedance of an array of orifices in a perforation (Guess, 1975b; Melling, 1973b). Similarly, equations (3.4), (3.6) and (3.7) need to be divided by the porosity in order to convert the impedance of a single orifice of an array of multiple orifices in the entire perforation as explained in section 2.1.4, and equation (2.17). Therefore, the total collected impedance Z_{ab} can be written as

$$Z_{ab} = \frac{1}{\sigma}\left[F(K_s r) + \frac{(l_t + 0.1l/2r)\sqrt{2\omega\rho\mu}}{2} + j\omega\rho\frac{16r}{3\pi}\right] + \frac{1.7j\omega\rho r}{\psi(\sigma)F(k_{sp}r)} - j\rho c\cot(kdc_f) \qquad (3.21)$$

$$Z_{ab} = \frac{1}{\sigma}\left[F(K_s r) + \frac{(l_t + 0.1l/2r)\sqrt{2\omega\rho\mu}}{2} + j\omega\rho\frac{16r}{3\pi}\right] + \frac{1.7j\omega\rho r}{\psi(\sigma)F(k_{sp}r)} - j\rho c\cos(kdc_f) \qquad (3.22)$$

3.6 Absorption coefficient

From this numerical model, the reflection coefficient can be derived from the source of the collected impedance, and characteristic impedance ρc can be introduced. If the collected impedance of the numerical model refers to Z_{ab} then the classical theory of the reflection coefficient can be expanded. In addition, Eldredge and Dowling's (Eldredge & Dowling, 2003) equation (2.103) or (4.33) is not the only definition of absorption; indeed, in some cases there are additional classifications that are more suitable for evaluating the performance of an absorbing device designated as an alternative definition of absorption. The reflection coefficient will be minimum at the resonance frequency of the perforated plate or liner. Once again, if there is an equality of the resistive part ρc and Z_{ab} the reflection coefficient will fall theoretically to zero at the resonance frequency of the perforated plate or liner.

$$\dot{R} = \frac{|B_u^-|}{|A_u^+|} = \frac{Z_{ab} - \rho c}{Z_{ab} + \rho c} \qquad (3.23)$$

Moreover, an absorption system is often used to prevent acoustic waves in a duct from returning to their source, and thus mitigate the growth of acoustically driven instabilities. If the transmitted $|C_d^+|^2$ and reflected $|D_d^-|^2$ acoustic energy in the downstream section is neglected, then equation (4.33) reduces to equation (3.24). Eldredge and Dowling's (Eldredge & Dowling, 2003) alternative definition of absorption is implemented in this present model.

The neglected transmitted and reflected downstream signal and energy analysis will be presented in chapter 5, section 5.9.1.

$$\Delta = 1 - \frac{|B_u^-|^2}{|A_u^+|^2} \tag{3.24}$$

3.7 Conclusion

In this chapter, a semi-empirical hybrid model is developed, predictions of which are compared with data from the experiments in chapter 5. From the collected impedance, perforation, end correction, surface resistance, interaction end correction, and cavity effects are developed from the literature to investigate the liner absorption coefficient, resistance and reactance term in the frequency domain. Absorption coefficient is developed from the magnitude of the reflection coefficient, and the reflection coefficient is developed from the collected impedance. The propagation of acoustic behaviour chosen for a single frequency will be checked throughout the number of experiments and chosen reference cases. Implementation of the absorption coefficient equation is verified utilising an alternative definition of absorption. The model predictions will be compared to the experiment in chapter 5.

Impedance due to the cavity, transcendental or transmission line theory, required modifications to predict combined liner impedance data. A cavity factor is added to the system to optimise the cavity depth, and to determine the resonance frequency. A second modification was to adopt the cosine function instead of cot function. Impedance due to the surface resistance required an addition in thickness constant, as well as 10-30 % of length to diameter ratio of the aperture to be mapped with the experimental data. Under this mapping, this empirical model provides an increase and decrease absorption profile by changing the orifice length. The model prediction suggests that by changing its length to diameter ratio, a combustor liner thickness effect can be deployed.

4 Experiment

Two different types of experiment will be subject to discussion: static pressure measurement and acoustic analysis. Static pressure measurement refers to the pressure ratio, orifice hole velocity, discharge coefficient of the orifice, and Mach number. Acoustic analysis refers to the absorption or dissipation coefficient, along with combustor liner resistance and reactance profile.

4.1 Static pressure measurement

In this section, the process of calculating the discharge coefficient C_d of an orifice from static pressure measurement across the cylindrical liner is explained. It is a critical process by which the discharge coefficient of the orifice is developed for the original combustor design. Bias flow is the controlling parameter of the combustion cooling system. It is essential to calculate the mass flow rate, which will be introduced to the test section. In order to calculate the discharge coefficient of the orifice from static pressure measurement, the first step is to measure the total mass flow rate of air from the bias flow delivery system.

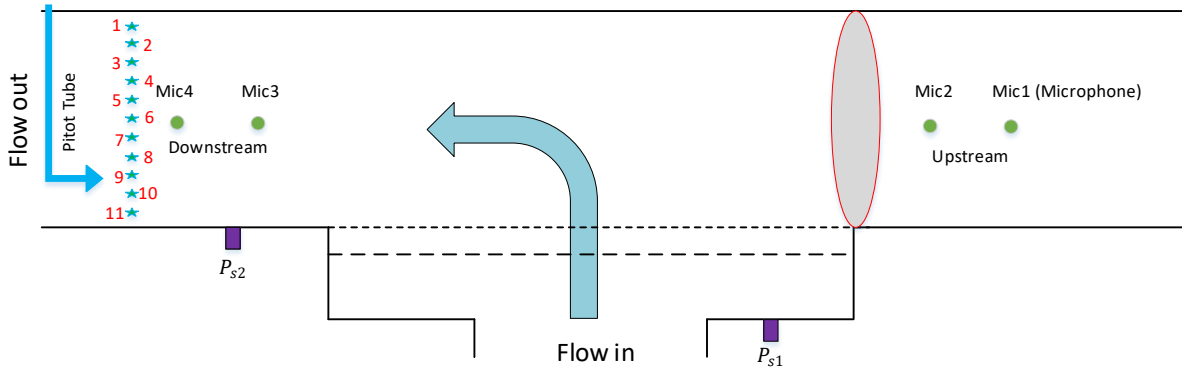

Figure 4.1 Experimental setup of static pressure measurement.

A schematic diagram of static pressure measurement is shown in Figure 4.1. During the static pressure measurement, the upstream section is blocked to divert all flow towards the exit port or the downstream section. The core purpose of blocking the upstream section is to calculate an exact amount of mass flow through the duct. To improve the accuracy of the mass flow from the 161.5 mm duct, the traversing Pitot tube method (Straightening, 2005) is introduced into the system to measure the duct velocity.

4.2 Duct area calculation

The central duct inside the test rig, where the Pitot tube traversed, is divided into six equal parts. The test duct is 161.5 mm diameter, as shown in Figure 4.1 and Figure 4.2.

Area point	Diameter (cm)	Total area (cm^2)	Associated area (cm^2)
1	2.69	5.69	5.69
2	5.38	22.76	17.07
3	8.08	51.21	28.45
4	10.77	91.04	39.83
5	13.46	142.26	51.21
6	16.15	204.85	62.59
Total duct area ΣA_T			2.05E-02 m^2

Table 4.1 Central and associated duct area calculation.

The total cross-sectional area of the duct is given in Table 4.1, where ΣA_T represents the total duct area 2.05E-02 m^2. The total duct area is the sum of the associated areas of the duct.

4.3 Duct velocity calculation

The duct in the test rig is divided into six equivalent diameters and areas, shown in Figure 4.2. The core of the duct area point 1 shows it has 2.69 cm equivalent diameter Ø, which refers to 5.69 cm^2 equivalent area. Also highlighted is that measured velocity corresponds to area point 1 and has a velocity of 0.28 m/s, measured by using a Pitot tube, given in Table 4.2 under the 2 Hz column. At the same time, during the duct velocity calculation cavity P_{s1} and duct P_{s2} pressure is also measured, and is shown in Figure 4.2. Mass flow controller is set for 2 Hz, 4 Hz, 6 Hz, 8 Hz and 10 Hz bias flow delivery system.

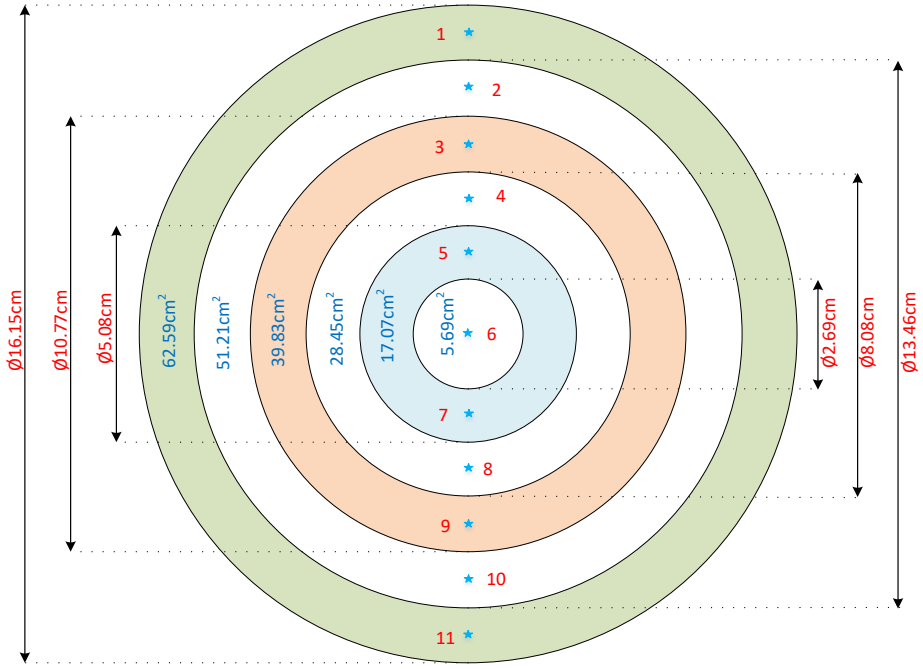

Figure 4.2 Traversing Pitot tube method circular duct alignment.

Figure 4.2 shows the cross-sectional area of the circular duct and the 11 points of intersection, at which duct velocity is captured using a Pitot tube. The next step is to calculate the

remaining five point's average duct velocity. In Figure 4.2 the second circle, in a light blue colour, shows that the two area points 5 and 7 indicate two different duct velocities, 0.24 m/s and 0.26 m/s respectively, specified below in Table 4.2, which refers to configuration 13's static pressure measurements.

Fan frequency	2 Hz	4 Hz	6 Hz	8 Hz	10 Hz
Area point	Red	Black	Magenta	Green	Pink
Unit	m/s	m/s	m/s	m/s	m/s
1	0.19	0.41	0.54	0.98	2.2
2	0.21	0.44	0.56	0.91	2.21
3	0.22	0.47	1.51	2.07	2.33
4	0.23	0.78	1.59	2.41	2.43
5	0.24	1.01	1.88	1.9	2.89
6	0.28	1.22	1.95	2.57	3.11
7	0.26	0.98	1.81	2.74	2.88
8	0.23	0.81	1.65	2.61	3.2
9	0.23	0.49	1.4	2.45	3.16
10	0.22	0.48	0.51	0.85	2.07
11	0.2	0.45	0.54	0.42	0.57
P_{s1} mbar	0.1	0.6	1.6	2.9	4.6
P_{s2} mbar	-0.03	-0.04	-0.01	-0.01	-0.02

Table 4.2 Velocity and pressure data across the cylindrical liner.

Configuration 13's duct velocity and static pressure data is shown in Table 4.2.

Area point	Ø (cm)	2Hz(m/s)	4Hz(m/s)	6Hz(m/s)	8Hz(m/s)	10Hz(m/s)
6	2.69	0.28	1.22	1.95	2.57	3.11
5 & 7	5.38	0.25	1.00	1.85	2.32	2.89
4 & 8	8.08	0.23	0.80	1.62	2.51	2.82
3 & 9	10.77	0.23	0.48	1.46	2.26	2.75
2 & 10	13.46	0.22	0.46	0.54	0.88	2.14
1 & 11	16.15	0.20	0.43	0.54	0.70	1.39

Table 4.3 Average duct velocity as a function of duct diameter.

In order to improve the overall mass flow rate calculation, the average duct velocity is developed from Table 4.2 and shown in Table 4.3. From the average duct velocity, the overall volume flow rate is calculated from the continuity equation (4.1). Altogether five different types of flow rate have been introduced into the bias flow delivery system: 2 Hz, 4 Hz, 6 Hz, 8 Hz, and 10 Hz. Aside from static pressure measurement, the special relationship is identified between the discharge coefficient and versus mass flow rate, and between the pressure ratio versus mass flow rate. This will be discussed later, in section 4.14.

4.4 Mass flow rate calculation

The volumetric flow rate in a system is a measure of the volume of fluid passing a point in a system per unit of time. In general, the volume flow rate is the product of the cross-sectional area and average duct velocity,

$$\Sigma Q_T = \Sigma A_T \cdot V_n \quad (4.1)$$

where Q_T is the total volume flow rate, A_T is the total area of the duct, V_n is the average duct velocity. Continuity equation (4.1) corresponding to the product of area and velocity provides total volume flow rate ΣQ_T= 4.46E-03 m^3/s. Substituting the values of ΣQ_T & ΣA_T in equation (4.1) provides the average duct velocity V_n 0.22 m/s.

$$\dot{m} = \rho Q_T \quad (4.2)$$

The mass flow rate of the duct, which signifies the movement of fluid passing a point through a unit area, generally depends on the density of the fluid and the fluid in the medium. By using equation (4.2), mass flow rate can be developed from the volume flow rate. The overall static pressure measurement of configuration 13 volume flow rate, duct velocity, mass flow rate, discharge coefficient of inner and outer liner, estimated effective area, estimated discharge coefficient, estimated velocity and Mach number is specified in Table 4.4.

4.5 Discharge coefficient of the orifice

In order to develop an estimated discharge coefficient of the orifice from static pressure measurement, the estimated effective area of inner and outer liners is developed from the difference between the measured mass flow rate and pressure. The discussion in this section refers to a double layer cylindrical combustor liner, configuration 13. It has two liners, the inner liner designated as configuration 7 and the outer liner designated as configuration 11. Once assembled, it is designated as a combined or double-layer combustor, configuration 13. Details of all the geometric properties of the configuration 13 single and double-layer liner are specified in section 4.10. The inner liner has 3402 orifices and the orifice diameter is 0.875 mm, whereas the outer liner has 480 orifices and the orifice diameter is 2.675 mm. The main purpose of static pressure measurement is to look at the behaviour of the discharge coefficient of the orifice when different rates of bias flow are introduced into the system. The discharge coefficient of the orifice varies considerably with changes in area ratio, and pressure ratio originates from the static pressure measurement. A discharge coefficient value 0.60 may be taken as standard, but the value varies noticeably at low values of the Reynolds number

(Engineeringtoolbox, 2004). In general, the discharge coefficient of an orifice is defined as the ratio of the actual discharge to the theoretical discharge from the orifice. For an orifice plate installation or cylindrical liner, the discharge coefficient will vary depending on the location of the pressure tappings (Neutrium, 2015). The discharge coefficient of the orifice is a function of the shape of its inlet edge and the area ratio and also of the Reynolds number (Idelchik & Fried, 2005). The volume discharge of a fluid through a circular orifice can be written as (Frank et al., 2005)

$$C_{di} = \frac{\dot{m}}{A_i\sqrt{2\Delta p\rho}} \tag{4.3}$$

where C_{di} is the discharge coefficient of the inner liner orifice, A_i is the total cross-sectional area of the inner liner orifice, $\dot{m}$ is the mass flow rate through the inner liner orifice, Δp is the pressure difference across the liner, ρ is the density of air. Substituting the values of total mass flow rate, the total orifice area of the inner liner and the measured pressure difference across the liner in equation (4.3) yields the discharge coefficient of the inner liner orifice, 0.47. Similarly, the outer liner discharge coefficient of the orifice can be developed from equation (4.4) given below,

$$C_{do} = \frac{\dot{m}}{A_o\sqrt{2\Delta p\rho}} \tag{4.4}$$

where C_{do} is the outer liner discharge coefficient of the orifice, and A_o is the total cross-sectional area of the outer liner orifice. Substituting the values of total mass flow rate, the total orifice area of the outer liner and the measured pressure difference across the liner in equation (4.4) yields the discharge coefficient (0.36.) of the outer liner orifice.

4.6 Estimated discharge coefficient of the orifice

Estimated effective area calculation is explained below. For original combustor design, it is essential to verify the experimental output with theory. Therefore, an estimated effective area calculation is numerically established for two-factor authentication. The equations for estimated effective area calculations for inner and outer liners are given below

$$A_{ei} = \frac{\dot{m}_i}{\sqrt{2\Delta p\rho}} \tag{4.5}$$

$$A_{eo} = \frac{\dot{m}_o}{\sqrt{2\Delta p\rho}} \tag{4.6}$$

where A_{ei} and A_{eo} are the effective areas of the inner and outer liners, $\dot{m}_i$ and $\dot{m}_o$ are the mass flow rates of the inner and outer liner orifice. Overall calculation of the estimated effective area and mass flow rate per hole is given in Table 4.4. From equations (4.5) and (4.6) an estimated (combined) effective area is developed to form a combined or estimated discharge coefficient of the orifice. Equations for the estimated effective area and estimated discharge coefficient of the orifice are specified below as (4.7) and (4.8) (Idelchik & Fried, 2005; Miller, 1990),

$$\frac{1}{{A_{ec}}^2} = \frac{1}{{A_{ei}}^2} + \frac{1}{{A_{eo}}^2} \tag{4.7}$$

$$C_{de} = \frac{A_{ec}}{A_{is}} \tag{4.8}$$

where A_{ec} is the combined or estimated effective area, A_{is} is the inner liner geometric orifice area and C_{de} is the estimated discharge coefficient (0.46) of the orifice.

4.7 Combined orifice velocity

In this section, a cylindrical combustor liner combined orifice velocity calculation is explained. The continuity equation is governed due to the complex behaviour of fluids passing through the cylindrical structures containing circular orifice shapes to measure a flow rate. Orifices are also known as head loss flow meters or differential pressure producing devices and can be characterised by orifice edge geometry, which is the ratio of orifice bore diameter to pipe diameter (Ntamba & Mulumba, 2011). The orifice flow rate is a function of the liquid head, hole diameter, plate thickness, punch direction, and whether or not the surface is deburred (Musa & Bityong, 2018). Some assumptions are made for the theoretical analysis of the stage-discharge relationship:

$$\Sigma Q_T = C_{de} A_i V_c \tag{4.9}$$

where C_{de} is the combined or estimated discharge coefficient of the orifice, V_c is the combined hole velocity, and A_i is the geometric area of the inner liner. The main aim of expanding the inner liner orifice area is the combined hole velocity yield inside the inner liner. Substituting the values of Q_T, A_i and C_{de} into equation (4.9) provides a combined hole velocity of 4.69 m/s. Therefore, velocity based on inner liner OHV will be designated in the acoustic analysis.

Point	Area cm^2	2Hz(cm^3/s)	4Hz(cm^3/s)	6Hz(cm^3/s)	8Hz(cm^3/s)	10Hz(cm^3/s)
1	5.69	1.59	6.94	11.10	14.62	17.70
2	17.07	4.27	16.99	31.50	39.60	49.25
3	28.45	6.54	22.62	46.09	71.41	80.09
4	39.83	8.96	19.12	57.96	90.02	109.34
5	51.21	11.01	23.56	27.40	45.07	109.59
6	62.59	12.21	26.91	33.80	43.82	86.69
Volume flow rate ΣQ_T m^3/s		4.46E-03	1.16E-02	2.08E-02	3.05E-02	4.53E-02
Duct velocity V_n m/s		0.22	0.57	1.01	1.49	2.21
Mass flow rate $\dot{m}$ kg/s		5.37E-03	1.40E-02	2.50E-02	3.67E-02	5.45E-02
Outer liner flow rate/hole $\dot{m}_o$ kg/s		1.12E-05	2.91E-05	5.21E-05	7.64E-05	1.14E-04
Inner liner flow rate/hole $\dot{m}_i$ kg/s		1.58E-06	4.11E-06	7.36E-06	1.08E-05	1.60E-05
Pressure difference Δp mbar		1.30E-01	6.40E-01	1.61E+00	2.91E+00	4.62E+00
Pressure ratio %		0.01	0.06	0.16	0.29	0.46
Outer liner effective area A_{eo} m^2		2.00E-06	2.35E-06	2.65E-06	2.89E-06	3.40E-06
Inner liner effective area A_{ei} m^2		2.82E-07	3.31E-07	3.74E-07	4.07E-07	4.80E-07
Discharge coefficient outer liner C_{do}		0.36	0.42	0.47	0.51	0.61
Discharge coefficient inner liner C_{di}		0.47	0.55	0.62	0.68	0.80
Velocity based on inner liner C_{di}		4.65	10.31	16.35	21.99	27.70
Estimated effective area A_{ec} m^2		2.79E-07	3.28E-07	3.70E-07	4.03E-07	4.76E-07
Estimated discharge coefficient C_{de}		0.46	0.55	0.62	0.67	0.79
Combined velocity V_o m/s		4.69	10.41	16.52	22.20	27.98
Mach number		0.014	0.030	0.047	0.063	0.080

Table 4.4 Discharge coefficient of the orifice verified from static pressure measurement.

Table 4.4 shows configuration 13 combustor liner's overall static pressure measurement data. It provides details of the most basic kinds of observation: Mach number, combined orifice hole velocity, estimated discharge coefficient of the orifice, pressure ratio, mass flow rate, and average duct velocity.

4.8 Acoustic analysis

In this section, typical gas turbine combustor operating conditions and factors related to the acoustic performance of a perforated liner are investigated. A brief review of bias flow and its damping effect is discussed. Plane acoustic waves in a circular duct are investigated in this experiment, which provides the groups, phase velocities of sound waves, and acoustic impedance in the medium. The one-dimensional plane wave equation is valid only when the wavelength λ is higher than the diameter of the duct D. When $\lambda \gg D$ the acoustic pressure p disturbance in a thin element of fluid in a duct is considered. A mathematical description of the fluid motion may be obtained by assuming that the amount of fluid in the element is conserved, net longitudinal force is balanced by the inertia of the fluid in the element, process

in the element is adiabatic, and undistributed fluid is stationary. Hence the acoustic pressure disturbance becomes

$$\frac{1}{c^2}\frac{\partial^2 p}{\partial t^2} - \frac{\partial^2 p}{\partial x^2} = 0 \tag{4.10}$$

where c is the speed of sound (phase speed), λ is the distance at which the wave begins to repeat, D is the duct diameter, and p is the acoustic pressure. Equation (4.10) represents a one-dimensional equation of motion, or acoustic wave equation. This equation relates to the second rate of change of sound pressure with the co-ordinate x. In order to solve equation (4.10), it is necessary to apply an initial boundary condition to solve the matrix, by considering a uniform cross-section of a duct separated by a liner followed by upstream and downstream sections. Sound pressure is the acoustic quantity measured by using a microphone. Also, sound pressure is the acoustic pressure perturbation or fluctuation about the time-averaged or undistributed pressure. The general solution for equation (4.10) is of the form

$$p(x,t) = f_1\left(t - \frac{x}{c}\right) + f_2\left(t + \frac{x}{c}\right) \tag{4.11}$$

where f_1 and f_2 are arbitrary functions such as sine, cosine, exponential log, and so on. By differentiating and substituting into equation (4.10), varying with x and t in equation (4.11) demonstrates that $f_1(t - x/c)$ represents a wave travelling in the positive x-direction with wave speed c, while $f_2(t + x/c)$ represents a wave travelling in the negative x-direction with wave speed c. For harmonic waves, the general solution for a liner containing upstream and downstream sections is of the form

$$p(x,t) = A_u^+ e^{j[\omega t - kx_1]} + B_u^- e^{j[\omega t + kx_1]} \tag{4.12}$$

$$p(x,t) = C_d^+ e^{j[\omega t - kx_1]} + D_d^- e^{j[\omega t + kx_1]} \tag{4.13}$$

where A_u^+ is the incident upstream complex amplitude of the plane wave, B_u^- is the reflected upstream complex amplitude of the plane wave, C_d^+ is the transmitted downstream complex amplitude of the plane wave, D_d^- is the reflected downstream complex amplitude of the plane wave, and $k = 2\pi/\lambda = \omega/c$ a translation factor that relates the change in phase (angle) to spatial displacement. k is also known as the acoustic wavenumber, and $\omega = 2\pi f$ is the circular frequency. At time $t = 0$, the duct (sound source) begins to oscillate about its mean position with speed $U(t)$. Since the duct extends from zero to ∞, the physical standard of interconnection means all waves must propagate from the source of sound outward, i.e.,

from the excitation signal (speaker) to the right. This is equivalent to a homogeneous boundary condition executed at infinity, such as the outcome

$$f_2\left(t+\frac{x}{c}\right)\equiv 0 \tag{4.14}$$

The fluid velocity v is related to the acoustic pressure p by the momentum equation.

$$\frac{\partial v}{\partial t}=-\frac{1}{\rho}\frac{\partial p}{\partial x} \tag{4.15}$$

It is a real quantity for a progressive plane wave; hence, the acoustic pressure p and acoustic particle velocity u are in phase. This gives

$$u(\mathrm{x},\mathrm{t})=\frac{A_u^+e^{j[\omega t-kx_1]}+B_u^-e^{j[\omega t+kx_1]}}{\rho c}=\frac{1}{\rho c}\,f\left(\mathrm{t}-\frac{\mathrm{x}}{\mathrm{c}}\right) \tag{4.16}$$

By applying the boundary condition at $x=0$, $u(t,0)=U(t)=(1/\rho c)\,f(t)$ for $t\geq 0$ and solving for f gives $f(t-x/c)=\rho cU(t-x/c)$ for $t\geq x/c$. It is crucial that the initial fluid velocity condition $u(0,x)=0$ for $x>0$ implies that the sound produced by the oscillation of the source will not be able to reach the location $x>ct$, which is equivalent to taking $U(t)\equiv 0$ for $t<0$. Substituting the expression of f into equation (4.16) gives $p(x,t)=\rho cU(t-x/c)$. If the speaker oscillates for a long time, the initial time is $-\infty$ instead of 0. In this case, $U(t)$ can be defined for all t. This is the case for harmonic oscillation, where $U(t)=A_u^+e^{-j\omega t}$. The solution takes the form $p=A_u^+\rho ce^{-j\omega(t-x/c)}$. Such a wave can be designated as a plane wave since its phase is constant in a plane perpendicular to the x-axis. The physical solution is the real part of this solution.

$$p=A_u^+\rho ccos\left[\omega\left(t-\frac{x}{c}\right)\right] \tag{4.17}$$

The acoustic intensity can be written in the form $u=p/\rho c$ particle velocity.

$$I=\ A_u^{+2}\,\rho ccos^2[\omega(t-x)] \tag{4.18}$$

Therefore, the average intensity $\bar{I}$ and acoustic power $\bar{P}$ can be calculated.

$$\bar{I}=\frac{1}{2}A_u^{+2}\rho c \tag{4.19}$$

$$\bar{P}=\frac{1}{2}A_u^{+2}\rho c\bar{S} \tag{4.20}$$

where $\bar{I}$ is the time average acoustic intensity, $\bar{P}$ is the time average acoustic power, and $\bar{S}$ is the duct cross-section. It can be written as upstream, and downstream pressure signals are propagating in the positive x-direction and negative x-direction. The complex amplitude of upstream and downstream travelling acoustic waves in each section was calculated by using

Seybert and Ross's (Seybert & Ross, 1977) two-microphone method, and the random amplitudes are not a function of distance x since the distance is fixed or constant. Hence the wave shape does not change during propagation. The speed of sound propagation induced by upstream and downstream flow can be calculated by observing that $c = c_0 + u$ for wave motion with incident flow, $c = c_0 - u$ for wave motion with reflected flow, and c_0 represents the speed of sound propagation with no flow. By introducing flow into the system, the wave number in the upstream and downstream sections changes. So the incident and reflected wave number can be written as

$$k_u^+ = \frac{\omega}{c_0 + u} = \frac{k}{1 + M} \tag{4.21}$$

$$k_u^- = \frac{\omega}{c_0 + u} = \frac{k}{1 - M} \tag{4.22}$$

$$k_d^+ = \frac{\omega}{c_0 + u} = \frac{k}{1 + M} \tag{4.23}$$

$$k_d^- = \frac{\omega}{c_0 + u} = \frac{k}{1 - M} \tag{4.24}$$

where k_u^+ is the upstream incident wave number, k_u^- is the upstream reflected wave number, k_d^+ is the downstream transmitted wave number, k_d^- is the downstream reflected wave number, and M is the Mach number. Pressure signals P_1,P_2,P_3 & P_4 are recorded at four points in the duct, followed by the distance x_2, x_1, x_3 & x_4, as shown in Figure 4.4. The sound field in the duct can be decomposed into the positive x-direction travelling wave and negative x-direction travelling wave. By applying TMM by Seybert & Ross (Seybert & Ross, 1977) in both the upstream and downstream sections the pressure signal can be written as

$$P_1(x_1) = A_u^+ e^{\frac{-jkx_1}{1+M}} + B_u^- e^{\frac{jkx_1}{1-M}} \tag{4.25}$$

$$P_2(x_2) = A_u^+ e^{\frac{-jkx_2}{1+M}} + B_u^- e^{\frac{jkx_2}{1-M}} \tag{4.26}$$

$$P_3(x_3) = C_d^+ e^{\frac{-jkx_3}{1+M}} + D_d^- e^{\frac{jkx_3}{1-M}} \tag{4.27}$$

$$P_4(x_4) = C_d^+ e^{\frac{-jkx_4}{1+M}} + D_d^- e^{\frac{jkx_4}{1-M}} \tag{4.28}$$

To solve A_u^+ , B_u^- , C_d^+ and D_d^- in an axial plane, the pressure waves from equations (4.25),(4.26),(4.27) and (4.28) result in the following expressions for the complex amplitude of four random variables:

$$A_u^+ = \left[\frac{\mathrm{P_2 e}^{\frac{\mathrm{jkx_1}}{1-\mathrm{M}}} - \mathrm{P_1 e}^{\frac{\mathrm{jkx_2}}{1-\mathrm{M}}}}{\mathrm{e}^{\frac{2\mathrm{jkx_1}}{1-\mathrm{M^2}}} - \mathrm{e}^{\frac{2\mathrm{jkx_2}}{1-\mathrm{M^2}}}}\right] \tag{4.29}$$

$$B_u^- = \left[\frac{\mathrm{P_2 e}^{\frac{-\mathrm{jkx_1}}{1+\mathrm{M}}} - \mathrm{P_1 e}^{\frac{-\mathrm{jkx_2}}{1+\mathrm{M}}}}{\mathrm{e}^{\frac{-2\mathrm{jkx_1}}{1-\mathrm{M^2}}} - \mathrm{e}^{\frac{-2\mathrm{jkx_2}}{1-\mathrm{M^2}}}}\right] \tag{4.30}$$

$$C_d^+ = \left[\frac{\mathrm{P_3 e}^{\frac{-\mathrm{jkx_3}}{1-\mathrm{M}}} - \mathrm{P_4 e}^{\frac{-\mathrm{jkx_4}}{1-\mathrm{M}}}}{\mathrm{e}^{\frac{-2\mathrm{jkx_3}}{1-\mathrm{M^2}}} - \mathrm{e}^{\frac{-2\mathrm{jkx_4}}{1-\mathrm{M^2}}}}\right] \tag{4.31}$$

$$D_d^- = \left[\frac{P_3 e^{\frac{jkx_3}{1+M}} - P_4 e^{\frac{jkx_4}{1+M}}}{e^{\frac{2jkx_3}{1-M^2}} - e^{\frac{2jkx_4}{1-M^2}}}\right] \tag{4.32}$$

In order to determine the transmission coefficient and reflection coefficients of the pressure amplitude of a cylindrical perforated liner $\dot{T} = C_d^+/A_u^+$; $\dot{R} = B_u^-/A_u^+$, where $\dot{T}$ is the transmission coefficient and $\dot{R}$ is the reflection coefficient of the pressure amplitude, Eldredge and Dowling (Eldredge & Dowling, 2003) used the acoustic absorption of the liner. Absorption Δ is defined as the net energy absorbed by the liner, scaled by the energy incident upon the lined section, described earlier (Section 2.15) in equation (2.103).

$$\Delta = 1 - \frac{|C_d^+|^2 + |B_u^-|^2}{|A_u^+|^2 + |D_d^-|^2} \tag{4.33}$$

From the principle of energy conservation, the dissipation coefficient can be calculated from the reflection and transmission coefficient. The amount of acoustic energy that enters the liner, the sum of reflection, transmission and dissipation are the unity.

$$\ddot{R} + \ddot{T} + \ddot{\Delta} = 1 \tag{4.34}$$

The total incident energy that enters into the liner is partially reflected, partially transmitted and partially dissipated by the damping module. The acoustic energy carried by propagating waves in the presence of a moving mass is given by (Blokhintsev, 1956) as

$$E = (1 \mp \mathrm{M})^2 |\bar{P}|^2 \tag{4.35}$$

where E is the acoustic energy flux in a moving medium, and $\bar{P}$ is the time-averaged acoustic power described in equation (4.20). From equation (4.34) dissipated energy coefficient can be written as

$$\ddot{\Delta} = 1 - \frac{(1-\mathrm{M})^2}{(1+\mathrm{M})^2}\left[\ddot{R} + \ddot{T}\right] \tag{4.36}$$

where $\ddot{\Delta}$ represents the dissipated energy, $\ddot{R}$ represents reflected energy, and $\ddot{T}$ represents transmitted energy coefficient. Acoustic energy is dissipated by the cylindrical combustor liner while the one-dimensional plane acoustic wave is introduced into the system. Normal incident TL can be considered as the difference between the upstream and downstream acoustic pressure; however, this approach neglects to evaluate the significance of the reflected components of the signal. As a result, the decomposed signal derived incident transmission loss is the preferred matrix. The sound transmission loss of material in a particular frequency band is ten times the common logarithm of the reciprocal of the sound transmission coefficient. The quantity obtained is expressed in terms of decibels. Standard test method (E-09, 2009).

$$TL = 10 \log 10 \left(\left| \frac{A_u^+}{C_d^+} \right|^2 \right) \tag{4.37}$$

4.9 Experimental setup

The test rig is 30 m in length, 1.2 m width and 0.8 m height in cross-section, lined with prime to aid acoustic exclusion. A schematic diagram of the acoustic test rig is shown in Figure 4.3

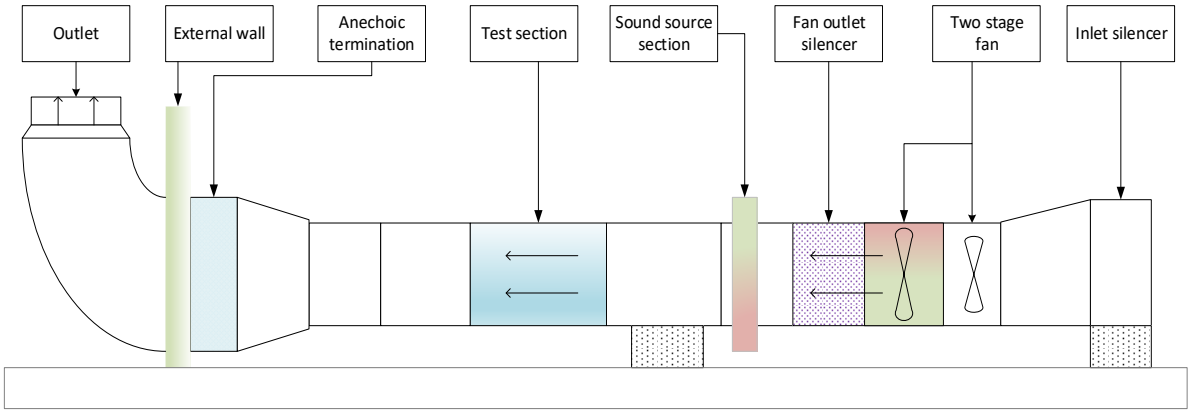

Figure 4.3 Schematic diagram of the test rig.

The duct has a 161.5 mm diameter to perform single and double layer cylindrical perforated liner acoustic and static pressure measurement. The test section has a cubic cross-section of 1.06 m length, 1.2 m width and 0.8 m height. At the beginning of the test rig, an inlet silencer is installed to remove environmental noise and a second silencer diminishes the fan noise. From the sound source, a transition duct is introduced to reduce the cross-section instantaneously to 161.5 mm diameter. In the downstream section, an anechoic termination is introduced into the system before the acoustic or bias flow velocity is released into the atmosphere, shown in Figure 4.3. The combustor liner installed into the test rig shown in

Figure 4.4. The length of the inner and outer liner is 524 mm and 504 mm, the diameter of the inner liner is 161.5 mm, and two different types of outer liner are used, 171.9 mm and 176.5 mm respectively. Two heavy-duty stainless steel rings attach the combustor liner into the test rig.

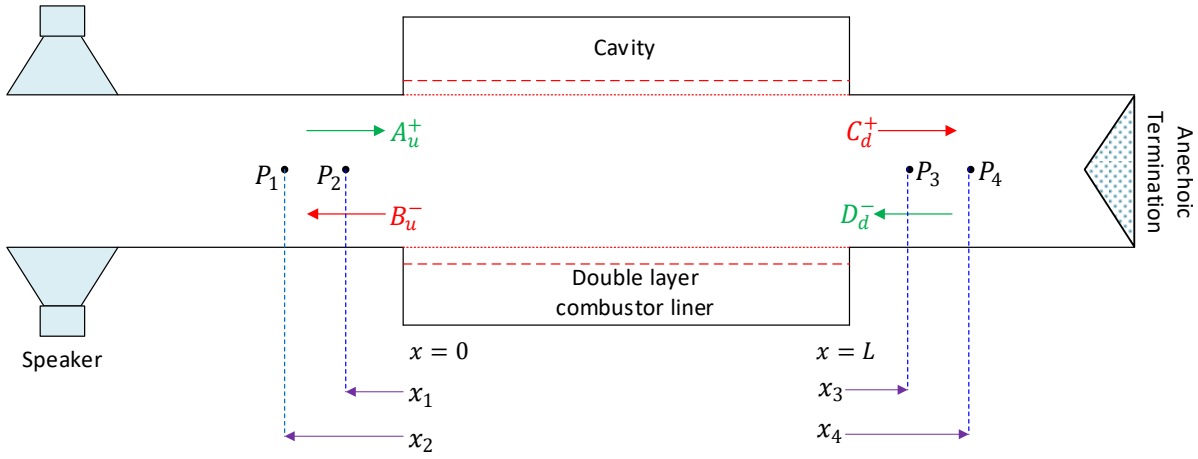

Figure 4.4 Schematic of the perforated liner experiment.

Single and double layer cylindrical combustor liners are installed between the upstream and downstream sections. In the upstream section the test rig has four radially mounted speakers and in the downstream section it has an anechoic termination and exit port. Four microphones are located at points P_1, P_2 ,P_3 & P_4 shown in Figure 4.4, followed by the distance of x_2, x_1, x_3 & x_4.

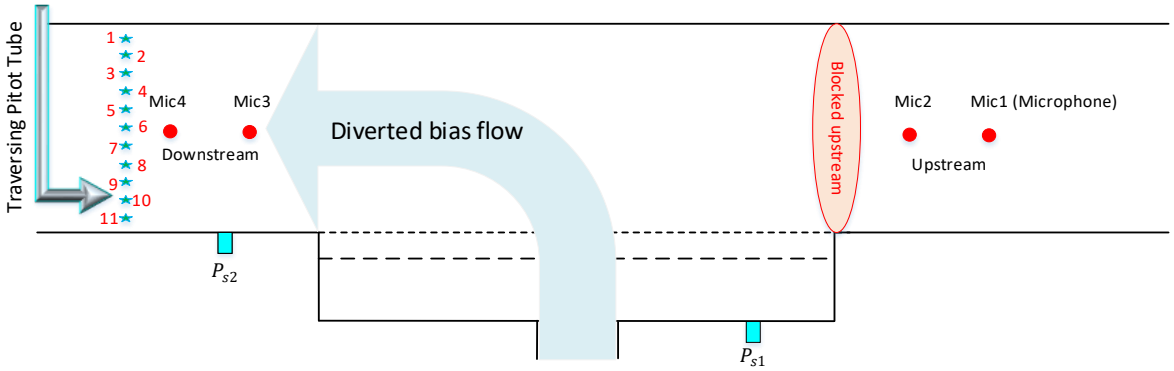

Figure 4.5 Experimental setup of static pressure measurement.

The mass flow rate is measured from the top to the bottom part of the duct by using the traversing Pitot tube Glen. E (Straightening, 2005) method. A detailed explanation of duct velocity calculation was given in section 4.2. From static pressure measurement, the discharge coefficient of the orifice was calculated $C_d = \dot{m}/A_o\sqrt{2\Delta p\rho}$ Mannan (Mannan, 2005). where $\dot{m}$ is the mass flow rate, Δp is the pressure difference across the liner, ρ is the density of air, C_d is the discharge coefficient of an orifice, and A_O is the cross-sectional area of the orifice.

Orifice hole velocity can be developed from the discharge coefficient. $V_o = \Sigma Q_T / A_o C_d$ where V_o is the orifice hole velocity of the outer liner, and ΣQ_T is the total volume flow rate. Orifice Mach number is calculated from orifice hole velocity. For a combined liner, the effective orifice area of the inner liner, $A_{ei} = \dot{m}_i / \sqrt{2\Delta p \rho}$ and the effective orifice area of the outer liner, $A_{eo} = \dot{m}_o / \sqrt{2\Delta p \rho}$ are developed from the estimated effective area $1/A_{ec}^2 = 1/A_{ei}^2 + 1/A_{eo}^2$ Idelchik and Miller (Idelchik & Fried, 2005; Miller, 1990). where A_{ei} is the effective area of the inner liner orifice, A_{eo} is the effective area of the outer liner orifice, A_{ec} is the estimated effective area, $\dot{m}_i$ is the mass flow rate of the inner liner orifice and $\dot{m}_o$ is the mass flow rate of the outer liner orifice.

4.10 Combustor liner configurations

A set of thirteen combustor liner experiment is carred out, including a dummy liner. The dummy liner geometry is the same as the inner liner without perforation.

Damping liner																		
Configuration	1	2	3	4	5	6	7	8	9	10	11	12	13	14	15	16	17	18
Liner length mm	59.5	66	59.5	66	59.5	59.5	524	524	524	524			524	524	524	524	524	524
Liner diameter mm	140	140	140	140	140	140	161.5	161.5	161.5	161.5			161.5	161.5	161.5	161.5	161.5	161.5
Orifice diameter mm	1	2.5	2.5	1	1	1	0.875	1.125	1.175	0.925			0.875	1.125	1.175	0.925	0.875	1.175
Number of orifices	364	60	364	60	364	364	3402	3402	2256	2256			3402	3402	2256	2256	3402	2256
Wall thickness mm	1	1	1	1	1	1	1.6	1.6	2	2			1.6	1.6	2	2	1.6	2
Porosity %	1.09	1.01	6.79	0.16	1.09	1.09	0.74	1.23	0.98	0.61			0.74	1.23	0.98	0.61	0.74	0.98
Axial pitch mm	8.5	22	8.5	22	8.5	8.5	9	9	10.5	10.5			9	9	10.5	10.5	9	10.5
Metering liner																		
Liner length mm					42	51					504	504	504	504	504	504	504	504
Liner diameter mm					162	192					176.5	171.9	176.5	176.5	171.9	171.9	171.9	176.5
Orifice diameter mm					1	1					2.675	3.675	2.675	2.675	3.675	3.675	3.675	2.675
Number of orifices					108	108					480	384	480	480	384	384	384	480
Wall thickness mm					1	1					1.6	1.6	1.6	1.6	1.6	1.6	1.6	1.6
Porosity %					0.40	0.31					1.41	2.65	1.41	1.41	2.65	2.65	2.65	1.41
Axial pitch mm					14	16					20	20	20	20	20	20	20	20
Cavity Depth mm	49	49	49	49	38	23	470	470	470	470	463	465	463	463	465	465	465	463
Cavity Diameter mm	240	240	240	240	240	240	1105	1105	1105	1105	1105	1105	1105	1105	1105	1105	1105	1105
Cavity factor	2.10	2.10	2.10	2.10	6.6	17.5	0.16	0.16	0.16	0.16	0.16	0.16	0.32	0.32	0.32	0.32	0.32	0.32

Table 4.5 Combustor liner configuration.

Configurations 1-4 single and 5-6 are the double liner Lahiri et al. (Lahiri, 2014; Lahiri & Bake, 2017; Lahiri et al., 2011). Configurations 7-10 single and 13-18 are the double liner combustor experiment carried out at the University of Hull Acoustic Research Centre (UHARC). Two single liners are assembled to form a double layer combustor, inner and outer liners are known as damping and metering liners respectively. Metering liner decides, the precise amount of mass flow introduced into the damping liner. Their geometric parameters are given in Table 4.5. For non-zero bias flow cases, for each configuration, an equal amount of mass flow is introduced into the test rig through a centrifugal pump, designated as a mass flow controller. Five different sets of non-zero bias flow is introduced into the test rig, designated as 2 Hz, 4

Hz, 6 Hz, 8 Hz and 10 Hz, represented by the red, black, magenta, green and pink lines previously mentioned in section 4.3.

Configuration 7 represents the inner single liner. In this configuration x_i represents the length of the single liner and y_i represents the width of the liner. Configurations 7 to 10 has the same liner length and width but different wall thickness, orifice diameter, orifice per row, number of rows, orifice pattern, axial pitch distance, total number of orifices and porosity. Configurations 11 and 12 represents outer single liner, which have the same liner length x_o but different liner width y_o to create different damping volume in between the liners. For these two different configurations, 11 and 12, wall thickness, the total number of rows, orifice pattern, and the axial pitch distance are the same, while orifice diameter, liner diameter, holes per row, total number of holes and porosities are different. Configurations 13 to 18 has damping and metering liner designated as double-layer combustor liner. Configurations 13, 14 and 18 has the same metering liner and contain higher damping volume, whereas configurations 15, 16 and 17 has different metering liner and contain lower damping volume. Configuration 14 has an inverse relationship of porosity compared to the rest of the double-layer configurations, which is high porosity in the damping liner and low porosity in the metering liner.

4.11 Equipment used

In order to introduce bias flow into the test section, the TEC electric motor and two-stage centrifugal pump is installed at the beginning of the test rig. In addition, Tektronix AFG 3022B dual-channel arbitrary/function generator (250MS/s, 25 MHz), G.R.A.S sound power module 12AG-8 channel recorder, SR-707 professional power amplifier, noise generator type 1405, Agilent technologies-U2781A, 6-slot USB modular instrument chassis, and four 600 Watt radially mounted speakers is used for this experiment. The configured sampling rate is 10000, single-shot sample size 100000, the microphone used is Brüel &Kjær Type 4937-A-011 ¼", signal to noise ratio is 32, sound pressure level is 93dB. In order to improve the shape and the accuracy of acoustic analysis output, each set of experiments is carried out twenty times and the signal is averaged by using the Savitzky and Golay (Savitzky & Golay, 1964) method.

4.12 SPL & SNR

Signal to noise ratio (SNR) is defined as the logarithmic power ratio of the signal and noise. Sound pressure level (SPL), SNR and their mathematical derivation will be described in

sections 8.13.2 and 8.13.3. In this section, SPL and SNR are implemented in the experimental analysis given below.

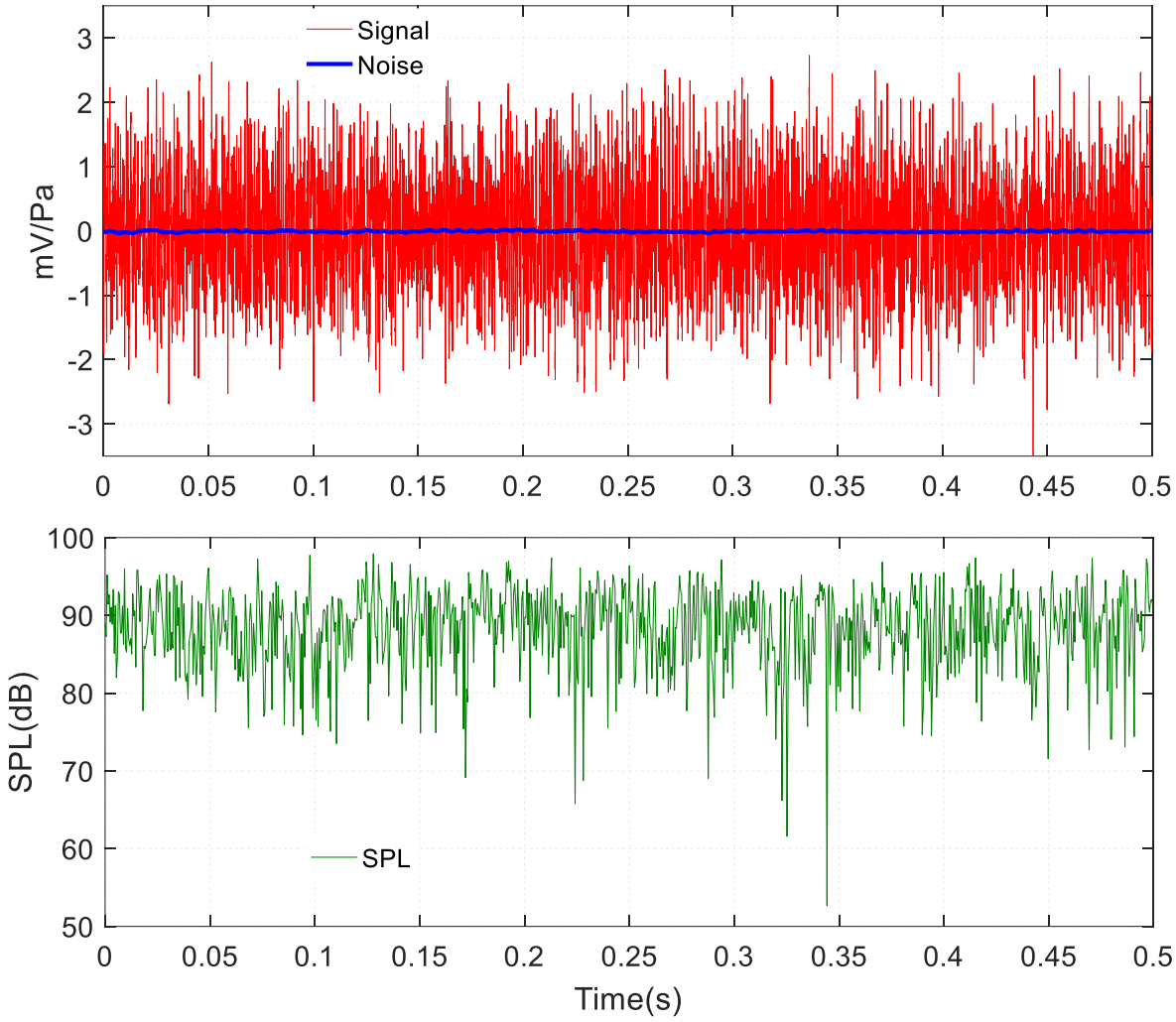

Figure 4.6 SNR and SPL analysis.

The acoustic analysis of SNR 30.76 and SPL 92.42 dB are shown in Figure 4.6 with respect to time. Once the dummy liner is installed into the test rig, it is necessary to measure the sound pressure level at each microphone with the sound source on and off. During this measurement, the sound source generated sufficient signal at all microphone locations. This measure describes the noise output of a device in terms of signal strength. Initially, the signal is recorded without the sound source on, then the signal is applied to the test rig and another set of measurements are carried out to determine the strength of SNR.

4.13 Dummy liner acoustic analysis

A dummy liner acoustic analysis is performed to check the accuracy of data manipulation technique and initiate a benchmark. To describe the reference measurement technique and

improve the data analysis, a liner without perforation is placed into the test rig and the experiment is carried out. For this type of configuration, expected values of transmission, absorption and dissipation of energy from the dummy liner acoustic analysis should be zero, or close to zero.

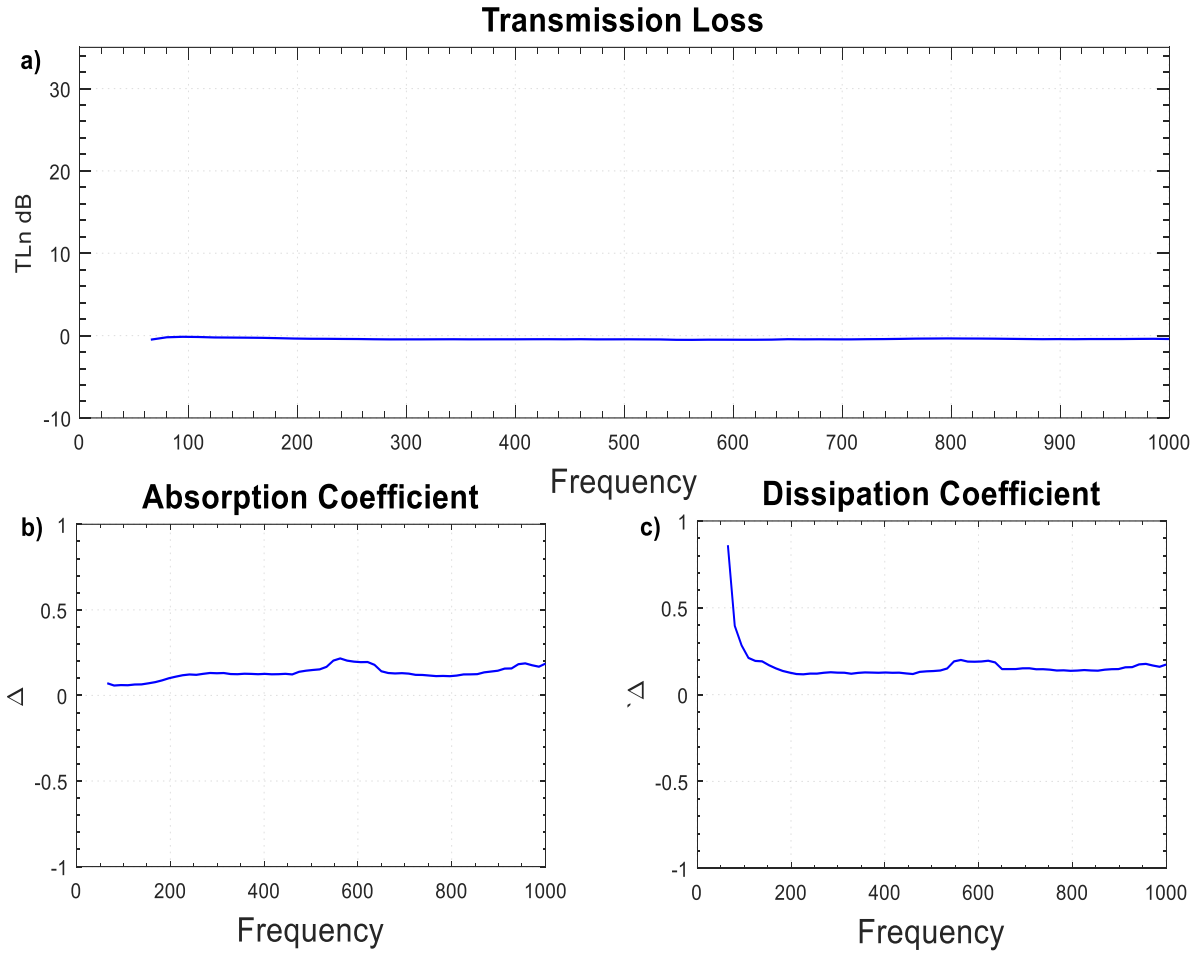

Figure 4.7 Dummy liner no flow acoustic analysis.

The dummy liner experimental analysis in Figure 4.7 a) shows that calculated transmission loss is close to zero, although it is slightly positive, which can be attributed to transmission error due to insertion loss or microphone phase mismatch. Similarly, in Figure 4.7 b) the absorption coefficient defined by Eldredge and Dowling (Eldredge & Dowling, 2003) and Figure 4.7 c) the dissipation coefficient defined by Lahiri Enghardt Bake (Lahiri et al., 2011) show slightly positive results due to the absorption and dissipation error. The impedance wall is a passive wall that absorbs energy at any frequency, i.e. the acoustic intensity into the wall is positive. As a result, the resistance has to be positive. In other words, the impedance satisfies the condition of passivity (Rienstra).

4.14 Effect of no flow and non-zero bias flow

In this section, acoustic and static pressure measurement analysis will be explained in terms of configurations rather than the generic name of the combustor liner. The generic names and configuration details can be found in Table 4.5. In addition, another factor is added to Table 4.5, represented as the cavity factor, which will be discussed in chapter 3, section 3.4.

4.14.1 Configuration 7 acoustic and static pressure measurement

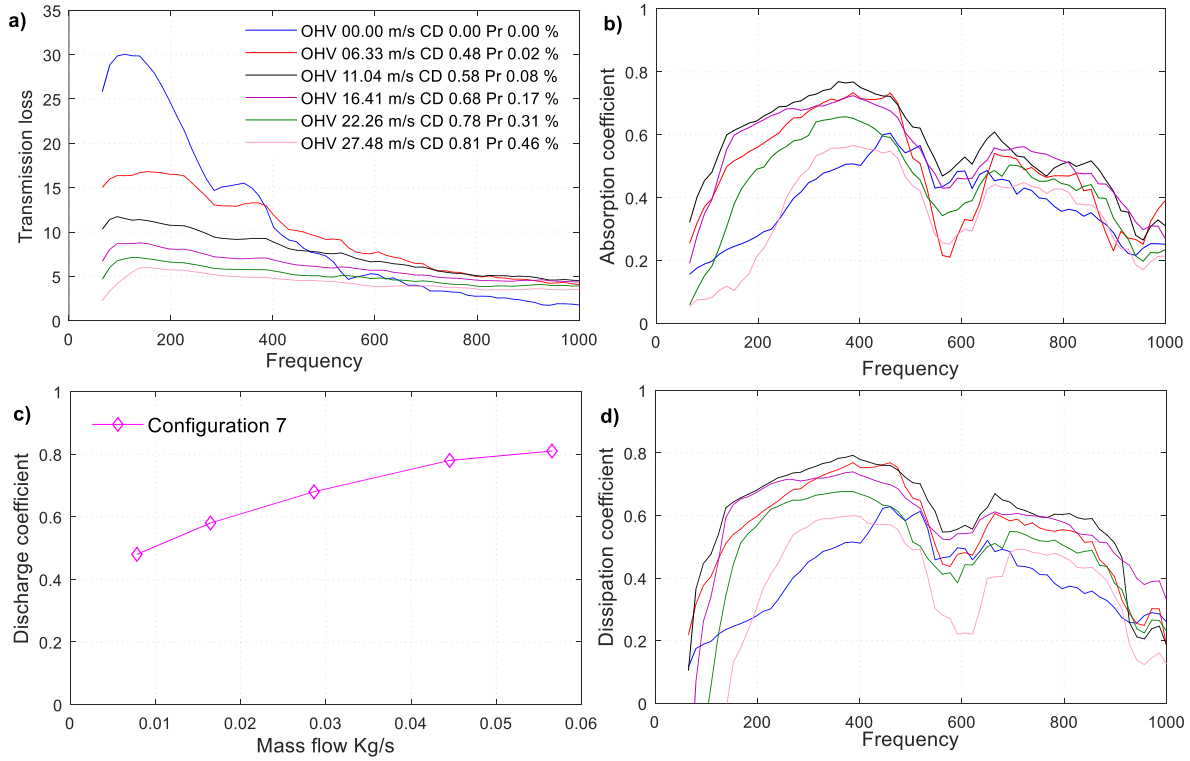

Figure 4.8 Acoustic and static pressure measurement configuration 7.

Configuration 7 represents a single liner cylindrical combustor, which has 3402 orifices, 0.875 mm orifice diameter, 9 mm axial pitch distance - which refers to 0.74 % of porosity - and 1.6 mm liner thickness. Configuration 7's geometric profile is shown in Table 4.5. Figure 4.8 a), the no flow case, shows the transmission loss plot in which the blue solid line has two peaks in the low-frequency range (0-500 Hz). Whereas for the non-zero bias flow cases, the red solid line has relatively weak peaks compared to the no flow case in the low-frequency range. The transmission attenuation is flat in the high-frequency range (500-1000 Hz). Figure 4.8 b) and d) show a broadband frequency range of absorption or dissipation profile for configuration 7 (black line). For non-zero bias flow cases, the absorption or dissipation profile exhibit two peaks: the first peak forms in the low-frequency range and the second peak in the high-frequency range. The two peaks are separated by the dip near to 550-600 Hz which appears

also in the presence of non-zero bias flow cases. It can be designated as absorption properties of the single liner due to the non-zero bias flow. For the no flow case, the dip is not very sharp. The combined liner no flow absorption spectrum turns out to be flat after the dip shown in section 4.14.7. In the high-frequency range, the black and magenta lines indicate that both absorption and dissipation coefficient overlap one another. Figure 4.8 also highlights that the absorption and dissipation plots are identical, C. Lahiri (Lahiri, 2014). In Figure 4.8 c), the discharge coefficient versus mass flow rate plot indicates that as the mass flow rate increases, the discharge coefficient of the orifice too increases.

4.14.2 Configuration 8 acoustic and static pressure measurement

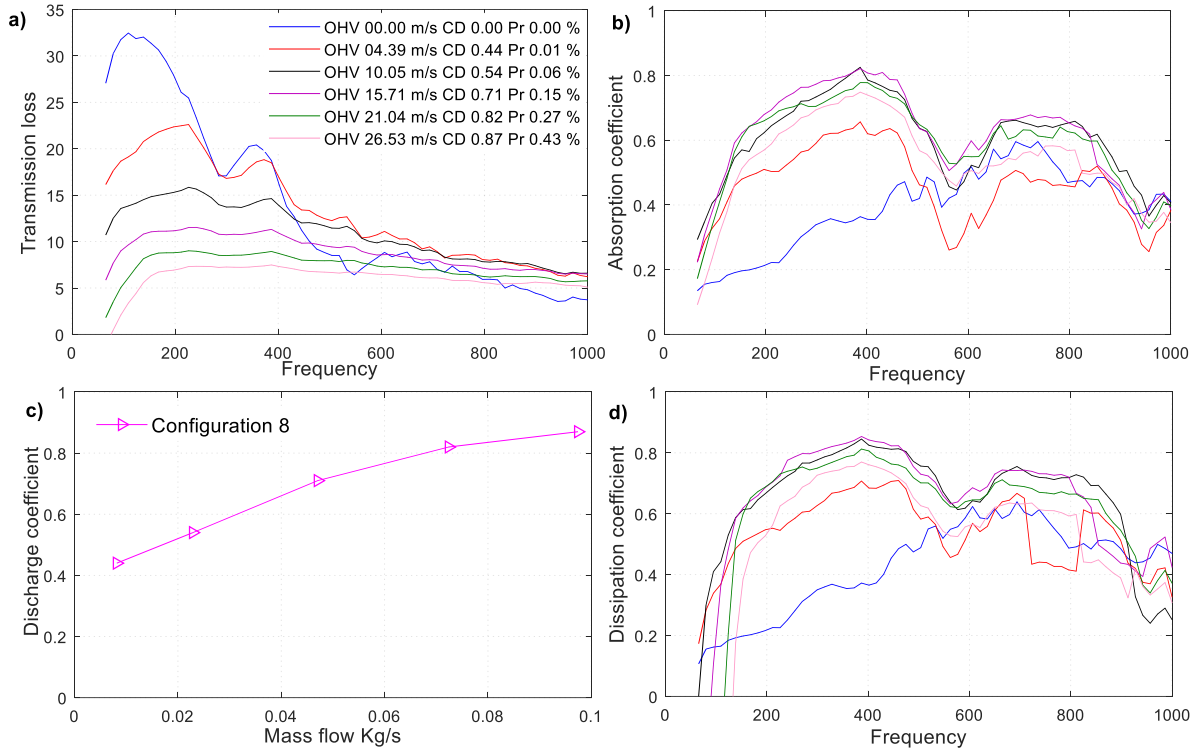

Figure 4.9 Acoustic and static pressure measurement configuration 8.

When compared with configuration 7, configuration 8's orifice diameter is increased slightly, which is associated with an increase in porosity, yet the rest of the geometric pattern remains the same. In Figure 4.9 a), the no flow case shows that the transmission loss plot's blue solid line has a better peak compared with configuration 7. For non-zero bias flow cases, it also highlights that the red and black solid lines have developed two peaks in the low-frequency range. In Figure 4.9 b) and d) the absorption and dissipation plots show that the magenta line dominates up to 800 Hz, but thereafter the black line takes over, overlapping the magenta line and slightly shifting its frequency beyond 800 Hz. Overall comparison between

configuration 7 and 8 indicates a slight increase in porosity from 0.74 % to 1.23 %, suggesting an improved absorption or dissipation profile. Axial pitch distance remains the same, but an increase in orifice diameter, along with an increase in porosity, is responsible for this improvement. In Figure 4.9 c), the discharge coefficient versus mass flow rate plot shows that as the mass flow rate increases, the discharge coefficient of the orifice also increases. It can be observed that with an equal amount of mass flow rate these two different configurations, 7 and 8, result in different pressure ratios. The liner with larger holes creates a lower pressure ratio.

4.14.3 Configuration 9 acoustic and static pressure measurement

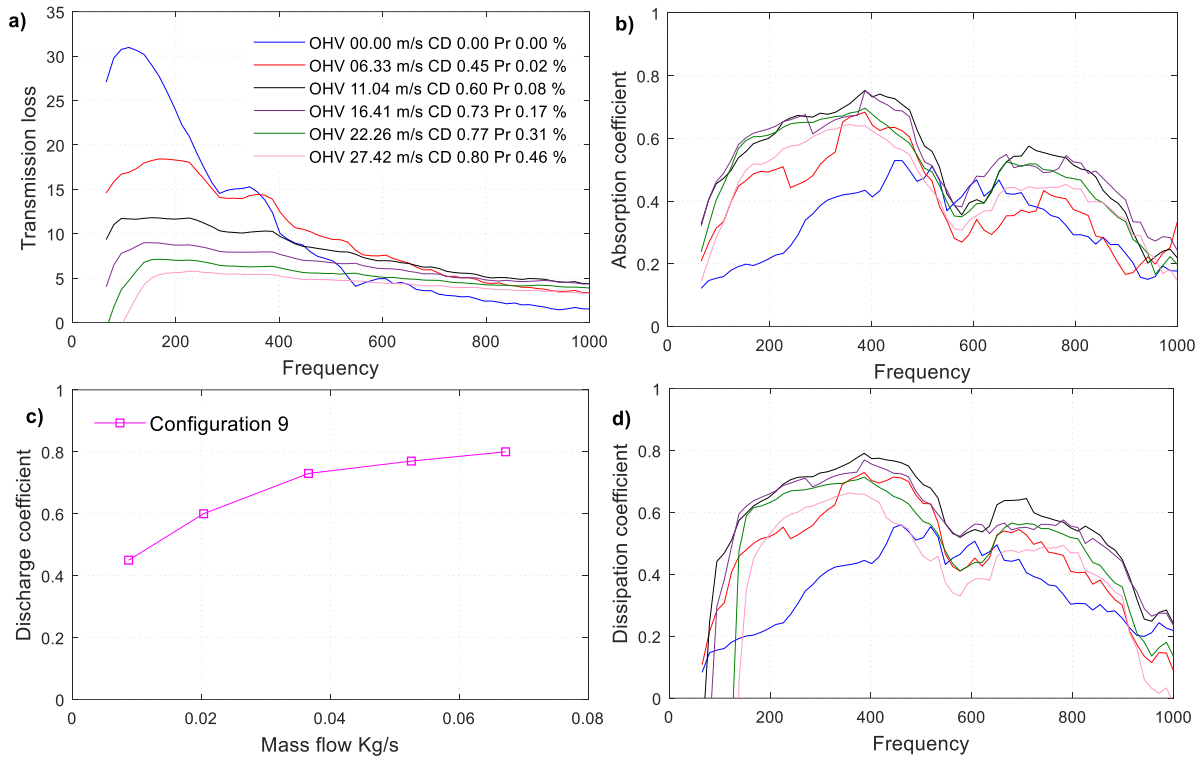

Figure 4.10 Acoustic and static pressure measurement configuration 9.

When compared with configurations 7 and 8, it can be seen that configuration 9's orifice diameter is increased to 1.175 mm, the liner wall thickness is increased to 2 mm, the axial pitch distance is increased to 10.5 mm and the hole pattern changed from uniform to staggered. The total number of orifices decreases to 2256. The influence of the increase in thickness, an increase in axial pitch distance and a change in porosity effect can be observed from acoustic and static pressure measurement. Figure 4.10 a) shows that for no flow and non-zero bias flow cases, transmission loss falls in between configurations 7 and 8. Figure 4.10 b) and d) indicate that the absorption and dissipation spectra are not broadband. The

magenta and black lines overlapped each other in the low and high-frequency ranges. It can be considered that either the magenta or black lines correspond to a broadband frequency range of absorption or dissipation. Due to the decrease in number of orifices and increase in axial pitch distance, the percentage of porosity falls in between configurations 7 and 8, along with liner overall damping performance. Figure 4.10 c) indicates that as the mass flow rate increases the discharge coefficient of the orifice increases within this range.

4.14.4 Configuration 10 acoustic and static pressure measurement

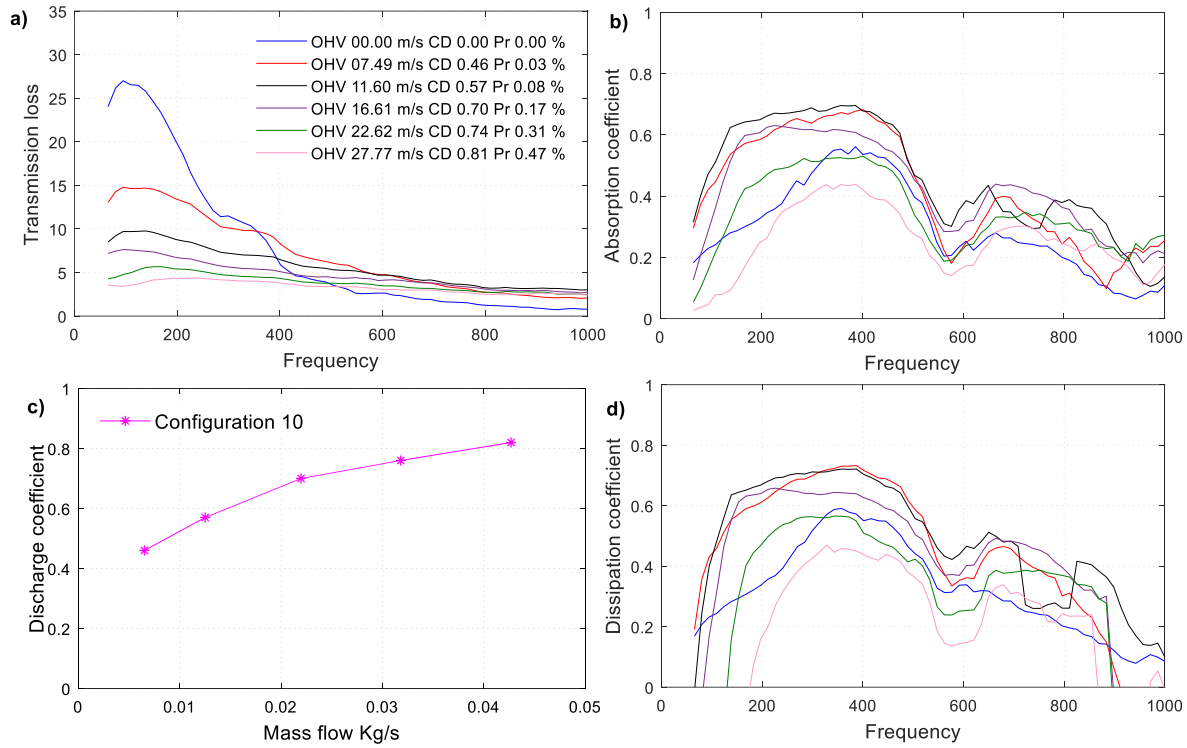

Figure 4.11 Acoustic and static pressure measurement configuration 10.

Configuration 10 is slightly different to the rest of the configurations; it has 0.925 mm orifice diameter, 2256 orifices and an axial pitch distance of 10.50 mm – which refers to 0.61 % of porosity. The rest of the geometric pattern remains the same as configuration 9, apart from the hole pattern. Figure 4.11 a) shows that for no flow and non-zero bias flow cases, the transmission loss of this combustor liner is very poor due to its low porosity; indeed, it has the lowest percentage of porosity when compared to the other configurations. Figure 4.11 b) and d) indicate that neither the absorption nor dissipation profile were successful in producing a broadband frequency range. Non-zero bias flow can create a nonlinear relation, which can be observed with configuration 10, which shows that the pink line corresponds to a lower absorption profile than the blue line. Configuration 10 has a wall thickness of 2 mm,

whereas configuration 7 has a wall thickness of 1.6 mm. Under these circumstances, the thickness effect does not increase the absorptive or dissipative properties of the liner due to the low percentage of porosity. From these four single (damping) liners, the experimental analysis indicates that porosity is the first primary parameter for real combustor design and depends on orifice diameter, axial pitch distance and number of orifices. Figure 4.11 c) shows that as the mass flow rate increases, the discharge coefficient of the orifice also increases within this range.

4.14.5 Configuration 11 acoustic and static pressure measurement

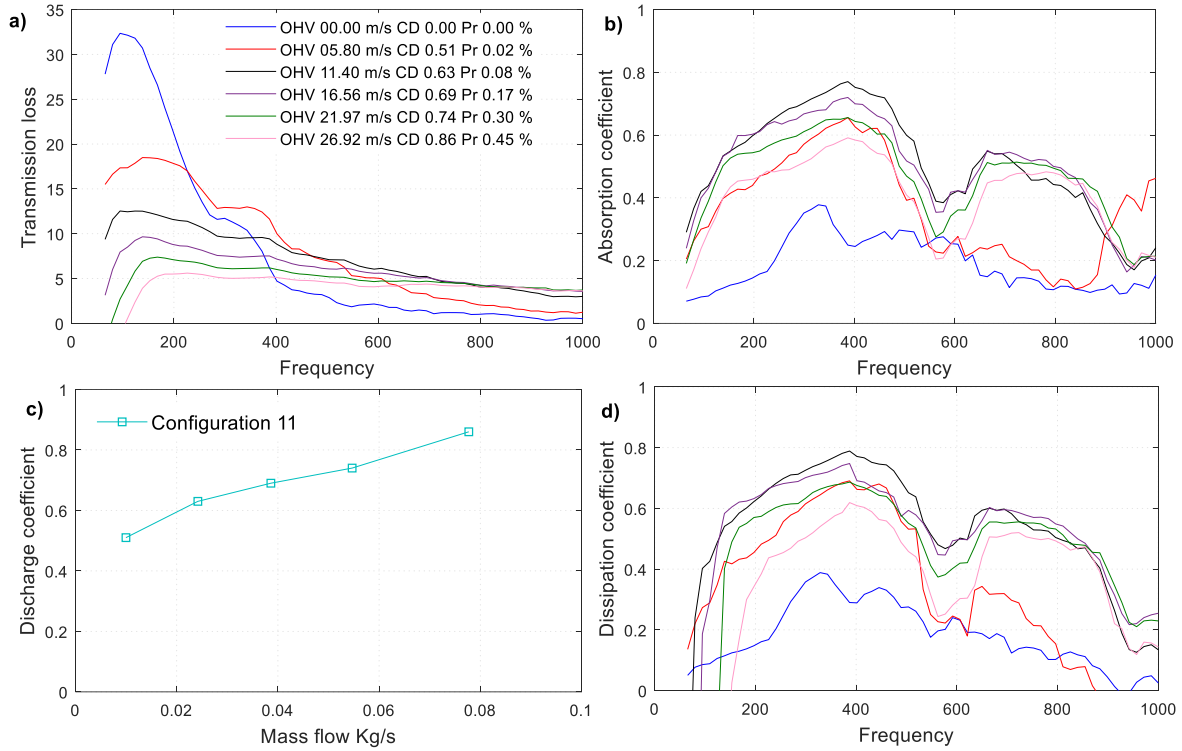

Figure 4.12 Acoustic and static pressure measurement configuration 11.

Configuration 11 is a metering liner. It has 1.6 mm wall thickness, 176.5 mm liner diameter, 2.675 mm orifice diameter, 480 orifices, and an axial pitch distance of 20 mm - which refers to 1.41 % of porosity. In Figure 4.12 a) for the no flow case, the transmission loss plot shows that the blue line can attenuate up to 32 dB in the low-frequency range and remain flat in the high-frequency range. For the non-zero bias flow cases, the red line displays a decrease in transmission attenuation in the low-frequency range and minor increase in the high-frequency range, compared to the no flow case. In Figure 4.12 b) and d) the absorption and dissipation profile show that the black line has relatively better peaks in the low-frequency range. Whereas in the high-frequency range the black, magenta and green lines are

overlapping one another. The precise level of liner performance can be found in the overall energy balance shown in Table 5.1. The absorption or dissipation spectra are not broadband, but can be considered for the black line, which refers to 11.40 m/s orifice hole velocity, 0.63 discharge coefficient of the orifice and pressure ratio of 0.08 %. Figure 4.12 c) displays a similar result to the previous configuration; as mass flow increases, the discharge coefficient of the orifice also increases.

4.14.6 Configuration 12 acoustic and static pressure measurement

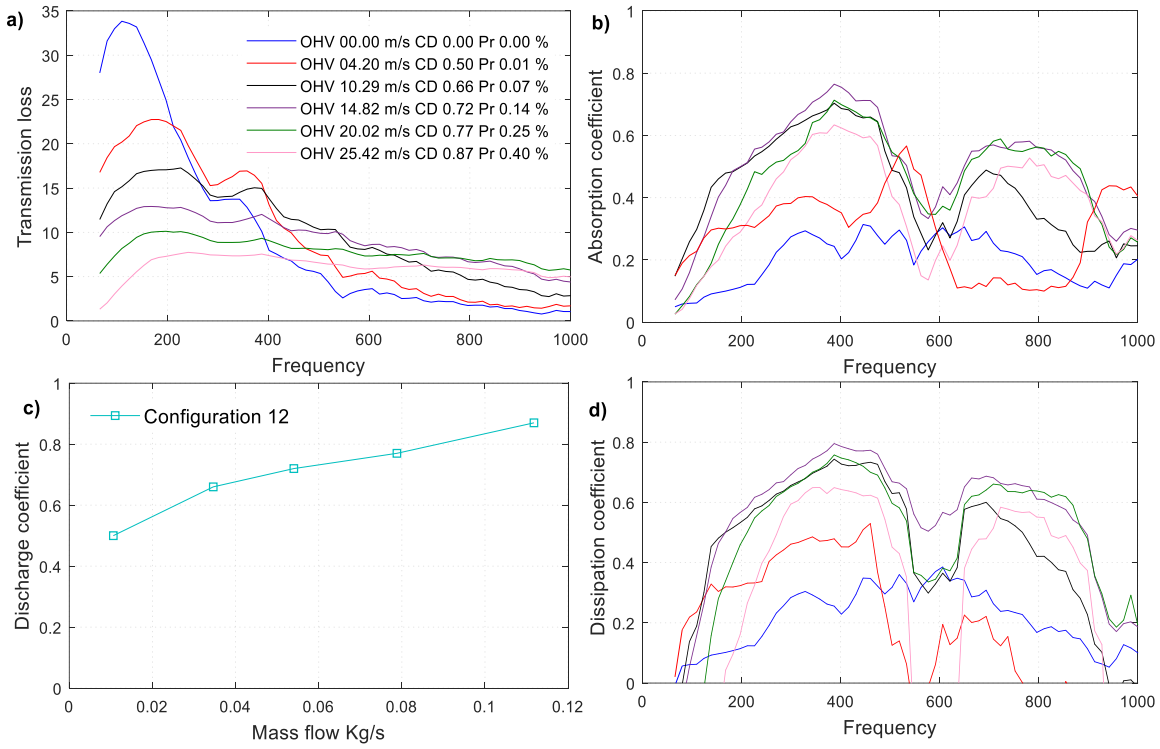

Figure 4.13 Acoustic and static pressure measurement configuration 12.

When compared to configuration 11, configuration 12's liner diameter, orifices per row, and number of orifices are decreased. The increase in orifice diameter refers to an increase in porosity despite the reduced number of orifices. The complete geometric profile of configuration 12 is provided in Table 4.5. For configuration 12, Figure 4.13 a) (for the no and non-zero bias flow cases) shows the transmission loss plot and illustrates that the blue, red, black, and magenta lines have formed a double peak in the low-frequency range. Figure 4.13 b) and d) illustrate that the magenta line has formed the maximum absorption or dissipation profile in the low-frequency range. In the high-frequency range, the magenta and green lines are overlapping. It can be considered that the magenta line exhibits an overall broadband frequency range of absorption or dissipation. A direct comparison of configurations 11 and

12 demonstrates that configuration 12 provides a better transmission attenuation, whereas configuration 11 provides a better absorption or dissipation profile. This relationship is not linear; it is a complex matrix where porosity is related to the orifice diameter, number of orifices and axial pitch distance. For configuration 12, the magenta line represents 14.82 m/s orifice hole velocity, 0.72 discharge coefficient of the orifice and 0.14 % pressure ratio, whereas in configuration 11 the maximum absorptive or dissipative energy profile shown by the black line represents 11.40 m/s orifice hole velocity, 0.63 discharge coefficient of the orifice and 0.08 % pressure ratio. Figure 4.13 c) shows discharge coefficient versus mass flow rate, which indicates that as the mass flow rate increases the discharge coefficient of the orifice increases within this range.

4.14.7 Configuration 13 acoustic and static pressure measurement

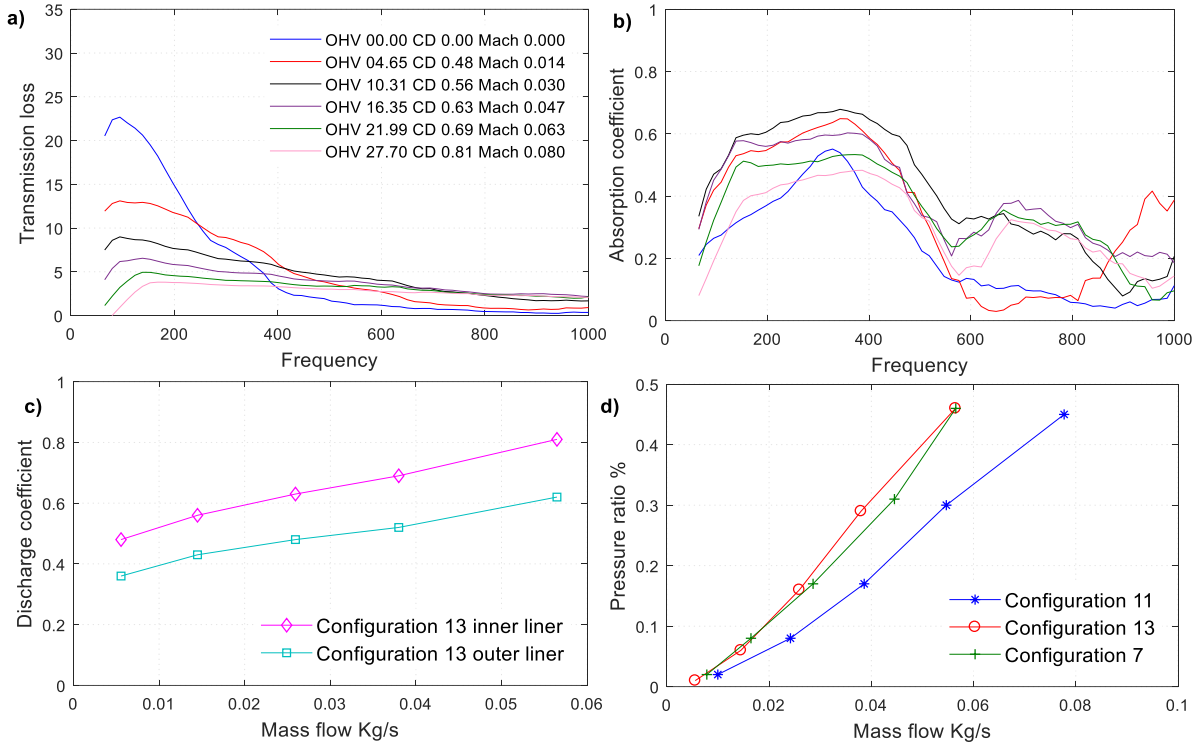

Figure 4.14 Acoustic and static pressure measurement configuration 13.

Configuration 13 is a full-scale cylindrical combustor liner which has a combination of two single liners (configuration 7 (damping liner) and configuration 11 (metering liner)) to form a double layer gas turbine combustor. Figure 4.14 a) shows the transmission loss plot, and for the no flow case the blue line can attenuate up to 22 dB in the low-frequency range, while in the high-frequency range transmission attenuation is flat. For the non-zero bias flow cases combustor liner transmission loss decreases in the low-frequency range (there is an increase

in transmitted energy and decrease in reflected energy), while in the high-frequency range, transmission loss increases (a decrease in transmitted energy and increase in reflected energy). Figure 4.14 b) absorption profile for the combined liner no flow case shows that the blue line exhibits a peak in the low-frequency range, yet remains flat in the high-frequency range. For the non-zero bias flow cases, the black line has maximum absorption profile in the low-frequency range, and the magenta line shows a better peak than the green line in the high-frequency range. Therefore, the absorption spectra are not broadband.

In configuration 13 a new geometric constraint is introduced, d', known as effective cavity depth (discussed previously in section 3.4), which is responsible for generating damping volume 2007 cm^3, and refers to the volume in between the liners. Figure 4.14 b) acoustic analysis signifies that in the presence of non-zero bias flow the combustor liner improves its absorption profile (Bellucci et al., 2004b; Eldredge & Dowling, 2003; Follet et al., 2001; Heuwinkel et al., 2007; Hughes & Dowling, 1990a; Jing & Sun, 1999; Lahiri & Bake, 2017; Lahiri et al., 2011; Lahiri et al.; Lawn, 2015). Introducing a bias flow into the combustor liner is a complex process; the relationship is not linear. There is a drawback to introducing bias flow into the combustor: an excessive amount of bias flow can cause a decrease in its performance, as can be observed in this acoustic analysis. Eldredge and Dowling (Eldredge & Dowling, 2003) developed an optimum Mach number for their investigated liner geometry for a single liner configuration, and their optimum relation becomes less valid at a high frequency. Figure 4.14 b) acoustic analysis shows that Mach number 0.03 or discharge coefficient 0.56 result in a maximum absorption in the low-frequency range, and the effect of an increased Mach number highlights that absorption performance progressively decreases. Figure 4.14 c) the discharge coefficient versus mass flow plot indicates that the discharge coefficient of the orifice is greater in the inner liner compared to the outer liner. The inner liner has a porosity of 0.74 %, and the outer liner has a porosity of 1.41 %. It can be considered that the double-layer liner's lowest porosity accounts for the greater discharge coefficient. In Figure 4.14 d) the pressure ratio versus mass flow plot shows that the pressure curve across configuration 13 (red line with a circle marker) is primarily governed by configuration 7 (green line with a plus marker). Geometric constraint porosity is responsible for governing the pressure curve as configuration 7 has the lowest porosity.

4.14.8 Configuration 14 acoustic and static pressure measurement

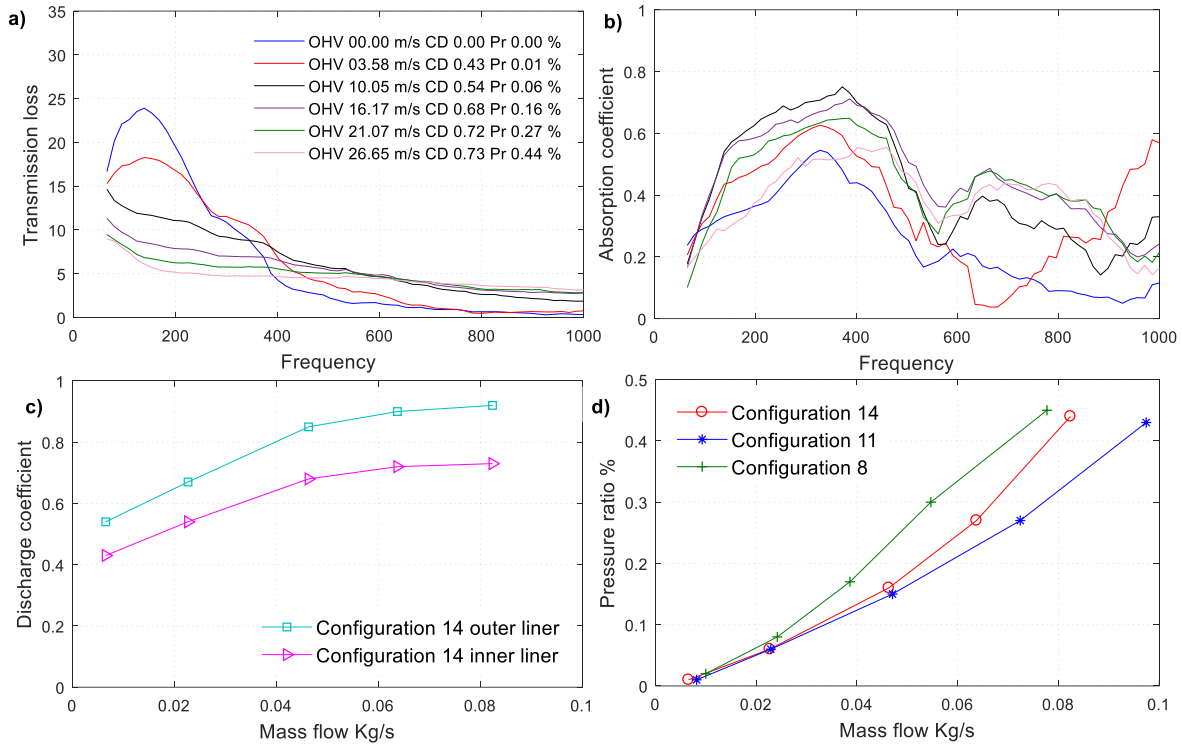

Figure 4.15 Acoustic and static pressure measurement configuration 14.

Configuration 14 is a combination of two single liners: configurations 8 and 11. In Figure 4.15 a) the transmission loss plot illustrates that the no flow case - the blue line - and the non-zero bias flow cases - the red line - have developed peaks in the low-frequency range, while in the high-frequency range they remain flat. In Figure 4.15 b) the absorption plot indicates that the blue line remains flat after the first peak in the absence of bias flow. In addition, it indicates that for the first time, for all combinations, the pink line exhibits the maximum absorption at 800 Hz. The pink line represents orifice hole velocity 26.65 m/s. In this circumstance, the discharge coefficient of the orifice is 0.73, the Mach number is 0.078 and pressure ratio 0.44 %. The absorption aspectra are not broadband for configuration 14. Figure 4.15 c) shows the discharge coefficient versus mass flow plot, and indicates that the discharge coefficient of the orifice is greater in the outer liner when compared to the inner liner. This correlation differs in comparison with other double liner configurations due to the effect of porosity. The inner liner has a porosity of 1.23 %, whilst the outer liner has a porosity of 1.41 %. The second primary parameter, the discharge coefficient of the orifice, depends on porosity, mass flow or pressure ratio. Figure 4.15 d) shows three different pressure ratio versus mass flow plots (two single and one combined liner). The pressure curve for combined liner configuration 14 is represented by the red line with a circle marker. Similarly, the pressure curve for single liner

configuration 8 (inner) and 11 (outer) are represented by the blue line with a star marker and the green line with a plus marker respectively. This experimental analysis of static pressure measurement indicates that the pressure curve formed by the combined liner lies in between the curves obtained from a single liner, although it seems to be exceptionally close to the curve formed by the outer liner. In other words, it can be declared that the pressure curve governed by the liner has the lowest percentage of porosity. In reality, in most cases, combustion stability occurs inside the inner liner. Further investigation is required to design a combustor in which the outer liner will be able to control the pressure ratio, and the inner liner would control the damping effect.

4.14.9 Configuration 15 acoustic and static pressure measurement

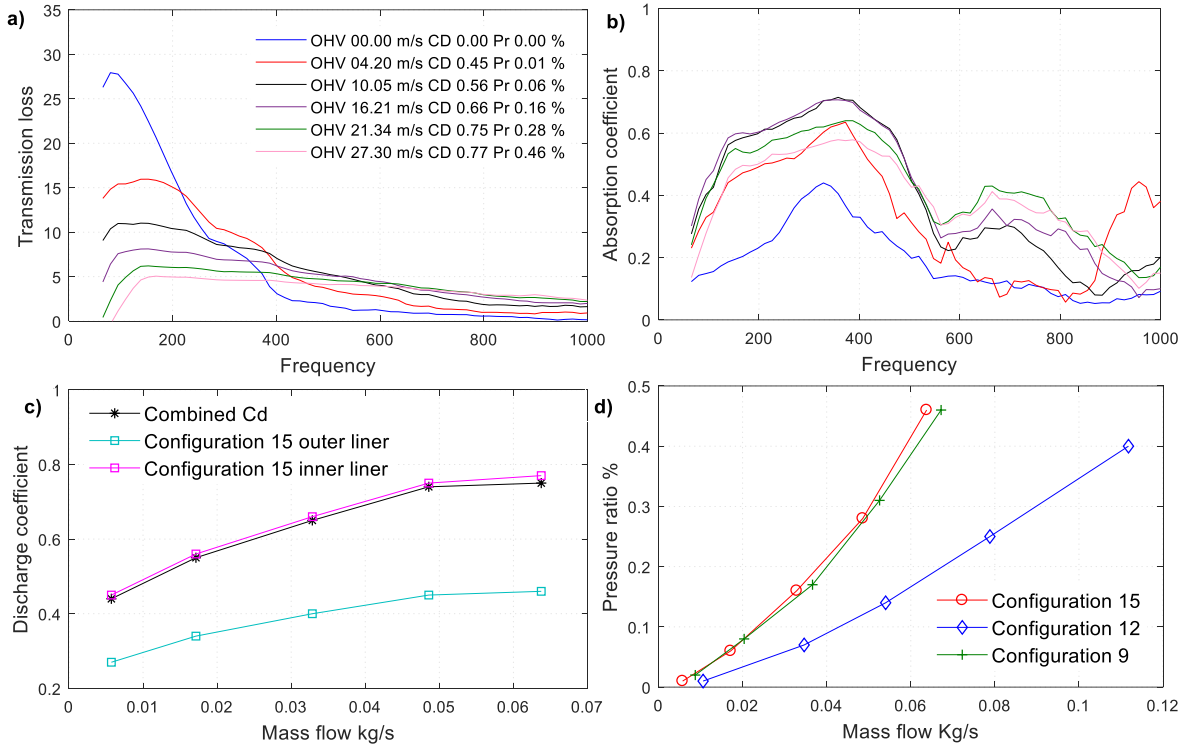

Figure 4.16 Acoustic and static pressure measurement configuration 15.

Combustor liner configuration 15 is a combination of configurations 9 and 12. In this configuration, the inner liner has a wall thickness of 2 mm and diameter of 161.5 mm, whereas the outer liner has a wall thickness of 1.6 mm and diameter of 171.9 mm. By decreasing the outer liner diameter compared to configuration 14, the damping volume for this configuration is reduced to 1373 cm^3. Figure 4.16 a), for the no flow case, shows the transmission loss plot in which the blue solid line can attenuate up to 28 dB in the low-frequency range, yet in the high-frequency range it remains flat. Whereas for the non-zero

bias flow cases the transmission attenuation decreases in the low-frequency range, and increases slightly in the high-frequency range. Figure 4.16 b) shows the absorption plot and highlights that in non-zero flow cases the black and magenta lines have overlaped each other in the low-frequency range, yet in the high-frequency range the green line exhibits the highest secondary peak. The absorption aspectra are not broadband for configuration 15. For the no flow case the blue line indicates a peak in the low-frequency range, but it remains flat in the high-frequency range. Figure 4.16 c), the discharge coefficient versus mass flow plot, proffers that the measured and combined (estimated) discharge coefficients of the orifice are almost identical. The inner liner exhibits a greater discharge coefficient than the outer liner. In Figure 4.16 d) the pressure ratio versus mass flow plot indicates that configuration 15's (combined liner) pressure curve is mainly governed by configuration 9 (inner liner). In configuration 15, the inner liner has 0.98 % porosity and the outer liner has 2.65 % porosity, which indicates that the liner with the lowest percentage of porosity (smaller orifice diameter) is responsible for governing the pressure curve. In conclusion, static pressure measurement signifies that the liner with the lowest percentage of porosity has a greater discharge coefficient, and establishes a pressure curve in a full-scale cylindrical double-layer combustor.

4.14.10 Configuration 16 acoustic and static pressure measurement

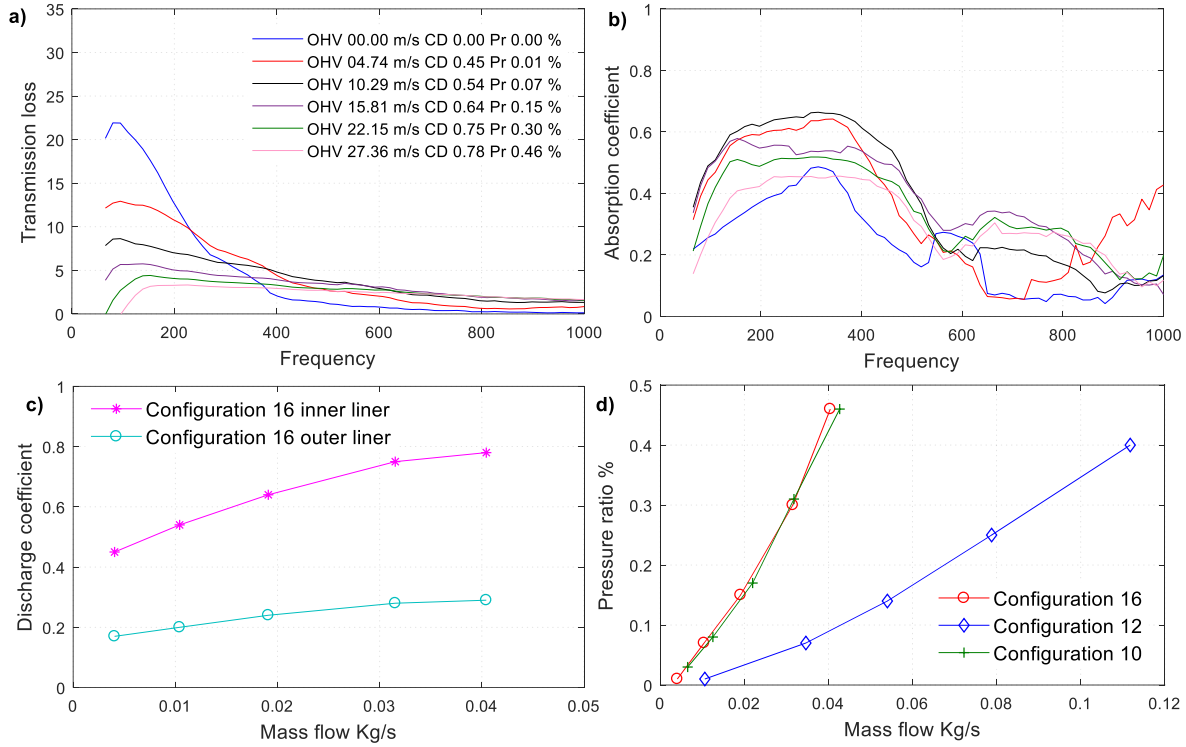

Figure 4.17 Acoustic and static pressure measurement configuration 16.

Combined liner configuration 16 is an amalgamation of configurations 10 and 12. The inner liner has a porosity of 0.61 %, and the outer liner has a porosity of 2.65 %. In Figure 4.17 a) the transmission loss plot shows that, for no flow and non-zero bias flow cases, configuration 16 provides the lowest transmission attenuation when compared with other double liner configurations. This can be specified as a porosity mismatch, or the excessively lowest percentage of the porosity in the inner liner. In Figure 4.17 b) the absorption plot highlights that liner performance is inferior when compared with other double liner configurations. The non-zero bias flow case reveals the weakest peak in the high-frequency range. The exceptionally low porosity of the damping liner could provide an explanation. The overall broadband frequency spectra are not present in configuration 16. Figure 4.17 c) displays the plot of the discharge coefficient versus mass flow rate, and demonstrates that the discharge coefficient of the orifice is minimal for the metering liner due to porosity mismatch. As a result of increasing inner liner thickness, the overall performance of this combined liner absorption profile is inadequate due to the decrease in porosity (inner liner) or porosity mismatch with the outer liner. Figure 4.17 d) shows the pressure ratio versus mass flow rate plot andreveals that the pressure curves for configuration 16 (the red line with a circle marker) and

configuration 10 (the green line with a plus marker) coincide with one another. From this configuration it can be deduced that the pressure curve formed by the combined liner is primarily dominated by the inner liner.

4.14.11 Configuration 17 acoustic and static pressure measurement

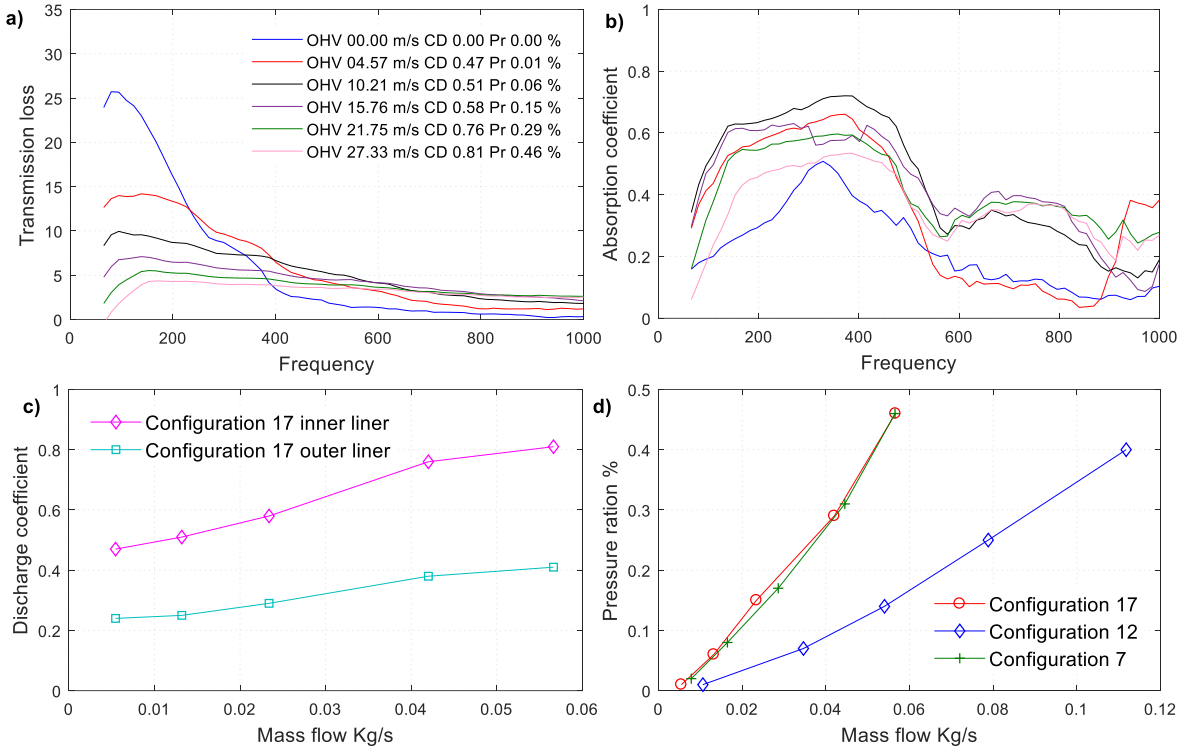

Figure 4.18 Acoustic and static pressure measurement configuration 17.

Combined liner configuration 17 is a combination of configuration 7 and configuration 12. The difference between configuration 17 and configuration 13 is that the outer liner diameter is slightly smaller with a larger orifice diameter, which refers to the decrease in damping volume and increase in porosity. The inner liner has a porosity of 0.74 %, and the outer liner has a porosity of 2.65 %. Both liners have the same thickness of 1.6 mm. In Figure 4.18 a) the transmission loss plot illustrates that for the no flow and non-zero bias flow cases configuration 17 provides a better transmission attenuation when compared with configuration 13, due to the increased porosity (larger orifice diameter) of the outer liner. In Figure 4.18 b), for the non-zero bias flow cases, the black line exhibits maximim absorption in the low-frequency range. The green and magenta lines have overlaped one another in the high-frequency range, indicating that broadband spectra are not present. No flow acoustic analysis shows that the solid blue line has a peak in the low-frequency range and subsequently remains flat in the high-frequency range. Therefore, a non-zero bias flow is required to form

a second peak in the high-frequency range. Figure 4.18 d) displays the pressure ratio versus mass flow plot, which indicates that the curve for configuration 17 (the red line with circle marker) and configuration 7 (the green line with plus marker), overlap one another. Furthermore, it indicates that the inner liner governs the combined liner pressure curve. In Figure 4.18 c) the discharge coefficient versus mass flow rate plot reveals that the discharge coefficient of the orifice is greater in the damping liner and lesser in the metering liner. The decrease in damping volume by 634 cm^3 compared to configuration 13 did not appear to have a negative impact on liner performance due to the increased porosity of the outer liner.

4.14.12 Configuration 18 acoustic and static pressure measurement

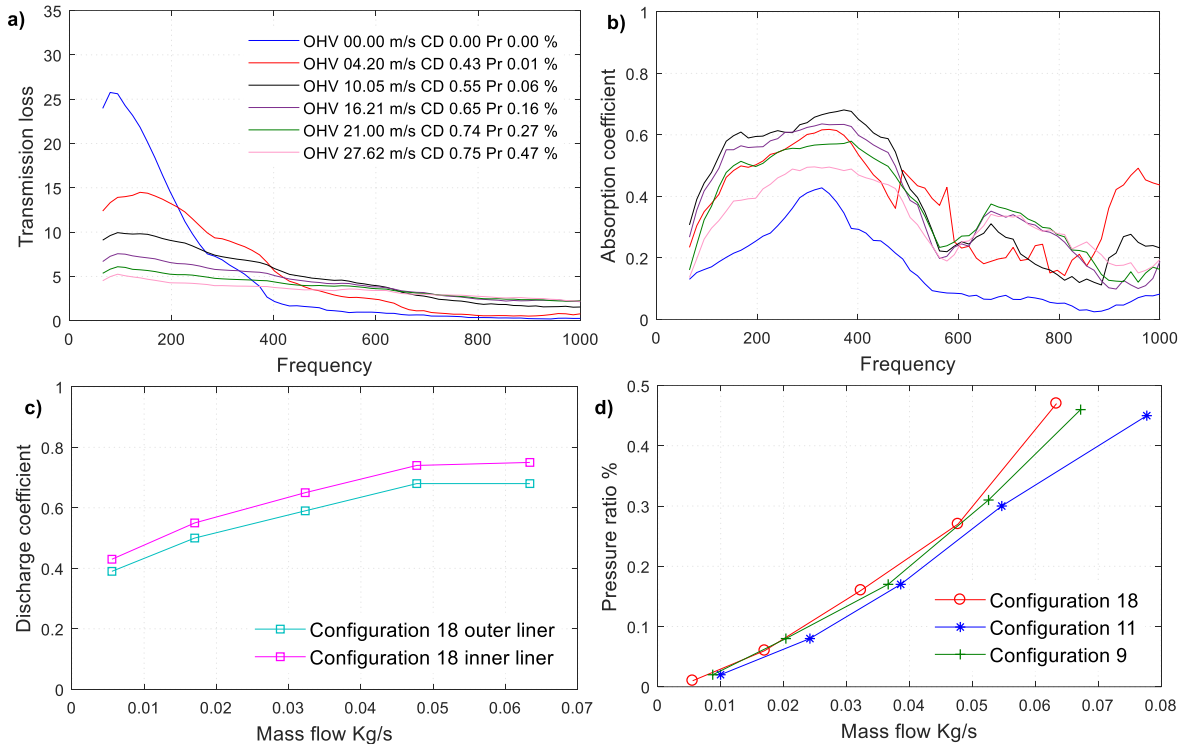

Figure 4.19 Acoustic and static pressure measurement configuration 18.

Double layer combustor liner configuration 18 is a combination of configuration 9 and configuration 11. Figure 4.19 a) shows the transmission loss plot, and for no flow case the blue line can attenuate up to 26 dB in the low-frequency range, while in the high-frequency range transmission attenuation is flat. For the non-zero bias flow cases transmission loss decreases in the low-frequency range, yet shows a slight increase in the high-frequency range. In Figure 4.19 b) the absorption plot highlights that for the non-zero bias flow case the black line shows the maximum absorption in the low-frequency range. The pink and green line overlap each other with a weak peak in the high-frequency range. The absorption spectra are

not broadband for configuration 18. For the no flow case the blue line exhibits the first peak in the low-frequency range, yet the high-frequency range remains flat. Figure 4.19 d) shows the pressure ratio versus mass flow plot, and indicates that the pressure curves are adjacent to one other in configurations 9, 11 and 18. The pressure curves are equivalent because the impact of inner (0.98 % porosity) and outer (1.41 % porosity) liner geometry (porosity). Configuration 14 also shows less porosity difference, but orifice diameter is small, number of orifices are greater and there is less axial pitch distance, therefore pressure curves are not similar to configuration 18. The observation from all combined liner static pressure measurements suggest that the pressure curve is dominated by the liner possessing the lowest percentage of porosity, and with a smaller orifice diameter. In Figure 4.19 c) the discharge coefficient versus mass flow plot indicates that the discharge coefficients of the orifices of the inner and outer liner are nearby due to the influence of porosity. It can be concluded that to develop a better absorption profile in the high-frequency range, a porosity variation between the inner and outer liner is required. Furthermore, non-zero bias flow is required to yield a better absorption profile in the high-frequency range. Increasing the damping volume between the liners did not appear to increase liner performance due to porosity mismatch of the inner and outer liner.

4.15 Conclusion

The primary purpose of static pressure measurements is to create a legend corresponding to acoustic analysis for enhanced interpretation. The legend is expressed in different formats, although they have the same meaning. The first task is to calculate the discharge coefficient of the orifice, then state the OHV and pressure ratio. It is also essential to designate liner accountability, i.e., which liner is responsible for forming the actual pressure curve. For single liners Configuration 7 to Configuration 12, discharge coefficient versus mass flow rate is used to enhance the findings, along with acoustic analysis. Later, for double liners (configurations 13 to 18), the discharge coefficient versus mass flow, and pressure ratio versus mass flow are examined to develop the findings, along with acoustic analysis. The total mass flow introduced into the cavity is assessed based on accurately calculating volume and duct velocity. From the duct velocity, the mass flow and discharge coefficient of the orifice is developed. Static pressure measurement indicates that the discharge coefficient of the orifice changes as the pressure ratio changes; it is essential to verify the result with theory. Precisely,

an estimated (combined) effective area calculation is carried out to develop a double layer combustor liner estimated discharge coefficient. Double layer combustor estimated discharge coefficient is compared with the measured (velocity-based) discharge coefficient of the orifice.

In section 4.14.9 the plot of the discharge coefficient versus mass flow rate illustrates the variance. Acoustic analysis and the damping effect are examined based on no flow and non-zero bias flow conditions. White noise is introduced as an excitation of an acoustic wave. Liner absorption and dissipation coefficients are defined along with the transmission loss measurement. SNR and SPL remained constant throughout the experiment. A dummy liner acoustic analysis is performed to create two factor authentications. To designate the acoustic analysis, the corresponding static pressure measurement is carried out. The result shows that in the presence of bias flow the liners damping effect improves. The non-zero bias flow exhibit a non-linear effect; low Mach bias flow can improve liner absorption or dissipation profile, while an excessive or high bias flow decreases the absorption or dissipation profile. Liner orifice pattern, porosity, axial pitch distance, damping volume, and thickness play a vital role in controlling the overall damping effect of a cylindrical combustor liner. Porosity and axial pitch distance are key parameters in controlling the peak and frequency shift. For a constant mass flow, a thinner liner delivers a higher-pressure ratio, while a thicker liner exhibits a lower pressure ratio. To determine the effect on the thickness of a cylindrical combustor liner it would be necessary to test a pair of otherwise identical liners with different thicknesses, which was not available at the time; however, both can be subject to future investigation.

5 Model validation

Model assessment and authentication is very beneficial for conductivity research as it provides greater accuracy for evaluation. In this chapter, experiments carried out in UHARC and Lahiri et al's. (Lahiri, 2014; Lahiri & Bake, 2017; Lahiri et al., 2011) experimental results are compared with the present semi-empirical model and the previously developed model for assessment. Chris Lawn's (Lawn, 2015) recent model investigation of the absorption of plane waves starting from one end of a lined duct is defined together with the theories and correlations used in describing the acoustic impedance of the orifices in the presence of various mean flows. A diverse range of geometric configurations exhibited acceptable accuracy for the entire configuration. Lawn's model (Lawn, 2015) data shows zero cross-flow or weak cross and bias flow, which concurs with Lahiri et al's. (Lahiri, 2014; Lahiri & Bake, 2017; Lahiri et al., 2011) experimental results. A range of peak absorption frequencies were observed related to small bias flow through a relatively large orifice in a single and double liner.

The concluding discussion is based on findings as to the parameter value that best fits the observed experimental data with the model-to-model comparisons. Therefore, in respect, the hybrid model with equations (3.14) and (3.15), which appears to have the best fit for both single and double-layer liner results, will be depicted here for model-to-model comparisons. The most recent model developed by Chris Lawn (Lawn, 2015) will be compared with Lahiri et al's. (Lahiri, 2014; Lahiri & Bake, 2017; Lahiri et al., 2011) experimental data, along with Melling's (Melling, 1973b), George B. Thurston's (Thurston, 1952b), Crandall (Crandall, 1926b), Bauer's (Bauer, 1977), Betts et al. (Betts et al., 2000; Betts, 2000) and Bellucci et al's. (Bellucci et al., 2004b; Bellucci et al.). To improve the accuracy of this assessment, several numerical models were developed in a Mat-lab platform and computed for display, yielding the output given below. Absorption profiles appear to have a straight line due to the nature of those impedance models. Therefore, from this present hybrid model equation (3.7), equation (3.20) has been added for overall comparison with all models, excepting Chris Lawn's (Lawn, 2015). The goal of this investigation is to identify the model that can best predict the measurement and provide an approximation of the truth.

5.1 Comparison of predictions with data

In this section, an interactive model prediction will be compared with the experiment. To conduct this type of higher-order analysis it is essential to establish a benchmark, thus theoretical interpretation will be easy to recognise. Earlier in section 4.13, dummy liner acoustic analysis was shown in Figure 4.7. In this section, dummy liner signal and integrated energy (50-1000 Hz) analysis is presented. Once again, dummy liner acoustic analysis will be compared with the semi-empirical hybrid model, along with liner resistance and reactance terms to create two factor authentications.

5.2 Dummy liner comparison of predictions with data

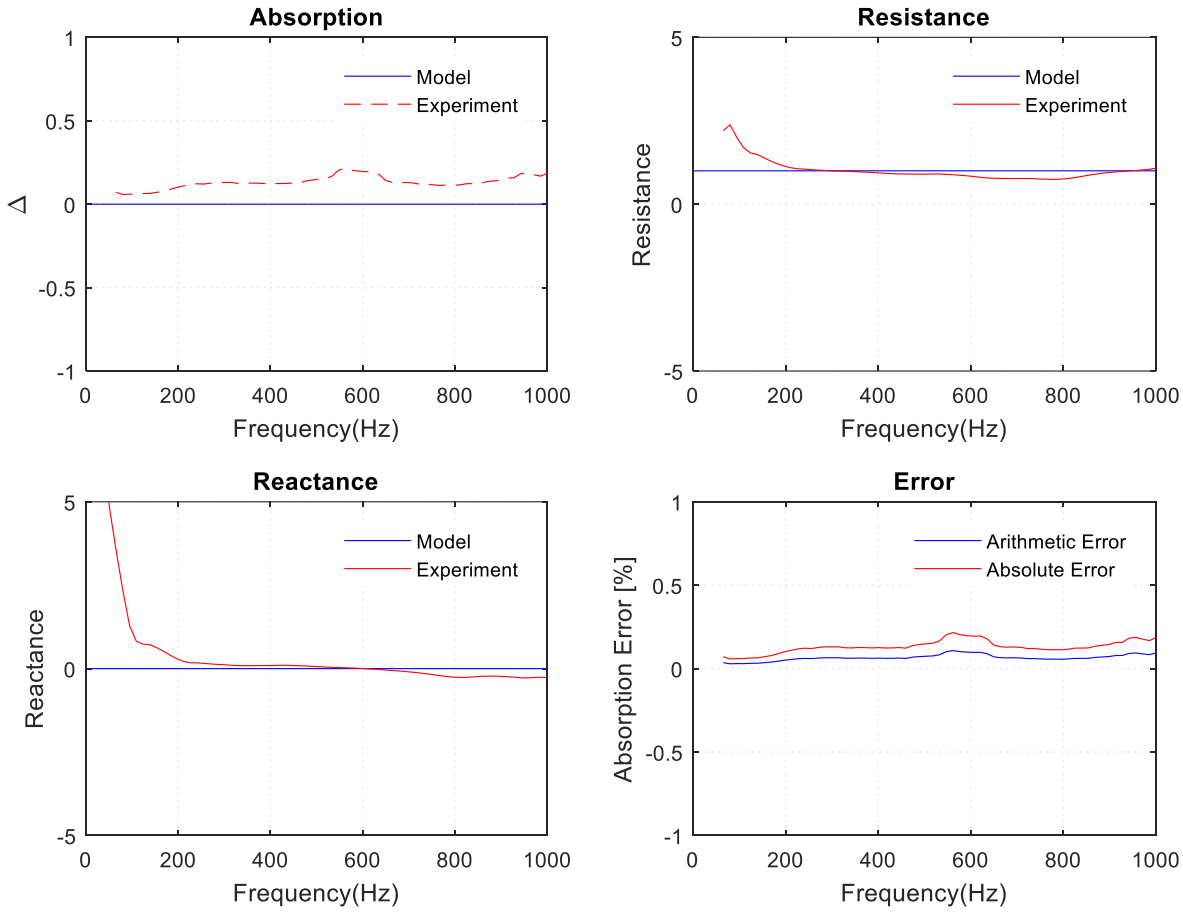

Figure 5.1 Dummy liner assessment with the model and experiment.

The numerical yield of this present semi-empirical hybrid model, along with experimental analysis, is illustrated in Figure 5.1. This present model has the capability of determining liner absorptive or dissipative profiles along with liner resistance and reactance terms. To improve the accuracy of these complex and intricate experiments, error analysis is presented to identify dominant errors and provide a guide as to where more care is necessary. Conversely,

the model prediction highlights that the dummy liner absorption profile is zero, whereas experimental analysis indicates that a slightly positive absorption profile has formed, shown in the overall energy balance (Table 5.1) calculation. This positive absorption profile supports the energy balance calculation showing that the dummy liner absorption profile has established a reasonable agreement. The cumulative calculation of all configurations overall energy balance is added towards the end of this chapter, in Table 5.1.

5.2.1 Dummy liner signal analysis

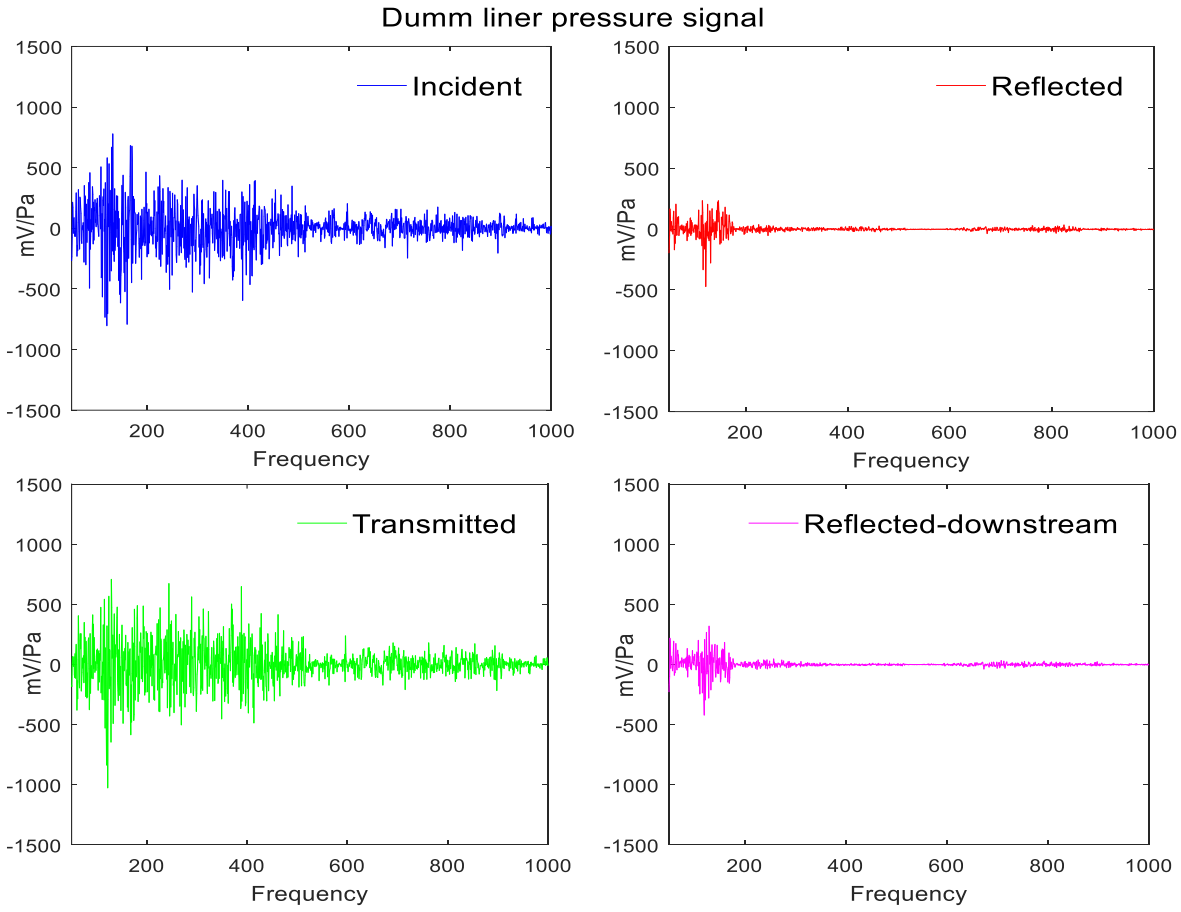

Figure 5.2 Dummy liner pressure signal analysis.

Dummy liner pressure signals only allow the incident wave to pass from the upstream to the downstream section without any attenuation as there is no perforation. Figure 5.2 shows that incident (blue) and transmitted (green) pressure signals are almost identical. Similarly, upstream reflected (red) and downstream reflected (pink) pressure signals remain the same, signifying that the experiment and data analysis carried out in UHARC shows acceptable results.

5.2.2 Dummy liner energy analysis

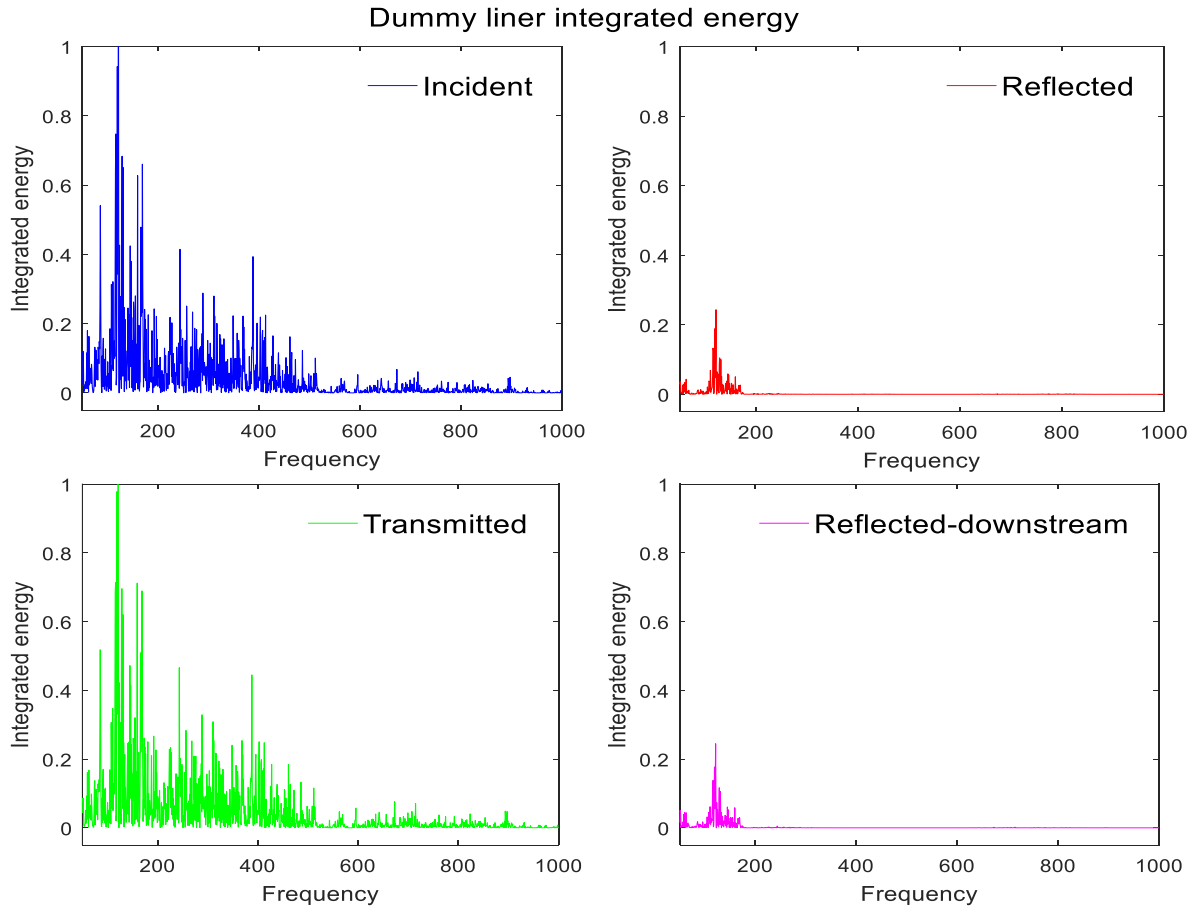

Figure 5.3 Dummy liner integrated energy analysis.

As previously discussed, Figure 5.2 shows that dummy liner experiment and data analysis provides higher-order accuracy. Figure 5.3 exhibits that the establishment of integrated energy data from the recorded pressure signal is performed by using trapezoidal integration (Burgos et al., 1998). From the energy balance calculation it is easy to calculate the total energy in and out of the system. As the dummy liner has no perforation, the energy in and out of the system should be identical. Therefore, the absorption of the dummy liner shows that energy out minus energy in is equal to 2.81, shown in the overall energy balance (50-1000 Hz) calculation in Table 5.1. The expected value of the liner absorption profile equals zero, but appears to show 2.81, which can indicate experimental error, insertion loss, or microphone phase mismatch amongst many other possibilities.

5.3 Configuration 1 comparison of predictions with data

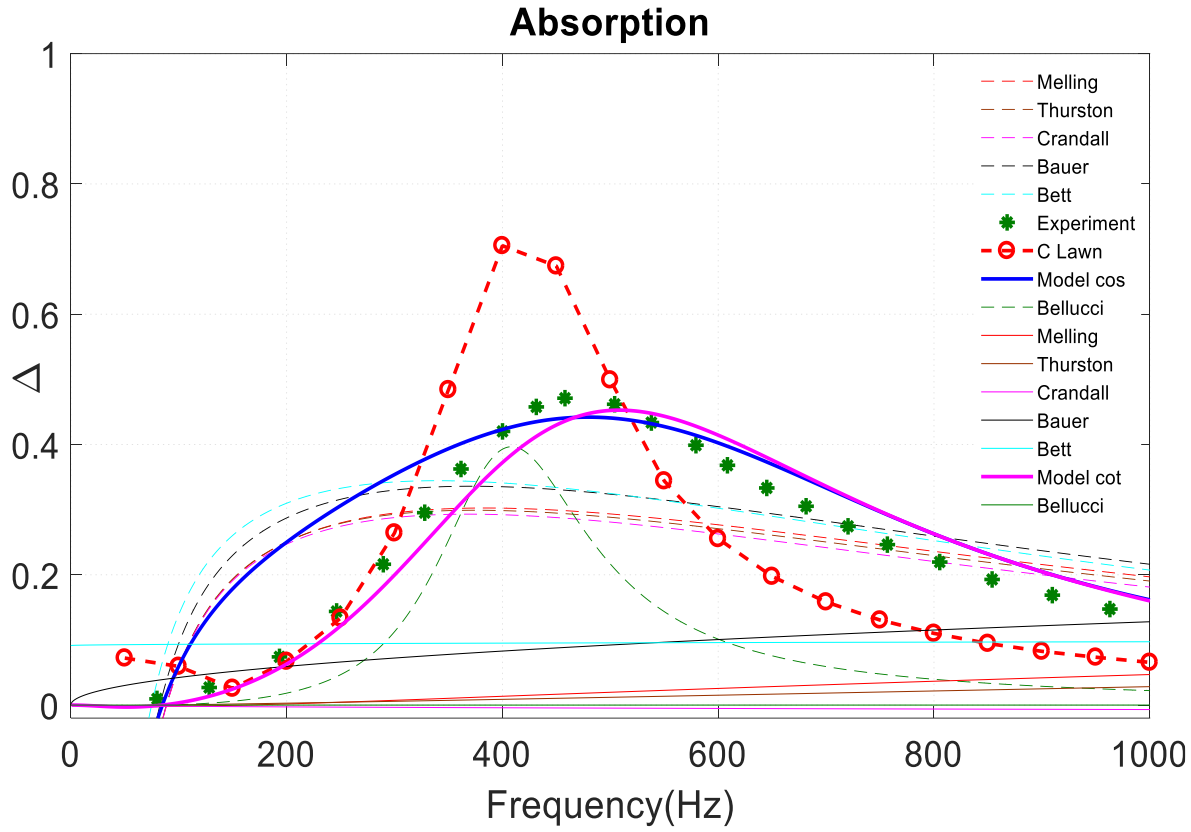

Figure 5.4 Configuration 1 model assessment with experiment.

Configuration 1 has a cavity depth of 49 mm, 140 mm liner diameter, 59.5 mm liner length, orifice diameter 1 mm and axial pitch distance 8.5 mm - which refers to 1.09 % of porosity. Figure 5.4 shows the absorption profile, and cot function with cavity factor (pink solid line) has an excellent agreement with the measurement (Lahiri, 2014; Lahiri & Bake, 2017; Lahiri et al., 2011) (green asterisks mark). It also shows that cos function with cavity factor (blue solid line) has formed a good agreement. This present semi-empirical hybrid model can predict liner resistance and reactance terms along with the absorption profile, which will be discussed later in section 5.9. Mathematical modelling tends to be utilised to formalise the assumption on how experimental data matches with the models. This present semi-empirical hybrid model offers a way to determine the amount of evidence the data provides to support one model over another. However, the sum of experimental data is insufficient to form a clear distinction between competing models. The present model is subsequently calibrated to experimental data using cavity factor within cos and cot functions, which is demonstrated in Figure 5.4.

Crandall's (Crandall, 1926b) magenta, George B. Thurston's (Thurston, 1952b) brown, Melling's (Melling, 1973b) red, Bauer's (Bauer, 1977) black, Bellucci et al's. (Bellucci et al., 2004b; Bellucci et al.) green, and Bett's et al's (Betts et al., 2000; Betts, 2000) cyan solid line exhibit a straight absorption profile. To improve the performance and justification of its expression, equation (3.7) (impedance due to the end correction) and (3.20) (impedance due to the interaction end correction) have been added to their models, which shows a formation of a partial absorption profile, represented as a dashed line in Figure 5.4. Exceptional evidence is observed, and once justification is added Bellucci et al's. (Bellucci et al., 2004b; Bellucci et al.) green dashed line forms a peak closer to the measurement. Chris Lawn's (Lawn, 2015) recently developed model (red dotted line with a circle marker) appears to agree better with the spectral forms of the Lahiri et al. (Lahiri, 2014; Lahiri & Bake, 2017; Lahiri et al., 2011) measurement data.

5.4 Configuration 2 comparison of predictions with data

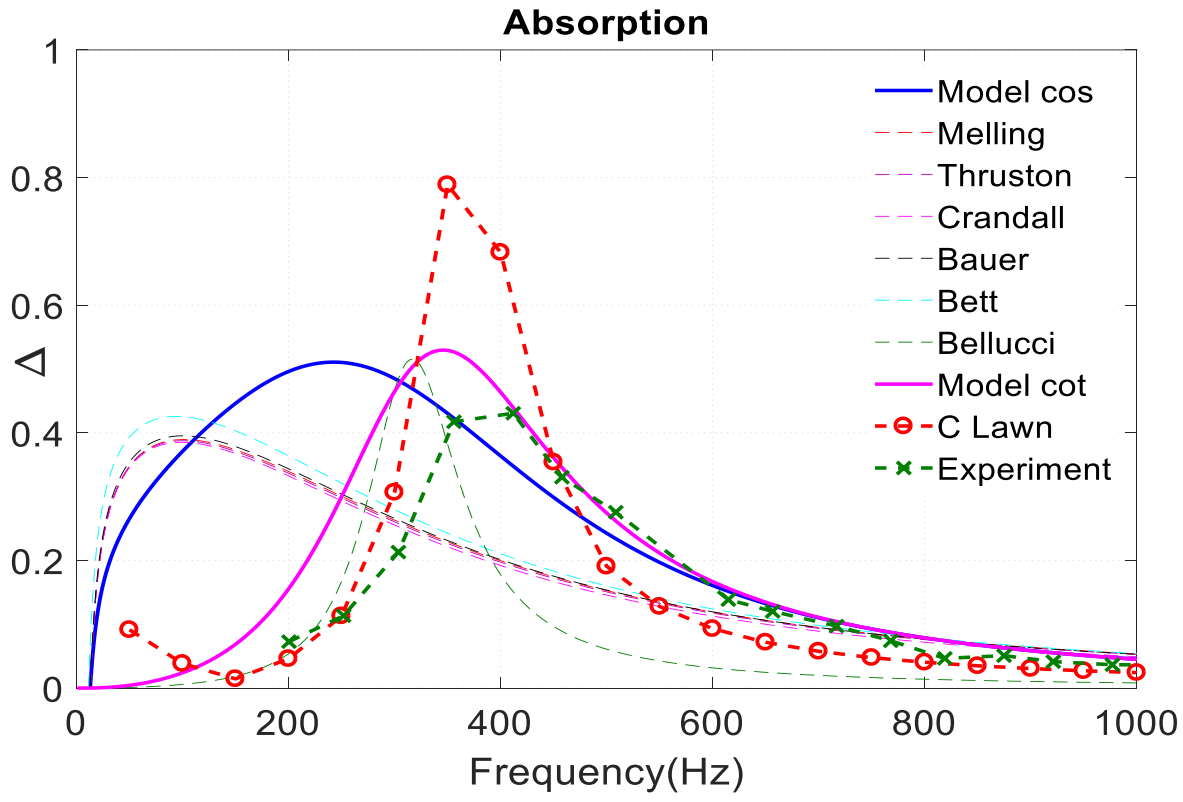

Figure 5.5 Configuration 2 model assessment with experiment.

Configuration 2 is a single liner combustor, which has a 140 mm liner diameter, 66 mm liner length, 49 mm cavity depth, 2.5 mm orifice diameter and 22 mm axial pitch distance – which refers to 1.01 % of porosity. Figure 5.5 shows a comparison of predictions; the solid pink line has a better absorption profile than the solid blue line with Lahiri et al.'s (Lahiri, 2014; Lahiri

& Bake, 2017; Lahiri et al., 2011) measurement data. The blue line shows a reasonable prediction from 350 Hz to the end; the resonance effect of this present numerical analysis is dominant when compared with the measurement. In the absence of bias flow, configuration 2 exhibits typical resonance damping behaviour. The prediction of the solid blue line and the measurement did not match very well in the low-frequency range. The critical magnitude for this transition mismatch seems to be the reactance, which may be responsible for shifting the peak slightly to the right in the low-frequency range. Helmholtz type resonance frequency and the expansion of the reactance contained by the model play a vital role in describing the behaviour in the transition region. Meanwhile, the model cot function with cavity factor shows a good agreement with the measurement. Chris Lawn's (Lawn, 2015) model (the red dotted line with circle marker) achieves a good fit with the measurement, although it shows a slightly larger peak (about 400 Hz), whereas Bellucci et al's. (Bellucci et al., 2004b; Bellucci et al.) model (dashed green line) with justification shows that the peak shift to 300 Hz goes slightly right compared to the measurement. Melling's (Melling, 1973b) red, Thurston's (Thurston, 1952b) brown, Crandall's (Crandall) pink, Bauer's (Bauer, 1977) black, and Betts et al's. (Betts et al., 2000; Betts, 2000) cyan dashed line appears to have a reasonable agreement beyond 600 Hz. The output from these models does not agree with the measurement, thus their predictions will not be shown further.

5.5 Configuration 3 comparison of predictions with data

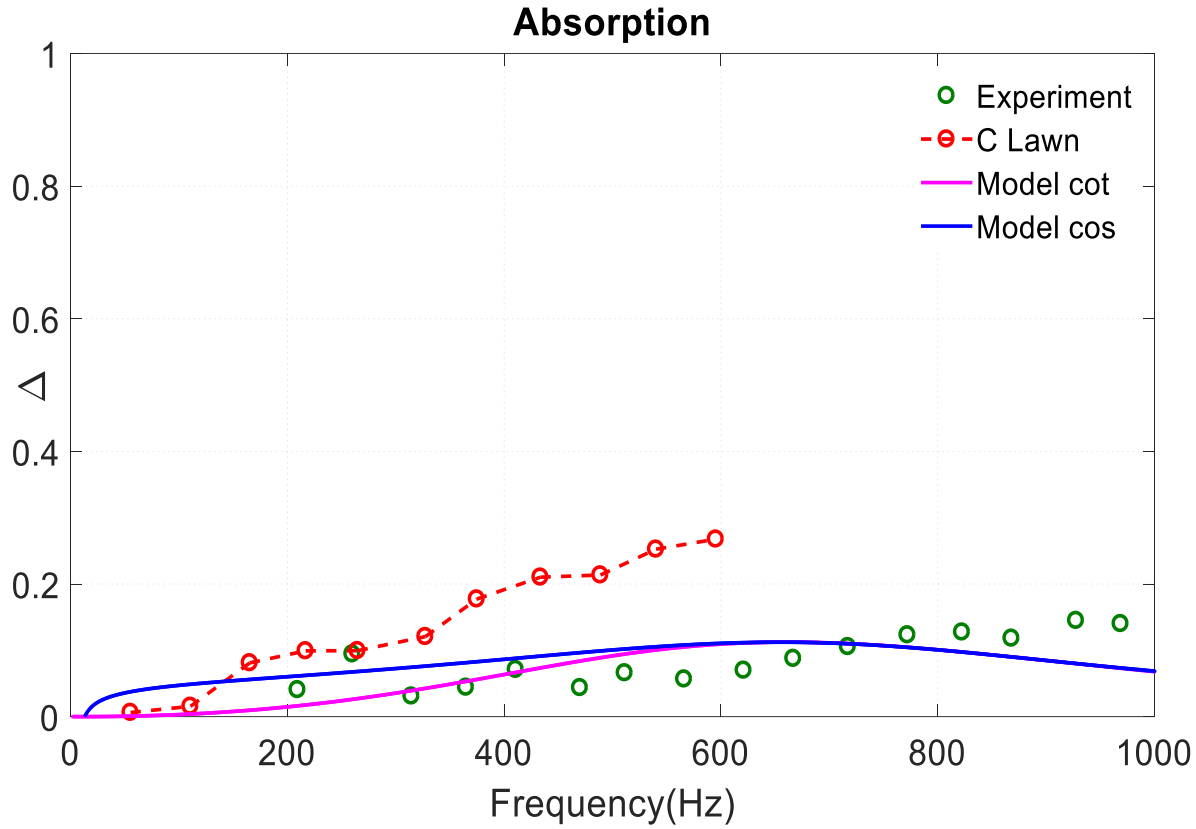

Figure 5.6 Configuration 3 model assessment with experiment.

Configuration 3 has a 140 mm liner diameter, 59.5 mm liner length, 2.5 mm orifice diameter, and 8.5 mm axial pitch distance, which refers to 6.79 % of porosity. Due to increased porosity, configuration 3 (single liner combustor) exhibit a flat absorption profile. For this configuration, a comparison of predictions (the blue and pink solid line) indicates an excellent agreement with the measurement (Lahiri, 2014; Lahiri & Bake, 2017; Lahiri et al., 2011). A comparison of predictions with the measurement suggest that porosity is responsible for generating a flat absorption profile, shown in Figure 5.6. With configuration 3, the axial pitch distance did not match the orifice diameter. A larger orifice diameter requires a slightly longer axial pitch distance to create a vortex, shedding to the neighbouring interaction area to absorb or cancel acoustic pressure. The formation of active vortex shedding is responsible for increasing liner absorption performance. Chris Lawn's (Lawn, 2015) (red dotted line with circle marker) model seems to agree with data only at low frequency.

5.6 Configuration 4 comparison of predictions with data

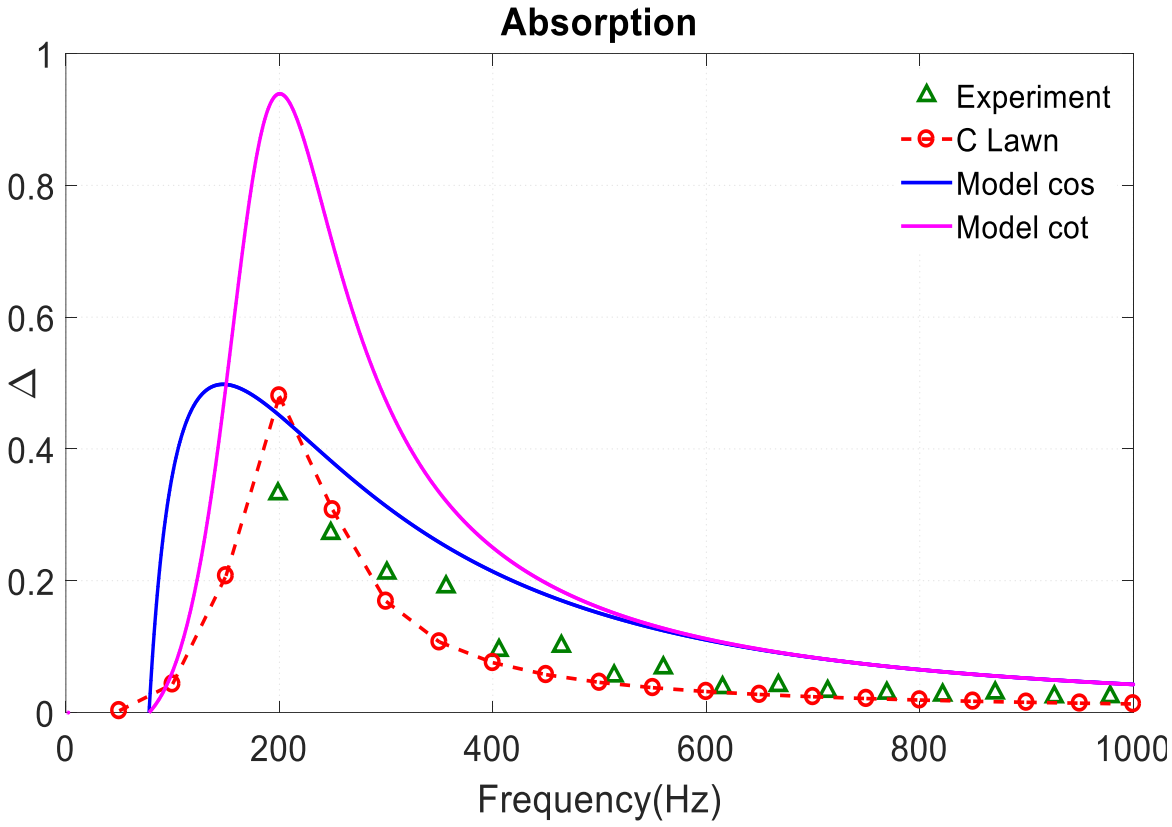

Figure 5.7 Configuration 4 model assessment with experiment.

Configuration 4 is a single liner combustor. It has 140 mm diameter, 66 mm liner length, 1 mm orifice diameter, and 22 mm axial pitch distance, which refers to 0.16 % of porosity. Figure 5.7 shows that a comparison of predictions, cos function (blue solid line) and Chris Lawn's (Lawn, 2015) model (red dotted line with circle marker) demonstrate a decent agreement with Lahiri et al.'s (Lahiri, 2014; Lahiri & Bake, 2017; Lahiri et al., 2011) measurement data (green upright triangles). It also shows that the peak absorption profile shifts towards the low-frequency range. It can be noted that keeping the percentage of porosity (0.16 %) low, with a larger axial pitch distance (22mm) and a small orifice diameter (1mm), has failed to produce a better absorption profile. It is necessary to optimise the axial pitch distance with orifice diameter to form a better interaction area of a real combustor design. Configuration 4 has a larger axial pitch distance compared to the smaller orifice diameter; the cylindrical combustor liner peak absorption shifts towards the low-frequency range, backing both the model and Lahiri et al.'s (Lahiri, 2014; Lahiri & Bake, 2017; Lahiri et al., 2011) measurements. Meanwhile, cot function with cavity factor (solid pink line) developed a greater peak compared to the measurement shown in Figure 5.7.

5.7 Configuration 5 comparison of predictions with data

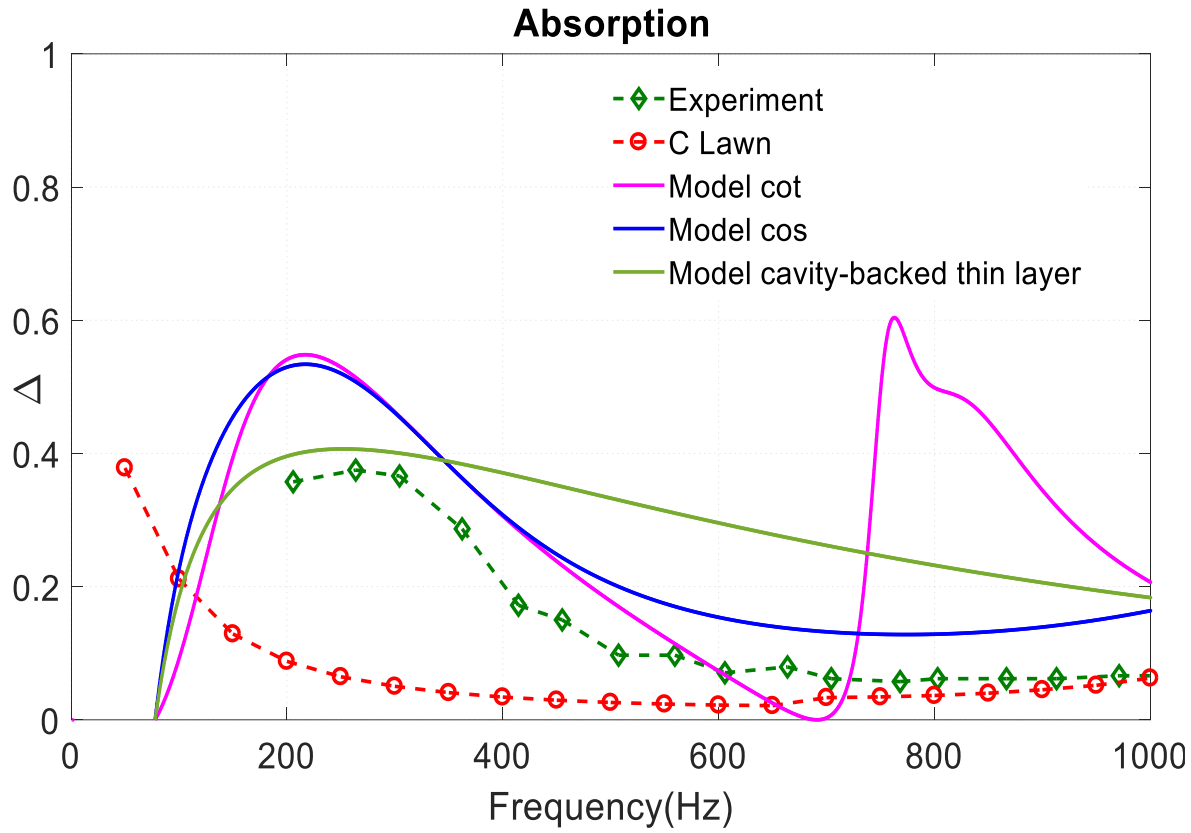

Figure 5.8 Configuration 5 model assessment with experiment.

Configuration 5 represents a double-layered combustor liner, with a combination of inner and outer liners. The inner liner, known as the damping liner, is configuration 1. The outer liner, known as the metering liner, has a 162 mm diameter, 42 mm liner length, 1 mm orifice diameter, and 14 mm axial pitch distance, which refers to 0.4 % porosity. Each liner has 1 mm thickness, and the distance between the liners d' is 11 mm, which is responsible for creating the damping volume. Figure 5.8 shows the comparison of predictions for configuration 5, and the solid blue line has shaped an identical absorption profile compared to the Lahiri et al. (Lahiri, 2014; Lahiri & Bake, 2017; Lahiri et al., 2011) measurement (diamond-shaped green dotted line). However, the prediction is slightly greater than the measurement. Chris Lawn's (Lawn, 2015) (red dotted line with circle marker) model seems to agree with the measurement only in the high-frequency range. Model cot function with cavity factor (solid pink line) fails at high frequencies. An alternative cavity impedance model for the double liner equation (2.11), discussed previously in section 2.1.2, shows that the cavity-backed thin layer

(solid green line) developed a reasonable agreement with the measurement in the low-frequency range.

5.8 Configuration 6 comparison of predictions with data

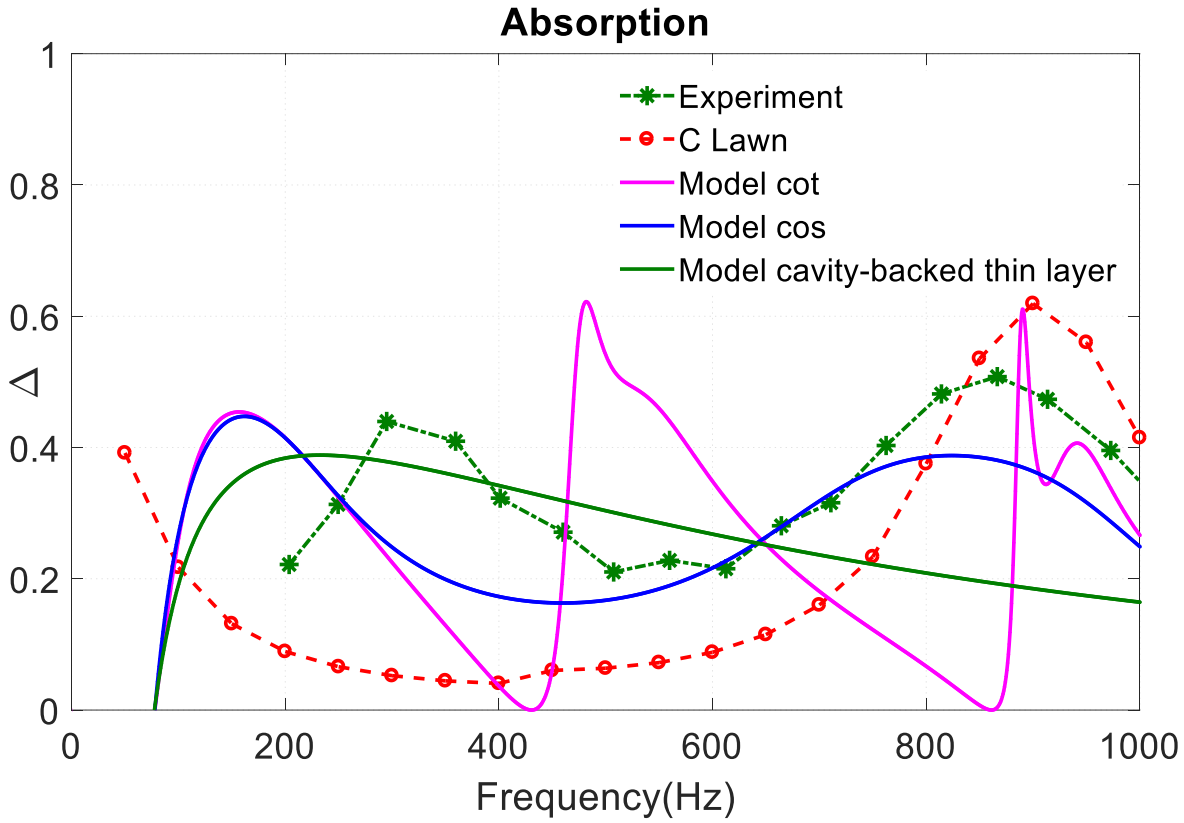

Figure 5.9 Configuration 6 model assessment with experiment.

Configuration 6 represents a double layered combustor liner. The inner liner is configuration 1, and the metering liner has a 192 mm diameter, 51 mm liner length, 1 mm orifice diameter and 16 mm axial pitch distance, which refers to 0.31 % porosity. Each liner has 1 mm thickness. Figure 5.9 shows configuration 6's comparison of predictions. The blue solid line has an identical absorption profile with Lahiri et al.'s (Lahiri, 2014; Lahiri & Bake, 2017; Lahiri et al., 2011) measurements (green asterisked dotted line). However, there is slight shift in peak to the right when compared with the measurement. The degree of agreement in peaks between the model and experimental data for this configuration is not particularly precise as the percentage of porosity (0.31 %) of the outer liner is exceptionally low due to the small orifice diameter and high axial pitch distance. Static pressure measurements carried out in UHARC suggest that the liner having the lowest percentage of porosity is responsible for drawing a pressure curve. Therefore, attached masses of the adjacent orifices are combined so that effective mass is reduced due to the loss of shear region when oscillation through both orifices

is in phase. This present model, interaction end correction term, displays the effect of reactance when porosity is very low. Meanwhile, once again, the model cot function with cavity factor (pink solid line) does not show a decent agreement with Lahiri et al.'s (Lahiri, 2014; Lahiri & Bake, 2017; Lahiri et al., 2011) measurement. Chris Lawn's (Lawn, 2015) (red dotted line with circle marker) model, however, appears to partially agree with the measurement in the high-frequency range. Moreover, an alternative cavity impedance model, cavity-backed thin layer (solid green line), seems to have a partial agreement with the measurement.

5.9 Configuration 7 comparison of predictions with data

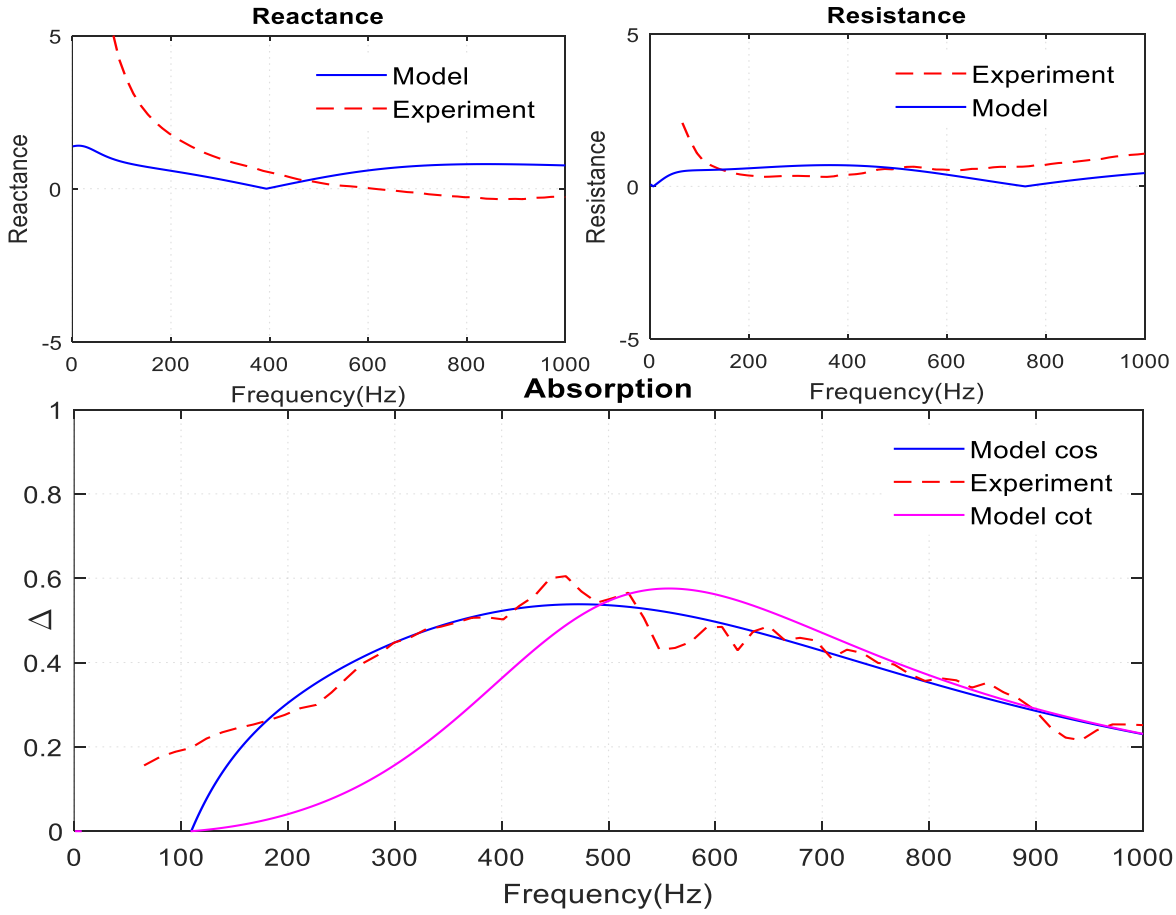

Figure 5.10 Configuration 7 model assessment with experiment.

Configuration 7 is a single liner combustor, which has 161.5 mm liner diameter, 1.6 mm thickness, 524 mm liner length, uniform pattern of 0.875 mm orifice diameter, and 9 mm axial pitch distance, which refers to 0.74 % of porosity. Figure 5.10 shows the prediction of configuration 7 with the experiment. The model cos (blue solid line) and cot (pink solid line) function with cavity factor represents a decent agreement with the experiment (red dotted

line). Modelling techniques are used in order to estimate liner absorption or dissipation performance, while comparisons among some of those models or techniques have been applied. On the other hand, semi-empirical hybrid models have been developed and compared to the various models to obtain greater accuracy with the experiment shown in Figure 5.10. The acoustic resistance and reactance of such kinds of liners are commonly understood to affect the intensity of the sound incident upon the panel. Since the pressure drop across the perforated liner increases with the bias flow velocity through the liner, this can be expressed as nonlinear resistance effect (Melling, 1973b). In this context, a semi-empirical frequency domain model has been used to predict the impedance of the incident wave on the magnitude of the reflection, which uses cotangent and cosine functions with cavity factor for the no flow case. This present model can predict liner resistance and reactance terms, along with the absorption profile, which is measured for typical perforated liners shown in Figure 5.10. Recently published, Chris Lawn's (Lawn, 2015) model is established based on acoustic pressure and velocity variables, and their ratio. The acoustic impedance is computed sequentially from one end of the duct to the other, so that the total length of the liner (59-66 mm) is considered based on Lahiri et al.'s (Lahiri, 2014; Lahiri & Bake, 2017; Lahiri et al., 2011) measurement geometry. The current investigated liner length (504-524 mm) is eight times larger than Chris Lawn's (Lawn, 2015) computation, and therefore Chris Lawn's (Lawn, 2015) model is incapable of predicting the absorption profile. This can be designated as a limitation of Chris Lawn's (Lawn, 2015) computation. A snapshot of configuration 7 suggests that equation (3.22) fits much better with the experiment. The cot function with the cavity factor equation (3.21) indicates a reasonable agreement with the experiment in the high-frequency range. The data from the experiment almost remains in between the predictions in the low-frequency range, thus their relation can be demonstrated in further analysis.

5.9.1 Configuration 7 signal analysis

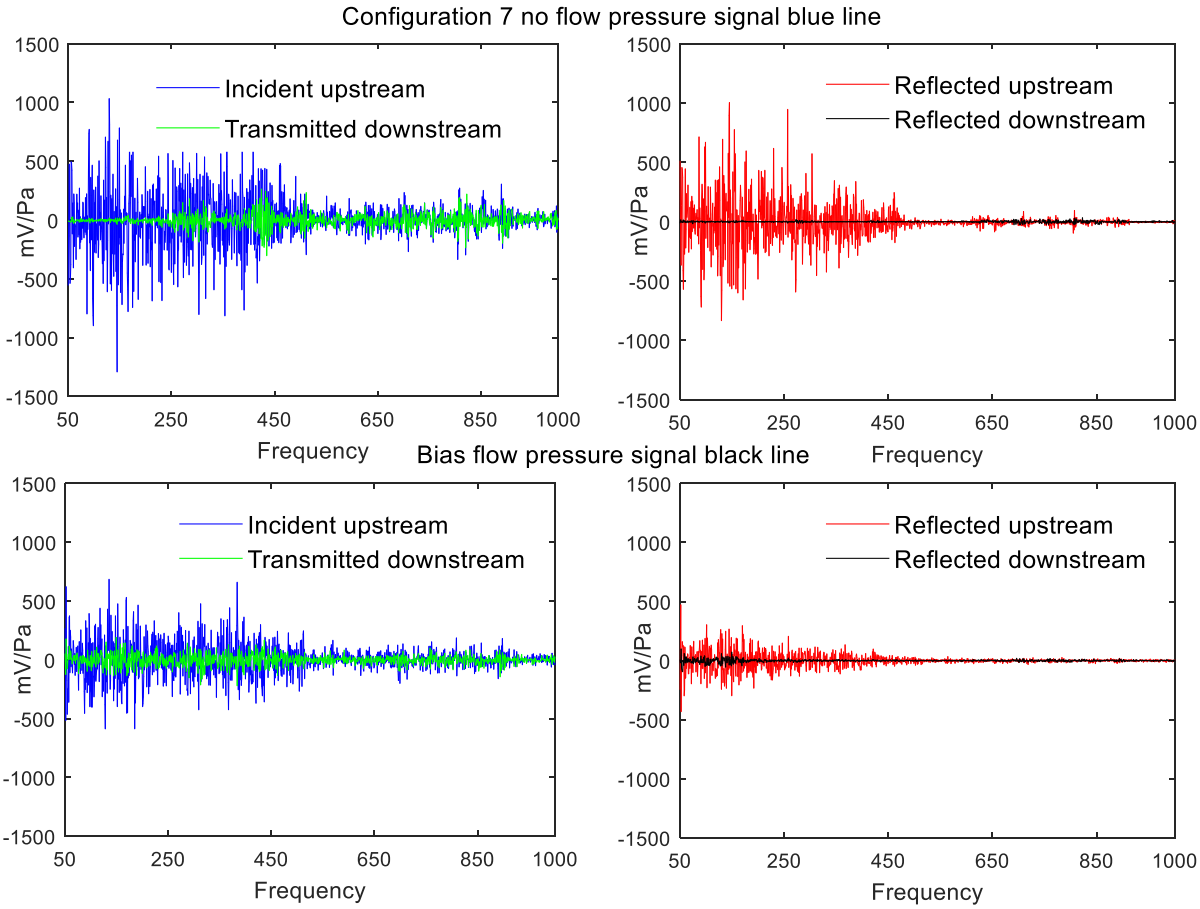

Figure 5.11 Configuration 7 no flow and non-zero bias flow signal analysis.

Figure 5.11 shows the no flow pressure signal (blue line) at the top, and non-zero bias (black line) at the bottom. As previously mentioned in section 4.13.1, the black line represents the maximum absorption profile. The no flow signal analysis refers to the capture of acoustic pressure only, and the bias flow signal analysis refers to the capture of acoustic pressure with flow. The primary objective of this investigation is to analyse the suppression of the acoustic pressure signal in the presence of bias flow, along with transmitted and reflected downstream pressure signals. This current semi-empirical hybrid model absorption profile is developed from the definition of reflection coefficient only; transmission coefficient is disregarded. For the no flow case, a large amount of incident upstream pressure signal is recorded in the low-frequency range, whereas reflection upstream is almost half of the incident upstream pressure signal. In the downstream section, the transmitted signal is low up to 250 Hz; however, following that, up to 500 Hz it creates an impulsive variation. Henceforth, there appears to be a minor difference in the incident and transmitted pressure signals in the high-frequency range. In the downstream section, the reflected pressure signal exhibits a flat line.

For the non-zero bias flow case, the black line pressure analysis shows that in the presence of bias flow the overall incident upstream and transmitted downstream pressure signal decreases, despite the increased transmitted pressure signal in the low-frequency range. The reflected upstream pressure signal decreases significantly when compared with the no flow case, while the reflection downstream signal increases.

5.9.2 Configuration 7 energy analysis

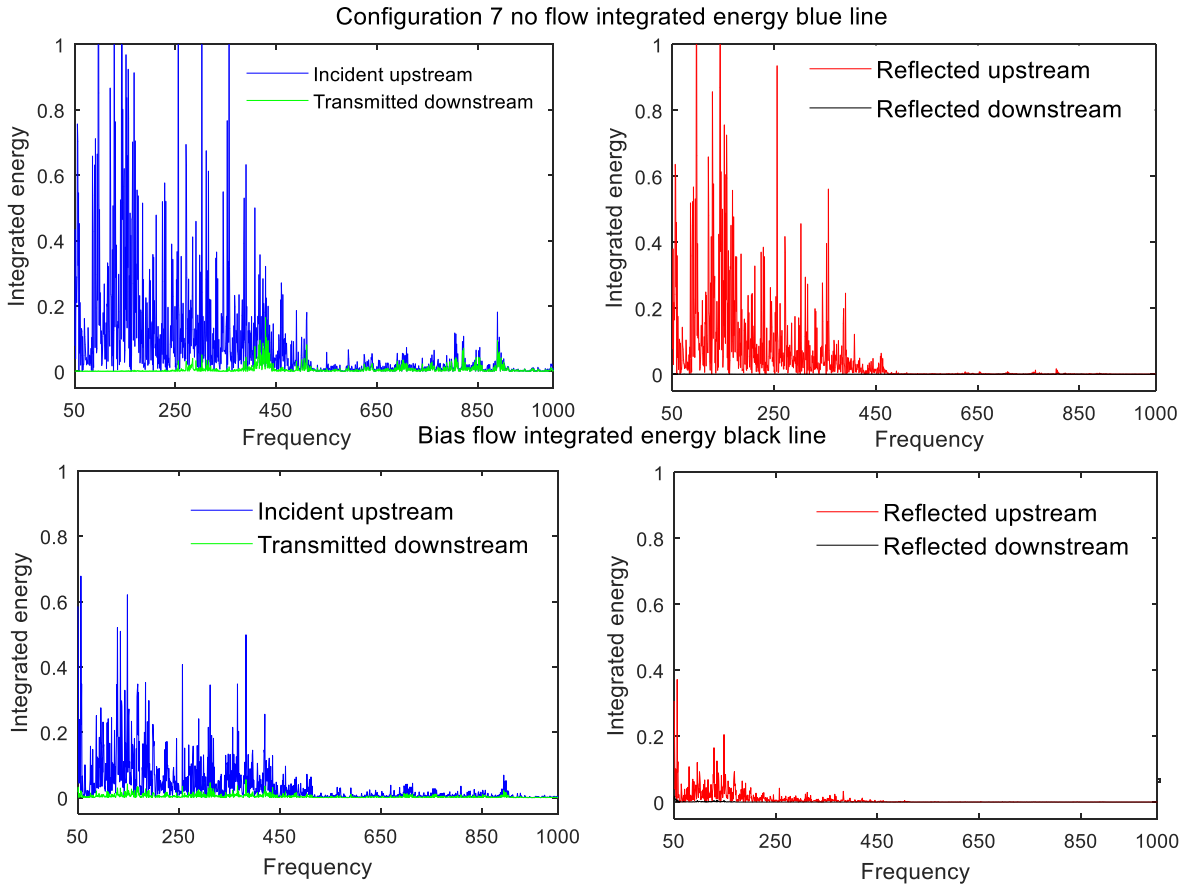

Figure 5.12 Configuration 7 integrated energy assessment.

Figure 5.12 shows the integrated energy assessment for configuration 7, with the no flow (blue line) at the top and the bias flow integrated energy (black line) at the bottom. Due to the nature of this experiment, signal detection is very high below 50 Hz; therefore, overall integrated energy balance calculation is carried out from 50-1000 Hz. Anechoic termination below 150 Hz is ineffective (Kang & Jung, 2001). For the no flow case, an integrated energy assessment shows that incident upstream energy is high compared to the transmitted downstream energy. Furthermore, it demonstrates that reflected upstream energy is high compared to the reflected downstream energy. For the impact of a non-zero bias flow case, the same constant sound pressure levels have generated low incident upstream, reflected

upstream and transmitted downstream energy when compared with the no flow. The overall transmitted and reflected downstream energy is minimal compared to the incident and reflection upstream energy. Configuration 7's overall energy balance calculation is provided in Table 5.1.

5.10 Configuration 8 comparison of predictions with data

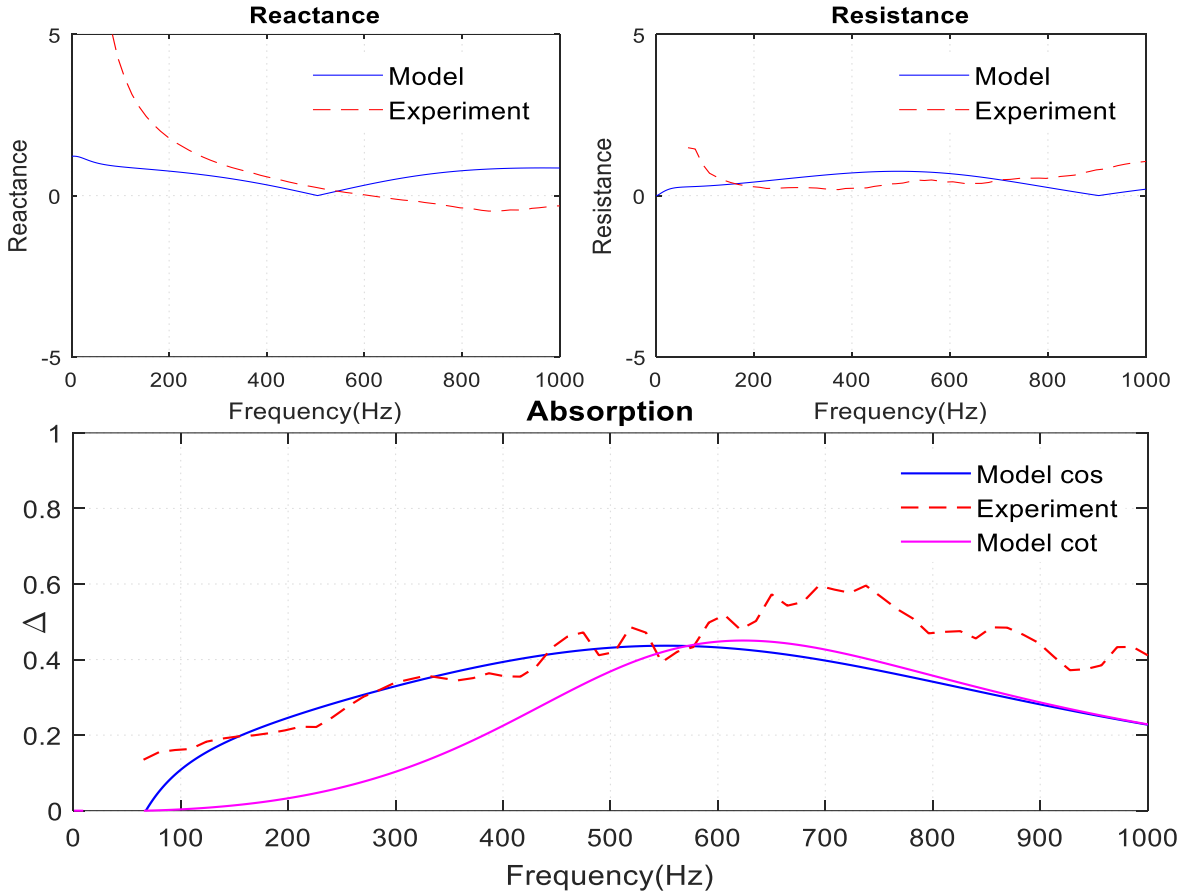

Figure 5.13 Configuration 8 model assessment with experiment.

In configuration 8, the geometric parameters are not unlike configuration 7, excepting the orifice diameter, which is increased to 1.125 mm and refers to the increase in porosity. Figure 5.13 shows the comparison of predictions, and the blue (3.22) and pink (3.21) solid lines exhibit a reasonable agreement with the experiment (red dotted line). In the low-frequency range, both the experiment and model overlapped the blue solid line up to 600 Hz. Nevertheless, in the high-frequency range, experimental data shows greater than the prediction. The model cot function with cavity factor (pink line) appears to have a partial agreement with the experiment. It intersects around 550-600 Hz, and beyond 600 Hz the model pink and blue solid lines display an identical profile. Configuration 8 has formed a slightly different type of absorption profile compared to the other configurations. It also

demonstrates that liner resistance and reactance term exhibit a reasonable agreement with the experiment.

5.10.1 Configuration 8 signal analysis

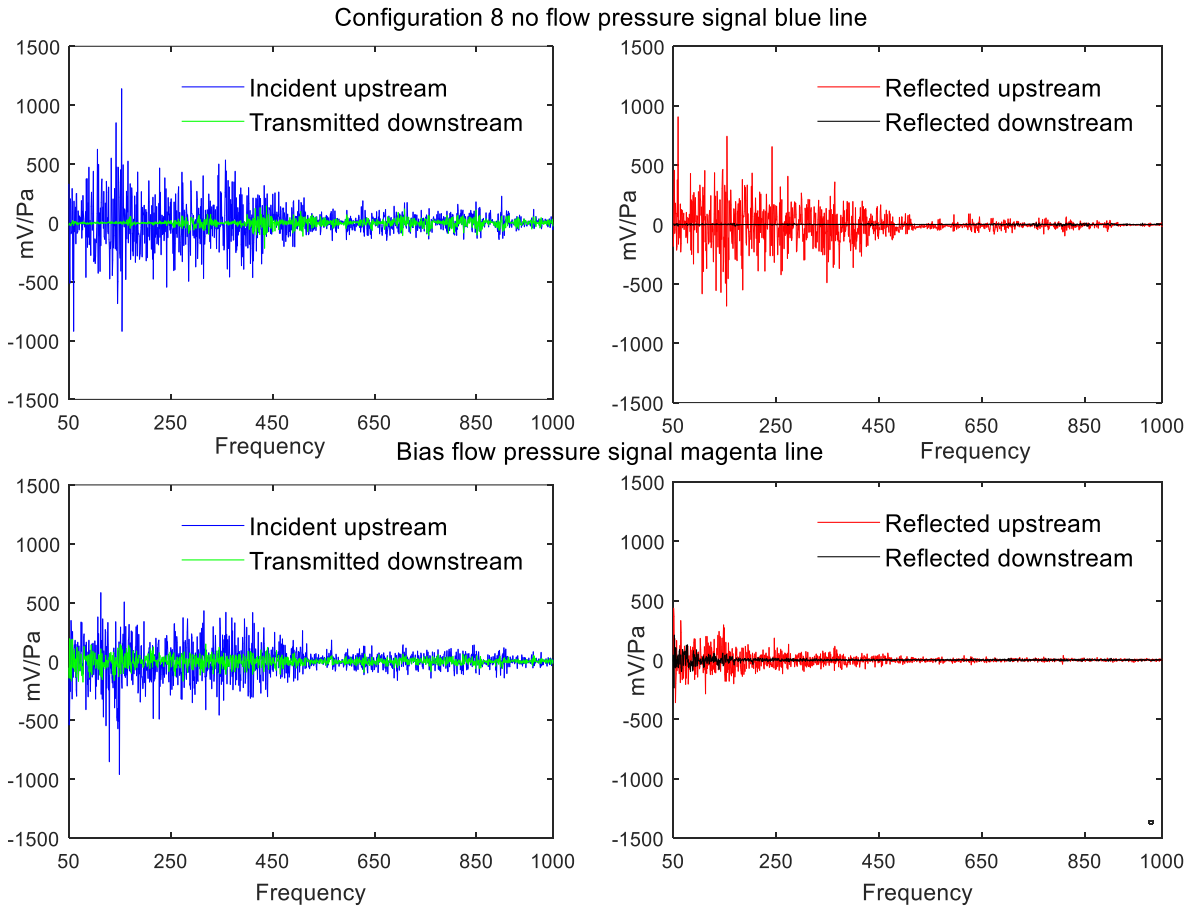

Figure 5.14 Configuration 8 no flow and non-zero bias flow signal analysis.

Figure 5.14 shows the no flow pressure signal (blue line) at the top, and the non-zero bias flow (magenta line) at the bottom. The magenta line represents the maximum absorption profile for configuration 8, as previously discussed in section 4.14.2. For the no flow case, the overall incident upstream pressure signal is high, and the transmitted downstream pressure signal is low compared to the bias flow case, shown by the magenta line. It also shows that reflection is nearly two-thirds of the incident in the upstream section. For the non-zero bias flow case, the pressure signal of the magenta line shows that the overall incident upstream pressure signal has decreased, whilst the transmitted pressure signal has increased compared to the no flow condition. In addition, the reflected upstream pressure signal has decreased compared to the no flow condition, whilst reflected downstream has increased.

5.10.2 Configuration 8 energy analysis

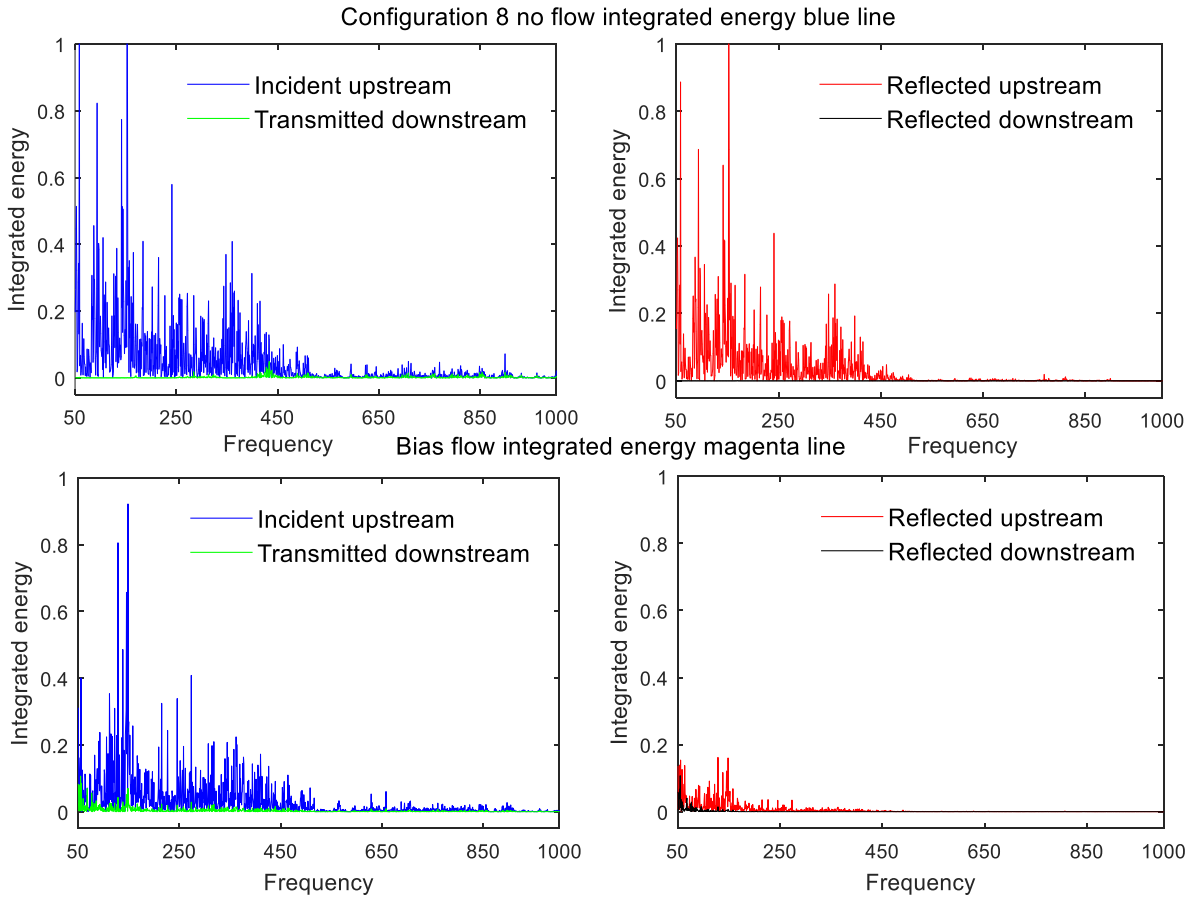

Figure 5.15 Configuration 8 integrated energy assessment.

The integrated energy assessment for configuration 8 is shown in Figure 5.15, with the no flow (blue line) at the top, and the non-zero bias flow (magenta line) at the bottom. For the no flow case, integrated energy analysis demonstrates that transmitted energy is low compared to the incident energy. It also exhibits that upstream reflected energy is high due to low transmitted energy in the downstream section in a single liner combustor. For the non-zero bias flow case, the magenta line represents a pressure ratio of 0.15 % and orifice hole velocity 15.71 m/s, while formation of incident and reflected upstream energy decreases. Meanwhile, transmitted and reflected downstream energy increases compared to the no flow condition. Configuration 8's overall energy balance calculation is presented in Table 5.1, which indicates that either the black or magenta line exhibits a broadband frequency range of absorption, which has been previously discussed in section 4.14.2.

5.11 Configuration 9 comparison of predictions with data

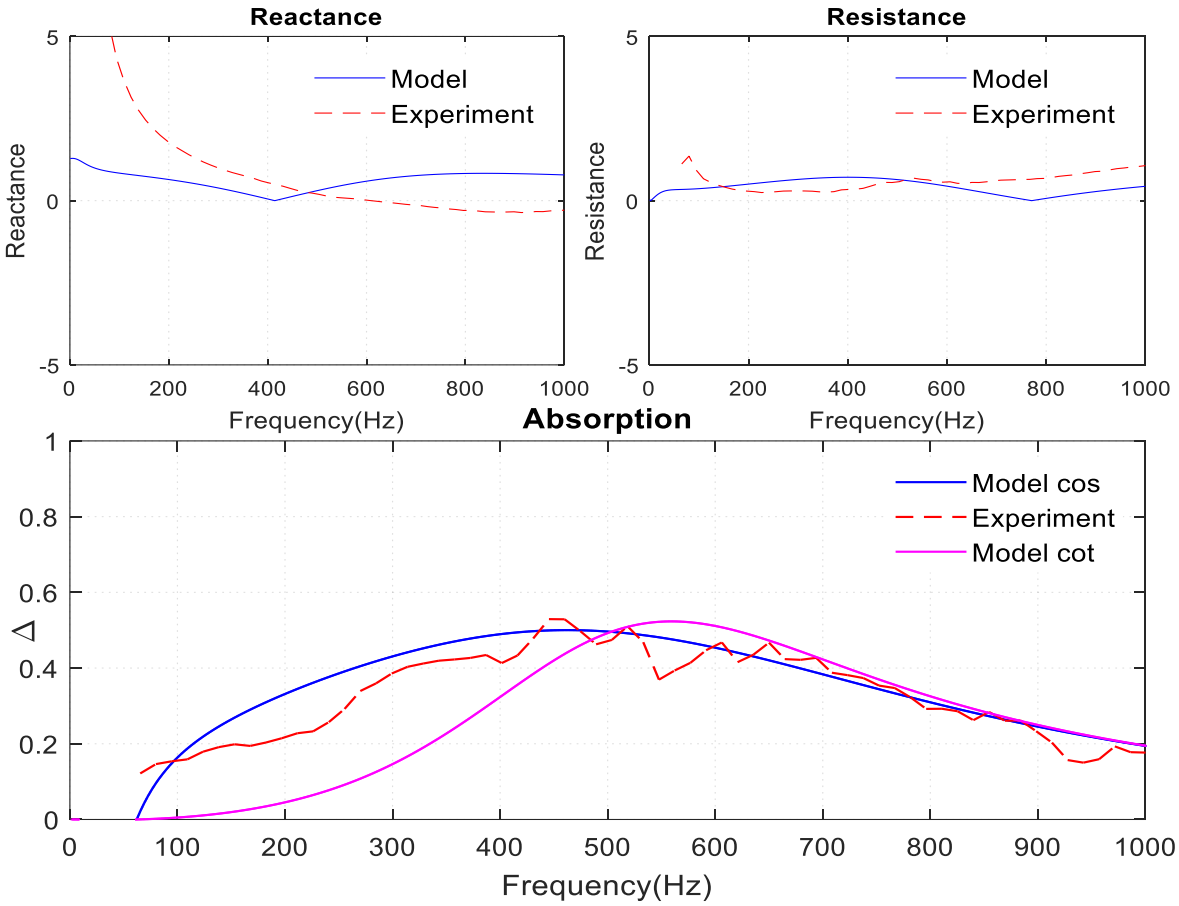

Figure 5.16 Configuration 9 model assessment with experiment.

Configuration 9 has a wall thickness of 2 mm, orifice diameter 1.175 mm, 2256 orifices, and an axial pitch distance of 10.5 mm, which refers to 0.98 % of porosity. Figure 5.16 shows the prediction of configuration 9 with the experiment - the blue solid line demonstrates an excellent agreement, whereas the pink solid line displays a similar profile in the high frequency range. The absorption spectra for the no flow case between the experiment and predictions are acceptable. However, the critical mapping of the cavity factor needs to be adjusted with the cavity diameter of the test rig. This cavity factor primarily depends on test rig boundary conditions, such as cavity depth d. The values of single- and double-layer liner cavity factors are established from equation (3.16), and their values are presented in Table 4.5. Single liner resistance and reactance terms appear to display a reasonable agreement with the experiment, shown in Figure 5.16.

5.11.1 Configuration 9 signal analysis

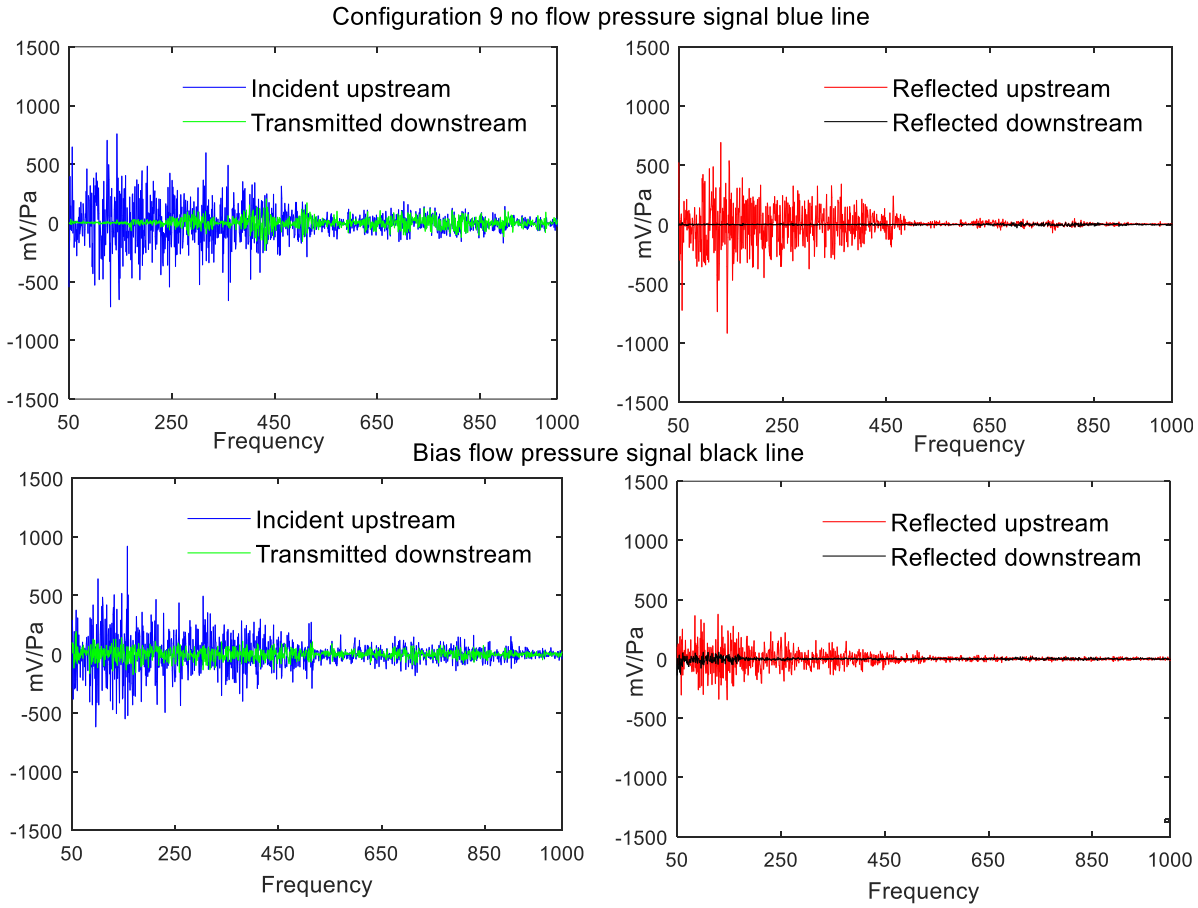

Figure 5.17 Configuration 9 no flow and non-zero bias flow signal analysis.

Figure 5.17 shows no flow (blue line) at the top, and non-zero bias flow (black line) at the bottom. For the no flow case, the incident upstream pressure signal is slightly high when compared with the transmitted downstream pressure signal in the low-frequency range. Also evidenced, the reflection upstream is nearly two-thirds of the incident upstream pressure signal. For the non-zero bias flow case, the incident upstream pressure signal decreases, whilst the transmitted downstream pressure signal increases. It can also be seen that the reflected upstream pressure signal decreases when compared with the no flow condition, while the reflected downstream pressure signal increases.

5.11.2 Configuration 9 energy analysis

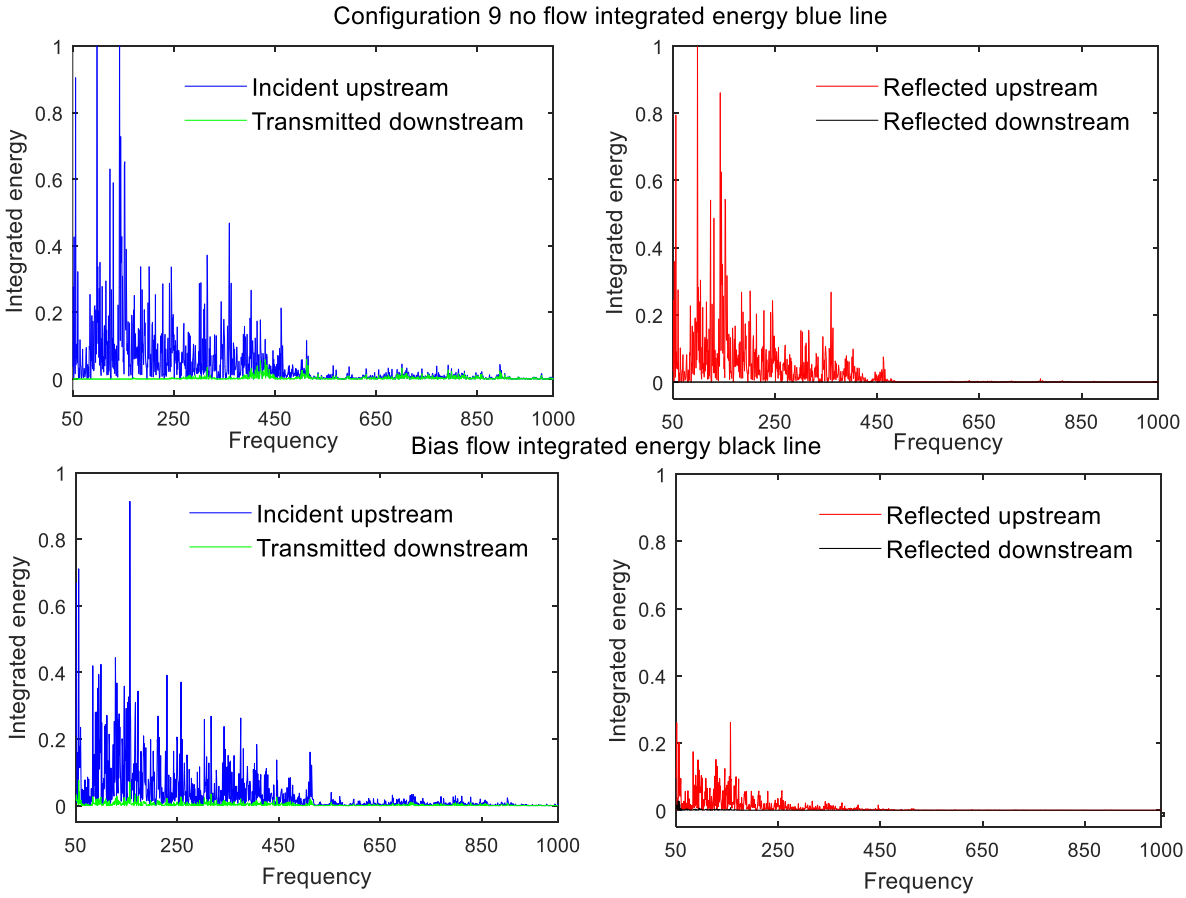

Figure 5.18 Configuration 9 integrated energy assessment.

The single liner integrated energy assessment for configuration 9 is shown in Figure 5.18, with no flow (blue line) at the top and non-zero bias flow (black line) at the bottom. For the no flow case, the integrated energy analysis shows that transmitted downstream energy is low compared to the incident upstream energy. It can also be seen that reflected upstream energy is high; hence the decrease in transmitted energy in the downstream section. For the non-zero bias flow case, the black line demonstrates that incident and reflected upstream energy decreases, while transmitted and reflected downstream energy increases when compared with the no flow condition. The absorption (black line) spectra are broadband, which was discussed earlier in section 4.14.3. The overall energy balance calculation of configuration 9 is presented in Table 5.1.

5.12 Configuration 10 comparison of predictions with data

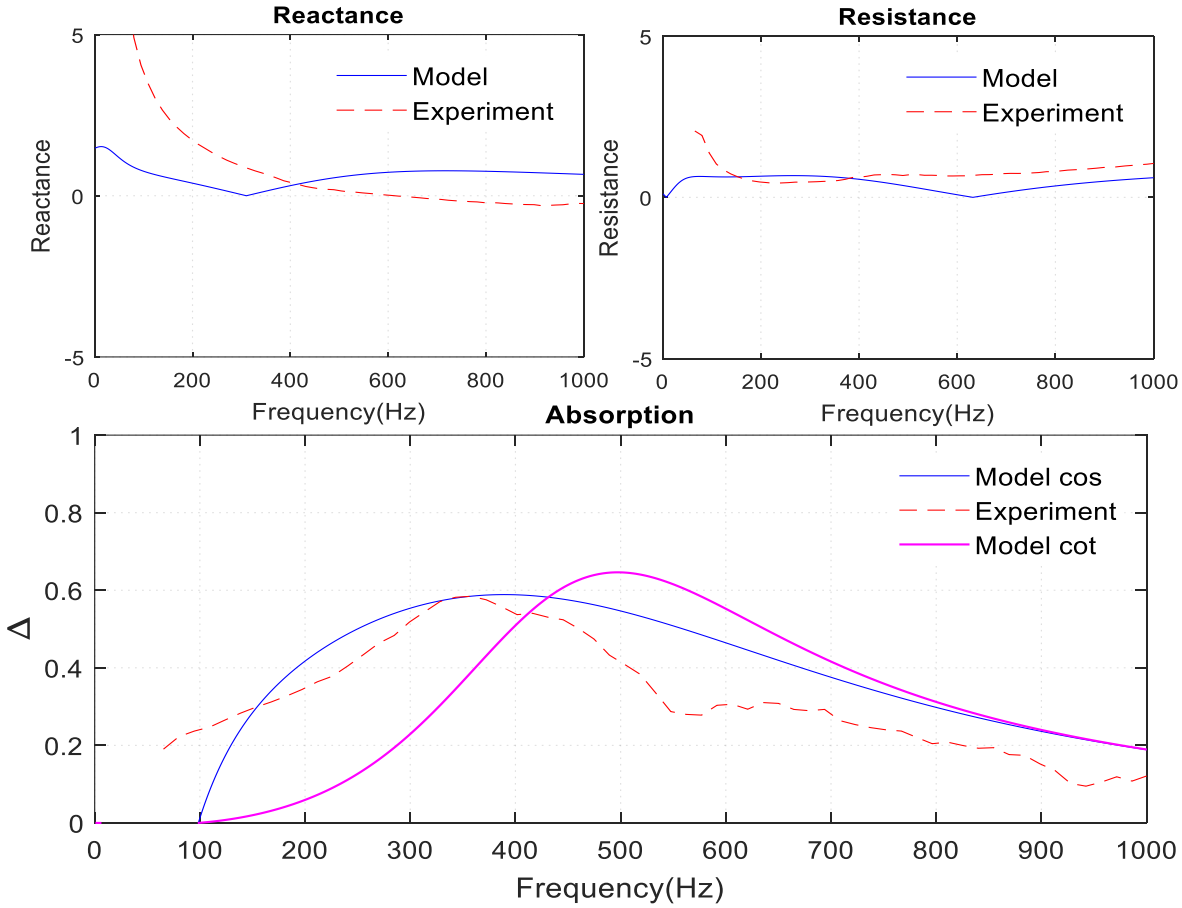

Figure 5.19 Configuration 10 model assessment with experiment.

Configuration 10's single liner geometric parameters are similar to configuration 9's, apart from the decrease in orifice diameter to 0.925 mm, and a decrease in porosity to 0.61 %. Figure 5.19 shows configuration 10's comparison of prediction with the experiment. The model cos function with cavity factor agrees well with the experiment. Due to a decrease in porosity compared to configuration 9, single liner combustor configuration 10 has developed a peak, which shifts towards the low-frequency range along with the experiment. The model cot function with cavity factor appears to have a greater peak, with it reaching 500 Hz, which shows a slight disagreement with the experiment. In addition, this semi-empirical hybrid model can predict the liner resistance and reactance characteristics, which is shown at the top of Figure 5.19.

5.12.1 Configuration 10 signal analysis

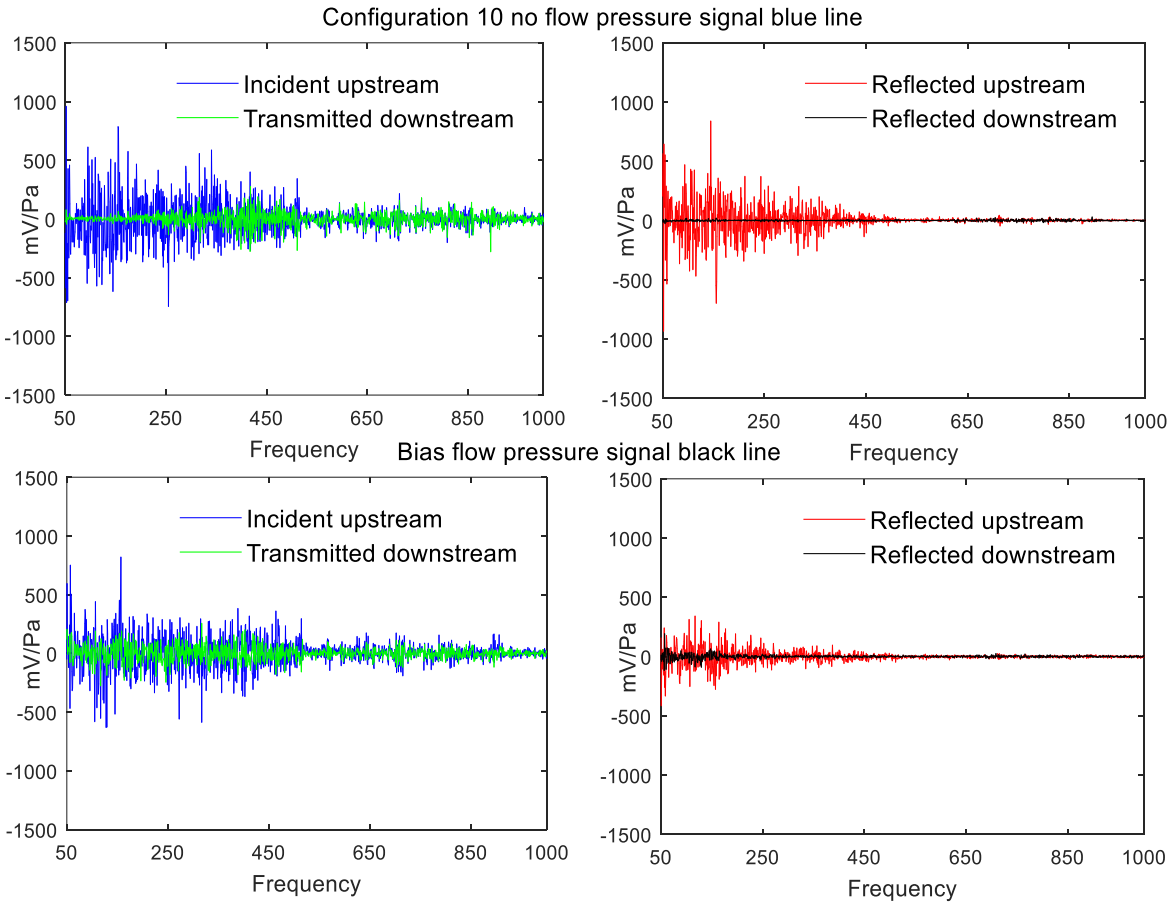

Figure 5.20 Configuration 10 no flow and non-zero bias flow signal analysis.

Figure 5.20 shows no flow (blue line) at the top and non-zero bias flow (black line) at the bottom. Configuration 10's single liner pressure signal analysis is presented in terms of mV/Pa with respect to frequency. For the no flow case, the signal analysis shows that the incident upstream pressure signal is large compared to the transmitted and reflected downstream section. It also displays that in the high-frequency range the incident upstream and transmitted downstream pressure signals are similar, and below 250 Hz the transmitted downstream pressure is low compared to the incident upstream pressure. For the non-zero bias flow case, the black line pressure signal illustrates that in the presence of bias flow the incident and reflected upstream pressure signal decreases, while the overall transmitted pressure signal has increased. Additionally, the reflected pressure signal has decreased when compared with the no flow condition.

5.12.2 Configuration 10 energy analysis

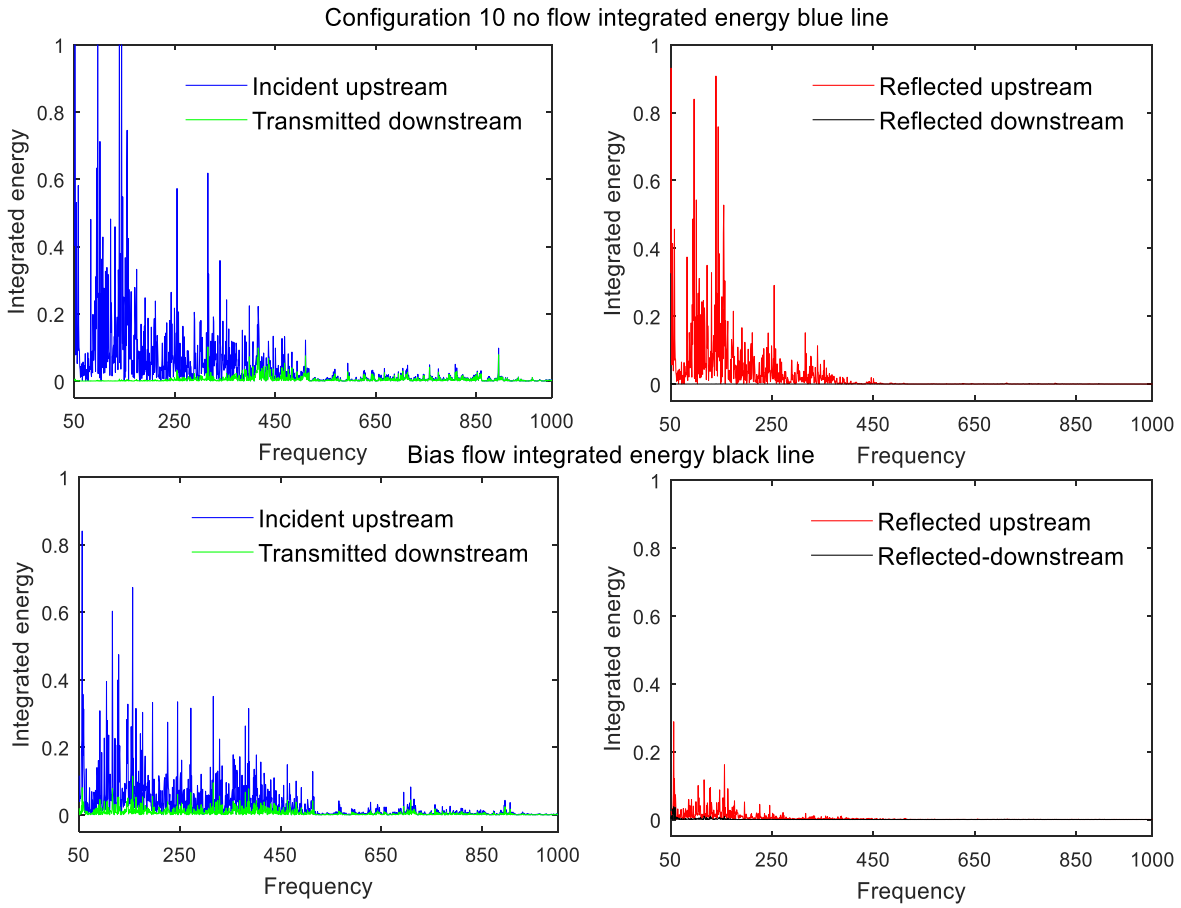

Figure 5.21 Configuration 10 integrated energy assessment.

Configuration 10's single liner integrated energy assessment is shown in Figure 5.21, with the no flow (blue line) at the top, and non-zero bias flow (black line) at the bottom. For the no flow case, the integrated energy analysis demonstrates that transmitted downstream energy is low compared to the incident upstream energy. Furthermore, it shows that reflected upstream energy is high compared to the reflected downstream energy. For the non-zero bias flow case, the black line absorption profile indicates that the formation of incident and reflected upstream energy decreases. Meanwhile, transmitted downstream energy increases when compared to the no flow condition. The overall energy balance calculation for configuration 10 is shown in Table 5.1, which indicates that either the red or black line has displayed a maximum absorption profile, previously discussed in section 4.14.4.

5.13 Configuration 11 comparison of predictions with data

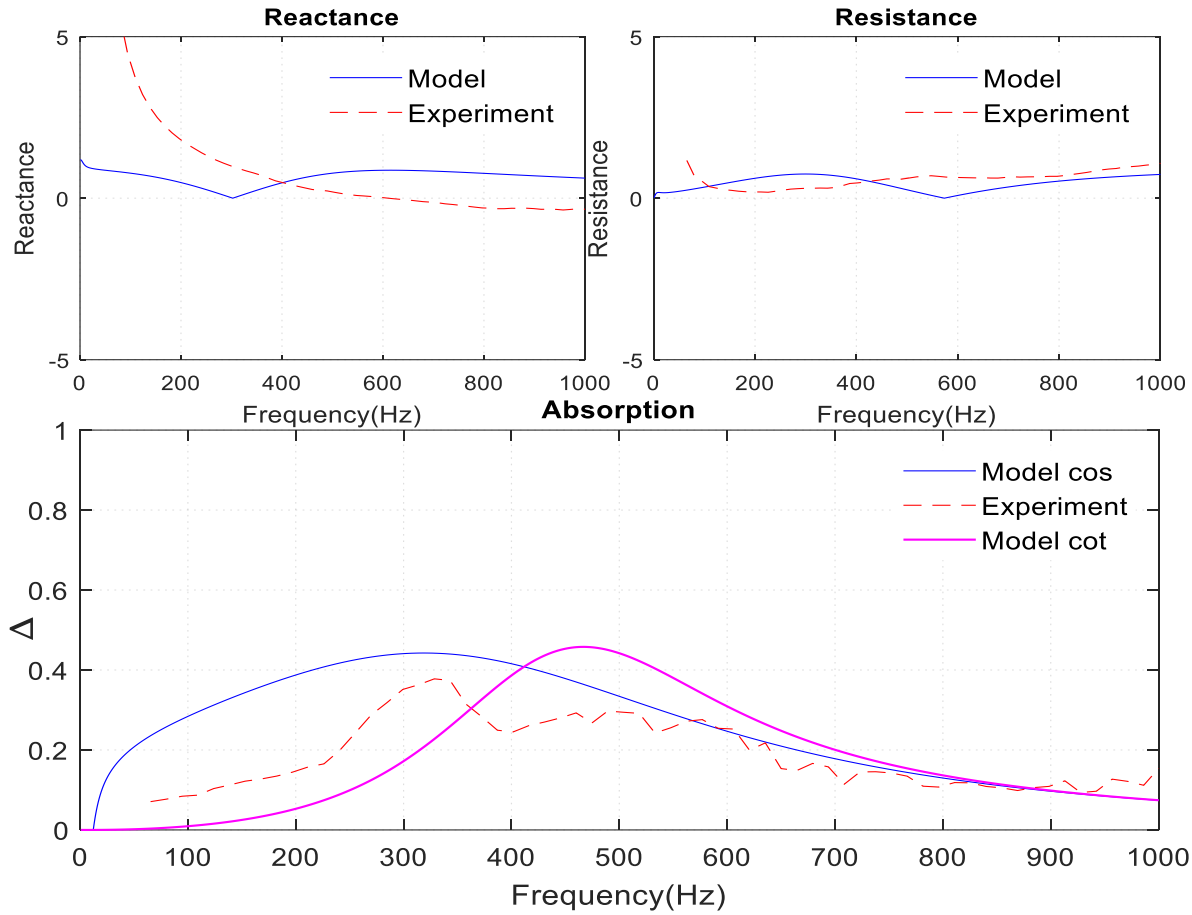

Figure 5.22 Configuration 11 model assessment with experiment.

Configuration 11 is a single liner combustor, which acts as a metering liner. It has 176.5 mm liner diameter, 504 mm liner length, 2.675 mm orifice diameter, and 20 mm axial pitch distance, which refers to 1.41 % porosity. For the no flow case, configuration 11's acoustic analysis is discussed in section 4.14.5, and its absorption profile is labelled as a solid blue line in Figure 4.12. Here it is represented as a dotted red line. Figure 5.22 shows that configuration 11's single liner experiment (red dashed line) appears to agree well with the prediction (solid blue line). Due to the change in geometry of this metering liner, both the prediction and experiment have introduced a similar absorption profile, but the prediction is slightly high in the low-frequency range. However, the increase in absorption with increasing frequency from the 0-300 Hz blue solid line compared with the experiment shows additional absorption is associated with the prediction. The difference in this computation with the experiment shows that considerably increasing the orifice diameter relates to the increase in porosity, yet a better absorption profile did not appear to be achieved with a higher axial pitch. The model

cot function with cavity factor (pink solid line) seems to have a slightly higher peak compared to the experiment in the region of 450-500 Hz.

5.13.1 Configuration 11 signal analysis

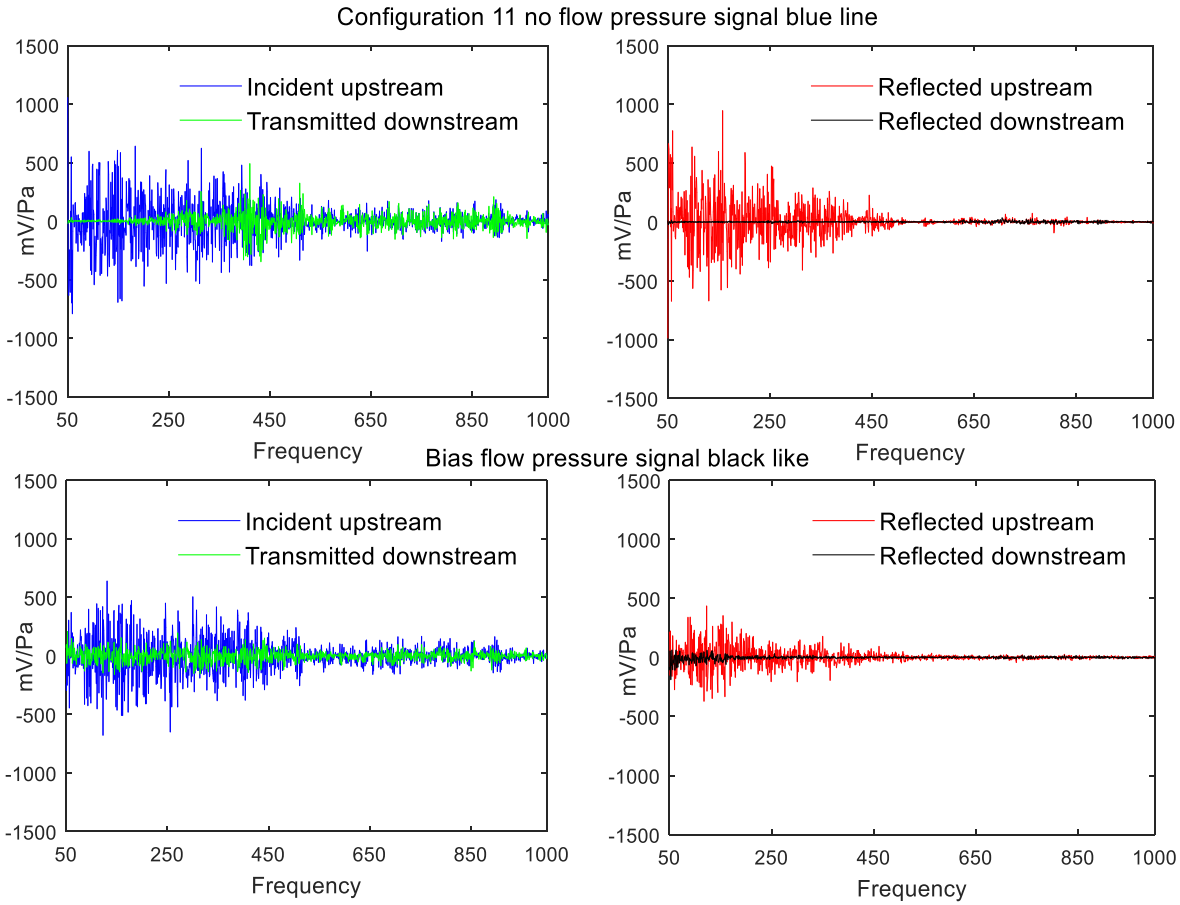

Figure 5.23 Configuration 11 no flow and non-zero bias flow signal analysis.

Figure 5.23 shows the no flow (blue line) at the top and non-zero bias flow (black line) at the bottom. For configuration 11, the outer liner signal analysis is shown in terms of mV/Pa with respect to frequency. For the no flow case, the overall signal analysis shows that incident upstream and reflected downstream pressure signals are large compared to the transmission and reflection downstream section. It also highlights that in the high-frequency range, the incident upstream and transmitted downstream pressure signals are close, yet below 250 Hz the transmitted downstream signal is extremely poor when compared to the incident upstream pressure. For the non-zero bias flow case, the black line pressure signal analysis illustrates that in the presence of bias flow, incident upstream and reflected downstream pressure signals have decreased. Meanwhile, the overall transmitted downstream pressure has decreased, and the reflected downstream pressure signal has increased when compared with the no flow condition.

5.13.2 Configuration 11 energy analysis

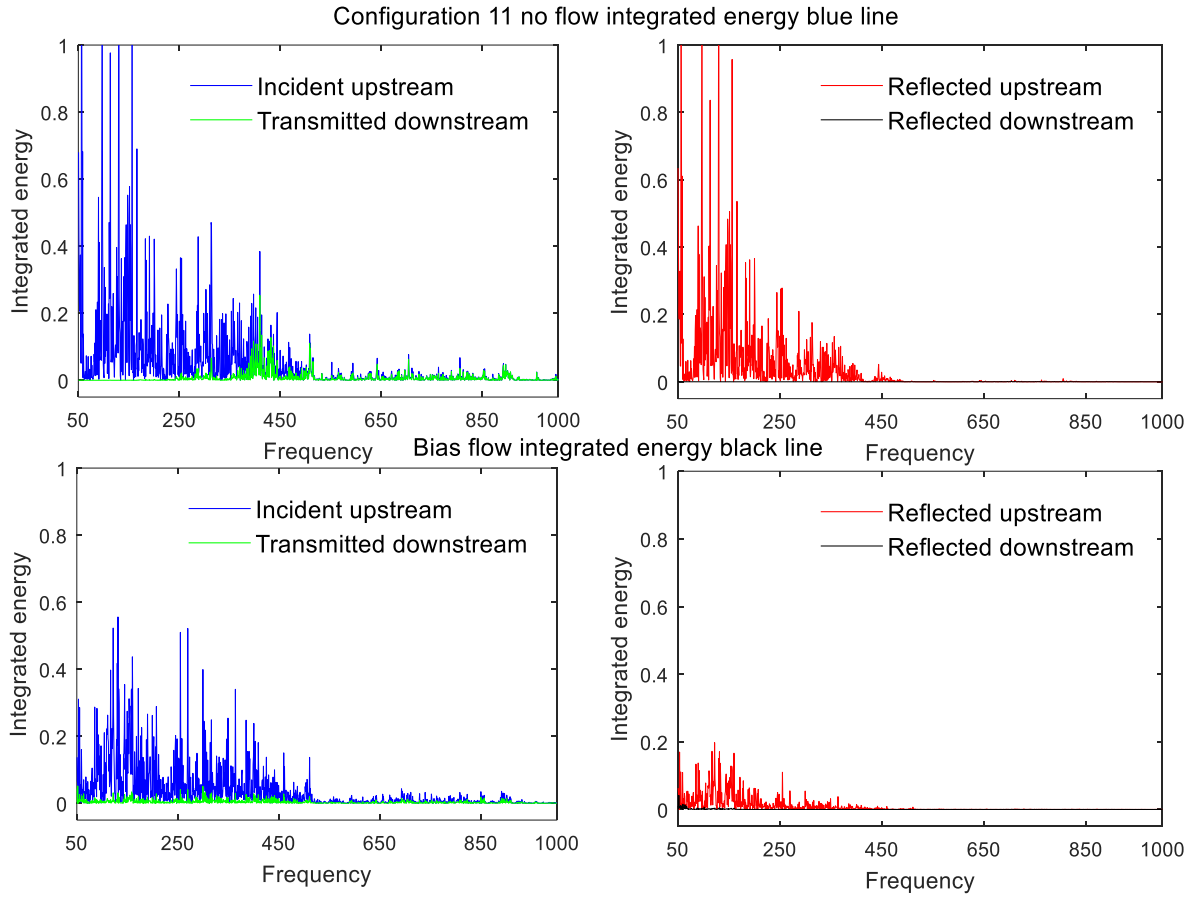

Figure 5.24 Configuration 11 integrated energy assessment.

Configuration 11's single liner integrated energy assessment is shown in Figure 5.24, with the no flow (blue line) at the top, and the non-zero bias flow case (black line) at the bottom. For the no flow case, integrated energy analysis indicates that transmitted downstream energy is low compared to the incident upstream energy. It also shows that reflected upstream energy is high; hence, the low transmitted energy in the downstream section. For the non-zero bias flow case, the black line represents that orifice hole velocity is 11.40 m/s, and the effect of bias flow decreases the incident and reflected energy in the upstream section. Similarly, in the downstream section, transmitted energy decreases and reflected energy increases compared to the no flow condition. The overall energy balance calculation is presented in Table 5.1, which shows the absorption spectra are not broadband for configuration 11, previously discussed in section 4.14.5.

5.14 Configuration 12 comparison of predictions with data

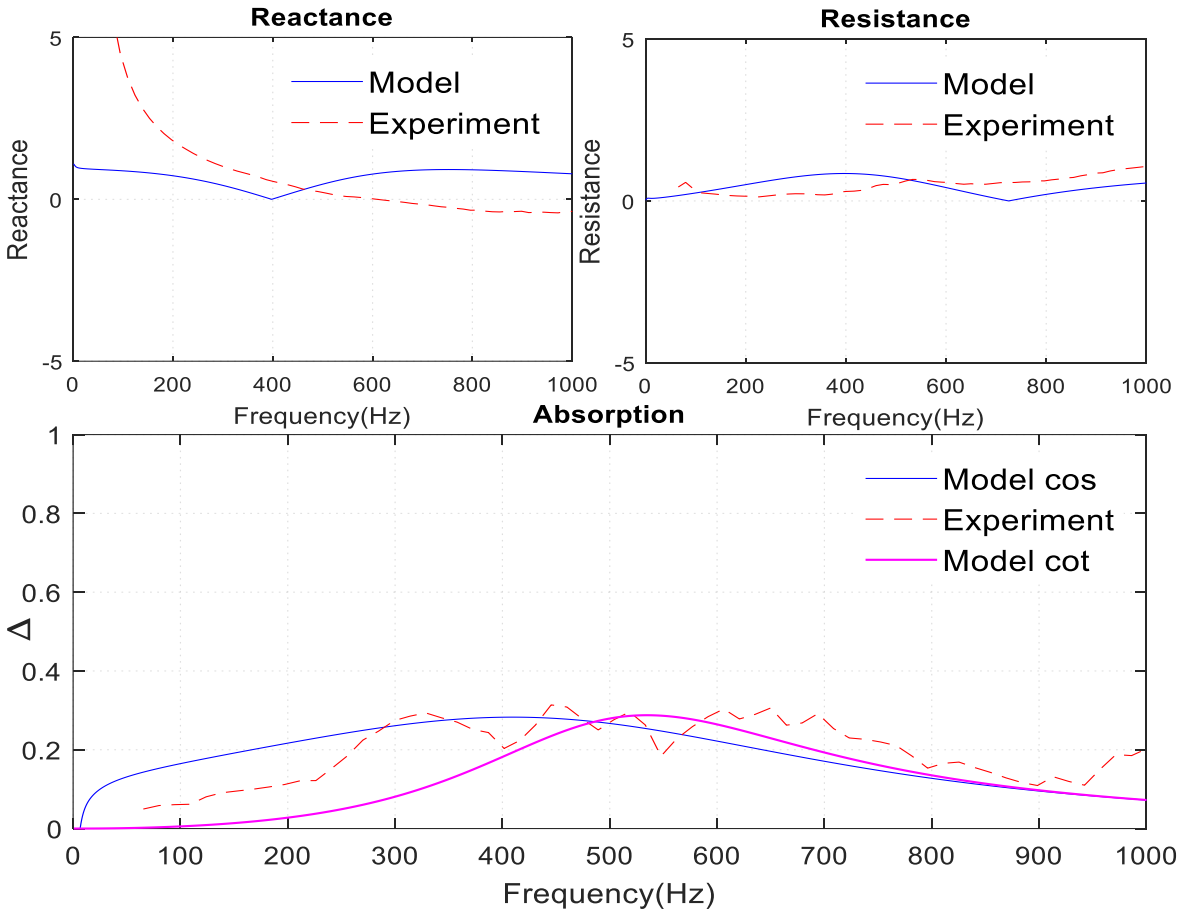

Figure 5.25 Configuration 12 model assessment with experiment.

Configuration 12 is similar to configuration 11 as both liners are designated as metering liners. It has 171.9 mm liner diameter, 504 mm liner length, 3.675 mm orifice diameter, and 20 mm axial pitch distance, which refers to 2.65 % of porosity. For the no flow case, configuration 12's acoustic analysis is discussed in section 4.14.6, and its absorption profile is labelled as a solid blue line in Figure 4.13. Here it is represented as a red dotted line. Figure 5.25 shows configuration 12's outer single liner experiment appears to have an acceptable agreement with the predictions. It is clear that the present computational results are acceptable and have the ability to predict the outcome of the experiment. Configurations 11 and 12 are greater in porosity when compared with the remaining single liner configurations, and their results are indicating a flat type absorption profile along with the predictions. It can also be seen that experimental outputs are remaining in between the pink and solid line in the low-frequency range.

5.14.1 Configuration 12 signal analysis

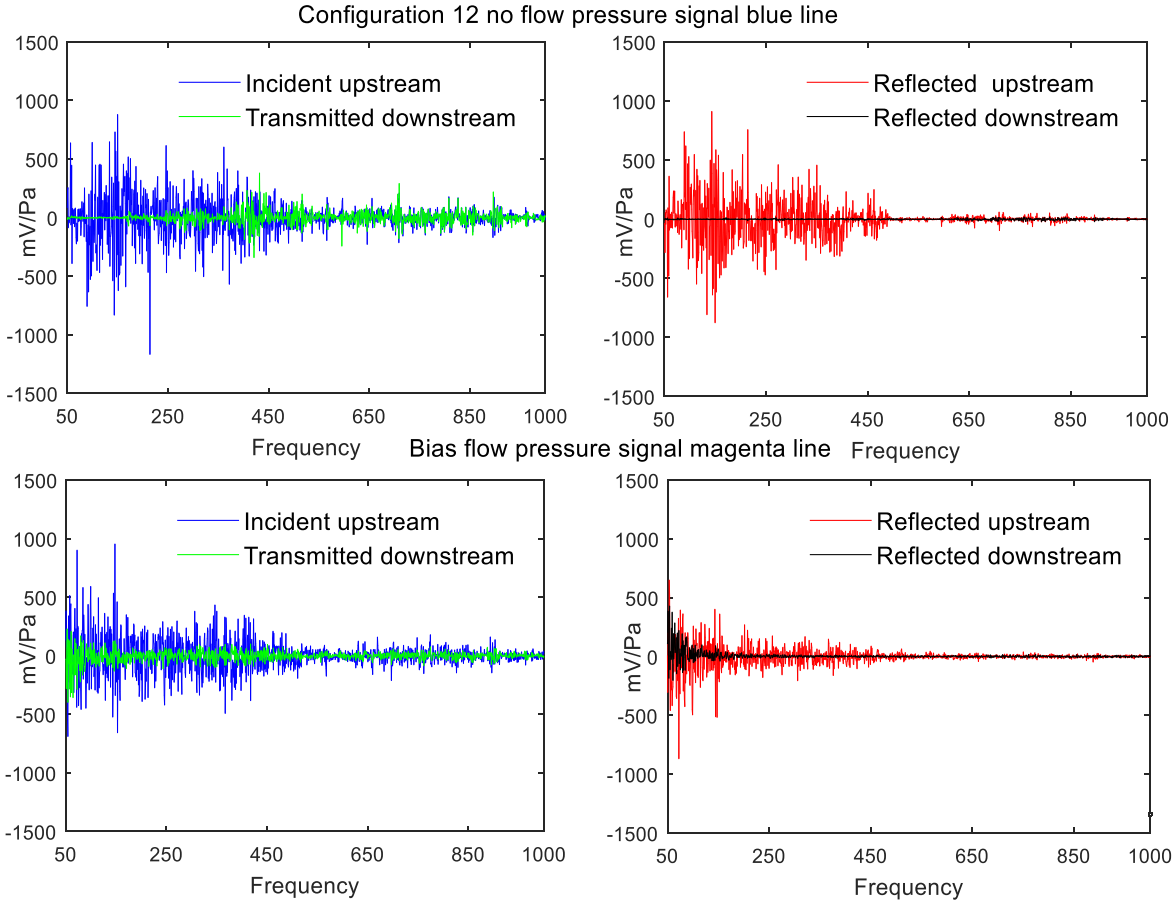

Figure 5.26 Configuration 12 no flow and non-zero bias flow signal analysis.

Figure 5.26 shows the no flow (blue line) at the top, and the non-zero bias flow (magenta line) at the bottom. Configuration 12's outer liner pressure signal analysis is expressed in terms of mV/Pa with respect to frequency. For the no flow case, the pressure signal shows that in the upstream section the incident and reflected pressure signal is large compared to the downstream transmission and reflection. It also demonstrates that in the high-frequency range, the level of incident upstream and transmitted downstream pressure is close, but below 250 Hz the downstream transmission signal is small. For the non-zero bias flow case the magenta line pressure signal shows that in the presence of bias flow the level of incident and reflected upstream pressure has decreased when compared with the no flow condition. Meanwhile, the overall transmission has decreased, and downstream reflection is increased compared to the no flow condition. Configuration 12's reflected downstream pressure signal is high (shown in Figure 5.26), in the range of 50-100 Hz.

5.14.2 Configuration 12 energy analysis

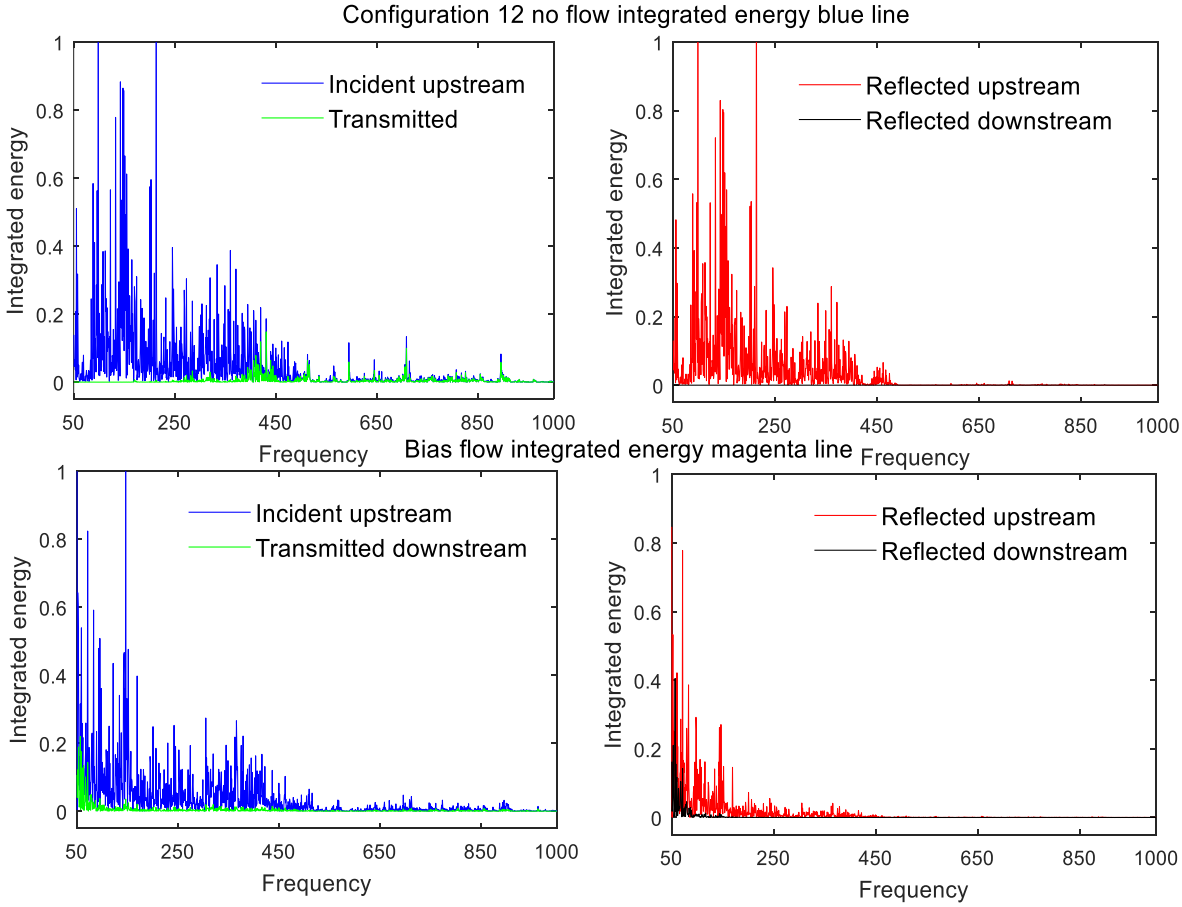

Figure 5.27 Configuration 12 integrated energy assessment.

Configuration 12's single liner integrated energy assessment is shown in Figure 5.27, with the no flow (blue line) at the top, and the non-zero bias flow (magenta line) at the bottom. For the no flow case, the integrated energy assessment shows that transmitted downstream energy is low compared to the incident upstream energy. It also highlights that upstream reflected energy is high; thus, transmitted downstream energy is low. For the non-zero bias flow case the magenta line represents the pressure ratio 0.14 %, and the effect of bias flow decreases the incident and reflected upstream energy. Meanwhile, in the downstream section, transmitted energy decreases and reflected energy increases compared to the no flow condition. The maximum absorption profile appears to be on the magenta or green line (previously discussed in section 4.14.6.), and its overall energy balance calculation is shown in Table 5.1.

5.15 Configuration 13 comparison of predictions with data

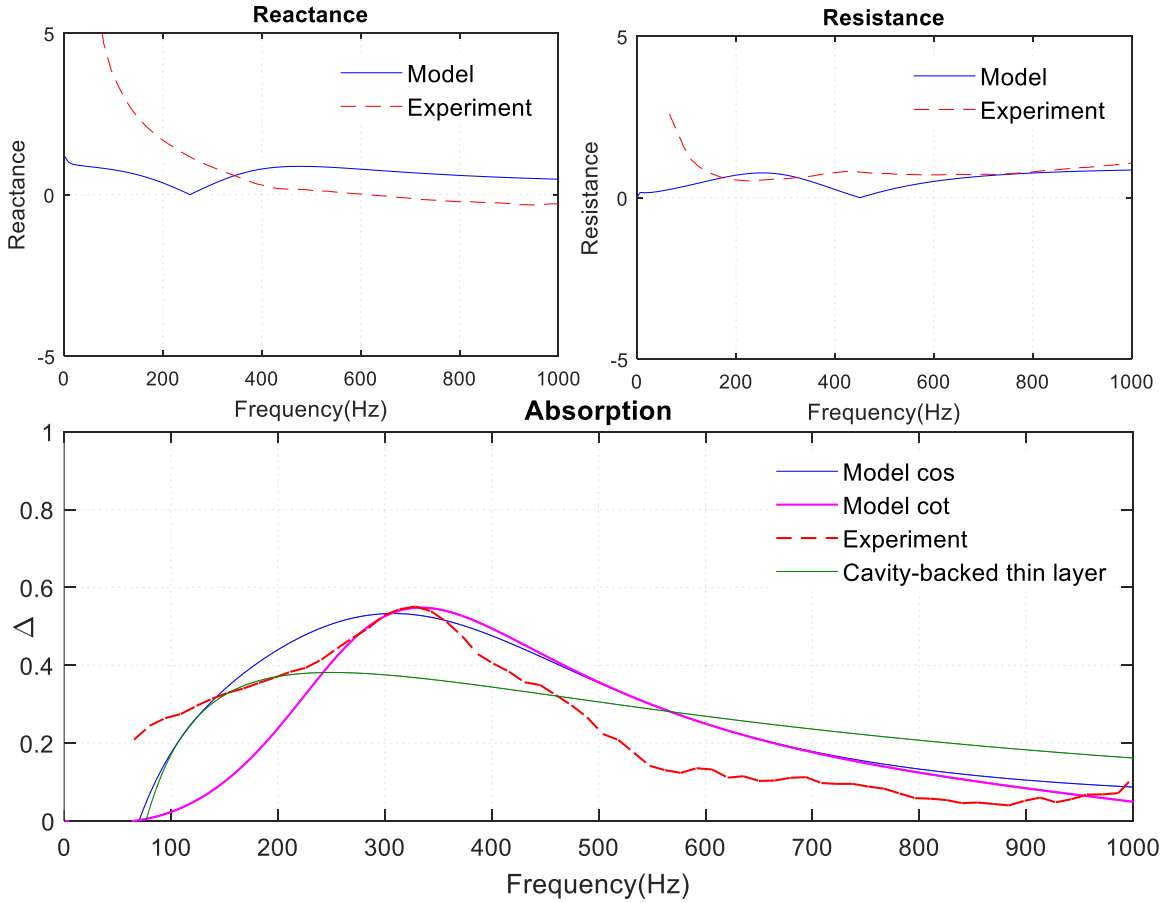

Figure 5.28 Configuration 13 model assessment with experiment.

Configuration 13 represents a combined liner. The inner liner represents configuration 7, and the outer liner signifies configuration 11. The outer liner has an orifice diameter of 2.675 mm with an axial pitch distance of 20 mm, which leads to porosity of 1.41 %, whereas the inner liner has an orifice diameter of 0.785 mm with an axial pitch distance of 9 mm, which leads to porosity of 0.74 %. Both liners are 1.6 mm thick. Figure 5.28 shows the comparison of prediction, with the blue solid line and the experiment's red dotted line intersecting at around 150 Hz and again at the peak, yet in the high-frequency range they create a gradient slope. Two alternative models both display an acceptable agreement with the experiment. However, model cos function with cavity factor agrees better with the spectral forms of the data from the measurement. There is an alternative cavity impedance model for the double layer liner, shown by the cavity-backed thin layer (solid green line), which appears to have an acceptable agreement without the peak. Combined liner resistance and reactance terms appear to have a reasonable agreement with the experiment, shown in Figure 5.28.

5.15.1 Configuration 13 signal analysis

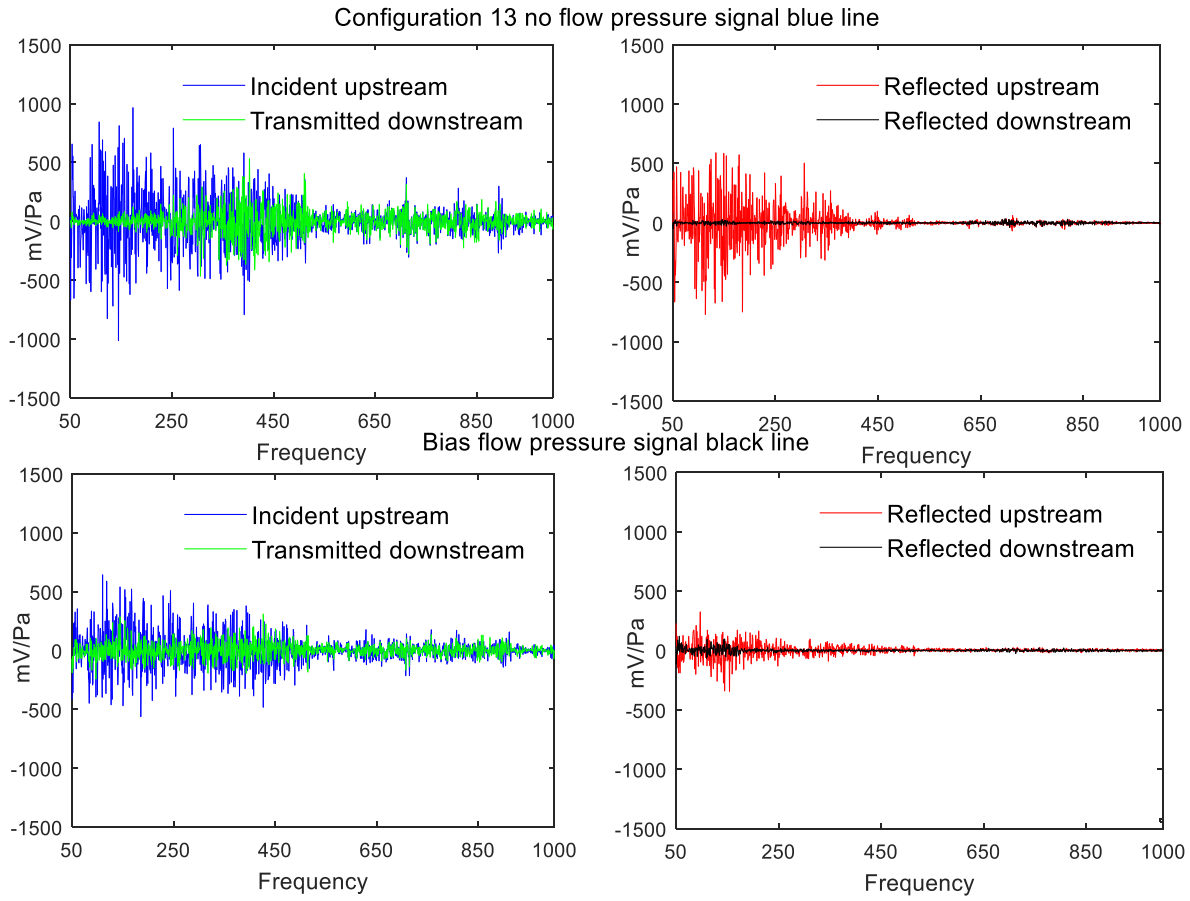

Figure 5.29 Configuration 13 no flow and non-zero bias flow signal analysis.

Configuration 13's combined liner pressure signal analysis, in terms of mV/Pa with respect to frequency, is shown in Figure 5.29, with the no flow (blue line) at the top and the non-zero bias flow (black line) at the bottom. For the no flow case, the combined liner incident upstream pressure signal is almost identical to configuration 7. The reflected upstream pressure signal is less than configuration 7, yet greater than configuration 11. The overall transmitted downstream pressure signal increases significantly compared to configurations 7 and 11. For the non-zero bias flow case, the black line pressure signal analysis illustrates that incident upstream, reflected upstream and transmitted downstream pressure signal decreases, except from the reflected downstream pressure signal, when compared with the no flow condition.

5.15.2 Configuration 13 energy analysis

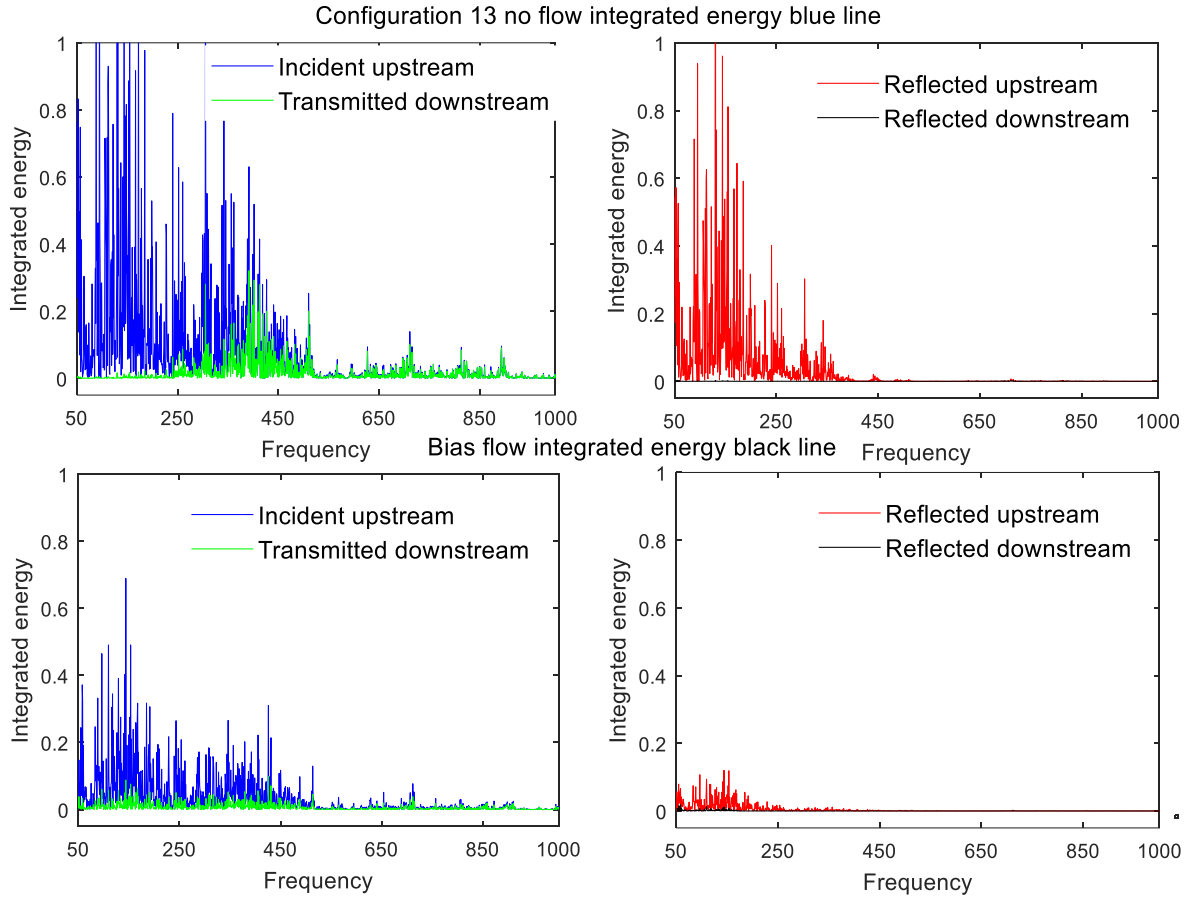

Figure 5.30 Configuration 13 integrated energy assessment.

Configuration 13's combined liner integrated energy signal analysis is shown in Figure 5.30, with the no flow (blue line) at the top and non-zero bias flow (black line) at the bottom. For the no flow case, integrated energy analysis shows that transmitted energy is low compared to the incident energy. Configurations 7 and 11 are combined to form configuration 13, which demonstrates that combined liner downstream transmitted energy increases. For the non-zero bias flow case the black line represents that orifice hole velocity is 10.13 m/s. The effect of bias flow decreases incident upstream, reflected upstream and transmitted downstream energy when compared with the no flow condition. However, the effect of the black line has caused a decrease in transmitted downstream energy compared to the no flow condition, but an increase in transmitted downstream energy when compared to configurations 7 and 11. The maximum absorption profile appears to be on the red or black line, previously discussed in section 4.14.7, and their overall energy balance calculations are provided in Table 5.1.

5.16 Configuration 14 comparison of predictions with data

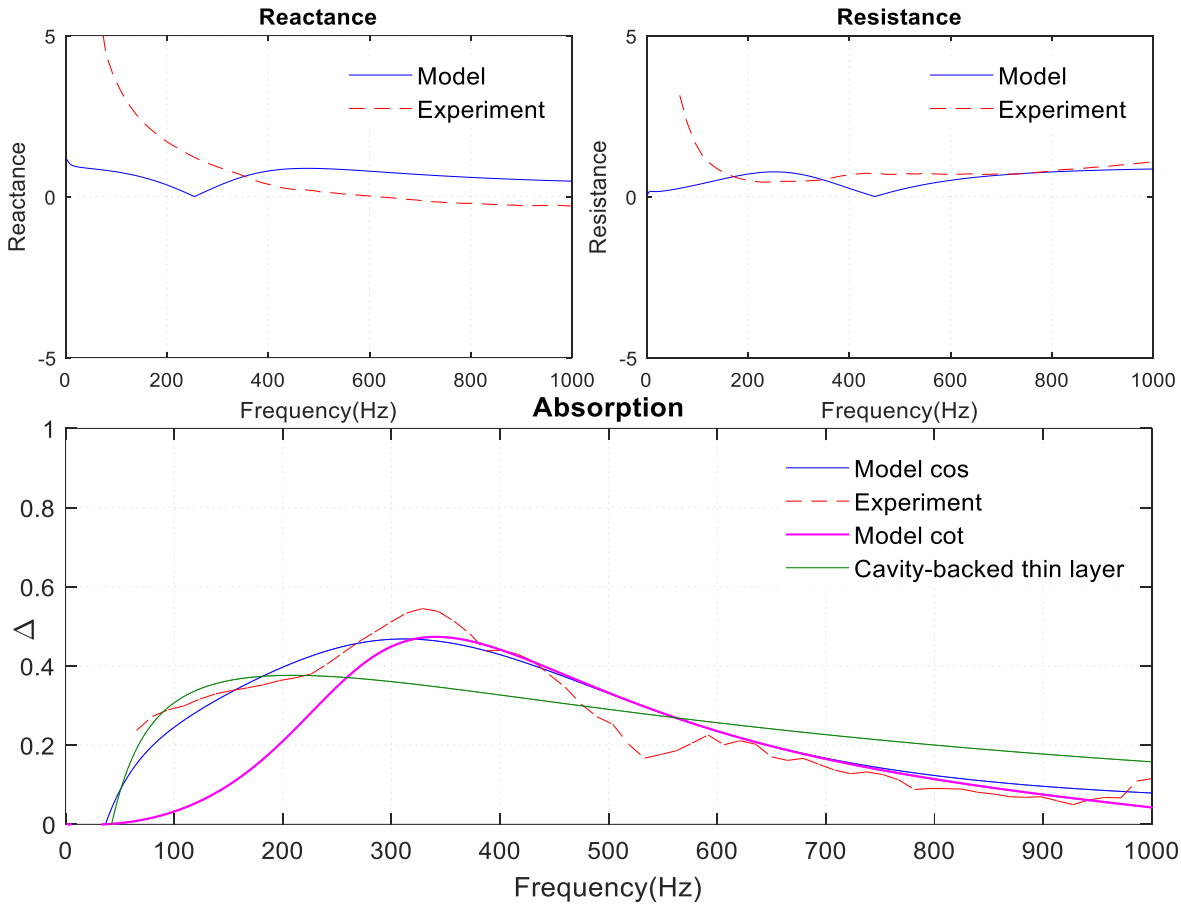

Figure 5.31 Configuration 14 model assessment with experiment.

Configuration 14 represents a double layer combustor liner, which is a combination of configurations 8 and 11. The porosity between the two liners is marginal: the inner liner has 1.23 % and the outer liner has 1.41 %, and each liner has 1.6 mm thickness. In configuration 14, the model blue solid line and red dotted line lead to a satisfactory agreement in the low- to high-frequency range. However, a systematic difference can be observed: the experimental data has formed a sharp peak, and the model cos function with cavity factor has generated a comparable peak in the low-frequency range. The model cot function with cavity factor has shaped a similar agreement, aside from a slight shift in the absorption profile in the low-frequency range. An alternative cavity impedance model for the double layer liner, shown by a cavity-backed thin layer (solid green line), appears to have an acceptable agreement in the high-frequency range. Since alternative cavity impedance model equation (2.11) does not agree with the measurement, future discussion will no longer be required. For combined liner configuration 14, the reactance and resistance profile exhibits a similar outline to the experiment shown in Figure 5.31.

5.16.1 Configuration 14 signal analysis

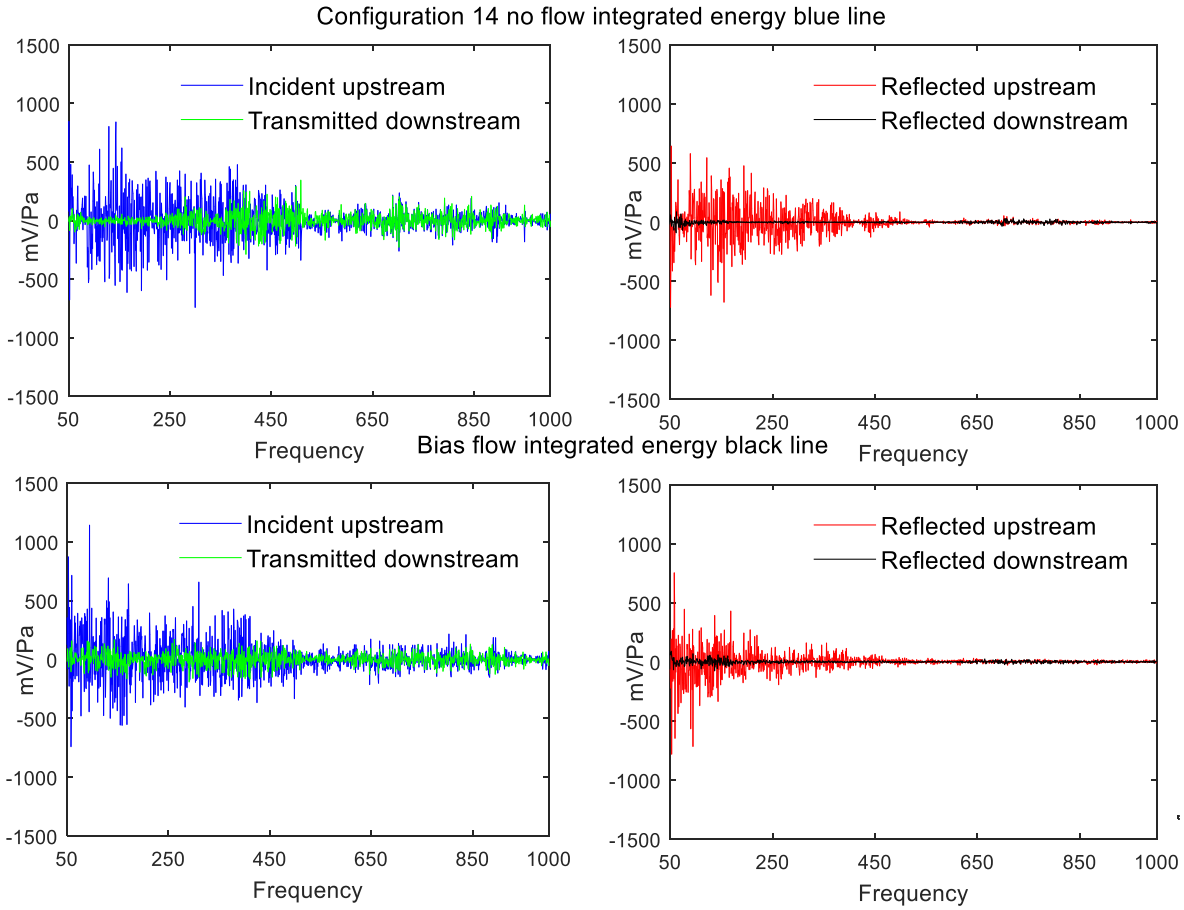

Figure 5.32 Configuration 14 no flow and non-zero bias flow signal analysis.

Configuration 14's combined liner combustor pressure signal analysis, in terms of mV/Pa with respect to frequency, is shown in Figure 5.32, with the no flow (blue line) at the top and the non-zero bias flow (black line) at the bottom. For the no flow case, the combined liner incident upstream pressure signal is slightly larger than configuration 8, yet smaller than configuration 11. The reflected upstream pressure signal decreases, whilst the transmitted downstream pressure signal increases when compared to configurations 8 and 11. For the non-zero bias flow case, the black line pressure signal analysis illustrates that incident and reflected pressure signal decreases in the upstream section. Meanwhile, transmitted downstream pressure signal decreases and reflected downstream pressure signal increases compared to the no flow condition.

5.16.2 Configuration 14 energy analysis

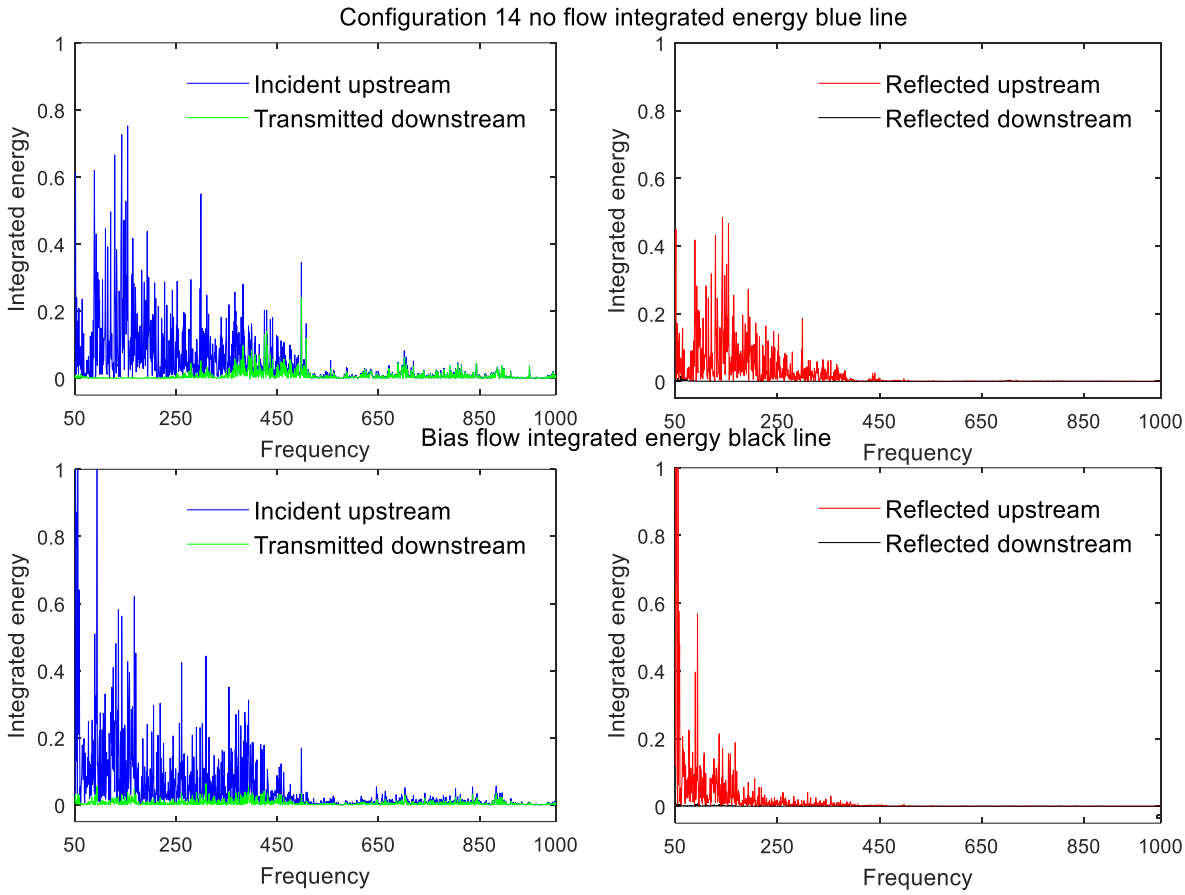

Figure 5.33 Configuration 14 integrated energy assessment.

An integrated energy assessment of configuration 14 combined liner is shown in Figure 5.33, with the no flow (blue line) at the top and the non-zero bias flow (black line) at the bottom. For the no flow case, integrated energy analysis shows that the transmitted downstream energy is low compared to the incident upstream energy. It can also be seen that the overall transmitted energy of configuration 14 increases compared to configurations 8 and 11. For the non-zero bias flow case, the black line represents that combined orifice hole velocity 10.05 m/s has impacted on incident upstream and reflected downstream energy when compared to the no flow case. However, the impact of the black line has caused a decrease in transmitted downstream energy compared to the no flow condition, but an increase in transmitted downstream energy compared to configurations 8 and 12. The broadband frequency range of the absorption profile appears to be on the black line, previously discussed in section 4.14.8, and the overall energy balance calculation is presented in Table 5.1. The pink line indicates that orifice hole velocity 26.65 m/s has been able to increase its transmitted downstream energy, whilst simultaneously decreasing its absorption coefficient.

5.17 Configuration 15 comparison of predictions with data

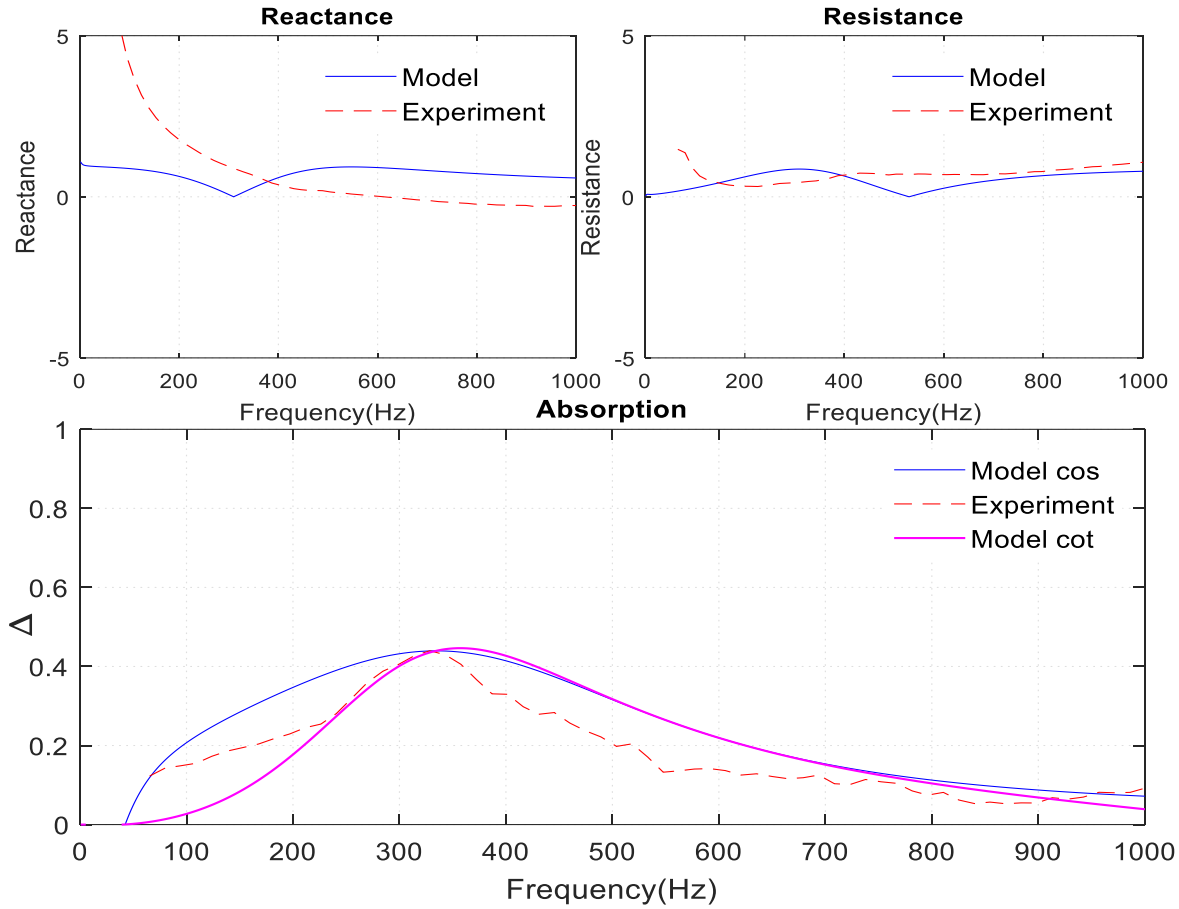

Figure 5.34 Configuration 15 model assessment with experiment.

Configuration 15 represents a combined liner of which the inner liner represents configuration 9, and the outer liner represents configuration 12. The outer liner is 1.6 mm in thickness, with orifice diameter 3.675 mm and an axial pitch distance of 20 mm, which refers to a porosity of 2.65 %, whereas the inner liner is 2 mm in thickness, with orifice diameter 1.175 mm and an axial pitch distance of 10.5 mm, giving a porosity of 0.98 %. In configuration 15 the model blue solid line and the red dotted line have established an excellent agreement with the experiment, illustrated in Figure 5.34, from the low to high-frequency range. The double layer combustor liner experiment shows that in the absence of bias flow in the high-frequency range, a gradient step absorption profile has been shaped along with the predictions shown in Figure 5.34. The experiment also shows that in the low-frequency range, experimental data remains in between the predictions. Liner reactance and resistance term agrees well with the experiment.

5.17.1 Configuration 15 signal analysis

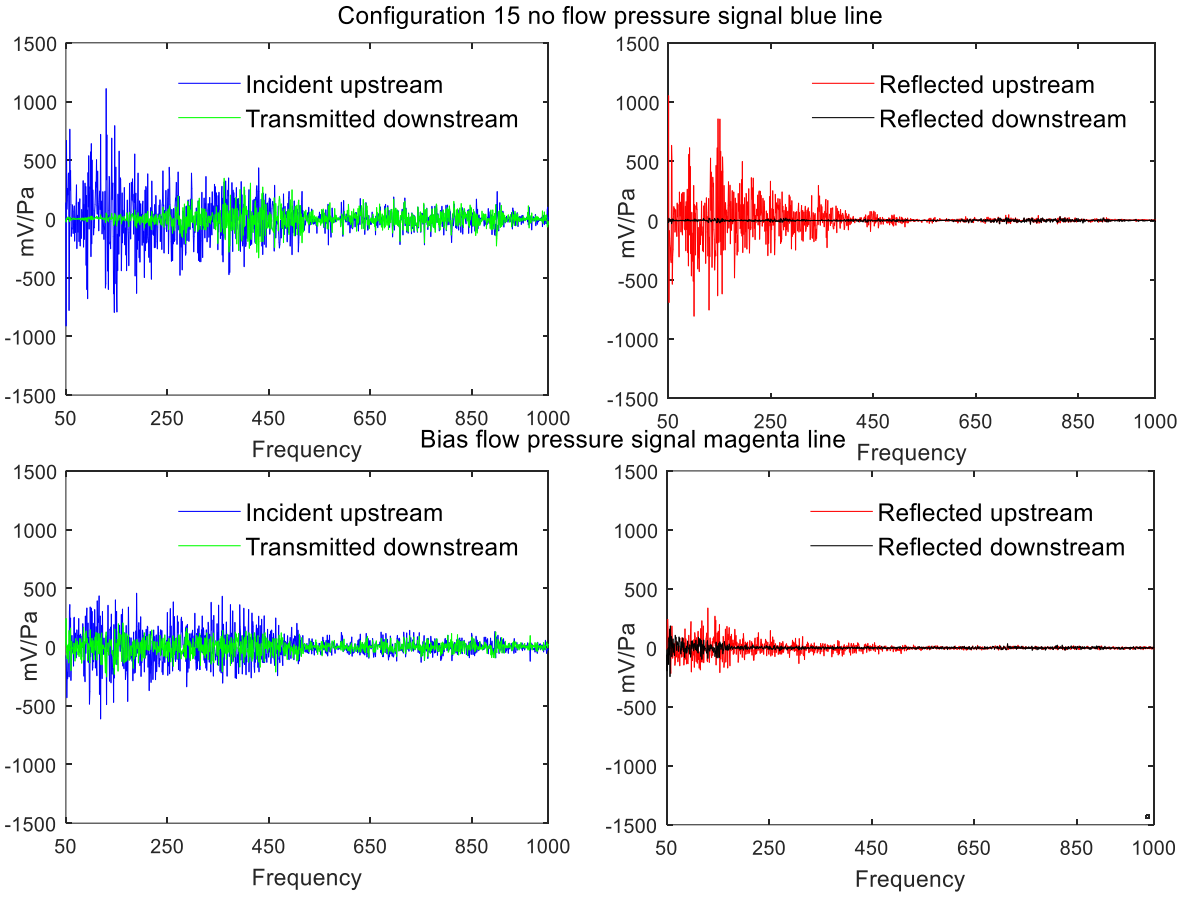

Figure 5.35 Configuration 15 no flow and non-zero bias flow signal analysis.

For configuration 15 combined liner combustor the pressure signal analysis, in terms of mV/Pa concerning frequency, is shown Figure 5.35, with the no flow (blue line) at the top and the non-zero bias flow (magenta line) at the bottom. For the no flow case, combined liner incident upstream pressure signal increases compared to configurations 9 and 12. The reflected downstream pressure signal is greater than configuration 9, yet smaller than configuration 12. The transmitted downstream pressure signal is greater than both configurations. For the non-zero bias flow case, the magenta line illustrates that incident and reflected upstream pressure signal decreases. Meanwhile, transmitted and reflected downstream pressure signal decreases and increases compared to the no flow condition.

5.17.2 Configuration 15 energy analysis

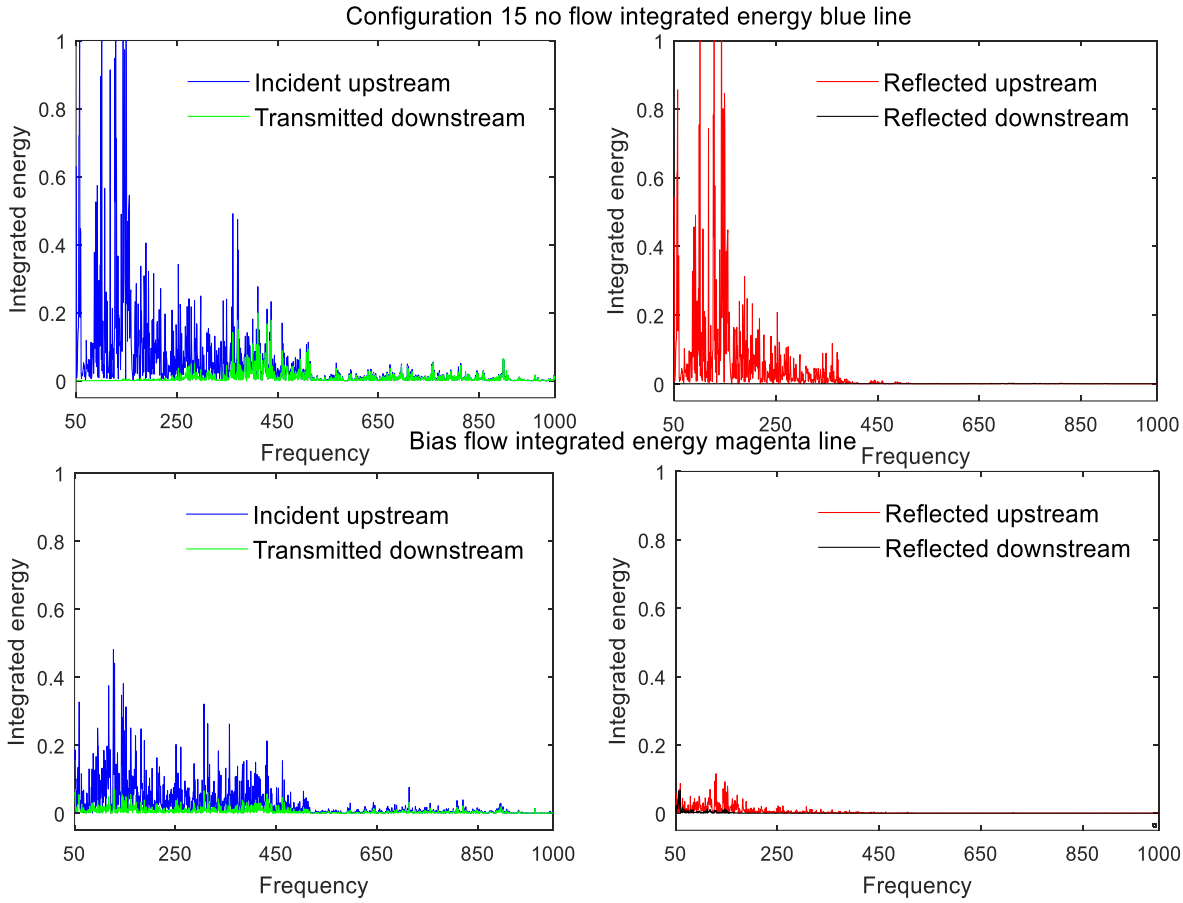

Figure 5.36 Configuration 15 integrated energy assessment.

The assessment of configuration 15 combined liner integrated energy signal analysis is shown in Figure 5.36, with the no flow (blue line) at the top and the non-zero bias flow (magenta line) at the bottom. For the no flow case, integrated energy analysis reveals that transmitted energy is low in comparison to the incident energy. Configuration 15's incident upstream energy is greater than configurations 9 and 12. Reflected upstream energy is greater than configuration 9, yet smaller than configuration 12. For the non-zero bias flow case, the magenta line represents the orifice hole velocity 16.21 m/s, which shows that the effect of bias flow has caused a decrease in incident and reflected energy in the upstream section. Meanwhile, in the downstream section, transmitted energy decreases and reflected energy increases compared to the no flow condition. The broadband frequency range of absorption appears to be on the black or magenta line, presented earlier in section 4.14.9, and their overall energy balance calculation is given in Table 5.1. The pink line represents the orifice hole velocity of 27.30 m/s, suggesting that transmitted downstream energy increases, whilst liner absorption profile decreases.

5.18 Configuration 16 comparison of predictions with data

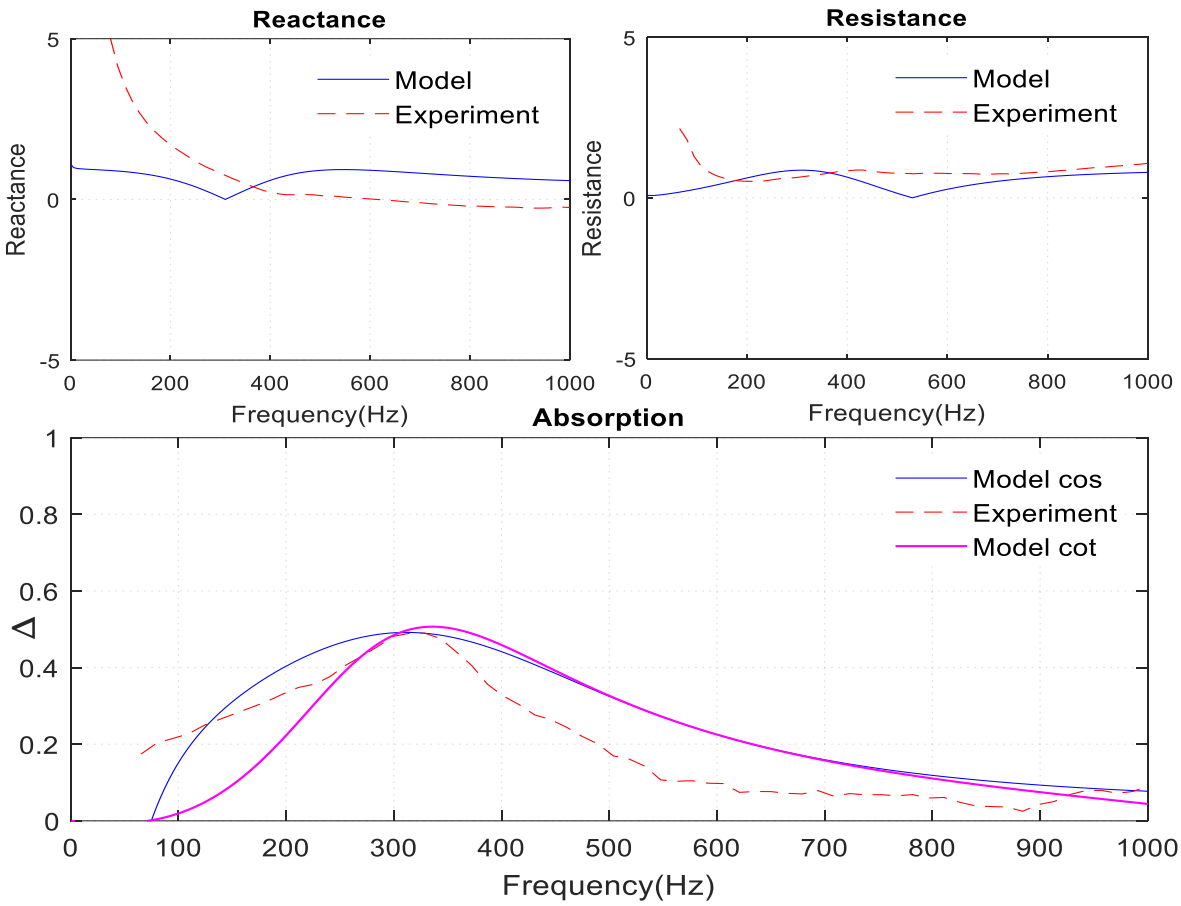

Figure 5.37 Configuration 16 model assessment with experiment.

Configuration 16 represents a combined liner of which the inner liner represents configuration 10, and the outer liner represents configuration 12. The outer liner is 1.6 mm in thickness, the orifice diameter is 3.675 mm and the axial pitch distance is 20 mm, giving a porosity of 2.65 %, whereas the inner liner is 2 mm in thickness, the orifice diameter is 0.925 mm and the axial pitch distance is 10.5 mm, giving a porosity of 0.61 %. Figure 5.37 shows configuration 16's comparison of predictions with data, revealing that the blue and pink solid lines have demonstrated a good agreement with the red dotted line. They have overlapped one another in the low to high-frequency ranges. Similarly, the reactance and resistance profile exhibits a decent agreement with the experiment, evidenced in Figure 5.37.

5.18.1 Configuration 16 signal analysis

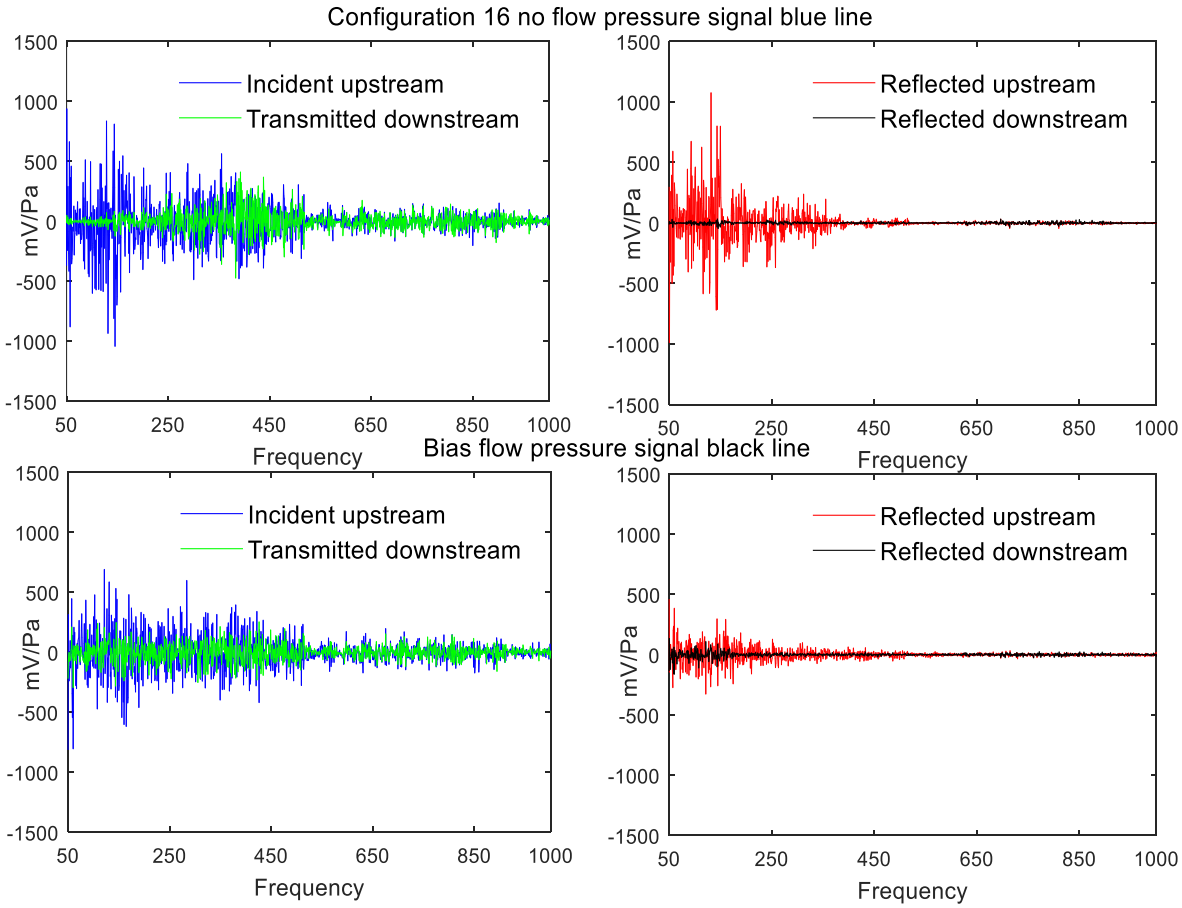

Figure 5.38 Configuration 16 no flow and non-zero bias flow signal analysis.

Configuration 16's combined liner combustor pressure signal analysis, in terms of mV/Pa concerning frequency, is shown in Figure 5.38,with the no flow (blue line) at the top and the non-zero bias flow (black line) at the bottom. For the no flow case, the combined liner incident upstream and transmitted downstream pressure signal increases. It can also be seen that the reflected upstream pressure signal decreases compared to configurations 10 and 12. For the non-zero bias flow case, the black line illustrates that incident upstream and transmitted downstream pressure signal increases compared to configurations 10 and 12. Furthermore, the incident and the reflected upstream pressure signal decreases compared to the no flow case.

5.18.2 Configuration 16 energy analysis

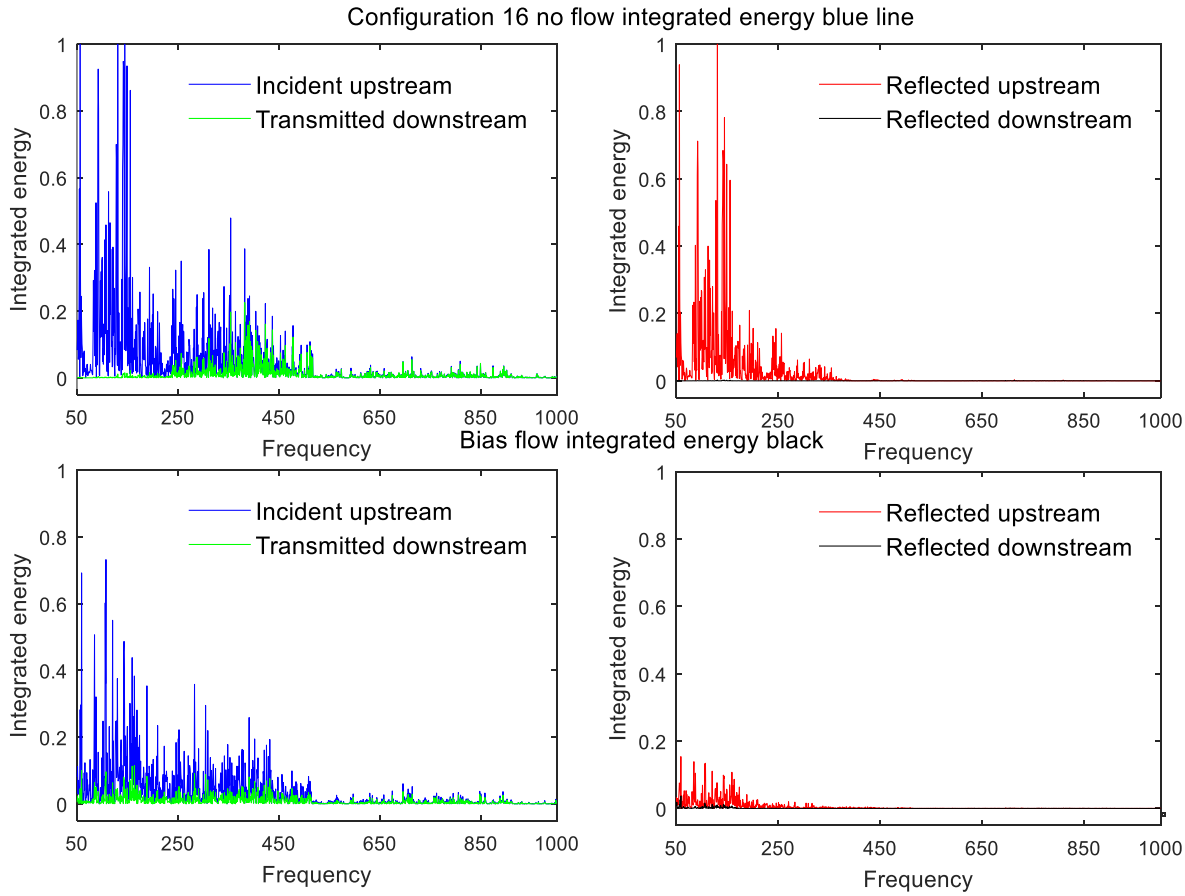

Figure 5.39 Configuration 16 integrated energy assessment.

Configuration 16's combined liner integrated energy assessment is shown in Figure 5.39, with the no flow (blue line) at the top and the non-zero bias flow (black line) at the bottom. For the no flow case, integrated energy analysis reveals that the transmitted energy is small when compared with the incident energy. The overall incident energy is greater and reflected energy is smaller compared to configurations 10 and 12. Furthermore, transmitted downstream energy increases compared to configurations 10 and 12. For the non-zero bias flow case, where the black line represents orifice hole velocity 10.29 m/s, the effect of bias flow has caused a decrease in incident and reflected energy in the upstream section compared to the no flow condition. Meanwhile, in the downstream section, transmitted energy increases compared to configurations 10 and 12. The maximum absorption coefficient appears to be on the black line, previously discussed in section 4.14.10, and their overall energy balance calculation is provided in Table 5.1. The pink line energy balance calculation indicates that transmitted downstream energy increases as the bias flow increases, yet the

absorption coefficient decreases. A nonlinear effect of bias flow can be observed from this investigation.

5.19 Configuration 17 comparison of predictions with data

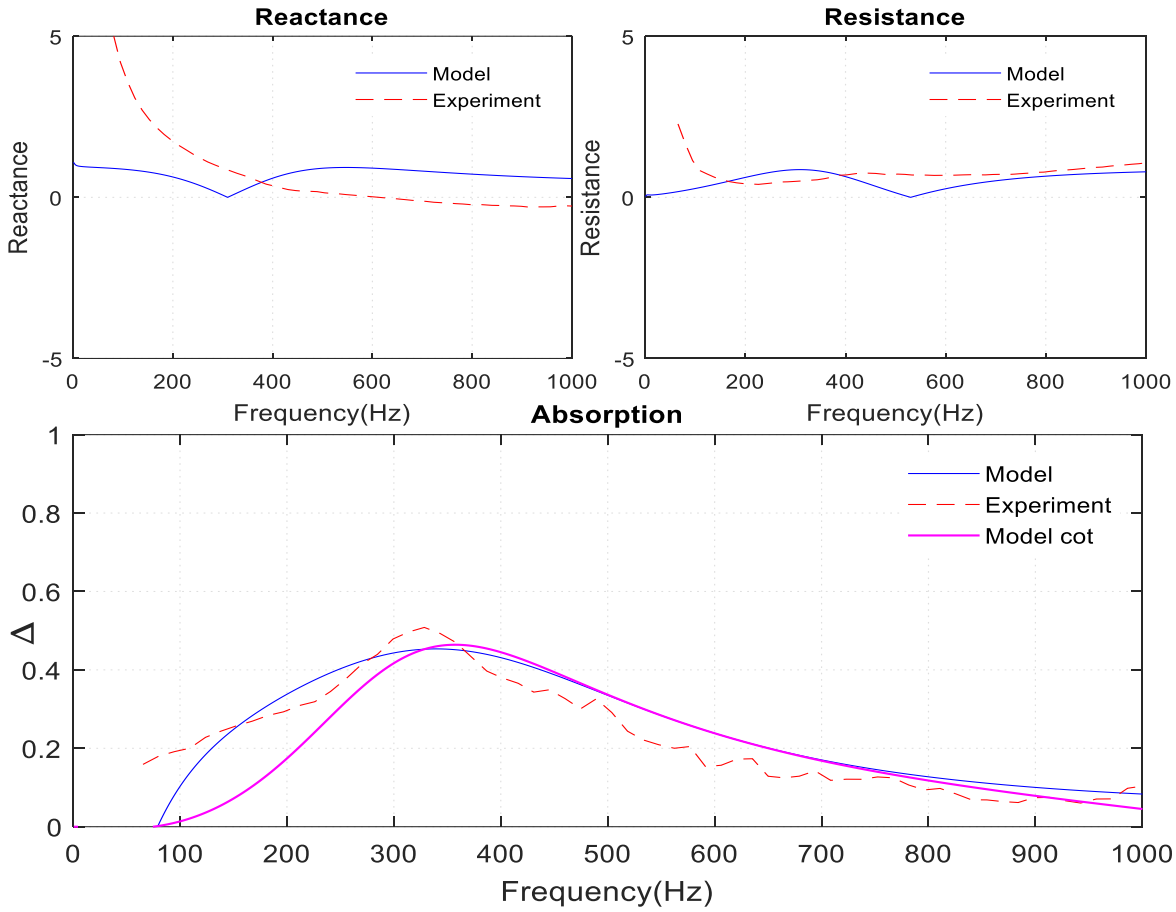

Figure 5.40 Configuration 17 model assessment with experiment.

Configuration 17 represents a combined liner, where the inner liner represents configuration 7, and the outer liner represents configuration 12. Both liners have a wall thickness of 1.6 mm. Figure 5.40 shows that in a comparison of prediction with the experiment, the model blue solid and red dotted line have overlapped one another and present a remarkable correlation from the low to high-frequency range. The model pink solid line also shows a decent agreement with the experiment, apart from a slight shift to the left in the low-frequency range, shown in Figure 5.40. Both predictions are close to the experiment, but the model blue solid line appears to have a strong agreement. Similarly, combined liner reactance and resistance profiles show a decent agreement with the experiment.

5.19.1 Configuration 17 signal analysis

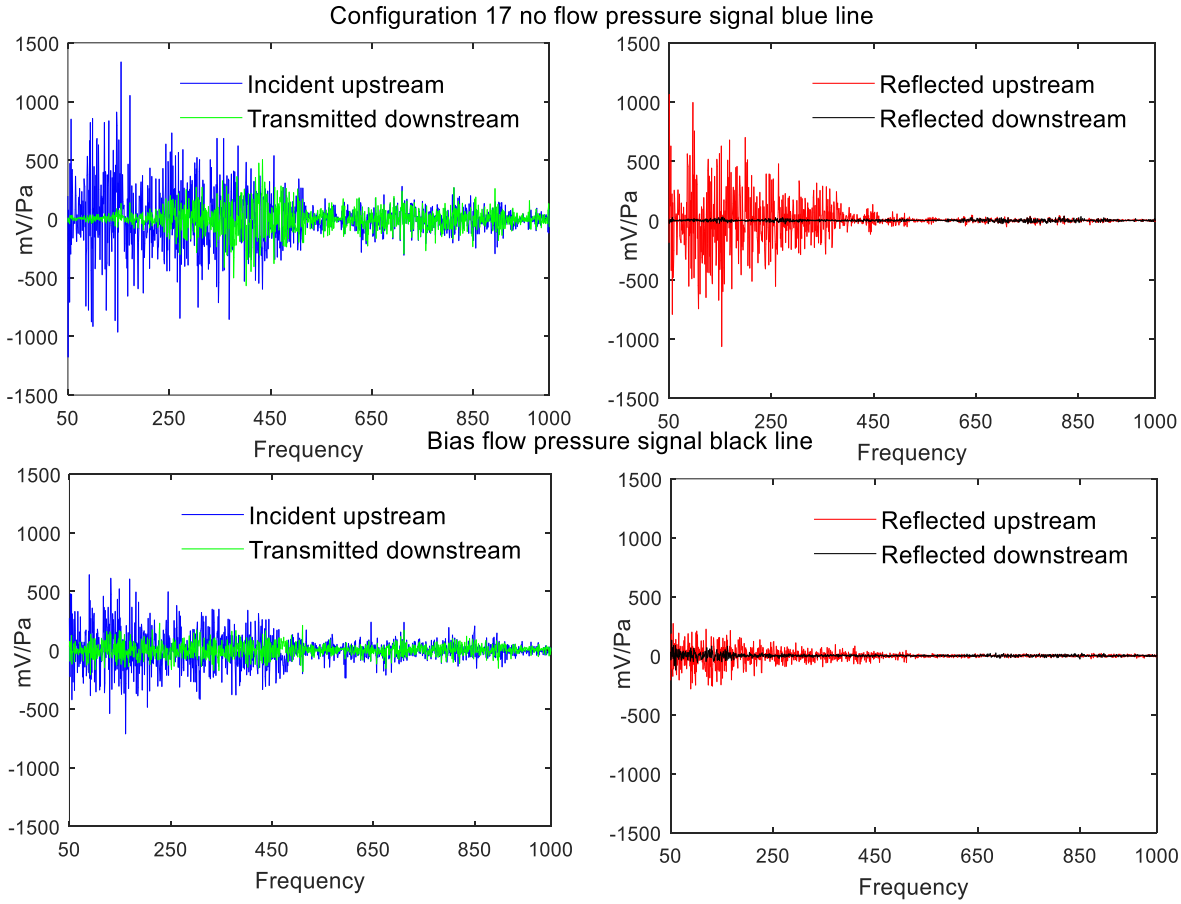

Figure 5.41 Configuration 17 no flow and non-zero bias flow signal analysis.

Configuration 17's double layered combustor pressure signal analysis, in terms of mV/Pa concerning frequency, is shown in Figure 5.41, with the no flow (blue line) at the top and the non-zero bias flow (black line) at the bottom. For the no flow case, combined liner incident upstream and transmitted downstream pressure signal increases compared to configurations 7 and 12. It can also be seen that the reflected upstream pressure signal decreases compared to configuration 7 and increases compared to configuration 12. For the non-zero bias flow case, the black line illustrates that both the incident and the reflected upstream pressure signal decreases. Meanwhile, transmitted downstream pressure signal decreases and reflected downstream pressure signal increases compared to the no flow condition. However, transmitted downstream pressure signal increases compared to configurations 7 and 12.

5.19.2 Configuration 17 energy analysis

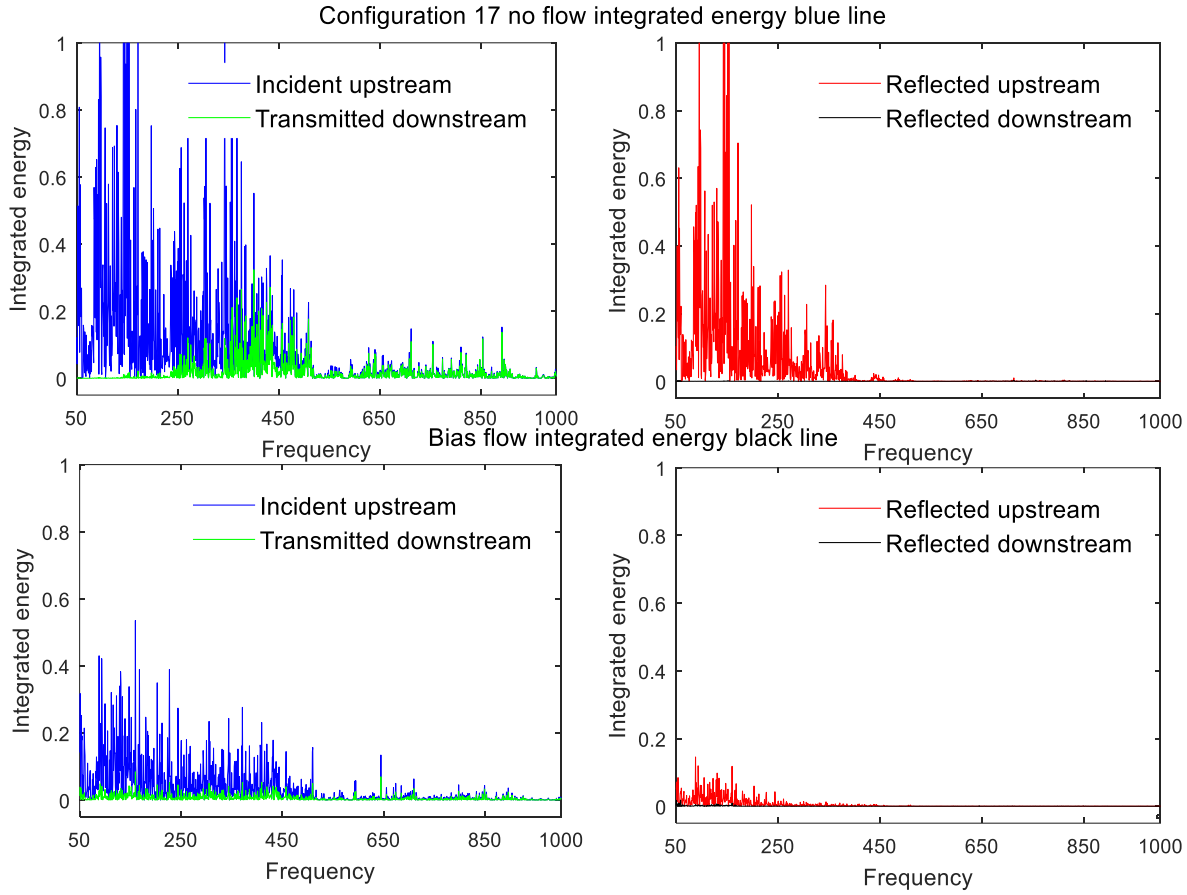

Figure 5.42 Configuration 17 integrated energy assessment.

Configuration 17's combined liner integrated energy assessment is shown in Figure 5.42, with the no flow (blue line) at the top and non-zero bias flow (black line) at the bottom. For the no flow case, integrated energy analysis shows that transmitted downstream energy is low when compared with the incident upstream energy. For the non-zero bias flow case, the black line represents that orifice hole velocity 10.21 m/s impacts (decreases) on incident and reflected energy in the upstream section when compared to the no flow condition. Meanwhile, in the downstream section overall transmitted energy increases compared to configurations 7 and 12. The broadband spectra are not present, however it can be considered on the red or black line, previously discussed in section 4.14.11, and its overall energy balance calculation is provided in Table 5.1. The pink line energy balance calculation indicates that bias flow is responsible for increasing transmitted energy in the downstream section. Furthermore, it signifies the formation of a nonlinear absorption profile.

5.20 Configuration 18 comparison of predictions with data

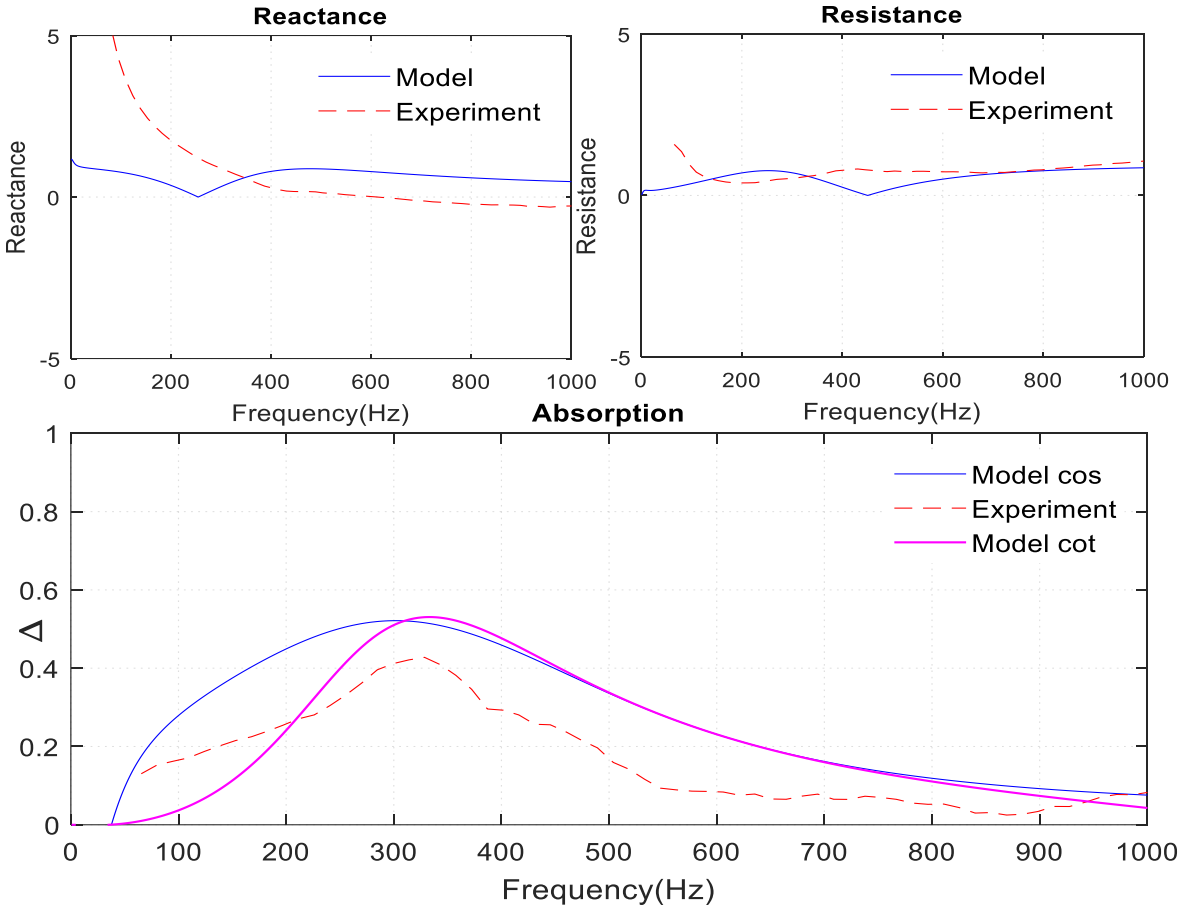

Figure 5.43 Configuration 18 model assessment with experiment.

Configuration 18 represents a combined liner, of which the inner liner represents configuration 9, and the outer liner represents configuration 11. The outer liner has an orifice diameter of 2.675 mm with an axial pitch distance of 20 mm, which refers to the porosity of 1.41 %, whereas the inner liner has orifice diameter of 1.175 mm with an axial pitch distance of 10.5 mm, which refers to the porosity of 0.98 %. Configuration 18's combined liner comparison of predictions (blue and pink solid line) with the experiment (red dotted line) shows that the absorption profile displays a reasonable agreement. However, experimental data exhibits a slightly lower absorption profile compared to the predictions. Metering liner configuration 11 has the strongest influence on developing the combined absorption profile. The prediction cot function with cavity factor appears to agree better with the experiment. Likewise, reactance and resistance term has formed a decent agreement with the experiment shown at the top of Figure 5.43.

5.20.1 Configuration 18 signal analysis

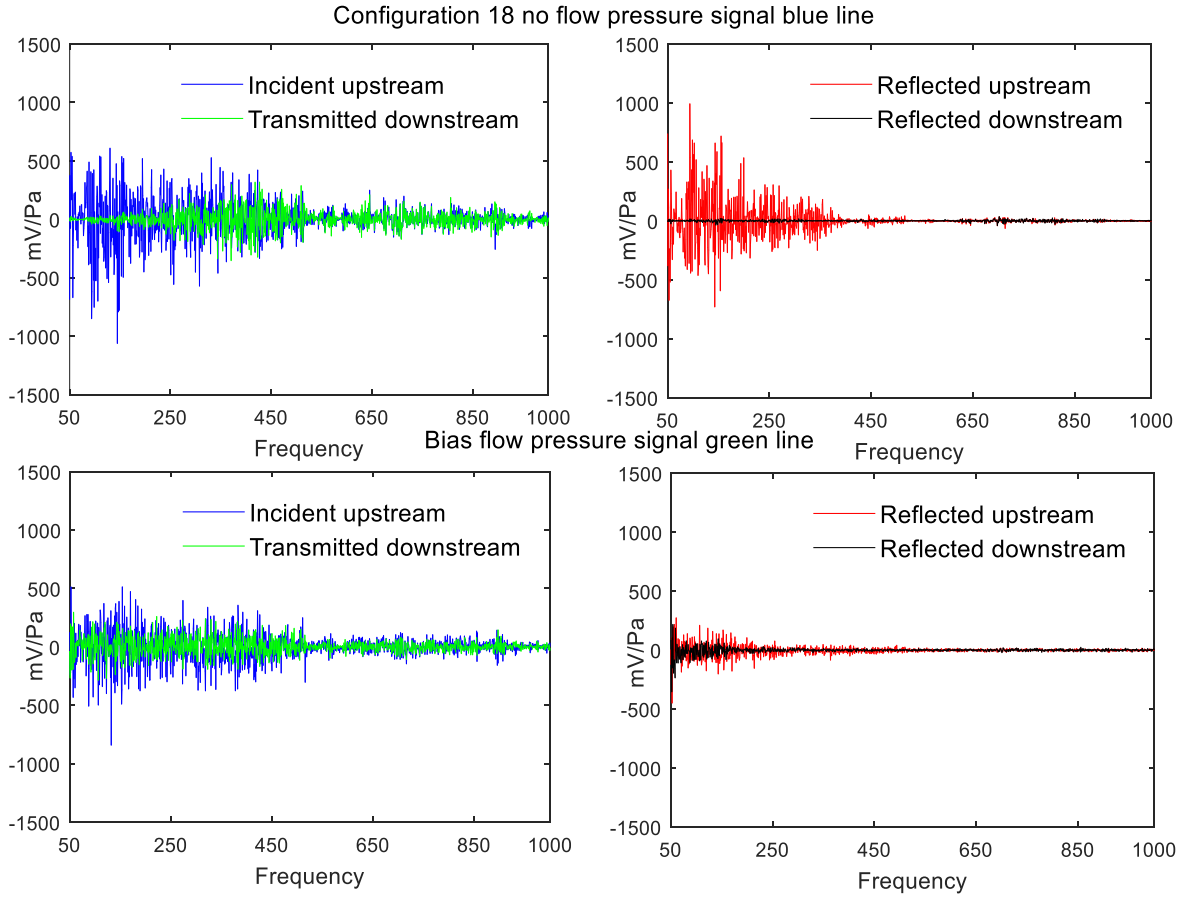

Figure 5.44 Configuration 18 no flow and non-zero bias flow signal analysis.

Configuration 18's combined liner combustor pressure signal analysis, in terms of mV/Pa concerning frequency, is shown in Figure 5.44, with the no flow (blue line) at the top and the non-zero bias flow (green line) at the bottom. For the no flow case, combined liner incident upstream pressure signal is greater than configuration 9 and smaller than configuration 11. The reflected upstream pressure signal is smaller than configurations 9 and 11. The transmitted downstream pressure signal is higher than both liners. For the non-zero bias flow case, the green line illustrates that incident and reflected upstream pressure signal decreases. Meanwhile, transmitted downstream pressure signal decreases slightly, and the reflected downstream pressure signal increases compared to the no flow condition. Additionally, transmitted downstream pressure signal increases compared to configurations 9 and 11.

5.20.2 Configuration 18 energy analysis

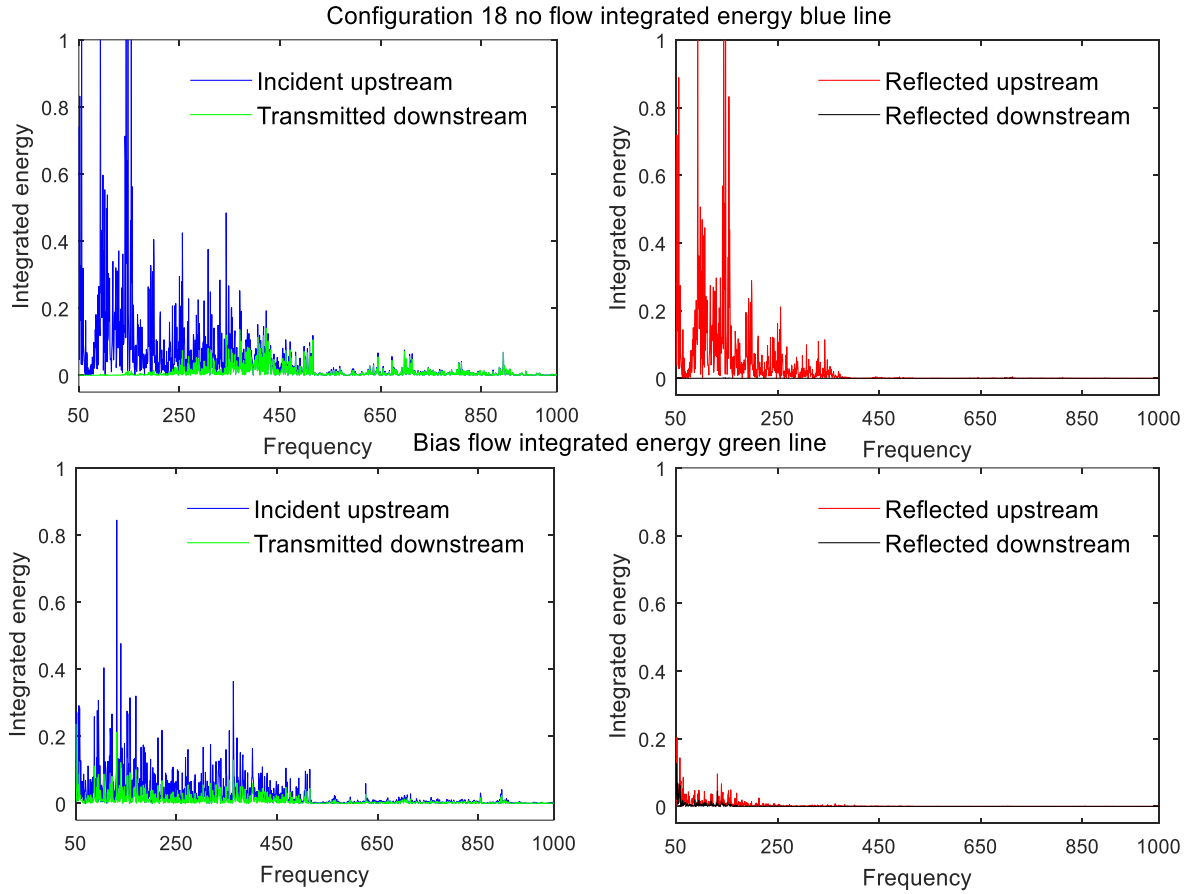

Figure 5.45 Configuration 18 integrated energy assessment.

Configuration 18's combined liner integrated energy assessment is shown in Figure 5.45, with the no flow (blue line) at the top and the non-zero bias flow (black line) at the bottom. For the no flow case, integrated energy analysis shows that transmitted downstream energy is small compared to the incident upstream energy. Overall incident upstream energy is smaller than configuration 9 and greater than configuration 11. Overall transmitted downstream energy is greater than configurations 9 and 11. For the non-zero bias flow case, the black line represents that orifice hole velocity is 10.21 m/s, which explains the decrease in incident and reflected upstream energy. Meanwhile, in the downstream section, overall transmitted energy increases compared to configurations 9 and 11. The broadband frequency range of absorption coefficient appears to be on the black line, earlier discussed in section 4.14.12, and its overall energy balance calculation is displayed in Table 5.1. The pink line overall energy balance calculation indicates that bias flow is responsible for increasing transmitted energy in the downstream section.

5.21 Overall energy balance calculation

Configuration	7	8	9	10	11	12	13	14	15	16	17	18	Dummy
No flow													
Incident upstream	78.53	42.59	40.30	42.62	48.77	43.08	78.57	43.85	51.04	46.16	88.35	45.33	40.75
Reflected upstream	44.56	28.79	25.89	22.17	31.57	31.75	32.93	19.03	29.77	22.12	41.99	24.66	2.49
Transmitted downstream	5.76	1.52	2.96	4.92	6.85	4.28	15.29	7.50	8.76	9.89	16.98	9.32	43.67
Reflected downstream	0.07	0.02	0.03	0.06	0.06	0.05	0.13	0.17	0.08	0.09	0.14	0.08	2.60
Energy in	78.60	42.61	40.33	42.68	48.83	43.13	78.71	44.02	51.12	46.25	88.49	45.41	43.35
Energy out	50.31	30.32	28.84	27.09	38.42	36.02	48.21	26.54	38.53	32.02	58.97	33.98	46.16
Absorption	28.29	12.29	11.49	15.59	10.41	7.10	30.50	17.48	12.59	14.23	29.53	11.43	2.81
Red line													
Incident upstream	38.33	36.58	34.14	33.70	36.09	32.09	33.65	42.87	33.50	33.73	37.24	32.95	-
Reflected upstream	11.98	13.15	12.02	8.60	13.55	15.83	7.38	15.73	11.24	7.89	9.59	9.04	-
Transmitted downstream	2.34	1.06	1.85	4.16	3.25	2.47	5.86	6.22	4.49	7.09	5.28	5.63	-
Reflected downstream	0.13	0.10	0.13	0.22	0.18	0.16	0.38	0.20	0.20	0.30	0.19	0.24	-
Energy in	38.45	36.68	34.27	33.92	36.27	32.25	34.03	43.08	33.70	34.03	37.44	33.19	-
Energy out	14.32	14.22	13.87	12.76	16.80	18.30	13.24	21.94	15.73	14.98	14.87	14.67	-
Absorption	24.13	22.46	20.40	21.16	19.47	13.94	20.80	21.13	17.97	19.05	22.56	18.52	-
Black line													
Incident upstream	34.69	30.66	33.47	29.62	34.82	31.20	31.70	43.46	33.00	32.44	31.35	34.26	-
Reflected upstream	6.56	7.32	7.40	4.36	8.10	11.60	4.19	13.48	6.49	4.65	4.53	6.14	-
Transmitted downstream	3.74	1.49	3.17	6.40	3.88	1.86	6.96	5.11	5.17	8.65	5.89	6.46	-
Reflected downstream	0.21	0.18	0.27	0.40	0.33	0.40	0.34	0.23	0.29	0.46	0.30	0.40	-
Energy in	34.90	30.84	33.75	30.02	35.15	31.60	32.04	43.69	33.29	32.90	31.65	34.67	-
Energy out	10.30	8.81	10.57	10.76	11.98	13.46	11.14	18.59	11.66	13.30	10.42	12.60	-
Absorption	24.60	22.03	23.18	19.26	23.17	18.14	20.90	25.10	21.63	19.60	21.23	22.07	-
Magenta line													
Incident upstream	32.38	29.18	29.69	28.84	32.06	34.82	28.53	33.32	26.56	31.59	29.75	30.18	-
Reflected upstream	4.71	4.88	4.67	3.15	5.74	13.04	2.79	5.34	3.58	3.38	3.03	3.62	-
Transmitted downstream	5.64	3.09	4.97	8.66	5.58	3.66	8.69	6.39	5.80	10.82	7.78	7.67	-
Reflected downstream	0.51	0.75	0.62	0.92	0.90	2.07	0.82	0.37	0.69	0.74	0.62	0.55	-
Energy in	32.89	29.93	30.31	29.76	32.97	36.89	29.34	33.69	27.25	32.32	30.37	30.73	-
Energy out	10.35	7.97	9.63	11.81	11.32	16.71	11.48	11.73	9.38	14.20	10.81	11.28	-
Absorption	22.54	21.96	20.67	17.95	21.64	20.18	17.86	21.96	17.87	18.12	19.56	19.44	-
Green line													
Incident upstream	30.23	27.35	25.44	25.07	28.26	43.32	27.01	34.44	25.25	29.97	28.80	24.94	-
Reflected upstream	5.98	4.81	2.87	2.31	4.38	19.25	2.25	8.52	2.86	3.41	2.86	2.80	-
Transmitted downstream	8.02	6.40	8.50	11.13	9.20	10.22	11.72	7.46	8.87	12.13	10.80	8.39	-
Reflected downstream	1.56	2.93	3.31	2.68	3.39	7.28	2.41	0.52	2.64	1.08	1.97	0.99	-
Energy in	31.79	30.29	28.75	27.76	31.66	50.59	29.42	34.96	27.89	31.05	30.77	25.93	-
Energy out	14.00	11.21	11.37	13.44	13.58	29.47	13.97	15.99	11.73	15.54	13.67	11.20	-
Absorption	17.79	19.08	17.38	14.32	18.08	21.12	15.45	18.98	16.16	15.51	17.10	14.74	-
Pink line													
Incident upstream	32.63	26.35	21.66	24.65	25.49	53.79	25.78	40.03	24.72	24.44	28.29	25.83	-
Reflected upstream	9.85	5.16	2.20	3.42	4.15	32.64	2.59	15.06	2.67	3.76	5.07	4.16	-
Transmitted downstream	11.75	13.54	12.77	15.30	24.39	32.61	19.97	8.59	11.98	11.32	12.48	9.43	-
Reflected downstream	4.85	9.17	6.96	6.01	18.56	30.79	10.80	0.72	5.46	1.66	4.66	1.15	-
Energy in	37.48	35.52	28.62	30.66	44.05	84.57	36.58	40.75	30.18	26.10	32.94	26.97	-
Energy out	21.60	18.70	14.98	18.73	28.53	65.25	22.56	23.65	14.65	15.08	17.56	13.59	-
Absorption	15.89	16.82	13.64	11.93	15.52	19.33	14.02	17.10	15.54	11.03	15.39	13.38	-

Table 5.1 Overall energy balance calculation from 50-1000 Hz.

From the microphone pressure data, overall energy balance calculation is carried out to develop authentication for all tested configurations (incident, reflected, transmitted and absorptive energy) shown in Table 5.1.

5.22 Conclusion

In this chapter, a comparison of predictions and empirical data is investigated. Experimental data is analysed in terms of pressure, energy, reactance, resistance, and absorption coefficient. High quality measurements and experiments carried out at the UHARC are compared with the semi-empirical hybrid model, along with other models from existing research. Experimental data shows that the scattering of energy from 0-50 Hz is extraordinarily high, and the decomposition of the overall energy balance leads to significant differences in terms of both signal and energy potentials. It appears that anechoic termination is ineffective from 0-50 Hz, thus signal analysis and overall energy balance calculation is carried out from 50-1000 Hz. Different configurations of the cylindrical combustor liner's signal, energy, and absorption profile is analysed in an isentropic condition. Setting up the benchmark by using a dummy liner shows that the acoustic analysis is acceptable, which is demonstrated in section 5.2, and its overall energy balance calculation is provided in Table 5.1.

A basic theoretical model is proposed, based on liner geometry, along with a cavity factor to predict the absorption profile of the no flow case. The present model introduces a cavity factor, which is a function of cavity depth. The cavity factor optimises the predictions as the different test rigs have diverse cavity depths, and therefore, without a cavity factor, the resonance frequency of the orifice cannot be determined accurately due to this range.

Transmission line theory is applicable for a single liner only with the cavity factor. In the case of the double liner there was no match, as the double liner has an extra parameter effective cavity depth d' (depth in between the liner), and an extra layer. An alternative cavity impedance model (cavity-backed thin layer) established a partial agreement with the experiment. A modification of the transcendental equation (cosine function with cavity factor) fits both the single- and double-layer liners, although proper justification is not given, which is the first limitation of further work with this numerical analysis. This investigation effected an extraordinary explanation, which has established two factor authentications from the dummy liner data and predictions. The second limitation of this model, the transmission coefficient, is not present, and for that reason an overall energy balance calculation is carried out to show that the transmission coefficient is extremely small and negligible.

6 Overview

The foremost aim of this research is to conclude a damping characteristics of a cylindrical combustor liner no flow and non-zero bias flow effect. A widespread array of available investigation has been collected and reviewed and a hypothesis is developed. The high-quality experimental results place the current information into perspective. The substantial structures of each constraint can be summarised as follows:

6.1 Conclusion

In this section, the effects of acoustic (SPL, transmission loss, absorption coefficient), geometric (porosity, thickness, orifice cross-section, liner configuration, damping volume, perforation pattern), and flow parameter (bias flow) will be discussed along with research contribution, limitation of the model and experiment, and potential future research.

6.1.1 Sound Pressure Level

The damping performance of the cylindrical combustor liner is tested under constant sound pressure level, which is approximately 90 to 95dB. Effect of non-zero bias flow onto the cylindrical combustor liner exhibit the non-linear absorption profile, while the SPL remain constant.

6.1.2 Bias Flow

Non-zero bias flow has the ability to improve the liner absorption performance for single- and double-layer liner configurations. A few examples can be evaluated for no flow and non-zero bias flow cases based on experimental analysis. Non-zero bias flow can create resonance and shift its peak compared to the no flow case. The bandwidth of the absorption or dissipation profile can be increased while its level is typically mapped. The true broadband frequency range of absorption can be obtained when the bias flow setting is adjusted to the configuration for both single- and double-layer liners.

6.1.3 Porosity

Porosity depends on orifice pattern, number, diameter, and its axial pitch distance. Porosity is the most important factor for combustor design, as it is responsible for drawing pressure curves, forming peak absorption and cooling factors. Porosity is required to map with non-zero bias flow settings to create the vortex, which can cancel or suppress the acoustic noise inside the combustor and convert the sound pressure into mechanical and heat energy.

Therefore, the effect of bias flow depends on the magnitude of the absorption or dissipation directly linked to the combustor liner porosity. A snapshot of porosity effect is given below.

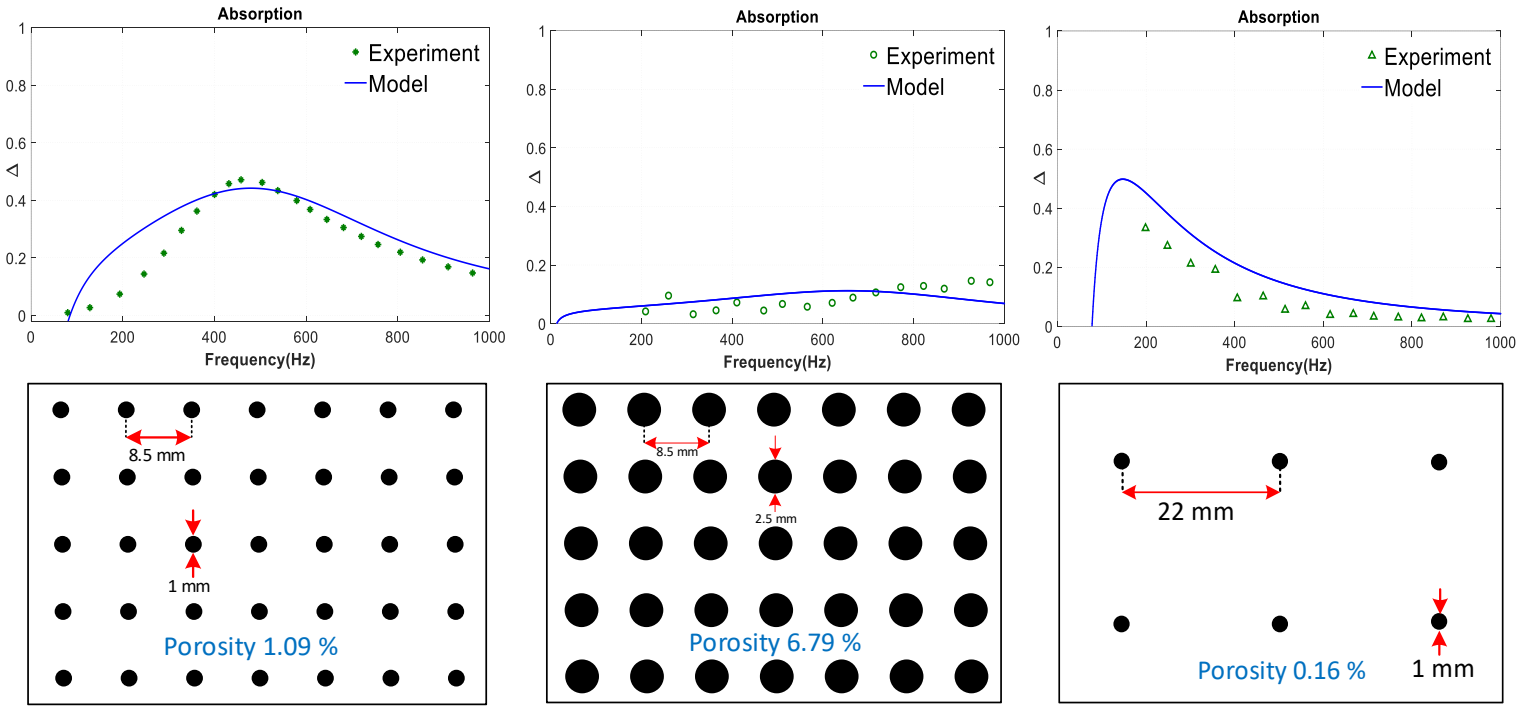

Figure 6.1 Comparison of predictions with experiment (Lahiri, 2014; Lahiri & Bake, 2017; Lahiri et al., 2011).

Figure 6.1 shows the influence of porosity over a full scale cylindrical combustor liner, and comparisons of prediction with the experiment (Lahiri, 2014; Lahiri & Bake, 2017; Lahiri et al., 2011). An excessively high porosity (6.79 %) is associated with the flat absorption profile shown in the middle. Comparisons of predictions with the data suggest that a larger orifice with a shorter axial pitch distance can explain the increase in porosity and is responsible for creating a flat absorption profile, shown in the middle of Figure 6.1. Similarly, an orifice with a greater axial pitch distance refers to the decrease in porosity and is responsible for a peak frequency shift towards the low-frequency range. An orifice diameter with an optimum interaction end correction area indicates optimum porosity and is responsible for drawing a broadband frequency range of absorption, shown on the right of Figure 6.1. In other words, a liner with an optimised orifice diameter and optimised axial pitch distance creates its peak in between the low and high-frequency range.

6.1.4 Liner thickness

Combustor liner thickness plays a vital role in developing a pressure ratio. Acoustic and static pressure measurements suggest that thick liners create a lower pressure ratio and orifice hole velocity compared to thin liners. From the prediction of the semi-empirical hybrid model it can be suggested that if the thickness of the liner increases, absorption increases by shifting

the frequency slightly; however, it is shallow. It requires two identical liners of greater thickness to engender discussion regarding the experiment, which is not applicable here. However, the greater thickness of the combustor liner does not appear to provide an improved absorption profile as the geometry of the liner is changed.

6.1.5 Orifice cross-section

The FRF analysis suggests that it is not solely a circular orifice which can create better damping. If the porosity remains constant, a different type of orifice cross-section can lead to an improved damping factor.

6.1.6 Inner liner configuration

The inner liner can create pressure difference if the percentage of porosity is lower than the outer liner with small orifice diameter. The inner liner mainly acts as a damper; its influence is to construct a combined effective area and combined discharge coefficient inside the combustor.

6.1.7 The outer liner configuration

The outer liner can also create pressure difference if the percentage of porosity is lower than the inner liner. The outer liner decides the amount of bias flow that should be introduced into the inner liner, and acts as a metering liner as well as a damper. Static pressure measurements suggests that if the porosity of the inner and outer liners is close, then the formation of pressure curves is also close.

6.1.8 Damping volume

Damping volume refers to the volume in between the inner and outer liners. For a single liner configuration, damping volume does not exist. It is a critical parameter; the effect of damping volume on a double-layer cylindrical combustor liner requires additional investigation. Speculative execution of acoustic analysis demonstrates that increasing damping volume does not appear to increase liner damping performance; however, for increased damping volume cases, the geometric pattern of the liner was transformed.

6.1.9 Perforation pattern

Perforation patterns play a vital role in the original combustor design for a single- or double-layer combustor liner. Perforation patterns provide an orifice interaction area, which is directly related to the axial pitch distance and orifice diameter. It is an extremely complex metric - to optimise the interaction area with the orifice diameter, along with the number of

orifices along with axial pitch distance, coordination amongst them is imperative, followed by the bias flow.

6.1.10 Transmission loss

For the no flow case, both the single- and double-layer liners provide maximum transmission attenuation in the low-frequency range, while in the high-frequency range the curve remains flat. For the non-zero bias flow cases, liner transmission attenuation decreases in the low-frequency range compared to the no flow case, while transmission attenuation increases in the high-frequency range but is minimal. By keeping incident energy constant in the low-frequency range, transmitted energy increases and reflected energy decreases. Similarly, in the high-frequency range, by keeping incident energy constant, transmitted energy decreases and reflected energy increases in the presence of non-zero bias flow cases.

6.1.11 Absorption or Dissipation

In the presence of bias flow, the performance of both the single- and double-layer combustor liners was improved, although bias flow demonstrates a nonlinear absorption profile. From a combination of experiments using acoustic and static pressure measurements, it is suggested that two parameters can be linked together to control the maximum absorptive or dissipative energy: porosity and the discharge coefficient of the orifice. Whilst porosity is a fixed geometric parameter, discharge coefficient of the orifice varies because as the mass flow rate increases the discharge coefficient of the orifice increases along with pressure ratio, Mach number and orifice hole velocity. In the high-frequency range the combined liner absorption profile is flat; bias flow is the primary solution to improve its absorption profile in the high-frequency range.

6.1.12 Static pressure measurement

Static pressure measurement is carried out to designate the acoustic analysis. From the static pressure measurement discharge coefficient of the orifice, orifice hole velocity, pressure ratio, and mass flow rate are developed. Comparison of the single- and double-liner static pressure measurement establishes that the liner with the lowest percentage of porosity creates a pressure difference. This is evidenced with either a damping or metering liner. Furthermore, it is indicated that the liner containing the lowest percentage of porosity provides a higher discharge coefficient. No flow acoustic analysis illustrates that for a double liner, absorptive or dissipative energy creates the first peak in the low-frequency range, and

then remains flat. In addition, it indicates that to form a second peak in the high-frequency range, non-zero bias flow is required. A double layer combustor requires a certain percentage of porosity difference between the outer and inner liners to form a second peak in the high-frequency range. Static pressure measurement can suggest which liner is responsible for drawing the pressure curve. Metering liner porosity is required to match damping liner porosity to form a broadband frequency range of absorption.

6.2 Research contributions

Plane wave propagation through a cylindrical combustor liner was investigated in the presence of no flow and non-zero bias flow cases. Also developed a semi-empirical hybrid model, based on the no flow data (DLR and UHARC). A two-factor authentication technique is incorporated into this investigation to improve the accuracy of data and prediction. Dummy liner acoustic analysis provides acceptable experimental output as well as prediction. Similarly, the output of this semi-empirical model is matched with the single- and double-layer combustor liner. Furthermore, this hybrid model can predict liner resistance and reactance terms along with the experiment. Each of the models presented in this research work were developed in a Mat-lab platform, and create an excellent contribution to science, along with reviews of previous work. A cavity factor is incorporated into the transmission line theory, where cavity factor is a function of cavity depth. The cavity factor optimises the predictions as the different test rigs have different cavity depths, which are then compared. Without cavity factor the resonance frequency of the orifice cannot be determined accurately as the different test rigs have different cavity depths.

6.3 Limitations of the model and experiment

There exist a number of limitations present with the model and experiment, and this investigation is not free from restrictions. Case 1 relates to the validity of the experiment. Although it is acknowledged that the dummy liner acoustic analysis acted acceptably and developed a flat absorption profile, the signal analysis indicates that below fifty hertz sound pressure is exceptionally high. The current test rig has an anechoic termination fitted towards the end of the downstream exit port. It is acknowledged that anechoic termination is not very active in the low-frequency range, and there are other limitations relating to the test rig duct diameter and microphone location, as identified during the signal analysis and energy balance calculation of the dummy liner. Therefore, the energy balance calculation is carried out from

fifty to one thousand hertz. Some conclusions may not be a hundred per cent perfect, but they are close. Instead of losing too much information in the low-frequency range, fifty hertz were considered rather than a hundred and fifty hertz.

Case 2 relates to the validity of the model and possesses a number of limitations. Firstly, this semi-empirical hybrid model focuses on the cavity depth and has a relatively high level of influence on the transcendental equation or transmission line theory, which refers to the impedance due to the cavity cot function. In the present model, this transmission line theory did not match with the experimental analysis without a cavity factor. Therefore, a cavity factor is added to the transmission line theory for justification, as the current test rig is made of a large cavity depth. Transmission line theory appears to have an acceptable agreement with the experiment carried out in UHARC and DLR Lahiri et al.'s (Lahiri, 2014; Lahiri & Bake, 2017; Lahiri et al., 2011) data. Conflict arises once compared with the double layer combustor liner data, as the double liner has an additional parameter - effective cavity depth with an additional layer. To adopt the double-layer combustor liner data, the present model computed for cosine function with cavity factor, which shows a decent agreement with both the single- and double-layer combustor liners. In addition, an alternative cavity impedance model for a double liner with cavity-backed thin layer was computed, which shows partial agreement. Therefore, the transmission line theory of both the cot and cos function, including cavity factor, is considered for computing: cot for a single liner and cos for both the single- and double-layer combustor liners prediction of absorption profile.

Secondly, in the model notation a transmission coefficient is not present for the computation, which is neglected. Therefore, signal analysis and an overall energy balance calculation is carried out to establish that the transmission coefficient is small and can be negligible. Ultimately, this semi-empirical hybrid model is developed from the classical theory of absorption coefficient; absorption coefficient is developed from magnitude of the reflection, and magnitude of the reflection is developed from collected impedance.

6.4 Future work

The outcome of this thesis raises several unanswered questions that are beyond the scope of the current work. First, the priority is to seek a theoretical justification for the use of cosine function. Further investigation may help to extend the outcome of this framework through more in-depth insights into the resolution processes. Second would be to add the

transmission coefficient into the semi-empirical hybrid model. Signal analysis shows that the transmitted downstream energy is small compared to the incident energy.

6.5 Justification of Appendix-A

A high-temperature test rig (HAT) design is carried out to look at the behaviour of an impedance effect. It is easy to predict, nevertheless, two-factor authentication will not be present for clarification. It is essential to examine the actual behaviour of the speed of sound in high temperature regions, as actual operating conditions of a gas turbine remain in the high temperature. At low temperatures the reaction undergoes kinetic control, and the primary product is derived from the quickest reaction. At high temperatures the response experiences thermodynamic control, which delivers more stable coordination and creation. Under dynamic control, the reaction is rate-based and is not reversible; however, under thermodynamic control, the reaction is in equilibrium and is also reversible under optimum conditions.

The verification of this HAT is imperative and will allow the extending of the theoretical model to include practical aperiodic information. In addition, an attempt should be made to verify other theoretical results for the enhancement of the estimation. The execution of this HAT test rig extension will be a real-time study to provide proper feedback to the current state-of-art protocols, which can be considered as a future extension of gas turbine research and development processes. The complete project proposal plan is ready for execution, and more details are given in chapter 8.1 as an Appendix-A.

6.6 Justification of Appendix-B

The slots type shape exhibits a better damping effect compared to the circular orifice. Also, shows that for the no flow case, increase in porosity refers to the peak amplitude shifts towards the high-frequency range. In the presence of cross-flow, low porosity refers to the decrease in peak without frequency shift. If the porosity increases significantly, the peak amplitude decreases, and the peak amplitude shifts towards the high-frequency range.

7 References

Allard, J. (1993) Propagation of sound in porous media, Modelling sound absorbing materials, edited by Elsevier Applied Science. Elesevier Science Publishers LTD, New York and London.

Allard, J. & Attala, N. 2009. *Propagation of Sound in Porous Media: Modelling Sound Absorbing Materials*.

Atalla, N. & Sgard, F. (2007) Modeling of perforated plates and screens using rigid frame porous models. *Journal of sound and vibration*, 303(1-2), 195-208.

Baldwin, C., Garrison, G., Russell, P. & Schnell, A. (1969) Suppression of combustion oscillations with mechanical devices Interim report.

BARON RAYLEIGH, J. (1871) On the theory of resonance. *Philos. Trans.*, 161, 77-118.

Batchelor, G. (1967) An introduction to fluid dynamics. 1967. *Cambridge,: UP xviii*, 615.

Bauer, A. B. (1977) Impedance theory and measurements on porous acoustic liners. *Journal of Aircraft*, 14(8), 720-728.

Bellucci, V., Flohr, P., Paschereit, C. & Magni, F. (2004a) On the use of Helmholtz resonators for damping acoustic pulsations in industrial gas turbines. *Journal of engineering for gas turbines and power*, 126(2), 271-275.

Bellucci, V., Flohr, P. & Paschereit, C. O. (2004b) Numerical and Experimental Study of Acoustic Damping Generated by Perforated Screens. *AIAA journal*, 42(8), 1543-1549.

Bellucci, V., Paschereit, C. O. & Flohr, P. Impedance of perforated screens with bias flow 2002.

Bellucci, V., Paschereit, C. O. & Flohr, P. (2002) Impedance of perforated screens with bias flow, *8th AIAA/CEAS Aeroacoustics Conference & Exhibit*.

Beranek, L. L. (1954) Acoustics New York. McGraw Hill Electrical and Elec.

Betts, J., Follet, J., Kelly, J. & Thomas, R. (2000) Evaluation of an impedance model for perforates including the effect of bias flow, *6th Aeroacoustics Conference and Exhibit*.

Betts, J. F. (2000) *Experiments and impedance modeling of liners including the effect of bias flow*Virginia Tech.

Bies, D. A. & Wilson Jr, O. (1957) Acoustic impedance of a Helmholtz resonator at very high amplitude. *The Journal of the Acoustical Society of America*, 29(6), 711-714.

Blokhintsev, D. (1956) *Acoustics of a Nonhomogeneous Moving Medium*National Advisory Committee for Aeronautics Washington, DC.

Boden, H. & Zhou, L. (2012) Acoustic properties of an in-duct orifice subjected to bias flow and high level acoustic excitation, *10th International Conference on Flow-Induced Vibration (& Flow-Induced Noise); Dublin, Ireland, 2nd-6th July 2012*.

Bolt, R., Labate, S. & Ingård, U. (1949) The acoustic reactance of small circular orifices. *The Journal of the Acoustical Society of America*, 21(2), 94-97.

Bräunling, W. (2009) *Berlin, Flugzeugtriebwerke-Grundlagen, Aero-Thermodynamik, ideale und reale Kreisprozesse, Thermische Turbomaschinen, Komponenten, Emissionen und Systeme, 3. auflage ed*[Video].

Burgos, R. P., Zapata, F., Wiechman, E. & Salazar, L. (1998) Power converter analysis and design using Matlab: a transfer function approach, *IEEE International Symposium on Industrial Electronics. Proceedings. ISIE'98 (Cat. No. 98TH8357)*. IEEE.

Champoux, Y. & Allard, J. F. (1991) Dynamic tortuosity and bulk modulus in air‐saturated porous media. *Journal of Applied Physics*, 70(4), 1975-1979.

Community PLM Siemens automation (2016, July 07) *Frequency response function*, 2016, July 07. Available online: https://community.plm.automation.siemens.com/t5/Testing-Knowledge-Base/What-is-a-Frequency-Response-Function-FRF/ta-p/354778 [Accessed June 21 2019].

Crandall, I. (1926a) Theory of Vibrating Systems and Sound,(1927). D. van Nostrand.

Crandall, I. B. (1926b) *Theory of vibrating systems and sound*D. Van Nostrand Company.

Crandall, I. B. (1954) *Theory of vibrating systems and sound*D. Van Nostrand Company.

Cremer, L. (1948) On the acoustic boundary layer outside a rigid wall. *Arch. Elektr. Uebertr*, 2, 235.
Cummings, A. (1984) Acoustic nonlinearities and power losses at orifices. *AIAA journal*, 22(6), 786-792.
Cummings, A. (1986) Transient and multiple frequency sound transmission through perforated plates at high amplitude. *The Journal of the Acoustical Society of America*, 79(4), 942-951.
Daniels, F. B. (1947) Acoustical impedance of enclosures. *The Journal of the Acoustical Society of America*, 19(4), 569-571.
Davern, W. A. (1977) Perforated facings backed with porous materials as sound absorbers—An experimental study. *Applied Acoustics*, 10(2), 85-112.
Dean, L. (1975) Coupling of Helmholtz resonators to improve acoustic liners for turbofan engines at low frequency.
Dean, P. (1974) An in situ method of wall acoustic impedance measurement in flow ducts. *Journal of Sound and Vibration*, 34(1), 97-IN6.
Dean, P. D. & Tester, B. J. (1975) Duct wall impedance control as an advanced concept for acoustic impression.
Deicon Dynamics & Control (2009) *Acoustic Impedance of Perforated Liners*, 2009. Available online: http://www.deicon.com/wp-content/uploads/2014/02/Acoustic-Impedance-of-Perforated-Liners1.pdf [Accessed 07/11/2019].
Dickey, N., Selamet, A. & Ciray, M. (2001) An experimental study of the impedance of perforated plates with grazing flow. *The Journal of the Acoustical Society of America*, 110(5), 2360-2370.
Dietrich, P. (2013) *Uncertainties in acoustical transfer functions: modeling, measurement and derivation of parameters for airborne and structure-borne sound*, *16*Logos Verlag Berlin GmbH.
Dowling, A. P. & Hughes, I. J. (1992) Sound absorption by a screen with a regular array of slits. *Journal of Sound and Vibration*, 156(3), 387-405.
Dowling, A. P. & Stow, S. R. (2003) Acoustic analysis of gas turbine combustors. *Journal of propulsion and power*, 19(5), 751-764.
E-09, A. (2009) Standard Test Method for Measurement of Normal Incidence Sound Transmission of Acoustical Materials Based on the Transfer Matrix Method. *American Society for Testing and Material*.
Eldredge, J. D. & Dowling, A. P. (2003) The absorption of axial acoustic waves by a perforated liner with bias flow. *Journal of Fluid Mechanics*, 485, 307-335.
Elnady, T. (2004) *Modelling and characterization of Perforates in Lined Ducts and Mufflers*Farkost och flyg.
Elnady, T., Bodén, H. & Kontio, T. (2004) Impedance of SDOF perforated liners at high temperatures, *10th AIAA/CEAS Aeroacoustics Conference*.
Engineeringtoolbox (2003,) *Specific heat ratio of air*, 2003,. Available online: https://www.engineeringtoolbox.com/specific-heat-ratio-d_602.html [Accessed January, 2018].
Engineeringtoolbox (2004) *Orifice, Nozzle and Venturi Flow Rate Meters*, 2004. Available online: https://www.engineeringtoolbox.com/orifice-nozzle-venturi-d_590.html [Accessed 02/07/2019].
Fok, V. A. (1941) Teoreticheskoe issledovanie provodimosti kruglogo otverstiya v peregorodke, postavlennoi poperek truby (Theoretical study of the conductance of a circular hole in a partition across a tube). *Doklady Akademii Nauk SSSR (Soviet Physics Doklady)*, 31(9), 875-882.
Follet, J., Betts, J. & Kelly, J. (2001) Improvements to acoustic liner broadband absorption using bias flow, *39th Aerospace Sciences Meeting and Exhibit*.
Foltz, H. L. (1993) Multi-hole film cooled combustor liner with rectangular film restarting holes. Google Patents.
Forchheimer, P. (1901) Wasserbewegung durch boden. *Z. Ver. Deutsch, Ing.*, 45, 1782-1788.
Forster, S. & Michel, U. (2003) Experimental investigation of the dissipation of acoustic energy in perforated walls with bias flow, *International Colloquium on Combustion and Noise Control*.
Frank, Lees, M., Lees, F. P. & Mannan, S. (2005) *Lees' loss prevention in the process industries*Butterworth-Heinemann.
Frey, A. P. & Kinsler, L. E. (1950) *Fundamentals of acoustics*John Wiley & Sons.
Gas-Turbine-Industries, M. H. (2011) Turbine Inlet Temperature.

Gerendas, M., Höschler, K. & Schilling, T. (2003) *Development and modeling of angled effusion cooling for the BR715 low emission staged combustor core demonstrator*.
Goh, C. S. & Morgans, A. S. (2013) The influence of entropy waves on the thermoacoustic stability of a model combustor. *Combustion Science and Technology*, 185(2), 249-268.
Goldman, A. & Panton, R. L. (1976) Measurement of the acoustic impedance of an orifice under a turbulent boundary layer. *The Journal of the Acoustical Society of America*, 60(6), 1397-1405.
Grace, S. M., Horan, K. P. & Howe, M. S. (1998) THE INFLUENCE OF SHAPE ON THE RAYLEIGH CONDUCTIVITY OF A WALL APERTURE IN THE PRESENCE OF GRAZING FLOW. *Journal of Fluids and Structures*, 12(3), 335-351.
Guess, A. (1975a) Calculation of perforated plate liner parameters from specified acoustic resistance and reactance. *Journal of Sound and Vibration*, 40(1), 119-137.
Guess, A. W. (1975b) Calculation of perforated plate liner parameters from specified acoustic resistance and reactance. *Journal of Sound and Vibration*, 40(1), 119-137.
Haynes, J., Janssen, J., Russell, C. & Huffman, M. (2006) *Advanced combustion systems for next generation gas turbines*.
Heidelberg, L., Rice, E. & Homyak, L. (1980) Experimental evaluation of a spinning-mode acoustic-treatment design concept for aircraft inlets.[suppression of YF-102 engine fan noise].
Hersh, A., Walker, B. & Celano, J. (2003) Helmholtz resonator impedance model, part 1: Nonlinear behavior. *AIAA journal*, 41(5), 795-808.
Hersh, A. S. & Rogers, T. (1976) *Fluid mechanical model of the acoustic impedance of small orifices*, *2682*.
Heuwinkel, C., Enghardt, L. & Rohle, I. (2007) Experimental investigation of the acoustic damping of perforated liners with bias flow, *13th AIAA/CEAS Aeroacoustics Conference (28th AIAA Aeroacoustics Conference)*.
Howe, M. (1979) On the theory of unsteady high Reynolds number flow through a circular aperture. *Proceedings of the Royal Society of London. A. Mathematical and Physical Sciences*, 366(1725), 205-223.
Howe, M. (1984) On the absorption of sound by turbulence and other hydrodynamic flows. *IMA Journal of Applied Mathematics*, 32(1-3), 187-209.
Howe, M. (1995) The damping of sound by wall turbulent shear layers. *The Journal of the Acoustical Society of America*, 98(3), 1723-1730.
Howe, M. (1997) Influence of cross-sectional shape on the conductivity of a wall aperture in mean flow. *Journal of sound and vibration*, 207(5), 601-616.
Howe, M. S. (1998) *Acoustics of fluid-structure interactions*Cambridge university press.
Howe, M. S. & Howe, M. S. (1998) *Acoustics of fluid-structure interactions*Cambridge university press.
Hughes, I. & Dowling, A. (1990a) The absorption of sound by perforated linings. *Journal of Fluid Mechanics*, 218, 299-335.
Hughes, I. J. & Dowling, A. P. (1990b) The absorption of sound by perforated linings. *Journal of Fluid Mechanics*, 218(1), 299-335.
Hughes, I. J. & Dowling, A. P. (1990c) The absorption of sound by perforated linings. *Journal of Fluid Mechanics*, 218, 299-335.
Idelchik, I. & Fried, E. (2005) Handbook if Hydraulic Resistance. Jaico Publishing House, Mumbai.
Ingard, U. (1953) On the theory and design of acoustic resonators. *The Journal of the acoustical society of America*, 25(6), 1037-1061.
Ingard, U. & Ising, H. (1967) Acoustic nonlinearity of an orifice. *The journal of the Acoustical Society of America*, 42(1), 6-17.
Ingård, U. & Labate, S. (1950) Acoustic circulation effects and the nonlinear impedance of orifices. *The Journal of the Acoustical Society of America*, 22(2), 211-218.
Jing, X. & Sun, X. (1999) Experimental investigations of perforated liners with bias flow. *The Journal of the Acoustical Society of America*, 106(5), 2436-2441.

Jing, X. & Sun, X. (2000) Effect of plate thickness on impedance of perforated plates with bias flow. *AIAA journal*, 38(9), 1573-1578.
Jing, X., Sun, X., Wu, J. & Meng, K. (2001) Effect of grazing flow on the acoustic impedance of an orifice. *AIAA journal*, 39(8), 1478-1484.
Johnson, D. L., Koplik, J. & Dashen, R. (1987) Theory of dynamic permeability and tortuosity in fluid-saturated porous media. *Journal of fluid mechanics*, 176, 379-402.
Kabral, R., Boden, H. & Elnady, T. (2014) Determination of liner impedance under high temperature and grazing flow conditions, *20th AIAA/CEAS Aeroacoustics Conference*.
Kang, Y. & Jung, I. (2001) Sound propagation in circular ducts lined with noise control foams. *Journal of sound and vibration*, 239(2), 255-273.
Keller, J. J. & Zauner, E. (1995) On the use of Helmholtz resonators as sound attenuators. *Zeitschrift für angewandte Mathematik und Physik ZAMP*, 46(3), 297-327.
Kinsler, L., Frey, A., Coppens, A. & Sanders, J. (1982) Fundamentals of Acoustics, John Wiley. *New York*.
Kinsler, L. E., Frey, A. R., Coppens, A. B. & Sanders, J. V. (1999) Fundamentals of acoustics. *Fundamentals of Acoustics, 4th Edition, by Lawrence E. Kinsler, Austin R. Frey, Alan B. Coppens, James V. Sanders, pp. 560. ISBN 0-471-84789-5. Wiley-VCH, December 1999.*, 560.
Kirchhoff, G. (1868a) On the influence of heat conduction in a gas on sound propagation. *Ann. Phys. Chem*, 134, 177-193.
Kirchhoff, G. (1868b) Ueber den Einfluss der Wärmeleitung in einem Gase auf die Schallbewegung. *Annalen der Physik*, 210(6), 177-193.
Knobloch, K., Lahiri, C., Enghardt, L., Bake, F. & Peitsch, D. (2011) Hot-acoustic-testrig (hat): A unique facility for thermoacoustic research, *ASME 2011 Turbo Expo: Turbine Technical Conference and Exposition*. American Society of Mechanical Engineers Digital Collection.
Kraft, R., Yu, J. & Kwan, H. (1999) Acoustic Treatment Design Scaling Methods. Volume 2; Advanced Treatment Impedance Models for High Frequency Ranges.
Krebs, W., Bethke, S., Lepers, J., Flohr, P., Prade, B., Johnson, C. & Sattinger, S. (2005) Thermoacoustic design tools and passive control: Siemens power generation approaches. *Combustion Instabilities in Gas Turbine Engines Operational Experience, Fundamental Mechanisms and Modeling*.
Lahiri, C. (2014) Acoustic performance of bias flow liners in gas turbine combustors.
Lahiri, C. & Bake, F. (2017) A review of bias flow liners for acoustic damping in gas turbine combustors. *Journal of Sound and Vibration*, 400, 564-605.
Lahiri, C., Enghardt, L., Bake, F., Sadig, S. & Gerendás, M. (2011) Establishment of a high quality database for the acoustic modeling of perforated liners. *Journal of Engineering for Gas Turbines and Power*, 133(9), 091503.
Lahiri, C., Knobloch, K., Bake, F. & Enghardt, L. Acoustic measurements of perforated liners in hot and pressurized flow 2013. American Society of Mechanical Engineers.
Lamb, H. (1932) *Hydrodynamics*Cambridge university press.
Lawn, C. (2015) Calculation of acoustic absorption in ducts with perforated liners. *Applied Acoustics*, 89, 211-221.
Lawn, C. (2016) The acoustic impedance of perforated plates under various flow conditions relating to combustion chamber liners. *Applied Acoustics*, 106, 144-154.
Lawrence, E. K., Austin, R. F., Alan, B. C. & James, V. S. (2000) Fundamentals of acoustics. *New yorks: John wileys*, 151.
Lee, S.-H. & Ih, J.-G. (2003) Empirical model of the acoustic impedance of a circular orifice in grazing mean flow. *The Journal of the Acoustical Society of America*, 114(1), 98-113.
Lee, S.-H., Ih, J.-G. & Peat, K. S. (2007) A model of acoustic impedance of perforated plates with bias flow considering the interaction effect. *Journal of Sound and Vibration*, 303(3-5), 741-752.
Lefebvre, A. H. & Ballal, D. R. (2010) *Gas turbine combustion: alternative fuels and emissions*CRC press.
Lieuwen, T. C. (2012) *Unsteady combustor physics*Cambridge University Press.

Lieuwen, T. C. & Yang, V. (2005) *Combustion instabilities in gas turbine engines: operational experience, fundamental mechanisms, and modeling*American Institute of Aeronautics and Astronautics.
Luong, T., Howe, M. S. & McGowan, R. S. (2005) On the Rayleigh conductivity of a bias-flow aperture. *Journal of Fluids and Structures*, 21(8), 769-778.
Maa, D.-Y. (1998) Potential of microperforated panel absorber. *the Journal of the Acoustical Society of America*, 104(5), 2861-2866.
Mannan, S. (2005) *Lees' loss prevention in the process industries*Butterworth-Heinemann.
Mathews Jr, W. (1986) Superposition and energy conservation for small amplitude mechanical waves. *American Journal of Physics*, 54(3), 233-238.
McAuliffe, C. E. (1950) The influence of high speed air flow on the behavior of acoustical elements.
Melling, T. (1973a) An impedance tube for precision measurement of acoustic impedance and insertion loss at high sound pressure levels. *Journal of Sound and Vibration*, 28(1), 23-IN1.
Melling, T. H. (1973b) The acoustic impendance of perforates at medium and high sound pressure levels. *Journal of Sound and Vibration*, 29(1), 1-65.
Meyer, E. (2012) *Physical and Applied Acoustics: An Introduction*Elsevier Science.
Miller, D. (1990) Internal Flow Systems, BHRA (Information Services). *The Fluid Engineering Centre, Cranfield, Bedford, UK*.
Mongia, H., Held, T., Hsiao, G. & Pandalai, R. (2005) Incorporation of combustion instability issues into design process: GE aeroderivative and aero engines experience. *Combustion instabilities in gas turbine engines*.
Morse, P. (1948) "Vibration and Sound." McGraw-Hill, New York; reprinted.
Morse, P. M. (1968) KU Ingard, Theoretical Acoustics. *Princeton University Press, 949p*, 4, 150.
Morse, P. M. & Ingard, K. U. Theoretical Acoustics 1968 New York. *CO: McGraw-Hill*, 419.
Munjal, M. L. & Doige, A. G. (1990) Theory of a two source-location method for direct experimental evaluation of the four-pole parameters of an aeroacoustic element. *Journal of Sound and Vibration*, 141(2), 323-333.
Musa, N. A. & Bityong, B. S. (2018) Determination of Orifice Coefficients for Flow through Circular and Rectangular Orifices. *ATBU Journal of Science, Technology and Education*, 6(1), 188-197.
Nesterov, V. (1941) An experimental study of the acoustical conductivity of a circular orifice in a partition placed across a tube, *Dokl. Akad. Nauk SSSR*.
Neutrium (2015) *Discharge coefficient for nozzles and orifices*, 2015. Available online: https://neutrium.net/fluid_flow/discharge-coefficient-for-nozzles-and-orifices/ [Accessed 02/07/2019].
Norris, A. & Sheng, I. (1989) Acoustic radiation from a circular pipe with an infinite flange. *Journal of Sound and Vibration*, 135(1), 85-93.
Ntamba, N. & Mulumba, B. (2011) *Non-Newtonian pressure loss and discharge coefficients for short square-edged orifices plates*Cape Peninsula University of Technology.
Panton, R. L. & Miller, J. M. (1975) Resonant frequencies of cylindrical Helmholtz resonators. *The Journal of the Acoustical Society of America*, 57(6), 1533-1535.
Parrott, T. & Zorumski, W. (1971) Nonlinear acoustic theory for rigid porous materials.
Peat, K. S., Ih, J.-G. & Lee, S.-H. (2003) The acoustic impedance of a circular orifice in grazing mean flow: Comparison with theory. *The Journal of the Acoustical Society of America*, 114(6), 3076-3086.
Peters, M., Hirschberg, A., Reijnen, A. & Wijnands, A. (1993) Damping and reflection coefficient measurements for an open pipe at low Mach and low Helmholtz numbers. *Journal of Fluid Mechanics*, 256, 499-534.
Picolet, L. E. (1927) Theory of vibrating systems and sound: By Irving B. Crandall, Ph. D., Member of the Technical Staff, Bell Telephone Laboratories, Inc. x–272 pages, 23× 15 cm., cloth. New York, D. Van Nostrand Company, 1926. Price, $5 net. Pergamon.
Premo, J. (1999) The application of a time-domain model to investigate the impedance of perforate liners including the effects of bias flow, *5th AIAA/CEAS Aeroacoustics Conference and Exhibit*.

Rademaker, E. R., van der Wal, H. M. M. & Geurts, E. G. M. (2009) Hot-stream in-situ acoustic impedance measurements on various air-filled cavity and porous liners.
Rayleigh, J. (1945a) The Theory of Sound, vol. 2Dover. *New York*, 226-235.
Rayleigh, J. W. S. (1870) On the theory of resonance. *Transactions of the Royal Society (London) A*, 161.
Rayleigh, J. W. S. (1945b) The Theory of Sound, Vol. II, 162. Dover Publication Inc.
Rayleigh, J. W. S. (1945c) The theory of sound, Volume Two. Dover Publications, Inc.: New York, NY, USA.
Rayleigh, L. (1940) Theory of Sound, Vol. II, 322 i. Macmillan.
Rice, E. J. (1971) A model for the acoustic impedance of a perforated plate liner with multiple frequency excitation.
Rice, E. J. (1976) Theoretical study of the acoustic impedance of orifices in the presence of a steady grazing flow. *The Journal of the Acoustical Society of America*, 59(S1), S32-S32.
Richter, C., Lahiri, C., Bake, F., Knobloch, K., Pongratz, R. & Redmann, D. (2016) Impedance and attenuation measurements of acoustic absorbers in a hot environment, *22nd AIAA/CEAS Aeroacoustics Conference*.
Rienstra, S. Impedance models in time domain, including the extended Helmholtz resonator model, *12th AIAA/CEAS Aeroacoustics Conference (27th AIAA Aeroacoustics Conference)*.
Rienstra, S. (1983) A small Strouhal number analysis for acoustic wave-jet flow-pipe interaction. *Journal of Sound and Vibration*, 86(4), 539-556.
Rupp, J., Carrotte, J. & Macquisten, M. (2012) The use of perforated damping liners in aero gas turbine combustion systems. *Journal of engineering for gas turbines and power*, 134(7), 071502.
Rzhevkin, S. N. (1963) *Acourse of Lectures on the Theory of Sound*Pergamon Press;[distributed in the Western Hemisphere by Macmillan, New York].
Salikuddin, M. & Ahuja, K. (1983) Acoustic power dissipation on radiation through duct terminations: Experiments. *Journal of Sound and Vibration*, 91(4), 479-502.
Saunders, N. (1996) Phase diagram calculations for Ni-based superalloys. *ROLLS ROYCE PLC-REPORT-PNR*.
Savitzky, A. & Golay, M. J. (1964) Smoothing and differentiation of data by simplified least squares procedures. *Analytical chemistry*, 36(8), 1627-1639.
Scarpato, A., Tran, N., Ducruix, S. & Schuller, T. (2012) Modeling the damping properties of perforated screens traversed by a bias flow and backed by a cavity at low Strouhal number. *Journal of Sound and Vibration*, 331(2), 276-290.
Schultz, T., Liu, F., Cattafesta, L., Sheplak, M. & Jones, M. (2009) Comparison Study of Normal-Incident Acoustic Impedance Measurements of a Perforate Liner, *15th AIAA/CEAS Aeroacoustics Conference (30th AIAA Aeroacoustics Conference)*.
Seybert, A. F. (2000) Fundamental of linear acoustics. Boundary element acoustics; Fundamentals and computer codes, edited by TW Wu, WIT Press.
Seybert, A. F. & Ross, D. F. (1977) Experimental determination of acoustic properties using a two-microphone random-excitation technique. *the Journal of the Acoustical Society of America*, 61(5), 1362-1370.
Siemens (1996 – 2019) *Siemens SGT-400 Gas Turbine* 1996 – 2019. Available online: https://new.siemens.com/global/en.html [Accessed 11/11/2019].
Sirignano, W. (1966) Nonlinear dissipation in acoustic liners. *Princeton University AMS Report*, 553-F31.
Sivian, L. J. (1935) Acoustic impedance of small orifices. *The Journal of the Acoustical Society of America*, 7(2), 94-101.
Soares, C. (2011) *Gas turbines: a handbook of air, land and sea applications*Elsevier.
Standard, B. (2001) Acoustics-Determination of Sound Absorption Coefficient and Impedance in Impedance Tubes—Part 2: Transfer-Function Method. *BS EN ISO*, 10534-2.

Stinson, M. R. & Shaw, E. (1985) Acoustic impedance of small, circular orifices in thin plates. *The Journal of the Acoustical Society of America*, 77(6), 2039-2042.
Stokes, G. G. (1851) *On the effect of the internal friction of fluids on the motion of pendulums*, *9*Pitt Press Cambridge.
Straightening, A. F. (2005) To: Dr. Glen E. Thorncroft, Mechanical Engineering Department From: William Blazejowski (initial by your name) Charles Lumley (initial by your name) Date: January 1, 2005.
Suhanek, M., Jambrosic, K. & Domitrovic, H. (2008) Student project of building an impedance tube. *Journal of the Acoustical Society of America*, 123(5), 3616.
Sullivan, J. W. & Crocker, M. J. (1978) Analysis of concentric-tube resonators having unpartitioned cavities. *The Journal of the Acoustical Society of America*, 64(1), 207-215.
Sun, X., Jing, X., Zhang, H. & Shi, Y. (2002) Effect of grazing–bias flow interaction on acoustic impedance of perforated plates. *Journal of Sound and Vibration*, 254(3), 557-573.
Tayong, R. (2013) On the holes interaction and heterogeneity distribution effects on the acoustic properties of air-cavity backed perforated plates. *Applied acoustics*, 74(12), 1492-1498.
Thurston, G. B. (1952a) Apparatus for absolute measurement of analogous impedance of acoustic elements. *The Journal of the Acoustical Society of America*, 24(6), 649-652.
Thurston, G. B. (1952b) Periodic fluid flow through circular tubes. *The Journal of the Acoustical Society of America*, 24(6), 653-656.
Thurston, G. B. & Martin Jr, C. E. (1953) Periodic fluid flow through circular orifices. *The Journal of the Acoustical Society of America*, 25(1), 26-31.
Tournadre, J., Förner, K., Martinez-Lera, P., Polifke, W. & Desmet, W. (2016a) Determination of acoustic impedance for Helmholtz resonators through incompressible unsteady flow simulations, *22nd AIAA/CEAS Aeroacoustics Conference*.
Tournadre, J., Förner, K., Polifke, W., Martínez-Lera, P. & Desmet, W. (2016b) Determination of acoustic impedance for Helmholtz resonators through incompressible unsteady flow simulations. *AIAA Journal*, 55(3), 790-798.
Umnova, O., Attenborough, K., Standley, E. & Cummings, A. (2003) Behavior of rigid-porous layers at high levels of continuous acoustic excitation: Theory and experiment. *The Journal of the Acoustical Society of America*, 114(3), 1346-1356.
Von Helmholtz, H. (1863) *Die Lehre von den Tonempfindungen*Friedrich Vieweg und Soyhn.
Wang, J., Rubini, P., Qin, Q. & Houston, B. (2019) A Model to Predict Acoustic Resonant Frequencies of Distributed Helmholtz Resonators on Gas Turbine Engines. *Applied Sciences*, 9(7), 1419.
Welch, M. & Igoe, B. M. (2013) Combustion, Fuels and Emissions for Industrial Gas Turbines.
Wendoloski, J. (1998) Sound absorption by an orifice plate in a flow duct. *The Journal of the Acoustical Society of America*, 104(1), 122-132.
Zinn, B. T. (1970) A theoretical study of non-linear damping by helmholtz resonators. *Journal of Sound and Vibration*, 13(3), 347-356.

8 Appendix-A

8.1 Hot Acoustic Test-Rig

Thermo-acoustic instability in a gas turbine is a critical implementation of modern combustion concepts. Advanced combustors are designed for low emission and higher efficiency. This has been achieved by rearranging liner walls and introducing a number of small holes into the system. There are variable parameters such as orifice shape, orifice edge, orifice profile, orifice thickness, orifice orientation and the introduction of double-layer combustor liners. To cool down the hot air uniformly, bias flow has been introduced progressively in the flame tube. Approximately one-third of it is used to reduce the gas temperature in the zone of dilution and the rest is used for cooling the combustor walls. This has been achieved by introducing variable bias flows into the combustor depending upon the operating load conditions. To advance a specific measure to prevent thermo-acoustic instability in a real combustor, it is essential to develop acoustic boundary conditions. To make that prediction, calculation of acoustic reflection coefficient, impedance, and absorption coefficient is required. This HAT test rig can provide a validation strategy, which can represent the difference between running the test in ambient conditions and a high-temperature region.

8.2 Vision

Large corporations are often concerned with organisational strategies and thus develop a wide range of test facilities. HAT determination can take an organisation one step forward in modern technology. This new HAT test rig is unique; it possesses a zonal cavity to create a temperature difference. The upstream side of the test rig can raise the temperature range up to 500^{o}C, and the downstream side of the test rig can cool the cavity to near 40^{o}C. The temperature difference can provide information to help observe and understand the effect of impedance in the ΔT region.

8.3 Benefits

The fundamental capabilities of the HAT largely outweigh the cost. The two Microphone Method (TMM) (Standard, 2001) has been applied to the HAT test rig to determine the reflection coefficient, absorption coefficient, and impedance. In this method, algorithms can be easily implemented by a Fast Fourier Transform (FFT) analysis. To determine impedance on the boundary plane, the liner can be actuated in between the upstream and downstream sections. Measuring impedance in ambient temperatures is not difficult, but in reality, where

the temperature is very high, measuring impedance is critical. Execution of this HAT measurement can provide valuable advancements in modern technological development.

8.4 Deliverables

On successful completion of the HAT test rig, it can perform calculations of acoustic impedance, absorption coefficient, and reflection coefficient by using different types of perforated plates. In addition, the HAT test rig has the capability of introducing bias flow into the system. This means the variable resonance mode of acoustic field excitation to the fluctuation can be controlled by the variable bias flow rate. It has been established that the bias flow may substantially increase the acoustic damping properties of the perforates (Forster & Michel, 2003). Reduction of pollutants such as nitrogen oxides (NO_x), lowering emissions such as carbon monoxide (CO) and unburnt hydrocarbon (UHC), and increasing the efficiency of gas turbine combustors are ongoing issues ubiquitous in the recent industrial revolution. Under these circumstances, it is necessary to investigate the acoustic flow interaction of perforated liner impedance in the high-temperature region in the presence of bias flow.

8.5 Bias flow as an impedance governor

Advanced combustors are made of a double-layer liner with a number of holes present. Determining the hole size of the liner for optimum combustion is critical. Similarly, controlling the bias flow rate of hole velocity related to hole size under variable load conditions is also a complex task; however, effective execution of the HAT experiment could provide a solution (Bauer, 1977). Andrew B. Bauer (Bauer, 1977) developed a mathematical model and performed testing of porous panels by using the two-microphone technique. Howe (Howe, 1979), in his first model, used a single circular orifice where the thickness of the perforation was assumed to be zero with a high Reynolds number flow through the hole. Moreover, the hole spacing-to-radius ratio is large so that apertures do not interact with each other. Hughes and Dowling (Hughes & Dowling, 1990c) and Dowling and Hughes (Dowling & Hughes, 1992) expanded Howe's model to a perforated screen with a solid back wall, which can predict the optimal geometry and bias flow to produce a highly absorptive liner.

Howe's first model has an insufficient assumption of an infinitesimal wall thickness, which is absent in his first model. Jing and Sun (Jing & Sun, 1999) modified Howe's model (Howe, 1979) by adding plate thickness, which was first used by Rayleigh (Rayleigh, 1945b) in the absence

of mean flow. Jing and Sun (Jing & Sun, 1999) investigation of the acoustic properties of perforated liners shows that in the presence of bias flow absorption coefficient and bandwidth increase significantly. Later Jing and Sun (Jing & Sun, 2000) included a finite wall thickness and correction of Howe's equations. Therefore, the equations were solved by using a boundary element method by considering the thickness effect. Luong T and Howe (Luong et al., 2005) used Cumming's equation (Cummings, 1984; Cummings, 1986) to develop a simple formula for the Rayleigh conductivity of a circular aperture in the presence of bias flow, in an infinitesimally thin wall and in a wall of finite thickness. Bellucci and Flohr (Bellucci et al., 2002) developed a model to predict the acoustic impedance of perforated screens with bias flow ranging from the nonlinear (no bias flow) to the linear (bias flow velocity larger than acoustic velocity). Eldredge and Dowling (Eldredge & Dowling, 2003) investigated Howe's model for a cylindrical perforated liner with mean bias flow in its absorption of plane acoustic waves. They developed equations for the stagnation enthalpy and the acoustic particle velocity in the line section of a duct by applying mass momentum balance to define control volume. Dean and Tester (Dean & Tester, 1975) investigated experimentally, and their results exhibited that acoustic impedance could be controlled by manipulating bias flow velocity.

Seong Hyun Lee (Lee et al., 2007) has discussed the effect of interaction between orifices on the acoustic impedance of perforated plates in the presence of bias flow, which was analysed both numerically and experimentally. Measured and predicted acoustic impedance were compared for varying porosity and thickness to radius ratio. If the porosity increases, the reactance tends to decrease because of the interaction effect between the orifices. The predicted impedance considering the interaction effect showed a reasonable agreement with measured data over the range of porosity used in their experiments. Ingard (Ingard, 1953) analysed the two apertures interaction effect and found that end correction was needed due to viscosity, heat conduction, and radiation on the separation. In his Master's thesis, McAuliffe (McAuliffe, 1950) explained that the acoustic mass or reactance of an orifice decreases sharply with airflow over a short range of values, and then remains reasonably constant at higher rates of flow. An investigation of acoustic interaction end correction conducted by Fok and Rzhevkin (Fok, 1941; Rzhevkin, 1963) provided the solution for the case of an infinitely thin plate, and expressed this end correction as a function of the ratio of hole diameter and distance between the hole midpoints. Ingard (Ingard, 1953) suggested that a

hole interaction effect takes place out of the aperture linked to the propagation inside the aperture.

8.6 Success criterion

On the effective accomplishment of experimental analysis, it will be possible to address the effect of impedance in a high-temperature region in the ΔT medium. Furthermore, there is the potential to measure the absorption coefficient and reflection coefficient. During the acoustic analysis of the plane wave inside the HAT test rig, a flat sample of gas turbine combustor liner will be used to determine the effect of acoustic pressure in the high-temperature region. From acoustic pressure, time-domain data needs to be converted in the frequency domain, then it will be assessed for impedance. Possible successful criteria may include increased gas turbine combustion efficiency, reduced fuel consumption, decreased NO_x level, lowering of CO_2 emissions, mapping combustion instability and prediction of a suitable solution. These can be addressed as a promotion of energy efficiency investment and improved energy management practice. Theoretically, the investment costs of this project are outweighed by the huge potential it can provide for the industry. The benefits of this project include lowered energy consumption, improved vibration, improved efficiency, and improved low carbon solutions, and can take this investigation to a brand new level of innovation.

8.7 Background work

In recent years the German Aerospace Centre (DLR) in Berlin has set up a HAT test rig developed by Knobloch et al. (Knobloch et al., 2011). The features of their HAT test are rig temperatures 500-600^{o}C, Mach number 0-0.8, frequency range 150-2800, maximum pressure 10 bar, mass flow rate up to 0.75 Kg/s and duct diameter 70-75mm. Their HAT test rig has been designed to overcome thermo-acoustic instability in a gas turbine combustor, which involves evaluating the influence of thermos-acoustic behaviour of hot streamliners in high pressure and temperature regions. In order to conduct high quality acoustic measurements in hot and pressurized flow, three major challenges need to be addressed: controllable and reproducible operating conditions, sufficiently sensitive sensor technology, and the data analysis methodology (Lahiri et al., 2011). Air temperature inside the acoustic liner cavities is an important acoustic quantity and needs to be monitored during the acoustic liner measurement (Richter et al., 2016).

The Royal Institute of Technology (KTH) in Sweden also have a HAT test rig setup. They have used four commercial hot air blowers to create hot crossflow, along with surface heaters to increase local temperature. To determine liner impedance in the high-temperature region under hot stream conditions, Karbal et al. (Kabral et al., 2014) performed the experiment to explain that the effect of high temperature is related to a change of medium properties. It was found that the temperature effect on the impedance can be predicted quite well by changing the fluid properties (density, viscosity, and speed of sound) Elandy et al. (Elnady et al., 2004).

The National Aerospace Laboratory (NLR) has performed Hot-Stream acoustic impedance measurements on various air-filled cavities and porous liners to reduce turbofan engine exhaust noise. It was useful and cost-effective to determine the acoustic liner properties. The test metrics covered six engine operating conditions and reveal that the perforated type has a resistance, which is strongly dependent on grazing flow, Mach number and sound pressure level, and is nearly independent of temperature. The linear type has a resistance, which is nearly independent of grazing flow, Mach number and sound pressure level, and is strongly dependent on temperature (Rademaker et al., 2009).

In collaboration with The University of Hull and Siemens Lincoln, there is a possibility of future work to initiate a test rig for HAT operation to perform experimental analysis to predict gas turbine liner impedance in a high-temperature region. In this HAT test rig, within the upstream section, an electrically heated ceramic surface heater can be used to raise the temperature up to 500^0C, and the downstream section has a cooling cavity to create ΔT. In addition, there is an option to introduce variable compressed bias flow to the system. The primary focus of this type of experimental analysis is to measure high-quality acoustic data in a hot stream environment. It is necessary to design a perforated liner which can address additional thermos-acoustic damping to the combustor liner. Regrettably, such an optimum design does not yet exist. Consequently, it would be extremely advantageous to develop a HAT test rig where acoustic parameters such as bias flow rate, orifice geometry, orifice orientation, orifice thickness, and complicated thermodynamic behaviour relationships can be addressed in relation to the prediction of additional thermos-acoustic damping.

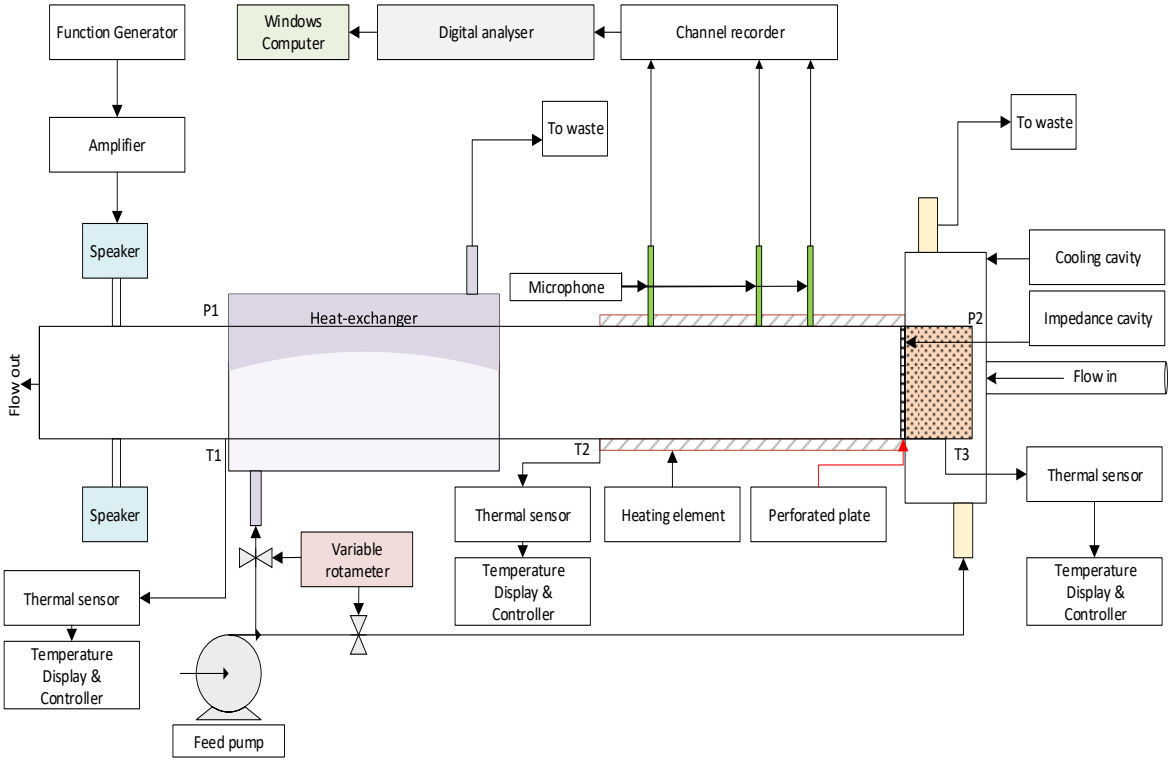

Figure 8.1 Schematic diagram of HAT test rig.

The schematic diagram of the HAT test rig shown in Figure 8.1. The flowchart shows that the upstream section has a radially mounted speaker, heat-exchanger, heating element, and microphone and the downstream section has a cooling cavity.

8.8 HAT configuration

The internal diameter of the test rig is 161.5 mm, and the total length of the test rig is 3160 mm. It has upstream and downstream sections. In the diagram shown in Figure 8.1 the upstream part has three radially mounded speakers connected to the impedance tube. Monacor KU-516 can be used as a loudspeaker; DLR in Germany (Knobloch et al., 2011) used the same type of speaker for their hot and pressurized experiment. To protect the sound source a heat exchanger has been introduced to the impedance tube. The function of this heat exchanger is to prevent heat propagating towards the loudspeaker. A temperature probe or thermal sensor needs to be introduced into the HAT test rig. Two temperature probes need to be installed in the upstream section. One is in the heating element where the temperature can be increased, and the second one is connected between the sound source and heat exchanger. The microphone can be installed closer to the sample liner to determine the acoustic pressure in the high-temperature region.

In the downstream section, a variable impedance cavity can be introduced along with differing load conditions. A water-cooled heat exchanger can be used to create ΔT across the liner. By using a feed pump, water can be introduced into the cooling cavity. Cavity temperature can be observed via a temperature probe connected to the impedance cavity. The mass flow rate of the water can be controlled by the variable rotameter. Based on cavity temperature requirements, the mass flow rate of water can be increased or decreased by a variable rotameter. On successful completion of measuring impedance into the HAT test rig in the no flow condition, it is possible to then introduce bias flow into the HAT test rig. There is an option to introduce compressed bias flow into the cavity through a variable piston type plunger. This is the most crucial part of the HAT test rig facility, where impedance measurement can be completed with the variable mass flow rate of bias flow in the high-temperature region. The measurement of acoustic pressure in the high-temperature region is extremely complicated. Acoustic data capture requires an accurate measurement technique, and the placement of the temperature sensor plays a vital role. In this HAT test rig, there are three positions where the temperature can be measured and controlled, shown in Figure 8.1 as T_1, T_2 & T_3.

8.9 Design view

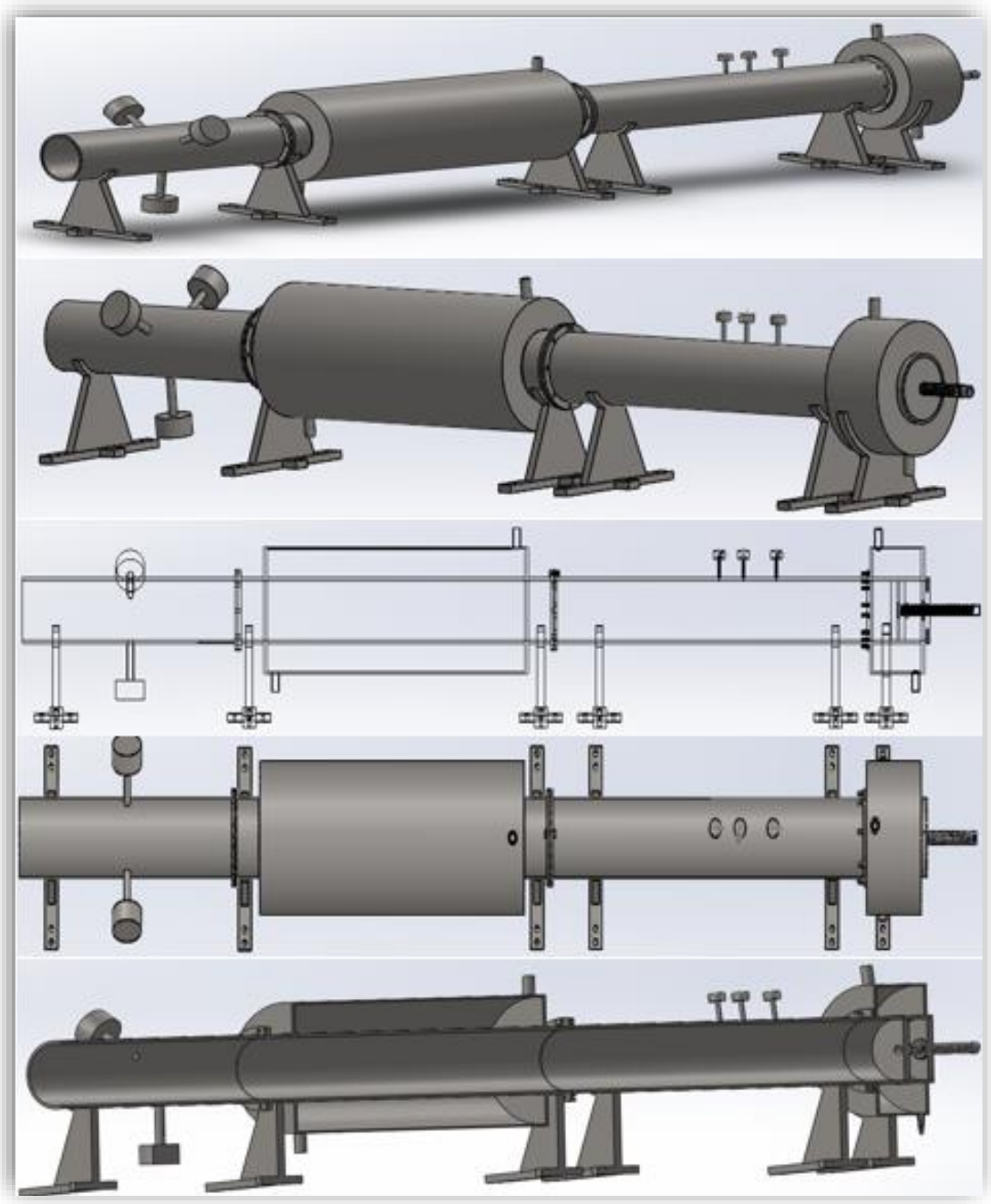

Figure 8.2 Isometric, skeleton, top and cross-sectional views of the HAT test rig.

Five different types of design view shown in Figure 8.2. The purpose of giving five different types of projection is to provide a more detailed explanation and clarification of the HAT test tig.

8.10 Thermal calculation

The framework of the HAT test rig is designed in such a way that components can be replaced and added based on necessity. The innovative idea of the HAT test rig is to observe the

impedance of a perforated plate in the high-temperature region. The American Society for Testing and Materials' (ASTM) A312 316 type stainless steel seamless pipe can be selected for the HAT test rig design. Wieldable and heavily cold worked austenitic stainless-steel pipes are intended to be more resistant than 304 types of stainless steel.

8.10.1 Impedance tube cooling load calculation

In this section, two different temperatures are selected for the HAT test rig experiment: 473K and 773K. The impedance tube cooling load calculation given in Table 8.2 and the schematic diagram is shown in Figure 8.3.

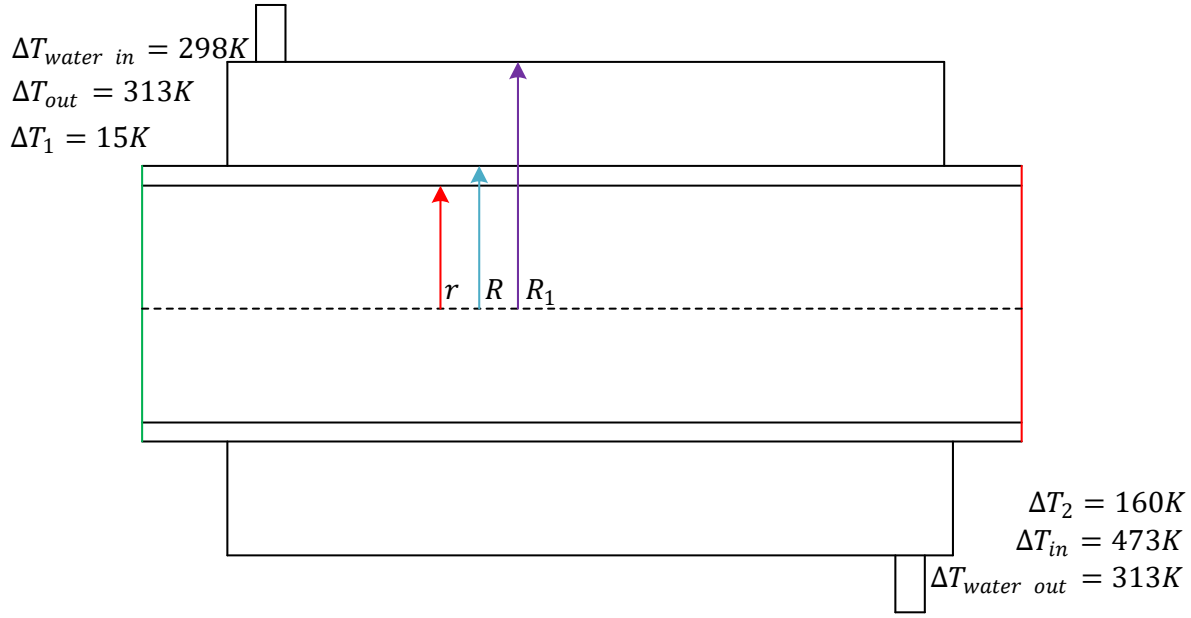

Figure 8.3 Schematic diagram of impedance tube counter-flow heat exchanger.

A counter flow double pipe heat exchanger is used to cool the impedance tube by using cold water. Assuming there is no airflow in the internal pipe, one end of the pipe is heated at $\Delta T_{in} = 473K$ and the working fluid (cold water) reduces the temperature at the other end of the pipe and leaves at $\Delta T_{out} = 313K$. The water flows in the counter heat exchanger at the entry point at $\Delta T_{water\ in} = 298K$ and leaves at $\Delta T_{water\ out} = 313K$. It is essential to calculate the mass flow rate ($\dot{m}_{water}$) to cool the impedance tube at $\Delta T_{out} = 313K$, the required length ($L_{water\ jacket}$) of a heat exchanger, and the total energy removed by the convective ($Q_{convection}$) heat transfer.

Material	*Specific heat*	*Thermal conductivity*	*Heat transfer coefficient*	*Mass density*
	J/Kg-K	*W/m-K*	*W/m^2-K*	*Kg/m^3*
Cast alloy steel	*440*	*38*	*4750*	*7300*
ASTM A312 316	*500 (485@200^{0}C)*	*16.3*	*4794*	*7990*
Stainless steel	*460*	*18*	*-*	*7800*
Cast carbon steel	*500*	*30*	*-*	*7800*
Alloy steel	*460*	*50*	*-*	*7700*
Water	*4200*	*0.6*	*1200*	*1000*
Air	*1005*	*0.024*	*200*	*1.225*
Radius				*Unit*
$\boldsymbol{r}$	*0.08075*	x	*0.0034*	*m*
$\boldsymbol{R}$	*0.08415*	l_c	*0.17*	*m*
$\boldsymbol{R_1}$	*0.17384*	l_{imp}	*0.9*	*m*
For 473K		*For 773K*		
$\Delta \boldsymbol{T_1} = \boldsymbol{T_{out}} - \boldsymbol{T_{waterin}}$*=15K*		$\Delta T_1 = T_{out} - T_{waterin}$ *=15K*		
$\Delta \boldsymbol{T_2}$*=*$\boldsymbol{T_{waterout}} - \boldsymbol{T_{in}}$*=160 K*		ΔT_2*=*$T_{waterout} - T_{in}$ *=460 K*		
$\Delta \boldsymbol{T_{water}}$*=15K*		ΔT_{water}*=15K*		
$\Delta \boldsymbol{T_{air}}$*=160K*		ΔT_{air}*=460K*		

Table 8.1 Impedance tube material characteristics and temperature difference.

Material characteristics of (ASTM) A312 316 type stainless steel specific heat, thermal conductivity, heat transfer coefficient, and mass density and impedance tube temperature differences are shown in Table 8.1. The solution for the impedance tube cooling load calculation is given in Table 8.2.

	For 473K	For 773K	*Unit*
$m_{air} = \pi\, r^2 l_i \rho_{air}$	*0.022584659*	*0.022584659*	*Kg*
$m_{material} = \pi(R^2 - r^2) l_i \rho_{material}$	*12.66597814*	*12.66597814*	*Kg*
$Q_{air} = C_{pair} * m_{air} * \Delta T_{air}$	*3631.613127*	*10440.88774*	*Joule*
$Q_{material} = C_{pmaterial} m_{material} \Delta T_{material}$	*982879.9036*	*2825779.723*	*Joule*
$Q_{Total} = C_{pwater} * m_{water} * \Delta T_{water}$	*986511.5168*	*2836220.611*	*Joule*
$m_{water} = Q_{Total} / \Delta T_{water} * C_{pwater}$	*15.65891296*	*45.01937477*	*Kg*
$V_{water} = m_{water} / \rho_{water}$	*0.015658913*	*0.045019375*	*m^3*
$A_{water\ jacket} = \pi\left({R_1}^2 - R^2\right)$	*0.072693699*	*0.072693699*	*m^2*
$L_{water\ jacket} = V_{water} / A_{water}$	*0.215409494*	*0.619302296*	*M*
$A = 2 * \pi * R * l$	*0.475857039*	*0.475857039*	*m^2*
$1/U = 1/h_{water} + 1/h_{material} + 1/h_{air}$	*165.5102386*	*165.5102386*	*w/m^2-K*
$\Delta T_{Lm} = \Delta T_2 - \Delta T_1 / ln(\Delta T_2 / \Delta T_1)$	*61.25577859*	*129.9962265*	*K*
$Q_{convection} = U * A * \Delta T_{Lm}$	*4824.456859*	*10238.40037*	*Watt*
$\dot{m}_{water} = Q_{convection} / C_{pwater} * \Delta T_{water}$	0.07657868	0.162514292	*Kg/s*

Table 8.2 Impedance tube cooling load calculation.

Thermal analysis shows that for 473K a mass flow rate of 0.076 Kg/s is required to cool the impedance tube with a 215 mm long water jacket. For 773K a mass flow rate of 0.163 Kg/s is required to cool the impedance tube with a 620 mm long water jacket. Therefore, a 900 mm

long water jacket has been designated for the HAT test rig. The overall impedance tube cooling load calculation of 473K and 773K is provided in Table 8.2.

8.10.2 Cavity cooling load calculation

For the cavity cooling process, two different temperatures have been considered: 473K and 773K. The thermal cooling process is described below. A counter flow double pipe heat exchanger is being used to cool the cavity by using cold water. Assuming there is no airflow of the internal pipe, one side of the internal pipe is heated at $\Delta T_{in} = 473K$ at an entry point and another side of the exit point cooled at $\Delta T_{out} = 313K$. The water flows in the counter heat exchanger at the entry point at $\Delta T_{water\ in} = 298K$ and exits at $\Delta T_{water\ out} = 313K$. It is essential to calculate the mass flow rate $\dot{m}_{water}$ to cool the impedance tube at $\Delta T_{out} = 313K$, the required length $L_{water\ jacket}$ of a heat exchanger, and the total energy removed by the convective $Q_{convection}$ heat transfer.

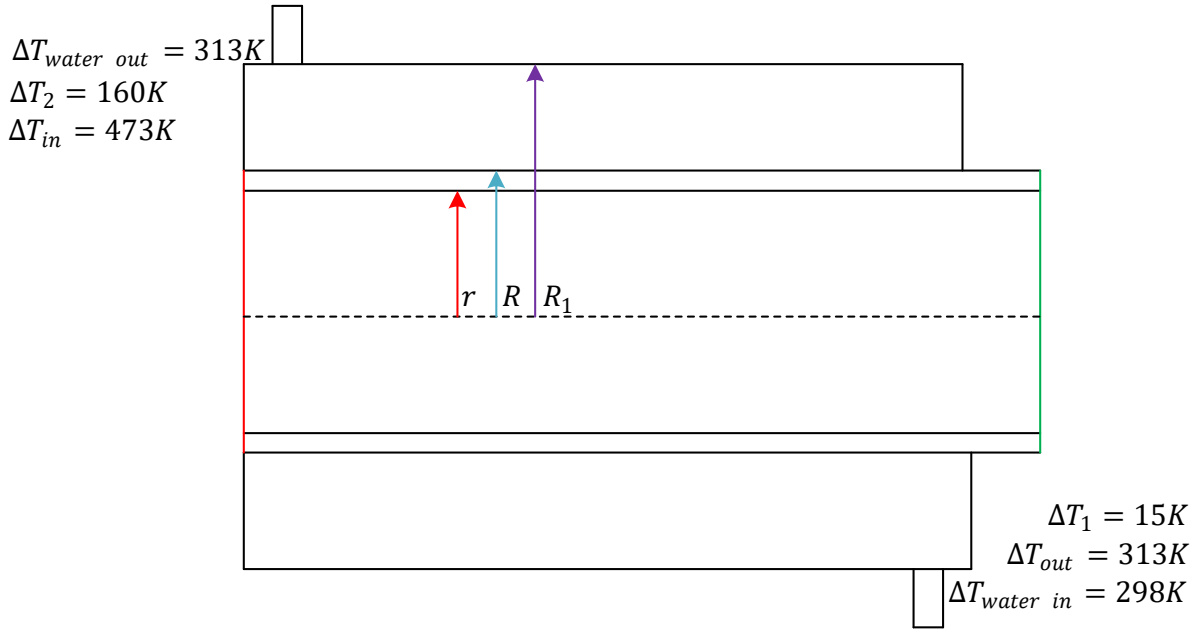

Figure 8.4 Schematic diagram of cooling cavity counter-flow heat exchanger.

The solution for the cavity cooling load calculation is specified below in Table 8.3.

	For 473K	For 773K	*Unit*
$m_{air} = \pi\, r^2 l_i \rho_{air}$	0.004265991	0.004265991	*Kg*
$m_{material} = \pi(R^2 - r^2) l_i \rho_{material}$	2.392462537	2.392462537	*Kg*
$Q_{air} = C_{pair} * m_{air} * \Delta T_{air}$	685.9713684	1972.167684	*Joule*
$Q_{material} = C_{pmaterial} m_{material} \Delta T_{material}$	185655.0929	533758.3921	*Joule*
$Q_{Total} = C_{pwater} * m_{water} * \Delta T_{water}$	186341.0643	535730.5598	*Joule*
$m_{water} = Q_{Total} / \Delta T_{water} * C_{pwater}$	2.957794671	8.503659679	*Kg*
$V_{water} = m_{water} / \rho_{water}$	0.002957795	0.00850366	m^3
$A_{water\ jacket} = \pi\left({R_1}^2 - R^2\right)$	0.072693699	0.072693699	m^2

$L_{water\ jacket} = V_{water}/A_{water}$	0.04068846	0.116979323	*M*
$A = 2 * \pi * R * l$	0.089884107	0.089884107	*m^2*
$1/U = 1/h_{water} + 1/h_{material} + 1/h_{air}$	165.5102386	165.5102386	*w/m^2-K*
$\Delta T_{Lm} = \Delta T_2 - \Delta T_1/ln(\Delta T_2/\Delta T_1)$	61.25577859	129.9962265	*K*
$Q_{convection} = U * A * \Delta T_{Lm}$	911.2862956	1933.920071	*Watt*
$\dot{m}_{water} = Q_{convection}/C_{pwater} * \Delta T_{water}$	0.014464862	0.030697144	*Kg/s*

Table 8.3 Cavity cooling load calculation.

The above thermal analysis shows that for 473K, a mass flow rate of 0.014 Kg/s is required to cool the cavity with a 40 mm long water jacket. For 773K, a mass flow rate of 0.030 Kg/s is required to cool the cavity with a 116 mm long water jacket. A 210 mm long cavity is selected for the HAT test rig. The overall cavity cooling load calculation of 473K and 773K are given in Table 8.3.

8.11 HAT design

The tube should be a uniform and constant diameter (maximum tolerance ±0.2 %) with a smooth wall. The tube wall should be firm and thick enough to prevent vibrations generated from a sound source and other sources. The thickness of the metal tube for circular cross-section should be approximately 5 % of the tube diameter (supposing the diameter is 161.5 mm, then the thickness of the wall should be 8 mm). The tube is required to be extensive enough to ensure the expansion of plane sound waves between the source and the sample. Vigilant designing for the placement of the microphones is imperative. It should be placed in such a way that it is positioned in the plane wave field. Generally, non-plane waves disappear at a distance from the sound source of approximately three times the tube diameter. The sound source is placed in the upstream section and the sample actuated at the other end, near the downstream section. In this system, the sound source governs the operating frequency range of the apparatus (Suhanek et al., 2008).

8.11.1 Tube frequency

The working frequency range is generally expressed as

$$f_l < f < f_u \tag{8.1}$$

where f is the operating frequency, f_l is the lower working frequency limit, $f_u$is the upper working frequency limit. The upper frequency limit is calculated from the equation given below

$$f_u < \frac{\ddot{K}c}{d} \; or \; d < \frac{\ddot{K}c}{f_u} \tag{8.2}$$

where d is the diameter of the tube 161.5 mm, $\ddot{K} = 0.586$ is the factor for circular cross-section, and c is the speed of sound. The selected diameter of $d = 161.5\text{mm}$. By substituting the values of c, d and $\ddot{K}$ in equation (8.2) the upper frequency limit f_u is 1300 Hz. The lower working frequency is calculated as shown in equation (8.3). The lower frequency limit depends on the distance between the microphone spacing and cavity volume of the system. The microphone spacing ought to be higher than 5 % of the wavelength for the specific lower frequency limit.

$$f_l > 0.05 \frac{c}{S_0} \tag{8.3}$$

In addition, the following condition must be satisfied in microphone position frequency calculation.

$$f_u * S_0 < 0.45\ c \tag{8.4}$$

For a selected distance $S_0 = 200\ \text{mm}$, the lower frequency limit is calculated from equation (8.3); therefore f_l is 86 Hz. Greater distance between the microphones increases the measurement accuracy. The spacing between the sound source and the microphone x, according to ISO 105342-2(Standard, 2001) should be:

$$x > 3 * d > 485\ mm \tag{8.5}$$

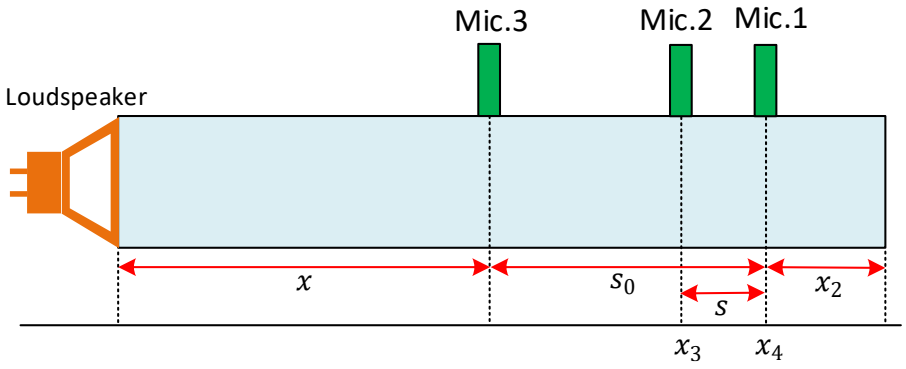

Figure 8.5 Schematic diagram of impedance tube and microphone position.

To design the selected space between the sound source and microphone 3, $x = 2050\ \text{mm}$

The distance x_2 between the test sample and microphone 1 depends on the tube diameter. Tube diameter refers to the size of the sample. To meet the condition given for the asymmetrical type:

$$x_2 \geq 2 * d = 323\ mm \tag{8.6}$$

designated x_2 is 325 mm. Therefore, the total length of the tube from the sound source to the sample is 3160 mm.

In general, molecules at high temperatures of 473K and 773K have more energy. Therefore they can vibrate faster. As molecules vibrate faster, the speed of sound can act faster in a high-temperature region. The method to define the speed of sound can be written as

$$c = \sqrt{\dot{\gamma} \mathrm{R} T} \tag{8.7}$$

where $\dot{\gamma}$ is the 1.390 specific heat ratio of air at 473K (Engineeringtoolbox, 2003,), R_m is the 8.314 J/mole-K molar gas constant, M_{air} is the 0.028 Kg/mole molar mass, $\mathrm{R} = \mathrm{R}_m / M_{air}$ is the 296.7 J/Kg-K specific gas constant. By substituting the values of $\dot{\gamma}$, R, and T in equation (8.7) C_{473} represents 442m/s. By substituting the values of C_{473} in equations (8.2) and (8.3) the upper and lower frequency limit calculation gives f_u 1600 Hz and f_l 110 Hz. Similarly, for 773K $\dot{\gamma}$ value is 1.357 (Engineeringtoolbox, 2003,). By substituting the values of $\dot{\gamma}$ R and T in equation (8.7) C_{773} represents 558 m/s. By substituting the value of C_{773} in equations (8.2) and (8.3) the upper and lower limit calculation shows the upper frequency limit is f_u 2000 Hz and the lower frequency limit is f_l 140 Hz.

8.11.1 Microphone location

There are three locations for a microphone in the impedance tube. This particular tube utilises a 1.7 mm diameter probe microphone, with a 160 mm long probe. The two microphones must have similar characteristics. Once the microphone is installed into the test rig or impedance tube, the probe-diameter must be aligned with the inner surface of the impedance tube. The position of the microphone is required to be within the maximum tolerance limit 0.2 mm, and the third opening needs to be sealed while using other microphones. During the experiment it is necessary to keep the test rig sealed as much as possible to avoid air leakage. To increase the measurement accuracy at a higher frequency, a third microphone location within distance S is implemented. The microphone diameter must be small in comparison with the ratio of C/f_u. It is recommended that the microphone diameter is smaller than 20 % of the distance between them - ISO 2001 (Standard, 2001).

$$d_{mic} < 0.2 * S \tag{8.8}$$

As a result, the smallest possible distance for the value of S 115 mm is designated. By taking equations (8.3) and (8.4) for the distance 115 mm, the upper and lower frequency limit calculations are $f_u < 1334$ Hz, $f_l < 148$ Hz. Similarly, for $\mathrm{S}_0$200 mm the upper and lower frequency limit calculation gives $f_u < 767$ Hz and $f_l < 85$ Hz. The above calculation shows

that an impedance tube with three microphone locations has a usable frequency range of 85 Hz to 1334 Hz in ambient temperature conditions.

8.11.2 Microphone frequency calculation

For 473K microphones 1 & 2, the smallest possible distance of S is equal to 115 mm. By substituting the value of S 115 mm into equations (8.3) and (8.4) upper and lower frequency limit calculation gives $f_u < 1728$ Hz and $f_l < 192$ Hz. Similarly, for S_0 200 mm upper and lower frequency limit calculation gives $f_u < 994$ Hz and $f_l < 110$ Hz. The above analysis shows that for 473K, a 161.5 mm diameter impedance tube with three microphone locations has a usable frequency range of 110 Hz to 1728 Hz. Similarly, for 773K microphones 1 & 2, substituting the smallest possible distance of S 115 mm into equations (8.3) and (8.4), the upper and lower frequency limits are $f_u < 2183$ Hz and $f_l < 242$ Hz. Similarly, for S_0 200 mm the upper and lower frequency limits are $f_u < 1255$ Hz and $f_l < 140$ Hz. From the above analysis, for 773K, a 161.5 mm diameter impedance tube with three microphone locations has a usable frequency range of 140 Hz to 2183 Hz.

8.11.3 Outline of impedance tube thermal calculation

Temperature Kelvin	Energy required watt	Water requires Kg	Required length mm	Mass flow Kg/s
473K	4824	15.66	215.41	0.08
773K	10238	45.02	619.30	0.16
Cooling the cavity to create ΔT				
473K	912	2.96	40.69	0.01
773K	1933	8.50	116.98	0.03

Table 8.4 Thermal and mass flow calculation.

Impedance tube overall thermal calculation of two different temperatures, required energy, mass flow, and length of the tube is specified in Table 8.4.

8.11.4 Outline of impedance tube frequency calculation

Temperature	Lower limit frequency	Upper limit frequency
Ambient	85 Hz	1300 Hz
473K	110 Hz	1603 Hz
773K	140 Hz	2025 Hz

Table 8.5 Impedance tube frequency calculation.

Impedance tube frequency range calculation of three different temperatures, lower and upper limit, is specified in Table 8.5.

8.11.5 Outline of microphone frequency range calculation

Microphones 1 & 2 S-115 mm

Temperature	Lower limit frequency	Upper limit frequency
Ambient	148 Hz	1334 Hz
473K	192 Hz	1729 Hz
773K	243 Hz	2184 Hz

Table 8.6 Frequency range for microphones 1 and 2.

Impedance tube, microphone location 1 and 2's three different temperatures lower and upper frequency range is specified in Table 8.6.

Microphones 1 & 3 S_0-200 mm

Temperature	Lower limit frequency	Upper limit frequency
Ambient	85 Hz	767 Hz
473K	110 Hz	994 Hz
773K	140 Hz	1256 Hz

Table 8.7 Frequency range for microphones 1 and 3.

Impedance tube, microphone location 1 and 3's three different temperatures lower and upper frequency range is specified in Table 8.7.

8.12 Conclusion

HAT design is carried out based on the current duct diameter of the test rig. It has two thermal heat exchangers. The first heat exchanger is to protect the sound source and the second heat exchanger is to create the temperature difference in the cavity. It has three convenient microphone locations to determine the variable frequency in the test rig. At the back of the cavity a plunger is mounted, which can create a variable cavity depth and introduce bias flow into the system. The cavity temperature can be controlled by the ceramic heater and by increasing or decreasing the mass flow of the cold-water cavity heat exchanger. Three thermal sensors are attached to the system to monitor the temperature near the sample, the microphone, and the sound source. The system has a usable frequency range of 85-2000 Hz for duct and 85-2200 Hz for the microphone. It can be constructed by using an A312 316 type stainless steel seamless pipe.

8.13 Appendix-B

The primary purpose of this experiment is to determine the magnitude of the amplitude and phase of the relationship between two different orifice shapes between the complex amplitudes of the acoustic pressure in the duct and the resonator cavity. The peak attenuation magnitude and phase for each case are analysed in an attempt to fit a mathematical relationship. In other words, it can govern the experimental modal analysis of frequency response function (FRF).

8.13.1 FRF analysis

FRF is an experimental analysis that has complex values, which contain magnitude and phase information to verify the relationship between acoustic pressure in the duct and resonator cavity (Wang et al., 2019). Mathematical representation of the relationship between the input and the output of a system is to identify functions such as frequency-based measurement, resonant frequency, and damping. It has mode shapes of physical structure sometimes referred to as a transfer function between the input and output of a system, and it can express the frequency domain relationship between an input and output of a linear time-invariant system. In an FRF measurement, the following can be observed. Formation of resonance peaks indicates the presence of the natural frequencies of the structure under test. Damping is proportional to the width of the peaks; a wider peak represents heavier damping. Frequency response functions are most commonly used for single input and single output analysis. The frequency response function is used in situations where the output of the system is expected to be noisy when compared to the input.

$$FRF = \frac{P_m}{P_{du}} \tag{8.9}$$

where FRF is the frequency response function, P_m is the mean pressure in the resonator cavity, P_{du} is the mean pressure in the duct. Any function that has an amplitude $\overline{\mathrm{A}}$ and phase $\emptyset$ can also be transformed into real γ and imaginary δ terms (Community PLM Siemens automation, 2016, July 07)

$$\overline{\mathrm{A}} = \sqrt{\gamma^2 + \delta^2} \tag{8.10}$$

$$\emptyset = tan^{-1}\frac{\delta}{\gamma} \tag{8.11}$$

8.13.2 Sound pressure level

It is a force of sound on a surface area (m^2) perpendicular to the direction of the sound. Unit is N/m^2 or Pascal. The mathematical definition of SPL can be written as

$$SPL = 10\log\left(\frac{p}{p_0}\right)^2 = 20\log\left(\frac{p}{p_0}\right) \tag{8.12}$$

where p is the pressure of an incoming sound wave, p_0 is the reference sound pressure corresponding to $2x10^{-5}$ (Pa) and SPL represents sound pressure levels. To consider the potential of acoustic SPL as a resonator saturation factor, a range of levels needs to be measured for typical cases, and then the performance metrics for each SPL condition compared. In general, it is expected that the physical quantity relevant to the nonlinear performance is the particle velocity in the orifice. Conversely, in most cases, it would take great effort to measure the particle velocity in the orifice so that the amplitude often expressed in terms of sound pressure level.

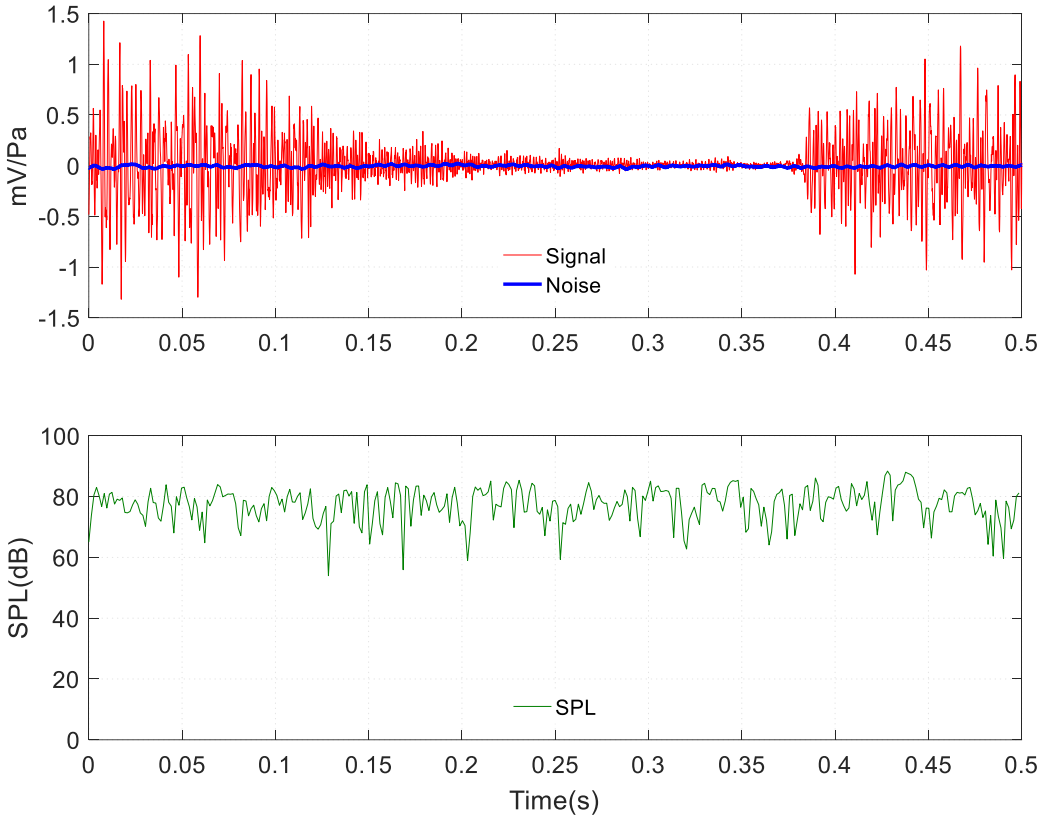

Figure 8.6 Analysis of SNR and SPL in the resonator.

Resonator performance factor arrangement with normal sound incidence is typical to specify the SPL at the liner surface. The measured experiment with a microphone installed at the liner surface section represents SPL 85 shown in the bottom part of Figure 8.6.

8.13.3 Signal to noise ratio

Signal to noise ratio is defined as the logarithmic power ratio of the signal and noise. It is the power ratio of independent signals, one called signal and the other called noise. When the signal is measured as a power, the mathematical definition can be expressed as

$$SNR = 10 \log \frac{Signal\ power}{Noise\ power} = 10\ log \frac{p_s}{p_n} dB \quad (8.13)$$

where SNR is the signal to noise ratio, p_s is the signal power and p_n is the noise power. If the signal is measured in the form of voltage, the mathematical expression of the signal to noise ratio becomes

$$SNR = 20 \log \frac{RMS\ Signal\ voltage}{RMS\ Noise\ voltage} = 20 \log \frac{V_S}{V_N} dB \quad (8.14)$$

where V_S is the RMS signal voltage and V_N is the RMS noise voltage. The measurement of the recorded SNR for resonator performance factor is calculated from equation (8.14), which is 23.87 and plotted at the top of Figure 8.6 with respect to time. Once the liner sample is introduced into the test rig, the sound pressure level is measured at each microphone with the sound source on and off. The sound source should generate a sufficient signal at all microphone locations. Careful consideration must take place to ensure that the measured signal in each test frequency band is at least 10 dB greater than the background noise. The input signal is equal to the output signal plus noise. SNR is a measure that describes how much noise output a device has in relation to the signal level. It is a two-level measurement. First, it is necessary to measure the output level under the test with no signal input then apply the signal to the test rig and record another level of measurement. SNR is generally a measure of the quality of the peak, which is proportional to the square root of the strength of the signal and the noise in the signal. In other words, it is the ratio of the magnitude of the signal and variance of the noise. It is a function of position. A low SNR means the noise is loud and will make it hard to determine the magnitude of the signal accurately. A high SNR means the noise is small.

8.13.4 Experimental setup

The resonator is installed on top of the dummy liner. The length of the dummy liner is 524 mm long and the diameter is 165 mm and can be removed from the test section. Two heavy-duty stainless-steel rings were used to attach the dummy liner into the test rig.

Figure 8.7 Resonator installed into the test section.

There are four $1/4^{"}$ duct microphone locations as shown in Figure 8.7 on the circumference of the dummy liner. One is installed on top of the resonator and the other three microphones are for FRF and higher-order modes. Apart from those four microphone locations, there are another four ports also available for $1/2^{"}$ microphones designated as the upstream and the downstream microphones. In addition, there are four small holes present in the test section to provide access for a pitot tube to enable static pressure measurement to calculate mass flow rate and pressure drop for static pressure measurement.

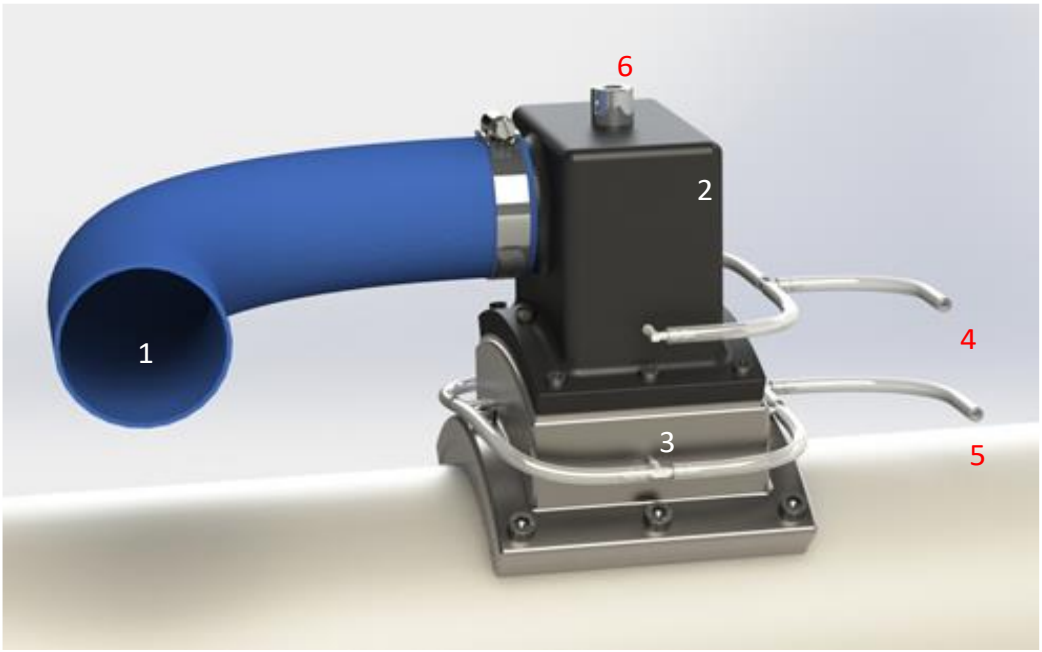

Figure 8.8 Resonator flow, cavity, static pressure tap & microphone location.

Figure 8.8 shows 1) Bias flow delivery system through the blue pipe, 2) Plenum of the bias flow, 3) Resonator cavity, 4) Static pressure tap for the plenum, 5) Static pressure tap for the resonator, 6) Microphone port for the resonator. Compressed air is used to introduce a bias

flow delivery system. In addition, three rotameters are connected in series to measure the range (small, medium and high) of the mass flow rate of the bias flow delivery system. To introduce cross flow into the system, a two-stage centrifugal pump is used into the 30 m long wind tunnel earlier shown in Figure 4.3. Rotameter is used to measure compressed air mass flow rate, Pitot tube anemometer is used to measure cross-flow velocity, differential pressure manometer is used to measure plenum, upstream, and downstream pressure. In this experiment, parameters are used to evaluate the sound attenuation, peak amplitude of the resonance, and FRF pressure response function.

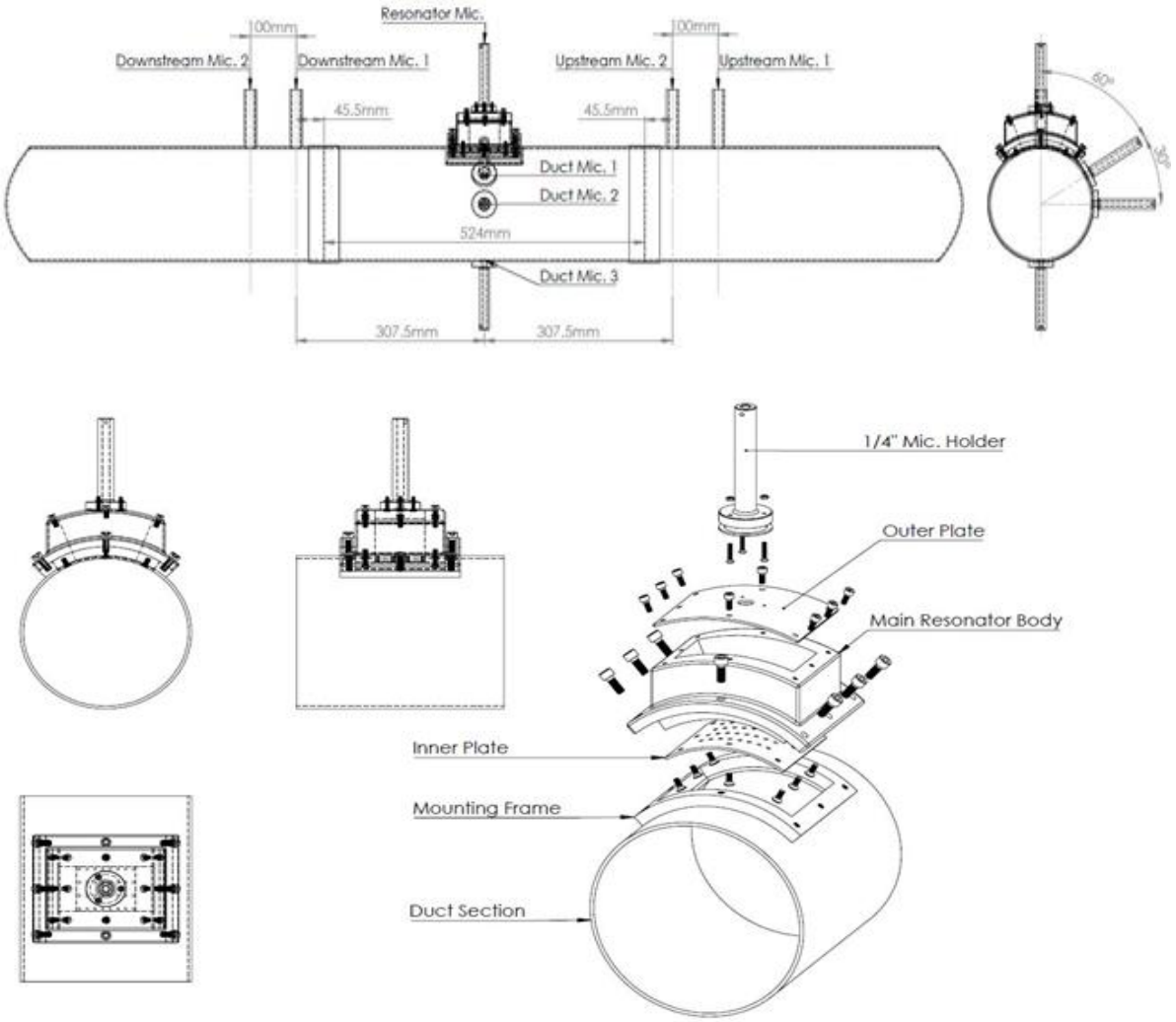

Figure 8.9 Schematic diagram of resonator assembly.

A detailed drawing of the central resonator cavity, mounting frame, duct section, inner plate, main resonator body, outer plate and mic holder is shown in Figure 8.9. Two different types of plate have been used for this experiment, circular and slots with various porosity. The details of the inner plates are given in Table 8.8.

Plate	Shape	Diameter	Porosity
Plate 1	Circular	1.08mm	2.48 %
Plate 2	Circular	2.45mm	4.26 %
Plate 3	Circular	3.05mm	6.97 %
Plate 4	Circular	4.05mm	12.23 %
Plate 5	Slots	-	2.48 %
Plate 6	Slots	-	4.48 %
Plate 7	Slots	-	6.97 %
Plate 8	Slots	-	12.23 %

Table 8.8 Geometric parameters of the inner plate.

8.14 Discussions

Input excitation and output response have been captured to calculate FRF (Wang et al., 2019). For this experimental analysis, a single microphone is actuated on top of the resonator and the other three placed in the circumference plane to produce three different FRF measurements. The white noise signal is filtered by using a signal processing toolbox in Mat-lab. The effect of this measurement is to confirm that when the truncated white noise signal is introduced only plane waves are transmitted in the line, because the measured response does not vary in the frequency domain with varied locations within the same circumference.

8.14.1 Plate 3 and 7 FRF magnitude & phase difference with no flow

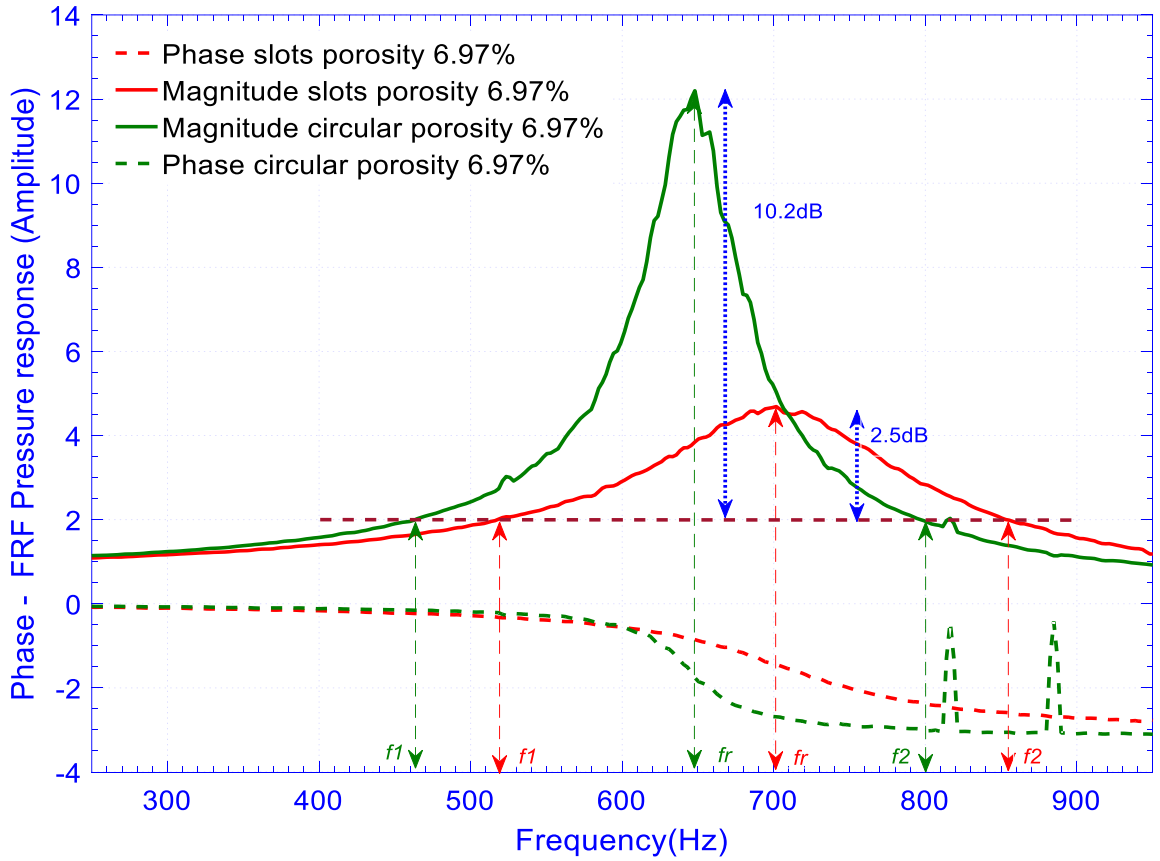

Figure 8.10 Shows plate 3 and 7 FRF magnitude & phase difference with no flow.

The amplitude and phase of an FRF function for plates 3 (circular) and 7 (slots) is shown in Figure 8.10. It can be observed that the solid green line displays a greater peak compared to the solid red line.

$$D_f = \frac{f_r}{f_2 - f_1} \tag{8.15}$$

where D_f is the damping factor, f_r is the frequency of the resonance peak and f_1, f_2 is the lower and higher frequency range related to the width of the peak shown in Figure 8.10. A peak indicates that natural frequency and damping is proportional to the width of the peak. For the green curve 10.2 dB down the associated damping factor is 1.91 (plate 3), whereas for the red curve 2.5 dB down the associated damping factor is 2.08 (plate 7). The loss factor is inversely proportional to the damping factor. Therefore, it can be stated that plate 7 would be considered to have more damping when compared to plate 3, for the no flow case. Overall analysis shows that the slots type shape exhibits the heavy damp.

8.14.2 Plate 4 and 8 FRF magnitude & phase difference with no flow

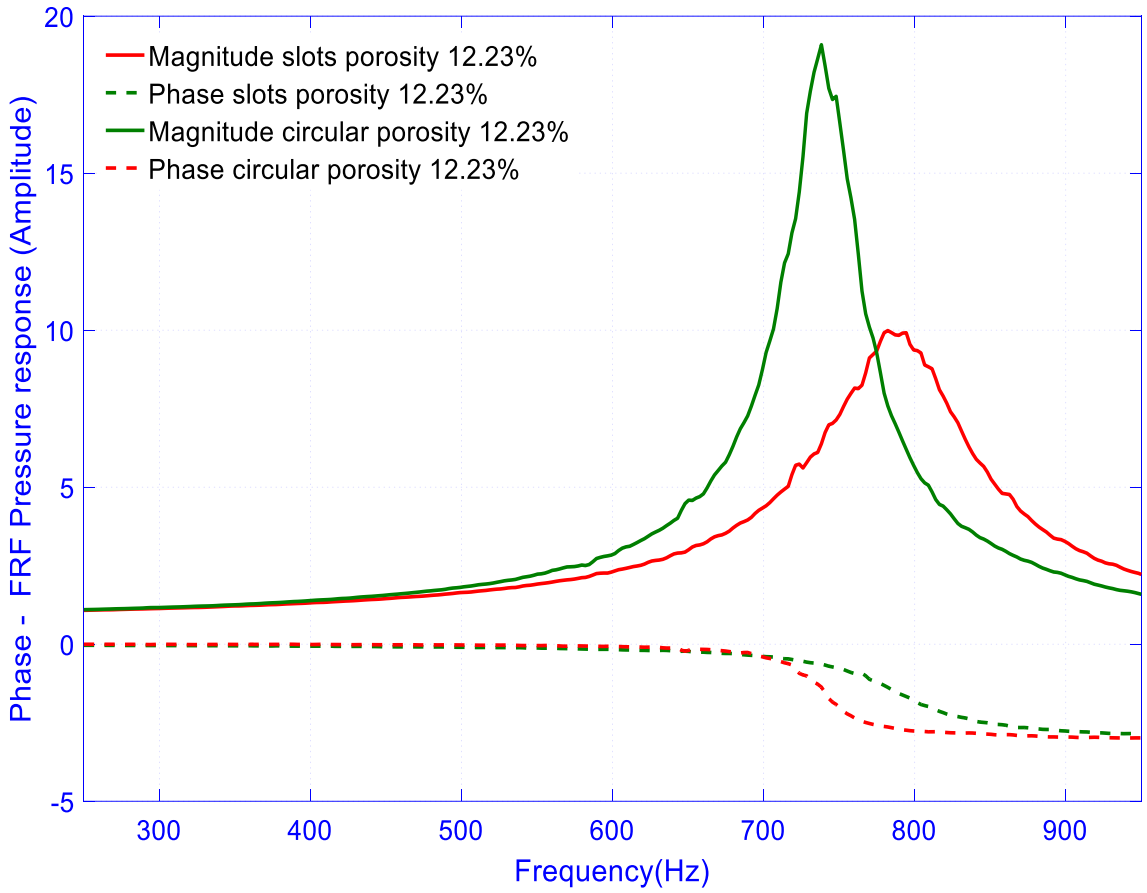

Figure 8.11 Shows plate 4 and 8 FRF magnitude & phase difference with no flow.

The plot of the amplitude and phase of an FRF function for plates 4 and 8 is shown in Figure 8.11. The FRF analysis displays that the solid green line appears to have a greater peak compared to the solid red line. Plate 4 has a circular orifice of diameter 4.05 mm and plate 8 has a slots type shape with similar porosity. By comparing plates of similar porosity with different shapes it is highlighted that the plate with the slots shape exhibits a heavier damping compared to the plate with circular orifices. The heavier the damping, the better the energy removed from the system as the amplitude of oscillations decreases with time. The greater the damping, the faster the oscillations will decrease in size.

8.14.3 Plate 2 and 6 FRF magnitude & phase difference with no flow

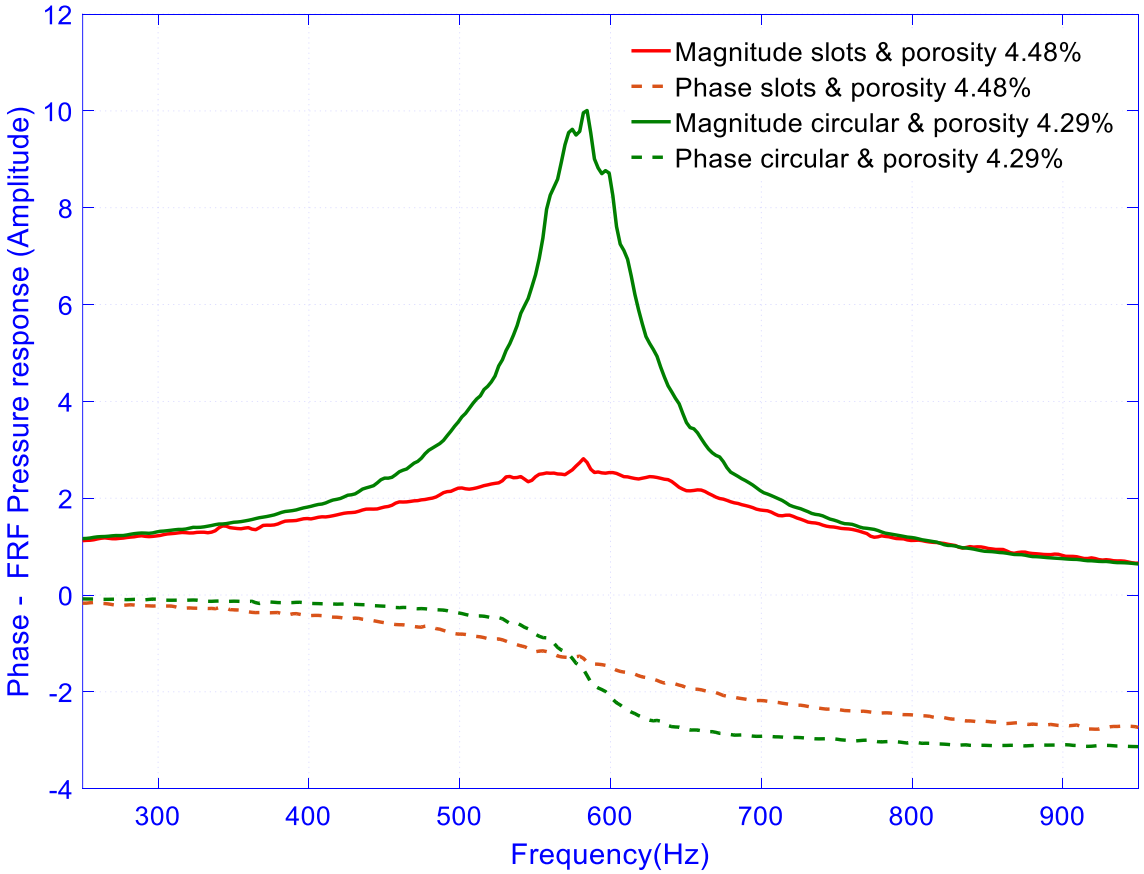

Figure 8.12 Shows plate 2 and 6 FRF magnitude & phase difference with no flow.

Plate 2 has a circular diameter of 2.05 mm equivalent to 4.29 % porosity, whereas plate 6 has a slots shape equivalent to 4.48 % porosity. Figure 8.12 shows that plate 2 (circular orifice) displays the greater amplitude compared to plate 6 (slots shape). Both plates have displayed a similar peak frequency and width. Overall comparison between the two profiles shows that the slots type shape has the capability to generate a heavier damp than the circular orifice. Loss factor is inversely proportional to the damping factor.

8.14.4 Plate 1 and 5 FRF magnitude & phase difference with no flow

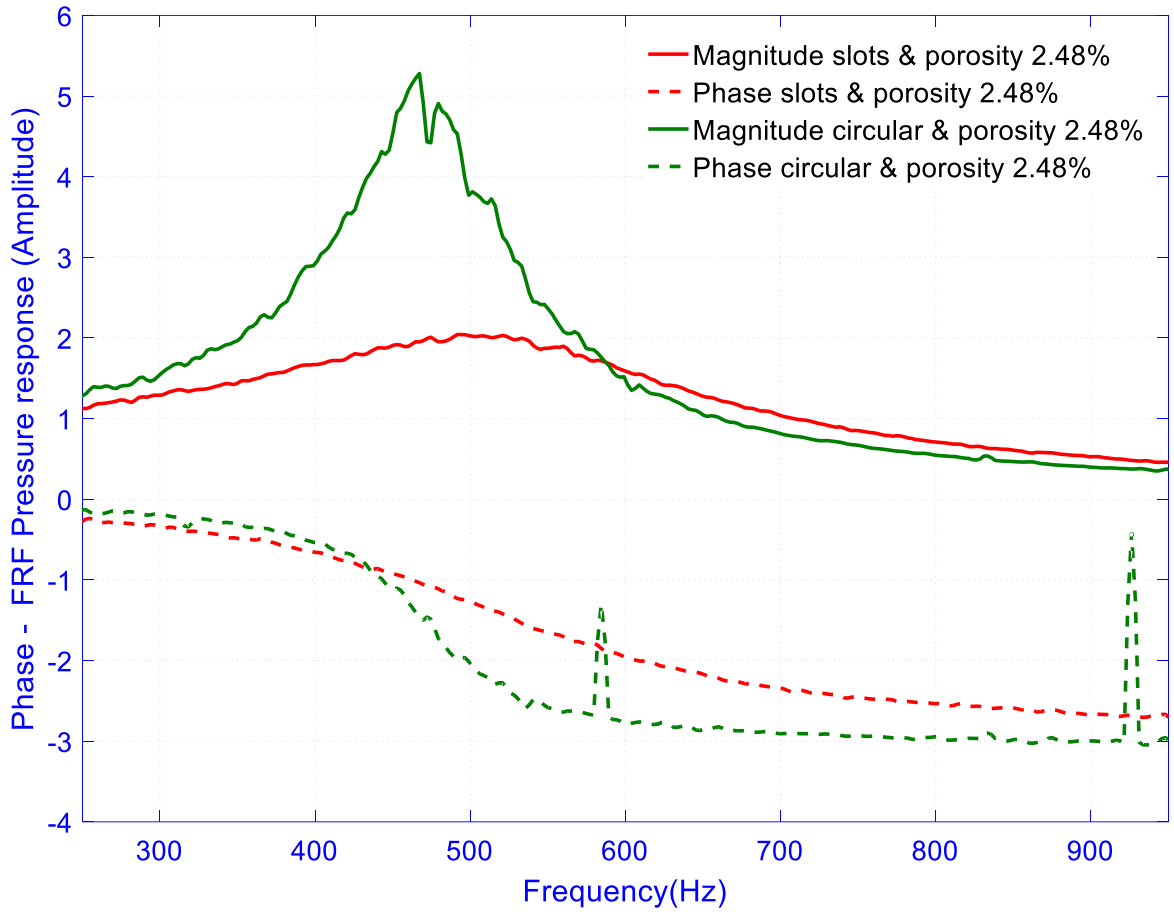

Figure 8.13 Shows plate 1 and 5 FRF magnitude & phase difference with no flow.

Figure 8.13 shows that plate 1 (circular orifice) has greater amplitude compared to plate 5 (slots shape). Both plates have similar porosity but developed different amplitudes due to their different geometry (shapes). Plate 1 has a circular orifice of diameter 1.08 mm, which refers to 2.48 % of porosity and plate 8 has a slots type shape with similar porosity. By comparing plates of similar porosity with different shapes it is highlighted that the plate with the slots shape (red solid line) exhibits a heavy damping compared to the plate with a circular orifice.

8.14.5 Plate 1-4 and 5-7 FRF magnitude comparison with no flow

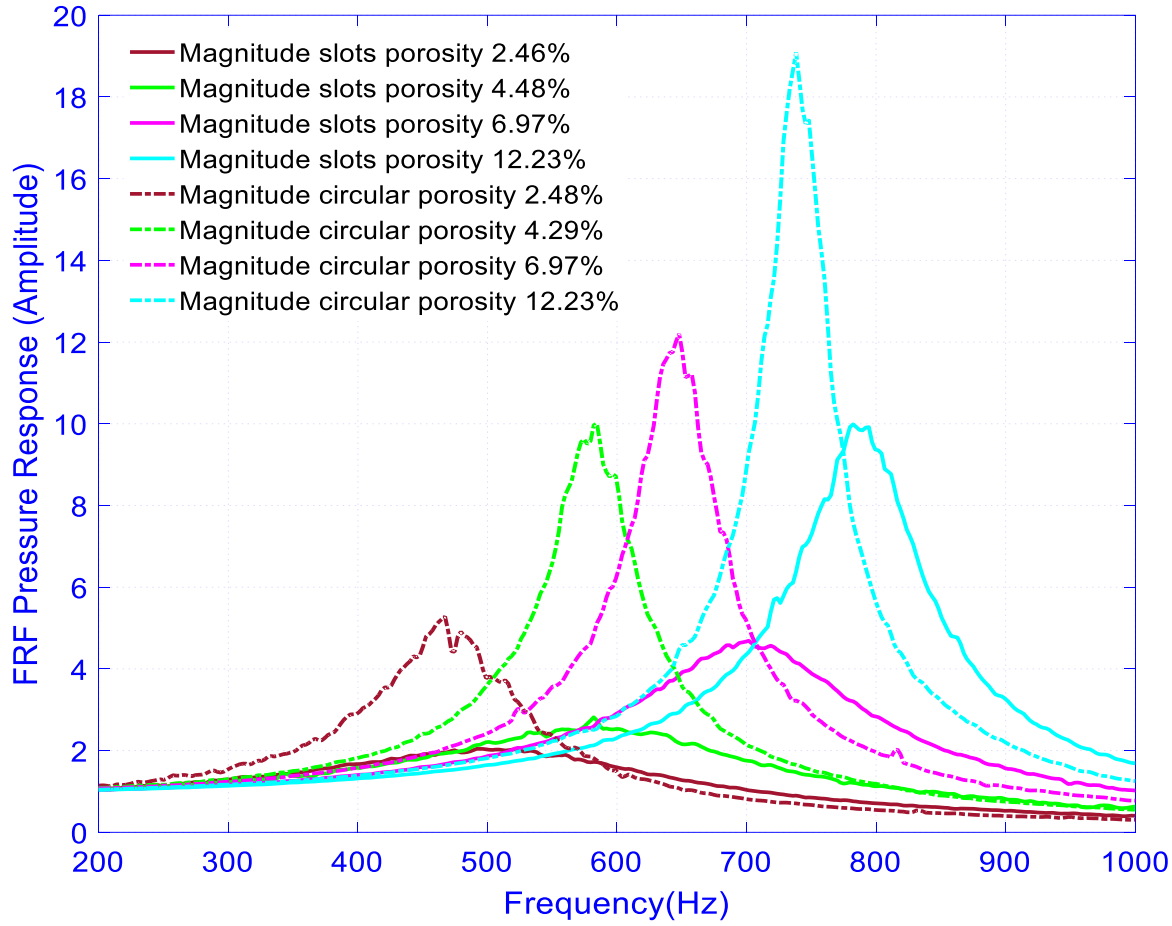

Figure 8.14 Shows overall FRF magnitude comparison with no flow.

FRF analysis of four different plates with a circular orifice shows that increasing porosity is associated with an increase in amplitude and peak frequency range. Figure 8.14 shows that the brown dashed line, representing porosity 2.48 %, indicates the lowest amplitude (5.25) and peak (470 Hz), whereas the cyan dashed line, representing porosity 12.23 %, indicates the highest amplitude (19) and peak (740 Hz) when compared with all other combinations. From the above analysis, it can be stated that plates with a slots type profile, with the smaller percentage of porosity, exhibit a weak peak in the low-frequency range, whereas plates containing the greater percentage of porosity exhibit a better peak, which shifts towards the high-frequency range. Overall, comparisons from the eight plates indicate that plates with a circular orifice developed greater amplitudes, and plates with slots shapes have produced heavier damping. While peaks in FRF environment become wider relative to the peak, the damping increases, which explains that any vibration of the system set in motion in the structure would decay faster due to increased damping.

8.14.6 Plate 1 and 5 FRF magnitude comparison with cross-flow

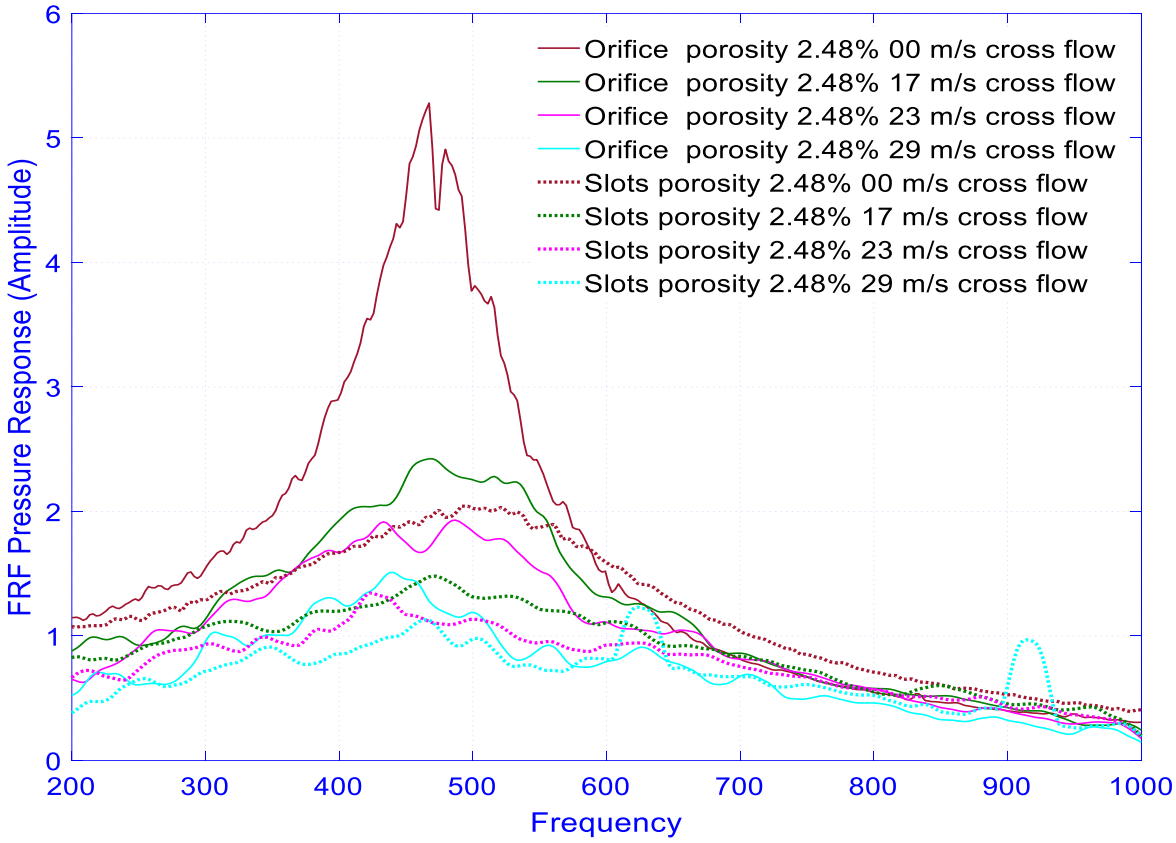

Figure 8.15 Shows plate 1 and plate 5 magnitude comparison with cross-flow.

In this framework, two different types of plates with four different flow settings are introduced. Eight different types of experimental analysis are illustrated in Figure 8.15. The above experimental analysis of FRF magnitude comparisons in the presence of cross-flow shows that increasing cross-flow velocity in the duct results in a decrease in amplitude. In addition, the peak frequency range remains the same for both plates 1 and 5. Overall comparison suggests that an increase in cross flow did not appear to have frequency shift but indicates that slots type shapes have the ability to exhibit more damping than the circular orifice.

8.14.7 Plate 4 and 8 FRF magnitude comparison with cross-flow

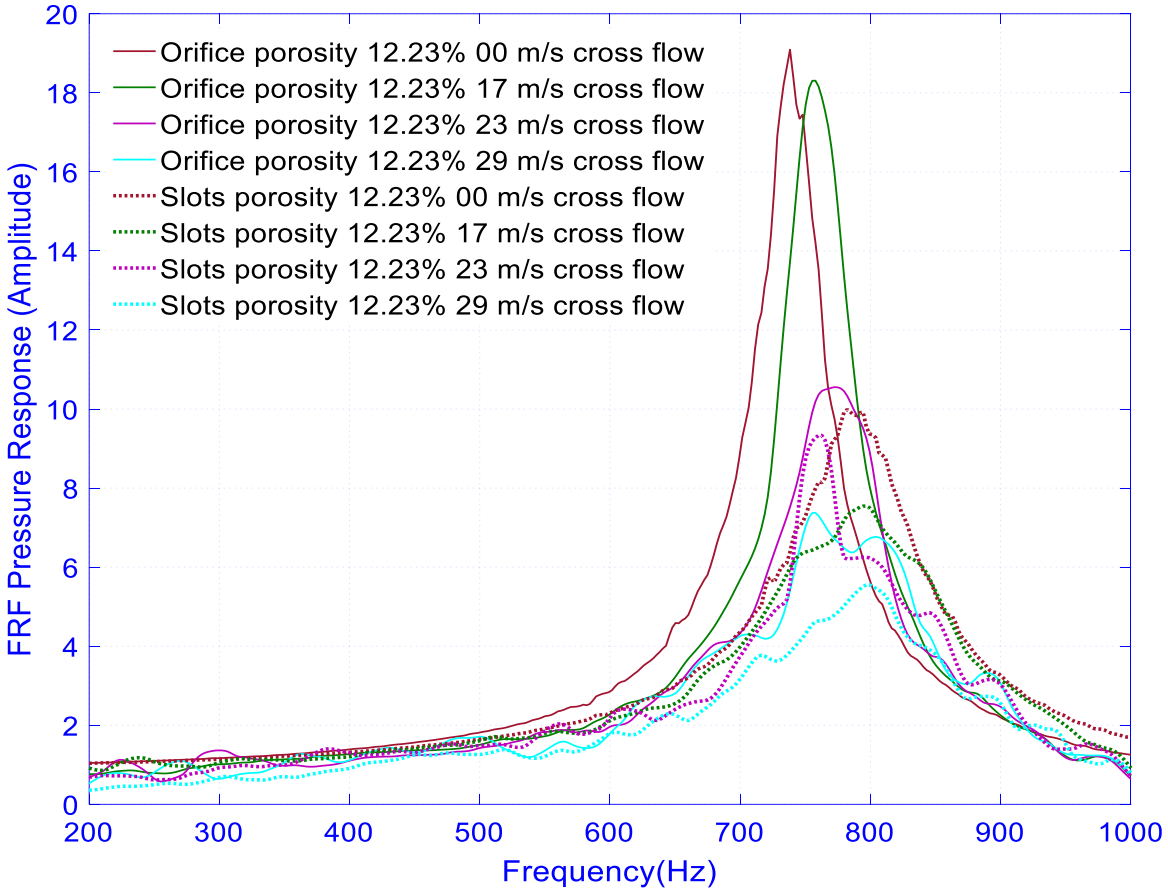

Figure 8.16 Shows plate 4 and plate 8 magnitude comparison with cross-flow.

The experimental analysis of plates 4 and 8 FRF magnitude comparisons in the presence of cross-flow are shown in Figure 8.16. Both plates have a similar porosity of 12.23 %, showing that by increasing cross-flow velocity in the duct there is a decrease in amplitude. Under these conditions, the peak frequency range is not similar to plates 1 and 5; in this case, the peak shifts towards the high-frequency range. Furthermore, it is evidenced that an increase in porosity refers to an increase in amplitude. Overall comparison of circular orifice and slots type shapes shows that the latter has the capability to enhance energy dissipation characteristics of the system under cyclic stress.

8.15 Conclusion

This additional work is carried out to check the difference between the slots and circular orifice damping performance, which can create better damp inside the resonator. For the no flow case, it shows that by increasing porosity, peak amplitude shifts towards the high-frequency range. In the presence of cross-flow, with a lower percentage of porosity, circular and slots type orifices decrease their peak amplitude without frequency shift. If the percentage of porosity increases significantly, in the presence of cross-flow peak amplitude decreases, and the peak shifts towards the high-frequency range.